Effects of Defects on Compressive Kinking and Fracture of Fiber Reinforced Composite Materials and Structures

by

Paul Davidson

A dissertation submitted in partial fulfillment
of the requirements for the degree of
Doctor of Philosophy
(Mechanical Engineering)
in The University of Michigan
2013

Doctoral Committee:

Professor Anthony M. Waas, Chair
Associate Professor Veera Sundararaghavan
Professor Alan S. Wineman
Chandra S. Yerramalli, Technology Director, Ming Yang Wind Power USA Inc.

To Father, Mother, Michelle, Jeevan, Eva, and Astro

ACKNOWLEDGEMENTS

I would like to express my deepest appreciation to my advisor and committee chair, Professor Anthony Waas, who possesses an attitude of a genius, a spirit of adventure, a limitless energy and an infectious enthusiasm towards research and scholarship. This dissertation would not have been possible without his guidance, and encouragement.

I would also like to thank my committee members, Professor Alan Wineman, Professor Veera Sundararaghavan and Dr. Chandra Yerramalli, for their valuable feedback and support. I would especially thank Dr. Yerramalli, who supervised my research during my internship at GE Global Research. I am also grateful to GE Global Research and Boeing Co, for funding my research.

I appreciate the spirit of fellowship among Composite Structures Lab members. I especially thank Amit, Mark, Christian, Pavana, Wooseok, Brian, Evan, and Trisha for their help with experiments, numerical models and the numerous technical discussions.

Staff and Technology support members of Aerospace Engineering Department are the some of the kindest and most helpful people I have met. I would like to thank, Denise for all the help and participating in the occasional prank, Terry for making parts often under very tight deadline, Tom & Eric for their immense knowledge about machines and labs.

I would like to thank my friends for all the good times; Amit, Abhijit & Vidya, Gayatri P & Victor, Mark & Neha, Ashwani & Chaitanya, Gayatri S, Devayani, Dhanajay, Debapriya, Chaitanya, Devesh, Saumil & Madhura, Pavana, Kalyan, Brian,

Nicolas, Eric, Christian, Trisha, Ken and all the other I missed.

Words would not describe my profound gratitude and love for my parents and sister, who have given me unwavering and absolute support through out my lifetime, and always encourage me to pursue my dreams.

TABLE OF CONTENTS

CHAPTER

LIST OF FIGURES

Figure

LIST OF TABLES

Table

LIST OF APPENDICES

Appendix

CHAPTER I

Introduction

1.1 Motivation and outline

Composites are combinations of two or more distinct materials usually resulting in a material that displays a variety of physical properties that are better than each of the constituents on their own. The successful implementation of composite materials in design is predicated upon establishing material properties early in the design cycle. As outlined in the ”Design and manufacturing guideline for aerospace composites” [69], a preferred design process should be able to, identify intended manufacturing process, identify defects during manufacturing, and approximate material allowables like strength, using the said manufacturing process. Strength allowables, tensile and compressive, are critical because these are the parameters that set the limits on the stability of structures, particularly in aerospace applications where weight is a critical factor.

As with any material system, defects in composites are an unavoidable consequence of unintended variations in the manufacturing processes. The design philosophy in dealing with defects has been to apply a large arbitrary factor of safety, of about $2 \sim 3$ [69], while designing, which in turn drives up the cost of structures. The obvious solution is to reduce the number and types of defects in the material, which is not always possible or has large a cost penalty associated with it. The alternative is to understand how defects can influence strength allowables and reduce the factor of safety such that the design is still tolerant to the observed defect. The latter approach is commonly known as *defect tolerant design*. The study of defects and its influence on strength allowables is broadly referred to as *defect mechanics*.

In this dissertation, studies on two prevalent failure mechanisms under defect mechanics are presented. These failure mechanisms are; (a) *Kinking*, under compressive loads, and (b) *fracture*. Kinking failure refers to kink band formation in composites under compressive loading. Fracture refers to initiation and progression of a crack from a pre-existing crack like defect within a composite, or homogeneous material under compressive or tensile loading.

In the first part, studies relating to kinking failure are introduced in section 1.2 and detailed in chapters II,III & IV. Experimental, analytical and numerical analysis were conducted to study kinking failure in composites with defects, like waviness and holes. Analysis methods with varying degree of fidelity are presented to compute strength knock-downs due to these defects. A new analytical formulation for kink band formation was also developed. This formulation provides pre-peak, peak and post-peak response during kinking failure. The formulation highlights some of the deficiencies of previous analytical models and can potentially replace micro-mechanics based finite element models for strength prediction.

In the second part, a fundamental and critical re-examination of fracture mechanics is introduced in chapter V and detailed in VI & VII. In chapter VIII, important results and significant contributions of the studies carried out in this dissertation are summarized. Using experimental results and examples from literature it is shown that Linear Elastic Fracture Mechanics (LEFM) based energy release rate methods are of limited use for predicting certain types of crack growth. An alternative theory of crack initiation and growth that does not rely on the criticality of the energy release rate for crack growth is presented. This theory is shown to cover a wider range of crack initiation and growth problems. It also provides a phenomenological explanation for non-smooth crack growth and R-curve behavior observed in experiments with composite specimens.

1.2 Introduction: Kinking failure due to defects

Defects in composites can be due to manufacturing processes, design or environment. For example, wrinkling, delamination, resin pockets are common manufacturing defects found in composites[35]. Defects can also be introduced as an unintended consequence of the design and manufacturing process; eg; optical fiber sensor inserts in composites [86] or ply drop-offs in non-uniform sections. Environmental factors like hail, lightning strikes, etc; can also induce damage/defects. These defects essentially act as local stress raisers. In compression, it is observed from experiments that these stress raisers cause failure due to kinking in localized region of the component. Therefore, the problem of compression of composites with defects can be understood as two sub-problems and can be solved as such. The two sub problems are; first, non-homogeneous stress in a structure because of a defect, and second, the kink band formation when the structure is stressed. Taking this idea further, there are two solution approaches, as shown in figure 1.1, available to solve the problem; first, referred to as *physics based analysis*, is where the actual physics of kink band formation during structural analysis is captured. In a second approach referred to as *criterion based analysis*, a strength value obtained from an independent kinking analysis is used as an input for a separate structural analysis where failure is determined by a failure criterion that uses the input from the kinking analysis. In the following chapters each of these methods are illustrated.

In chapter II, a physics based approach is described to study the compressive strength knock-down because of kinking failure in wavy composites. Compression strength experiments were conducted on carbon fiber unidirectional specimens with

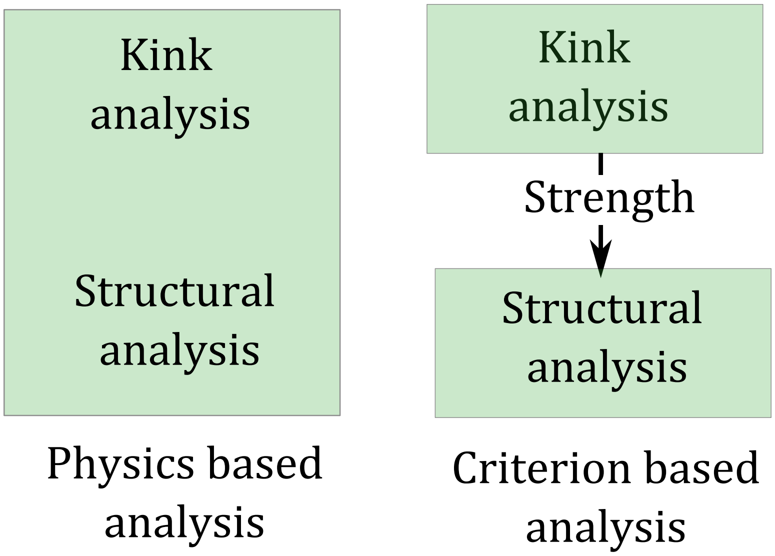

Figure 1.1: Physics based and criterion based analysis methods for composite strength

defects of varying aspect ratios. A local-global modeling approach was used to simulate and predict kink banding, which was observed to be a strength limiting mechanism. The numerical model was also used to conduct a parametric study on the influence of misalignment angle and defect aspect ratio. Chapter III outlines an analytical, criterion based model, and a numerical, physics based, model to predict the compressive strength of a relatively thin laminate with a hole.

The analysis approaches described above are not restricted to compressive failure. These can also be applied to tensile loading cases as is shown in Appendix B. However, under tensile loading the mechanism of failure is different, thus, a criterion similar to kinking (i.e. fiber fracture) has to be first developed to proceed. As shown in Appendix B, a unified model that can be used for predicting both tensile and compressive strengths using the *same set* of coupon level, material property data is presented.

From the studies conducted in chapters (II,III) and Appendix B, it will be evident that physics of kink band formation plays an important role in the compressive strength of composites. In chapter IV, a new analytical formulation for kink band formation will be presented. This formulation is developed with the aim of replacing computationally expensive finite element based micro mechanics models.

The results and methods presented are practical and validated against experimental data. They serve as a step in establishing a virtual building block, bottom-up approach to designing future airframe structures with composite materials. The results are useful for aerospace design engineers, particularly those that deal with airframe design.

CHAPTER II

Compression of thick composite with waviness

2.1 Introduction

The compression strength of a laminated composite structure is a design driver in many applications in the aerospace, automotive and wind turbine industries. Typically, any part designed using composite materials, to be used under compression, is designed with high factor of safety, ie; it is intentionally over designed. This is because of the fact that even small misalignment in fiber angles, of composite, with respect to loading direction, can lead to a drastic knock down in compressive strength [20, 61]. Misalignments are generally attributed to and are inherent part of the manufacturing process involved in making of a component. This is especially true in wind turbine blade industry because it requires a labour intensive manual manufacturing process. Misalignments can be caused due to incorrect curing procedure, foreign body, defects, inserts, crimping, etc. Manufacturing induced misalignments broadly fall under two criterion, (a) small mis-alignments; ie, mis-alignment angle (ϕ) less the 5° or (b) gross mis-alignments or waviness; ie; $\phi > 5^\circ$. Small mis-alignments are in general localized within a certain region of the composite and do not cause measurable, change in profile. Gross mis-alignment or waviness leads to a measurable change in profile of a composite section. An important point to note here is that waviness can have small mis-alignments within it. Since manufacturing induced misalignment cannot be completely eliminated, it is important to understand the basic failure mechanisms induced by these defects, and how these influence the compressive strength of composites.

Compression failure in composite, in the presence of defects, is complex because there are multiple failure modes (kinking[20], splitting[61], delamination and buckling) that can occur, and in some cases these modes can interact [76]. Each failure mode results in the lowering of compressive strength of the composite, but some failure modes are more catastrophic than others, like kinking. What complicates matter is that in thick composites with gross defects have a non-uniform geometry which induces non-uniform stresses in the composite. Hence, predicting compressive strength of thick composite with defects is essentially a problem of kinking failure due to non-uniform stress caused by waviness of the fiber.

Past studies on the effect of fiber waviness have examined the interaction of waviness with the reduction in the tangent stiffness of the matrix [61]. Other studies by Mandell and Samborsky [66] have looked at the effect of fiber waviness experimentally on the strength knock-downs. In this study we concentrate on failure due to fiber waviness in thick unidirectional carbon composites. The effects of a single type of defect on compression strength has been examined systematically by conducting coupon level experiments to obtain compressive response. Since, kinking failure is the dominant failure mode in compressive loading of composite, a parametric micro-mechanical modeling approach is proposed to simulate and predict the observed experimental results. This approach aims to capture kink band formation using a reduced model through a global-local approach, and consequently predict the compressive strength of wavy composite.

2.2 Experiment

2.2.1 Fabrication & Testing

The first task of the study was to manufacture coupons with controlled defect geometry that reflects the actual defects in field. Field defects are categorized based on shape of the defect as being sinusoidal (generally low aspect ratio) or high aspect ratio. Sinusoidal defects conform to a sine profile, whereas high aspect ratio defects induce waviness due to the edge profile but have a flat peak.

Defects were introduced by inserting pre-cured resin blocks located at the center of the coupon with respect to length and at a height, h_d, measured from the bottom flat surface. The size of the defect is commonly defined by the normalizing parameter $R_d = A_d/L_d$, which is the ratio of amplitude of defect and the length of defect. Similarly, the bulge on the surface of the defect is characterized by the ratio $R_b = A_b/L_b$, as shown in Figure 2.1. Measurement of cured coupons reveal that $R_d > R_b$, which is due to the tendency of fibers to assume a minimum bending angle, causing the defect wavelength to increase as one moves outwards from the root of the defect. Due to this, the fiber volume fraction varies from near the defect to the outer edge. Post cure nominal volume fractions of the specimens was determined from microscopic image analysis of samples and found to be $V_f = 0.434 \pm 0.027$, figure 2.2. It was also noticed that cured samples showed distinct unidirectional layers of thickness $0.4907 \pm 0.1071mm$, as seen in figure 2.3. In addition, misalignment angle (α) of fiber above the defect, was also measured by pixel measurement of scanned cross-sections of the specimens. Table(2.1) provides the nominal dimensions of specimens used for the experiments, where specimens are classified based on defect location as: BD-bottom defect, MD-middle defect, TD-top defect.

Quasi-static compression tests were conducted on an MTS® high force servo-hydraulic test system with a Wyoming Combined Loading Compression (CLC) Test

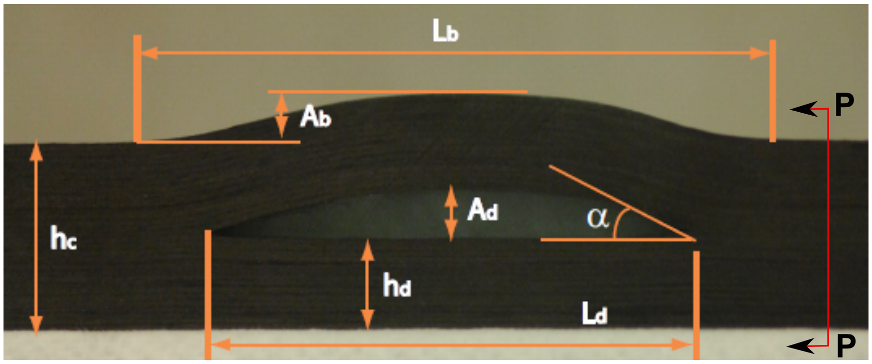

Figure 2.1: Dimensions of compression test coupons with defect inserts.

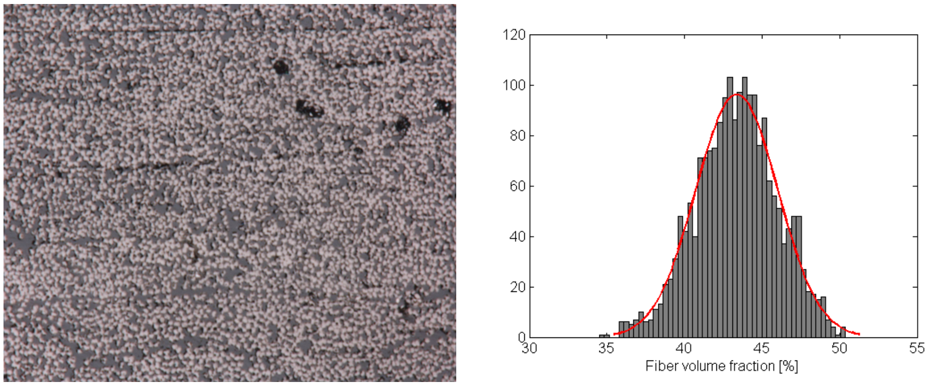

Figure 2.2: Microscopic image of composite cross-section (P-P in figure 2.1) and volume fraction PDF ($\mu = 43.37\%$, $\sigma = 2.64\%$).

Fixture. The ends of each specimen were squared and assembled flush with the test fixture to avoid end effects. The CLC fixture is used to apply compressive load axially along the length of the specimen, and to clamp the specimen on the ends as shown in Figure 2.4. Tests were conducted at a crosshead displacement rate of $1mm.min^{-1}$. For measurement of strains, a speckle pattern was applied on each specimen and high resolution images were taken using a digital camera at a framing rate of 1 frame per second. Strain fields were obtained by post processing the images using Digital Image Correlation (DIC) software Aramis®.

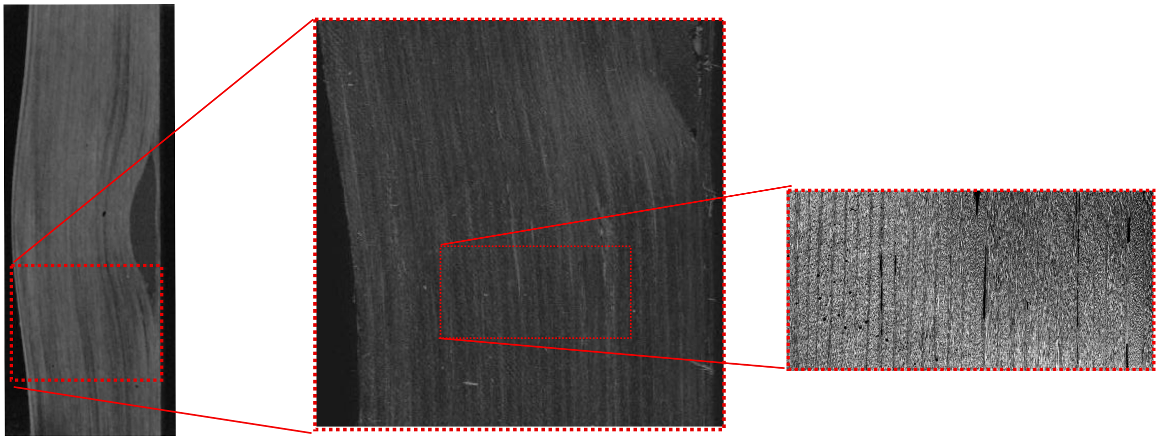

Figure 2.3: Microscopic image showing layers in UD coupon.

Table 2.1: Specimen type and dimensions.

Class (−)	H_c/H_d (mm)	R_d (deg)	R_b (mm)	α (mm)	L_b
BD	0.03	0.16∼0.25	0.014∼0.24	12.53 ∼33.69	44.0∼ 154.5
MD	0.5	0.041∼0.068	0.03∼0.04	18.05∼19.29	86.28∼142.09
TD	0.730	0.027	0.021	9.94	113.38

2.2.2 Observations

All specimens failed catastrophically characterized by the sudden and large drop in load measurement and an audible sound. It was also observed that in all cases the insert debonded first usually along the bottom of the defect. This caused the propagation of a delamination along the plane of insert thereby separating the wavy and straight part of the component. Though the delamination did not result in significant loss in load, it did cause global buckling in large aspect ratio defects. Failure mode causing catastrophic load drop varied from kink band formation to wave delamination and also out-of-plane kink banding*. Figure 2.5 depicts different failure modes, out-of-plane kinking (OK), in-plane kinking (IK) and delamination (DL) observed in experiments.

---

[0] *Prior studies by Yerramalli and Waas [108], have alluded to the 3-D nature of kink banding

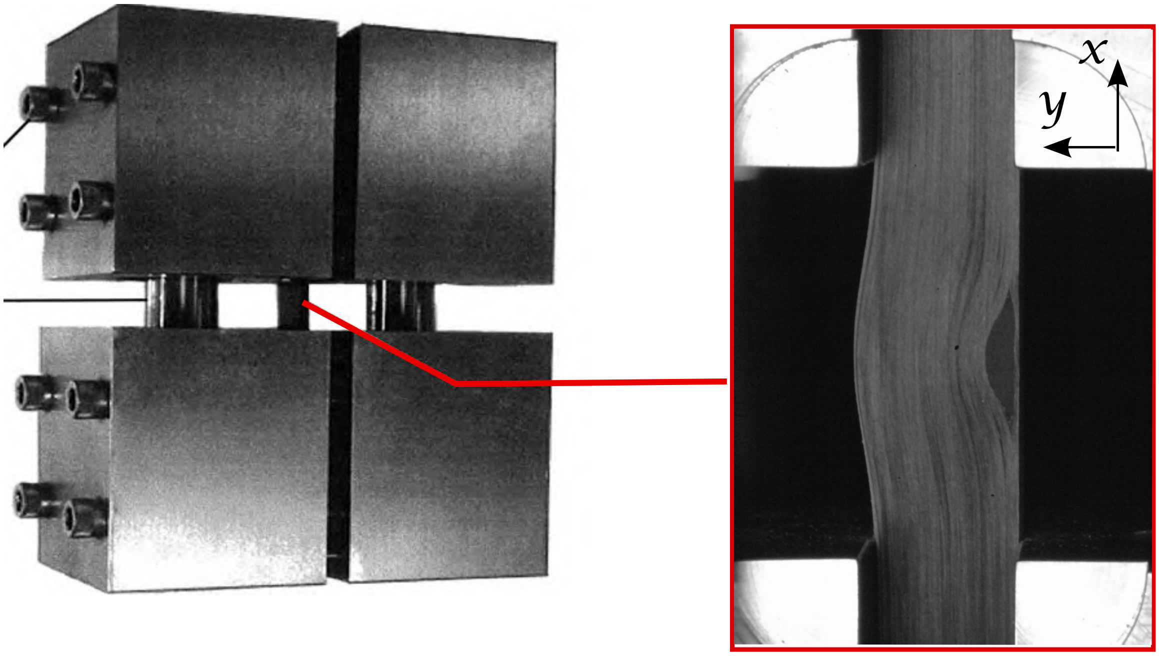

Figure 2.4: Wyoming CLC compression fixture.

Figure 2.14 & 2.15 shows typical force displacement plots for IK and DL failures. In both cases, as the loading progresses, regions of strain concentration are observed approximately at the start of non-linear response exhibited by the force-displacement response. In case of a sharper defect like in figure 2.14, strain concentration band is narrower than that of a shallower defect. IK failure is predominantly observed in small aspect ratio defects with high degree of fiber misalignment.

Figure 2.6, shows examples of failure of coupons due to IK and failure due to a mix of delamination and kinking. It is interesting to note that in case of pure IK failure, as seen in higher α misalignments, even the matrix rich region undergoes bending due to kinking and does not delaminate. Whereas for misalignments in the range of $15° \sim 20°$ both delamination and kinking are observed.

2.2.3 Results

The results of compression tests are shown in figure(2.7,2.8) where experimental compressive strength (X_c) normalized by the compressive strength of UD carbon (X_c^b),

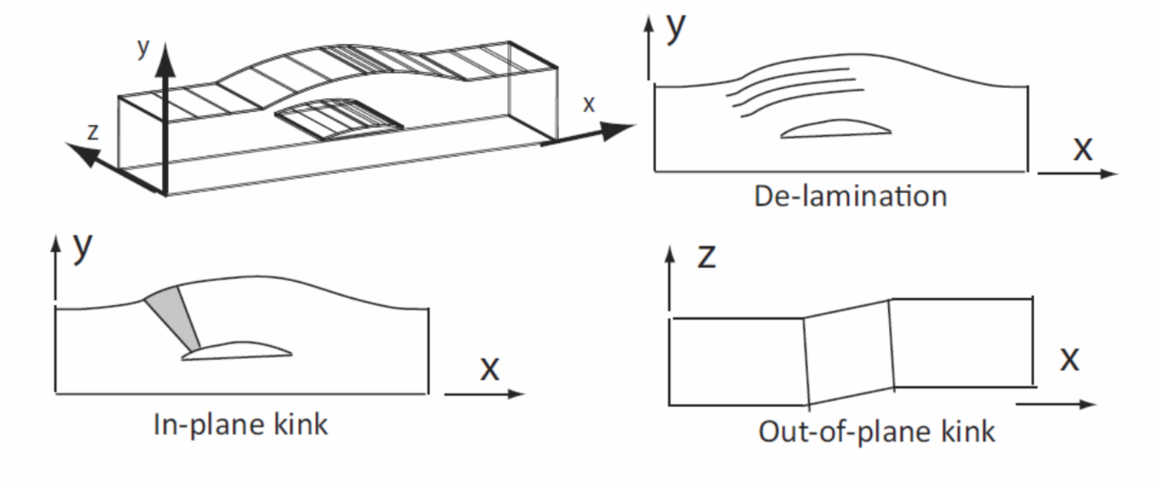

Figure 2.5: Failure modes seen in experiments.

calculated for 2° imperfection using Budiansky's model [19] ($X_c^b = G_m/(1+\frac{\bar{\phi}}{\gamma_m})$). The results are plotted against R_d figure(2.7) and α figure(2.8). One outlier in the data corresponds to $BD3$ which, due to it's large aspect ratio and thin wavy section, showed global buckling and delamination.The results seem to be insensitive to R_d as is seen from figure(2.7), which is because the aspect ratio of defect R_d is not a true measurement of fiber misalignment. Though the defect causes misalignment, the profile of the fiber over the defect will not conform to the cosine profile of the defect, but will conform to a profile offering least angle of bend. As is seen in figure(2.8), the compressive strength shows much better spread with respect to α. Coupons with small ($\sim< 10°$) misalignments tend to kink out of plane (in $x - z$ plane) because the cross-section is constraint free in the z direction but clamped in the y direction. By comparing the failure modes observed with the corresponding misalignment angle, a transition in the failure mechanism from out-of-plane kinking to in-plane kinking is observed, with a region in between where delamination and kinking can both occur, as show in figure (2.8). In general, compressive strength reduced with increasing misalignment angle.

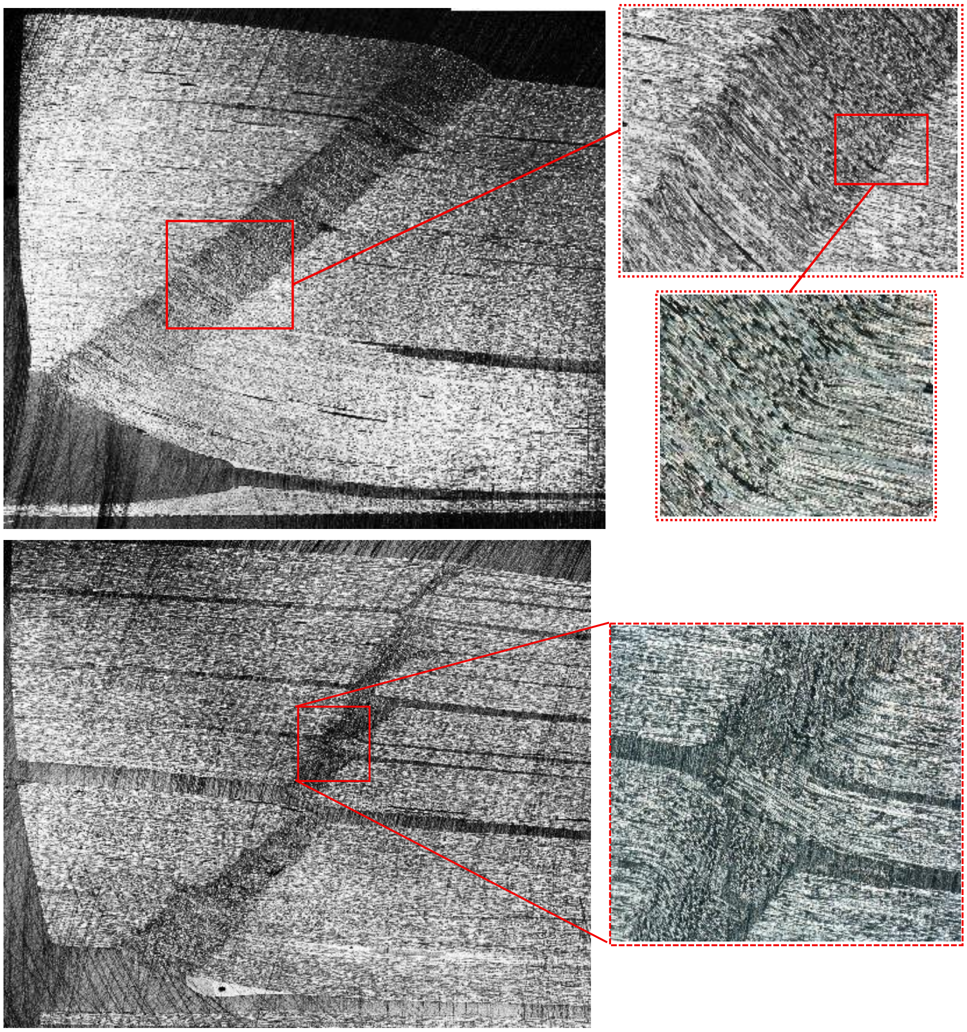

Figure 2.6: Micro-graphs showing kinking dominated failure & mix of kinking and delamination failure.

2.3 Numerical analysis

2.3.1 Modeling

An examination of the coupon geometry indicates that there are six parameters that control the fiber waviness as shown in Figure 2.9; $\alpha, \phi, L_d, L_b, A_d, A_b$. However, the number of variables can be reduced to three, α, ϕ, and L_d. This is achieved by considering the profile as a cubic spline defined as:

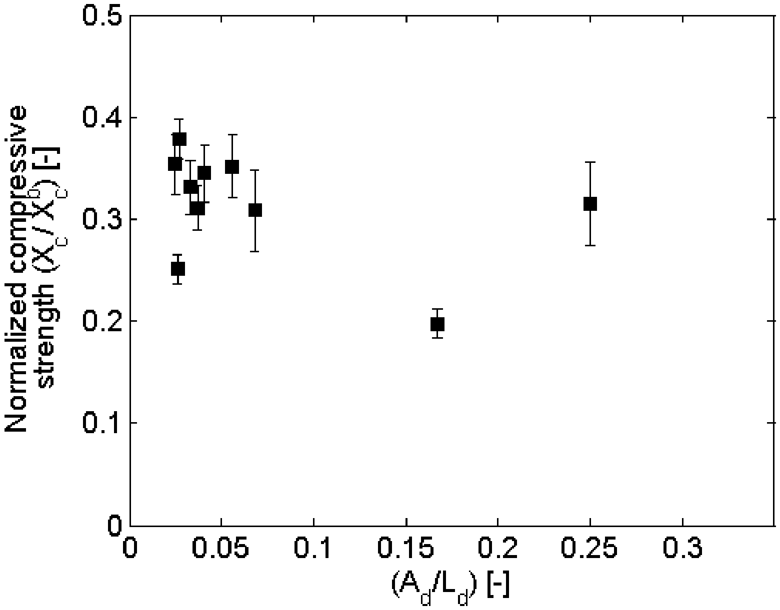

Figure 2.7: Normalized peak compressive stress plotted against defect aspect ratio R_d.

$$P_X(x) = \begin{cases} \frac{3}{4}\frac{A_d}{h^2}(x+L_d)^2 - \frac{1}{4}\frac{A_d}{h^3}(x+L_d)^3 & \forall \quad -L_d \leq x \leq -h \\ \frac{A_d}{2} + \frac{3}{4}\frac{A_d}{h}(x+L_d/2) - \frac{1}{4}\frac{A_d}{h^3}(x+L_d/2)^3 & \forall \quad -h \leq x \leq 0 \\ A_d - \frac{3}{4}\frac{A_d}{h^2}(x)^2 + \frac{1}{4}\frac{A_d}{h^3}(x)^3 & \forall \quad 0 \leq x \leq h \\ \frac{A_d}{2} - \frac{3}{4}\frac{A_d}{h}(x-L_d/2) + \frac{1}{4}\frac{A_d}{h^3}(x-L_d/2)^3 & \forall \quad h \leq x \leq L_d \end{cases} \tag{2.1}$$

where, $h = L_d/4$ and the inflection point of curvature is at $(\pm h, A_d/2)$. This formulation only requires α & L_d. A_d is obtained from the relation for maximum misalignment angle given by:

$$tan(\alpha) = \frac{3}{2}\frac{A_d}{L_d} \tag{2.2}$$

It should be noted that the traditional non-dimensional parameter R_d does not give the maximum misalignment angle which is at the inflection point of the curvature over the defect. This is especially true for high aspect ratios. Using the above equations we can now define the fiber profile over the defect, however, as we move from the

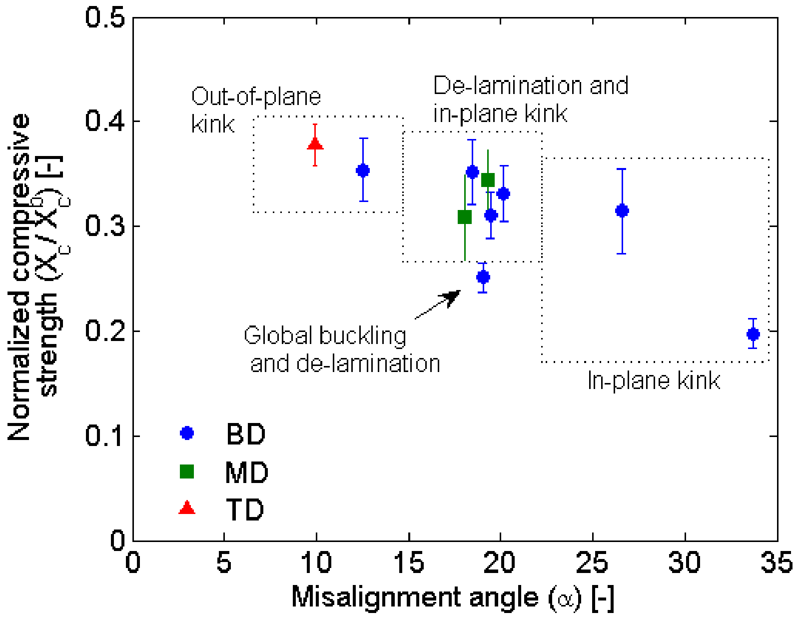

Figure 2.8: Normalized peak compressive stress plotted against misalignment angle α.

defect to the outer edges, the wavelength increases. To capture this, a propagation angle ϕ is used, which is defined as:

$$tan(\phi) = \frac{(H_c - H_d)}{(L_b - L_d)} \tag{2.3}$$

Propagation angle will be a function of fiber bending stiffness, coupon thickness, location of defect, curing pressure and matrix properties. Predicting the propagation angle (due to manufacturing) is beyond the scope of this study, hence, an empirical value measured from the coupons were used. For the bottom defect, it was found that $\phi = 21.707 \pm 2.71^\circ$, and for the middle defect and top defect $\phi \approx 12^\circ$, $\phi \approx 10^\circ$ were obtained, respectively. For the finite element based micro-mechanical model, the same cubic spline and propagation angle is followed with an additional constraint that the diameter of fiber is kept constant. The additional constraint ensures that change in volume fraction due to non-normal propagation, as seen in coupons, is captured.

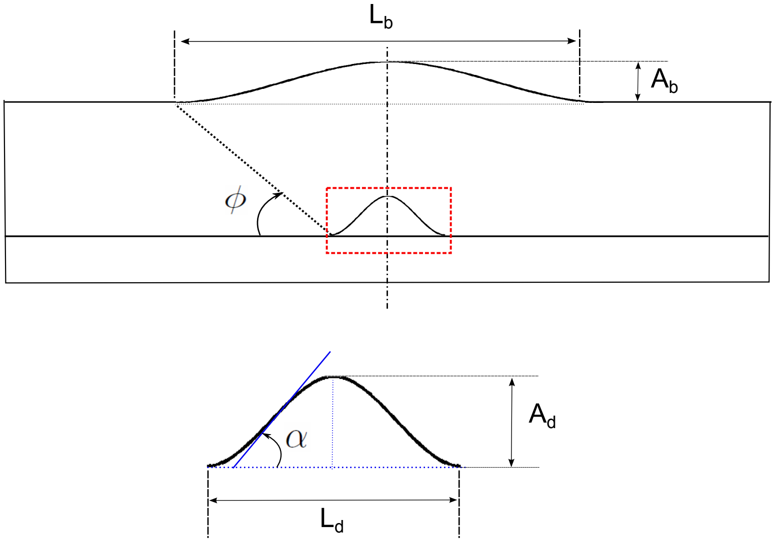

Figure 2.9: Geometry corresponding to the modelling parameters.

This is important because the location of shear stress concentration will also depend on the fiber volume fraction change along the wave.

2.3.2 2D Micromechanics based kink-band analysis

For in-plane kinking, a micro-mechanical model of the composite with alternating layers of fiber & matrix is used. Fibers are modeled as homogeneous orthotropic continua and the matrix is modeled as an isotropic material. In the past, Lee et al [61], Pimenta et al[72] have used a similar approach to obtain the kinking strength of a composite. Yerramalli et al[109] have also shown scaling studies where in lieu of conducting a full scale micro-mechanics model, which is computationally expensive, a scaled down coupon can be used. For this study we follow a global-local approach as defined in the work by Ahn & Waas [2].

The global macro-mechanical model is a layered full scale homogenized model, with each layer modeled as homogeneous orthotropic material and the local material orientation is changed continuously based on the profile of the layer, as shown in Figure 2.10. Thickness of each layer is kept as $0.5mm$ (mean thickness measured from coupons is 0.491 ± 0.107). The local micro-mechanical model is a sub-region of the global model but with fiber and matrix modeled explicitly. The fiber is modeled orthotropic, elastic, while the matrix is modeled as an elastic-plastic using J2 incremental theory of plasticity solid. Here again, the material orientation of the fiber follows the fiber profile.

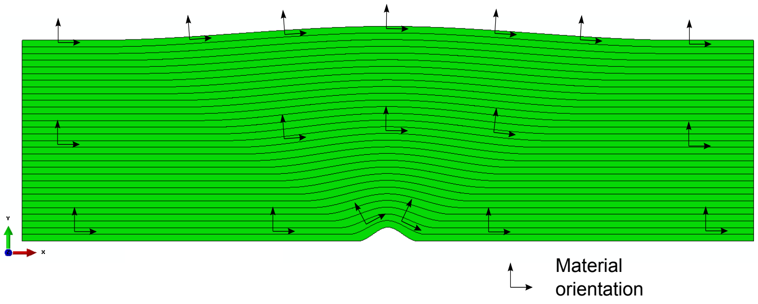

Figure 2.10: Modeling of layers and material orientation.

Lamina properties were obtained from the Concentric Cylinder Model (CCM) using fiber (listed in table 2.2) and matrix material properties obtained from Ng et al [70]. The matrix non-linear in-situ equivalent stress-strain properties were taken from Ng et al [70].

Table 2.2: Fiber Properties

E_{11} (GPa)	E_{22} (GPa)	E_{33} (GPa)	G_{12} (GPa)	G_{13} (GPa)	G_{23} (GPa)	ν_{12} $(-)$	ν_{13} $(-)$	ν_{23} $(-)$
276	20.5	20.5	32.8	32.8	7.6	0.28	0.28	0.28

The local-global approach implemented here is a three step procedure using a macro-mechanical model and a micro-mechanical model as depicted in Figure 2.16. Step 1, is a linear elastic step where a known displacement is applied in the axial(x) direction and the displacements ($\Delta_{x,y}$) at nodes corresponding to local boundary ($A' - B' - C' - D'$) are obtained. These displacements $\Delta_{x,y}$ are then applied on the local micro-mechanics model boundary and a linear elastic analysis is performed in step 2, henceforth called "Local Liner Model". In step 3, the reaction forces obtained ($R_{x,y}$) in step 2 are applied on boundaries $(A' - B')\&(C' - D')$ along with $\Delta_{x,y}$ on $(A' - D')\&(B' - C')$ and a non-linear Riks response analysis is conducted ("Local Non-linear Model"). By applying reaction forces instead of displacement, the top and bottom boundaries are kept free of constraints, thereby allowing for kink band formation. The application of reaction forces is also important to ensure that the local model follows the global deformation profile in the elastic regimen.

The axial reaction force R_x obtained from steps 1 & 2 provide the linear relation between local and global as a simple ratio $\hat{R} = (R_x^{global}/R_x^{local})$. Now, from step 3, we get the micro-kink initiation load (R_k^{local}) which will correspond to the global kinking strength σ_k as ;

$$\sigma_k = (R_k^{global})/A = (\hat{R}\ R_k^{local})/A \tag{2.4}$$

To determine the appropriate size of the local-region, a scaling study was conducted where the size was scaled by the number of fibers in the thickness direction as shown in Figure 2.11, while keeping the aspect ratio $(\frac{A'-B'}{A'-D'})$ fixed. Figure 2.11 also shows the plot of normalized X_c as the number of fibers are increased. Strength values converge with increasing number of fibers and the number of fibers for subsequent simulations is taken as 150.

2.3.3 Results

Simulations were conducted for defect angles, $\alpha = 30°, 20°, 15°, 10°, 5°$ with $H_d = 1, 2, 3mm$ to examine the trend in kinking strength. Figure 2.12 shows the results of the parametric study. With an increase in both misalignment angle and defect height, a decrease in kinking strength is predicted. Defect height is seen to have less influence on the kinking strength with increasing misalignment angle. The results were compared with experimental data for defects of $H_d = 1mm$ as shown in Figure

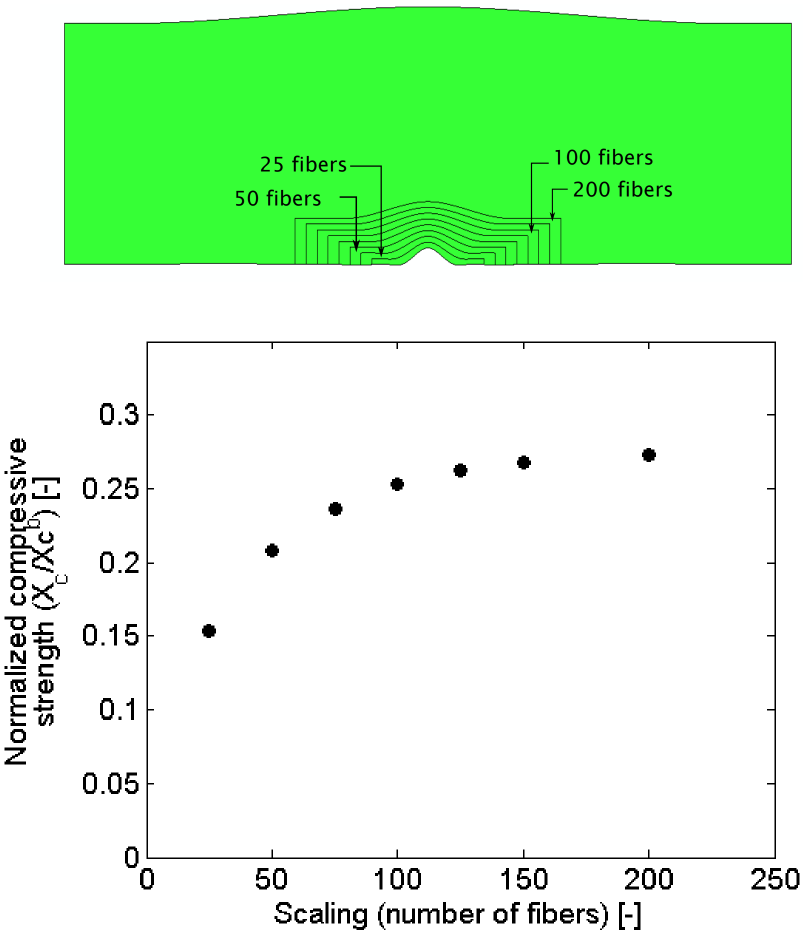

Figure 2.11: Scaling study to determine the local model size.

2.13. Simulations were conducted on specimens corresponding to mean and maximum fiber volume fractions estimated from image analyses. The simulation results are within the experimental scatter as shown in the figure 2.13.

2.4 Conclusions & future work

The experimental studies conducted have shown that there is a significant knockdown in compressive strength of unidirectional composite laminates due to fiber waviness, induced by defects. By post-experiment observations of failed coupons, three modes of failure are identified; (a) In-plane kinking (IK), (b) out-of-plane kinking (OK), and (c) delamination (DL). As expected, compressive strength is observed to

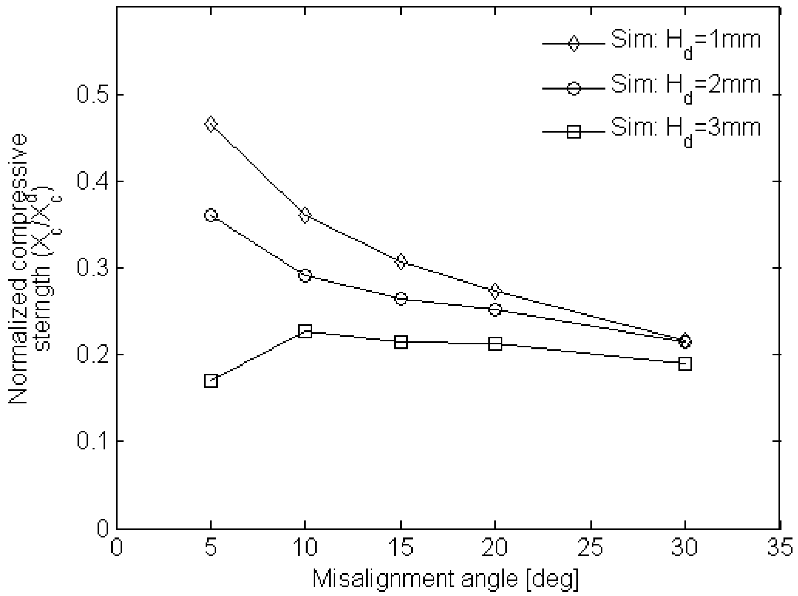

Figure 2.12: Parametric study results for in-plane kinking.

drop with increase in misalignment angle (α). However, the mode of failure changes with changes in misalignment. For low $\alpha < 10°$ OK is dominant, for $10° < \alpha < 25°$, failure occurs by a combination of kinking and delamination, and for $\alpha > 25°$ failure is due to IK. Though delamination is observed, kinking is a dominant failure mode in observed. To capture the kinking failure and the non-homogeneous stress field due to waviness, a global-local analysis approach is utilized. Using this approach the size of the model can be significantly reduced as compared to using a complete micro-mechanics model of the component. The analysis results indicate that the compressive strength is strongly influenced by misalignment angle. The influence of height of defect reduces with misalignment. Overall, the approach used for modeling appeared to provide a good match with experiments, both in terms of strength prediction and failure mode.

Current model is able to capture kink band formation. However, it does not capture delamination failure. Incorporating delamination failure in micro-mechanics based models is a computationally expensive method. Instead, an up-scaled homog-

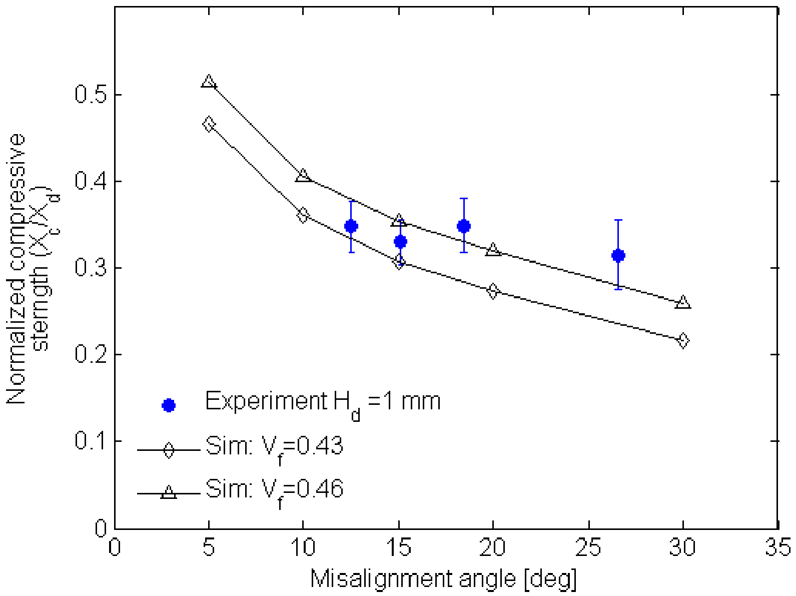

Figure 2.13: Micro-mechanical computational results compared against experimental results.

enized model with delamination incorporated using cohesive methods is required. A possible method to homogenization which can also capture kinking was presented by Davidson and Waas [33], which needs to be explored further and is left as future work.

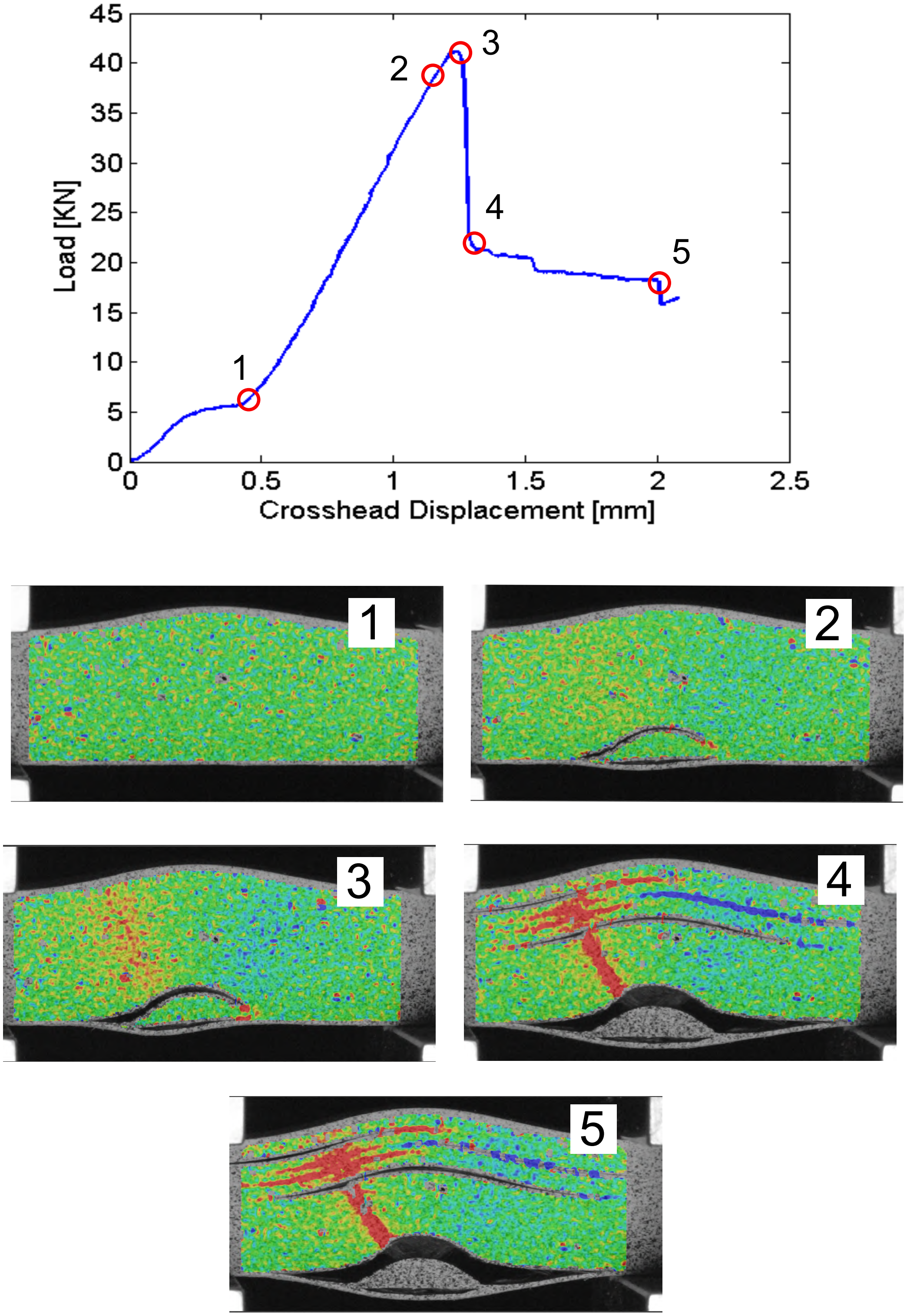

Figure 2.14: Load-displacement plot and corresponding shear strain DIC contours showing kinking dominated failure subsequently leading to delamination.

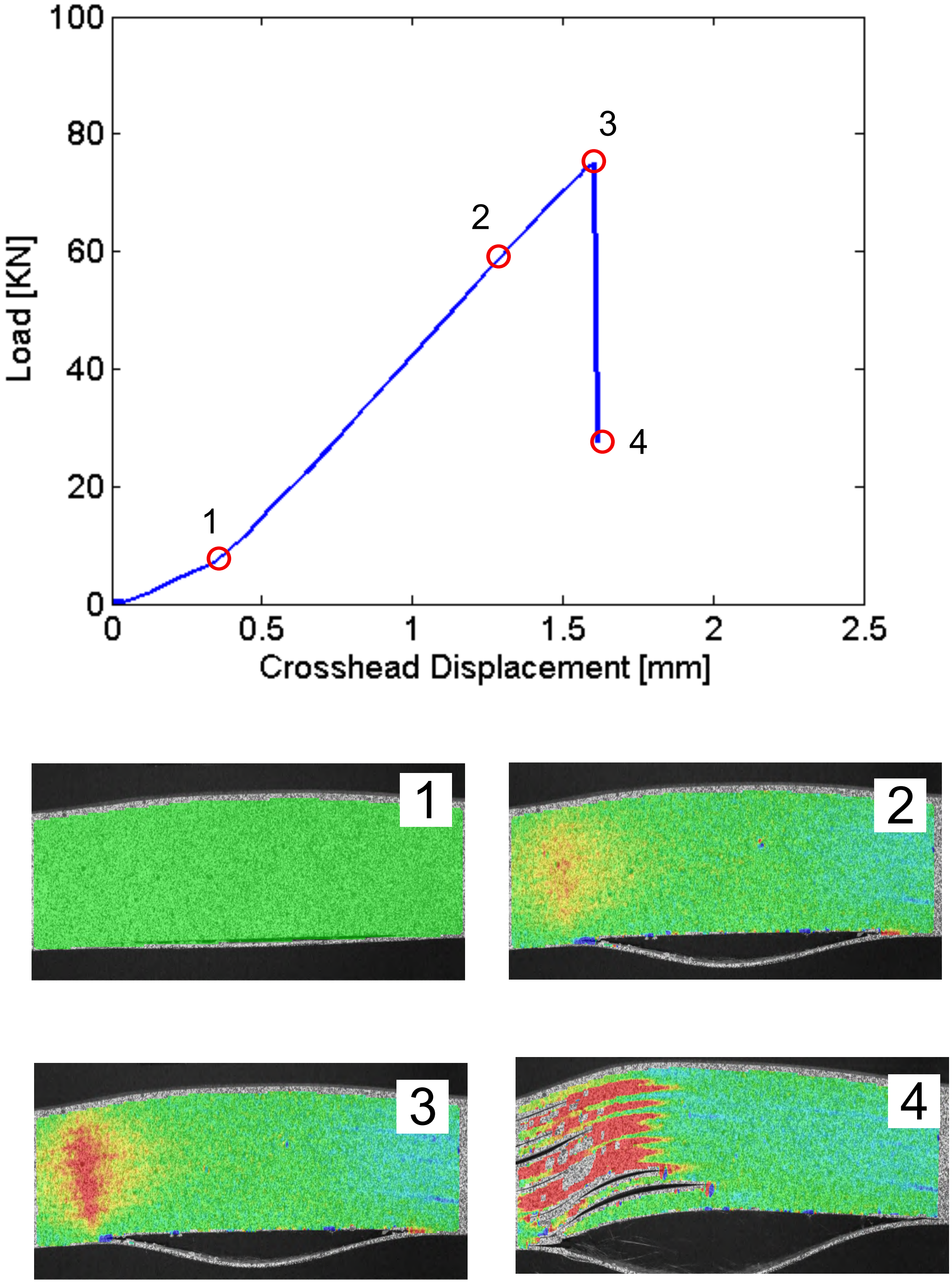

Figure 2.15: Load-displacement plot and corresponding shear strain plot showing delamination dominated failure

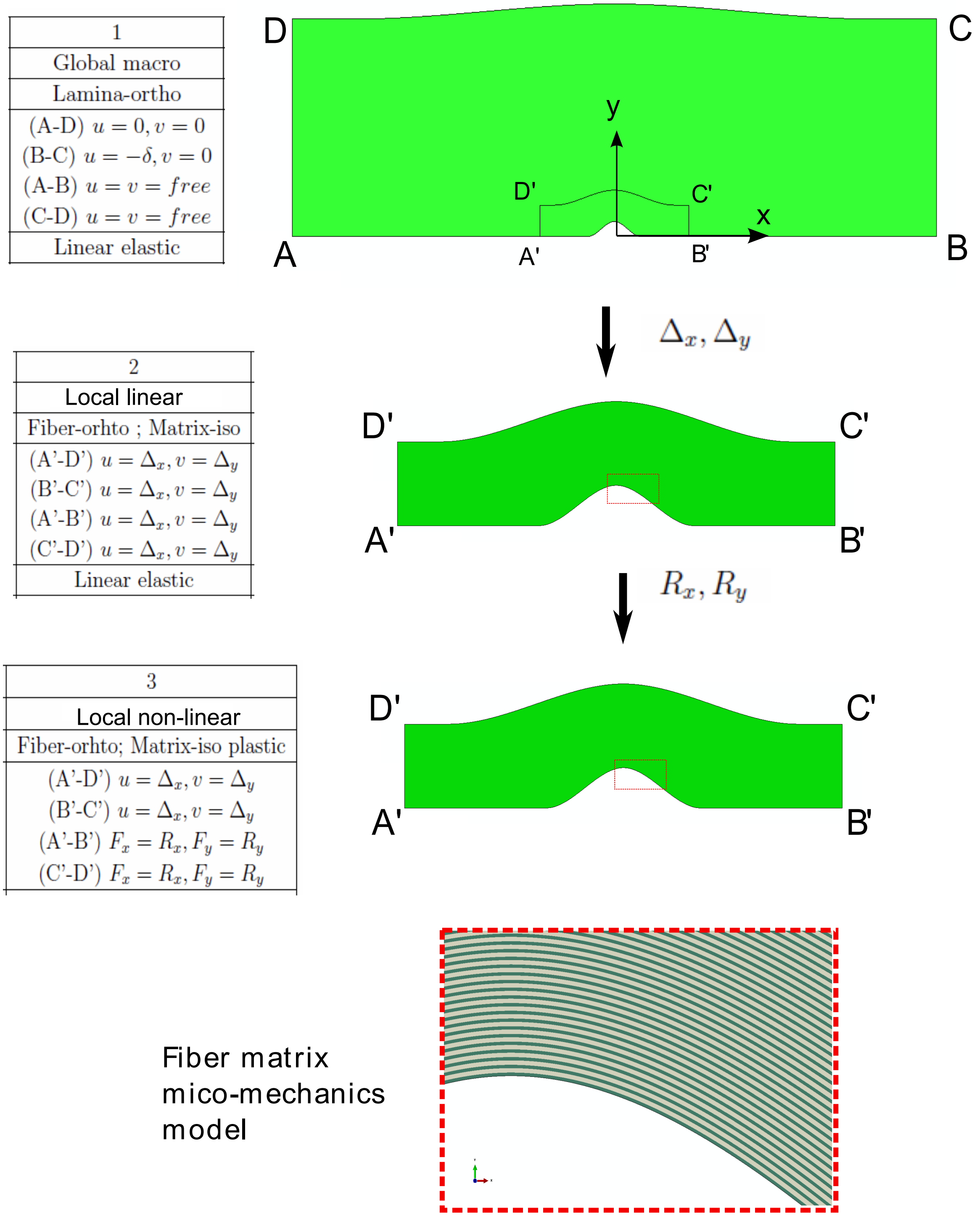

1
Global macro
Lamina-ortho
(A-D) $u = 0, v = 0$ (B-C) $u = -\delta, v = 0$ (A-B) $u = v = free$ (C-D) $u = v = free$
Linear elastic

2
Local linear
Fiber-orhto ; Matrix-iso
(A'-D') $u = \Delta_x, v = \Delta_y$ (B'-C') $u = \Delta_x, v = \Delta_y$ (A'-B') $u = \Delta_x, v = \Delta_y$ (C'-D') $u = \Delta_x, v = \Delta_y$
Linear elastic

3
Local non-linear
Fiber-orhto; Matrix-iso plastic
(A'-D') $u = \Delta_x, v = \Delta_y$ (B'-C') $u = \Delta_x, v = \Delta_y$ (A'-B') $F_x = R_x, F_y = R_y$ (C'-D') $F_x = R_x, F_y = R_y$

Figure 2.16: Global-local analysis procedure.

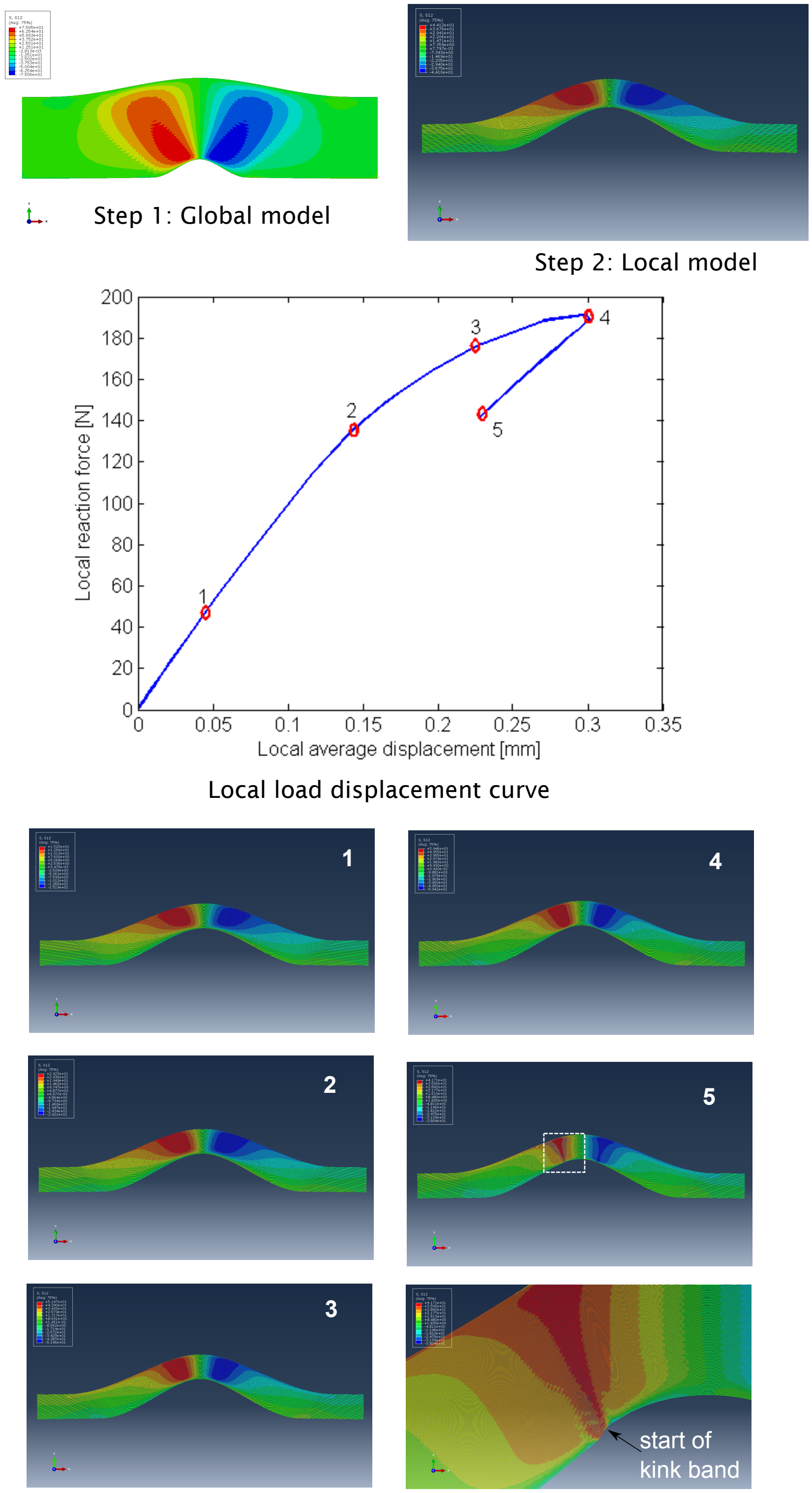

Figure 2.17: Computational results from a global-local analysis with matrix shear stress plots showing evolution of shear stress and kink banding.

CHAPTER III

Compression of thin laminates with hole

3.1 Introduction

Predicting the open hole compression strength of a laminated fiber reinforced composite is an important consideration in material qualification for aerospace structural design. Experimental results of fiber reinforced composite panels with holes and cutouts show a significant drop in compressive strength as a function of hole size due to stress gradients generated by the hole and because of the large stresses that concentrate at the hole edge. In cross-ply laminates the failure is generally dominated by the 0° ply kink banding failure. Hence, though the problem of predicting compressive strength of laminated composite with a cutout is complex, it can be simplified by focussing attention on the failure of the 0° lamina within the laminate. There are two main points that needs to be taken into consideration; first the compressive strength of the 0° lamina and second, the influence of the hole on the stress distribution around the hole. Prior studies, [100], [23], [2], and [3], have examined the problem in detail and have developed both analytical and numerical methods based on careful experimental results to predict Open Hole Compressive Strength (OHCS) with varying degrees of sophistication in the modeling. In this chapter, we have developed a novel two-level approach, which is analytical and numerical, that can be used to predict OHCS.

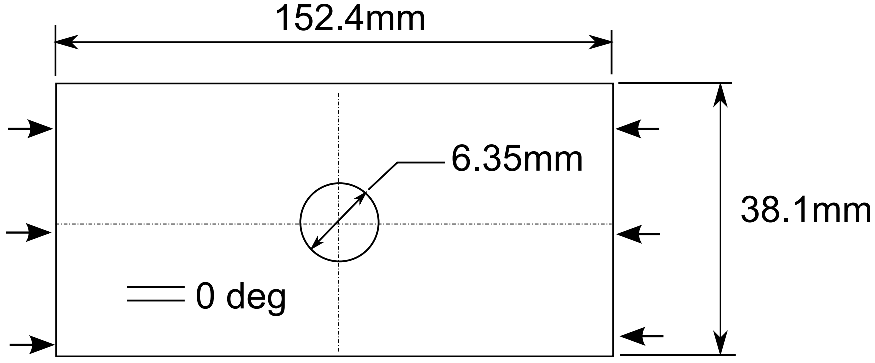

Figure 3.1: Dimensions of compression test coupons with hole.

At the zeroth level, we present a simple engineering approach using a combination of the Considere construction [89], and Lekhnitskii's [62] formulation to approximate the compressive strength of multi-directional laminates with a hole. At the first order level, this model is refined by a combination of micromechanics and classical lamination theory, implemented using the finite element method to capture kink-band formation using a global-local approach, [3], to arrive at an accurate prediction of OHCS for a class of popular laminates. The model uses constitutive properties of the fiber and the *in-situ* in-plane lamina shear-stress strain response.

Predictions of OHCS obtained from the two approaches are compared with experimental results for laminates with varying percentages of 0° plies. The geometry of the OHC coupon in shown in figure(3.1).

3.2 Measuring the lamina in-situ shear response

Characterization of the in-situ lamina shear response is done using the procedure described by Ng et al [70]. Tensile tests of dog-bone shaped specimens of $\pm 45^\circ_s$ were conducted to obtain the in-plane lamina shear stress response, and the tests followed the guidelines of ASTM D3518 and D3039 for strain gauge requirements and gauge section dimensions. Dogbone-shaped specimens were used rather than standard coupon-shaped because previous work showed a tendency of specimen failure within the grips for straight-sided coupons and within the gauge section for dog-bone coupons.

A speckle pattern was implemented on one side of the specimens to capture full field strain data using an optical camera and the speckle images were analyzed using the ARAMIS digital image correlation (DIC) software. Strain gauge data was compared to, and agreed with, the strains obtained through DIC. However, strain gauges did not cover the full range of strains seen in the experiments and failed prior to sample ultimate failure. Hence, DIC measurements were used for calculating full field strain data and used for the analysis.

Using the shear response of the lamina, the in-situ shear response of the damaging matrix, which is shown in figure (3.2) was extracted as described in [70]. From this, the in-situ matrix equivalent stress vs equivalent strain response can be calculated (Ng et al [70]) and is shown in figure (3.3).

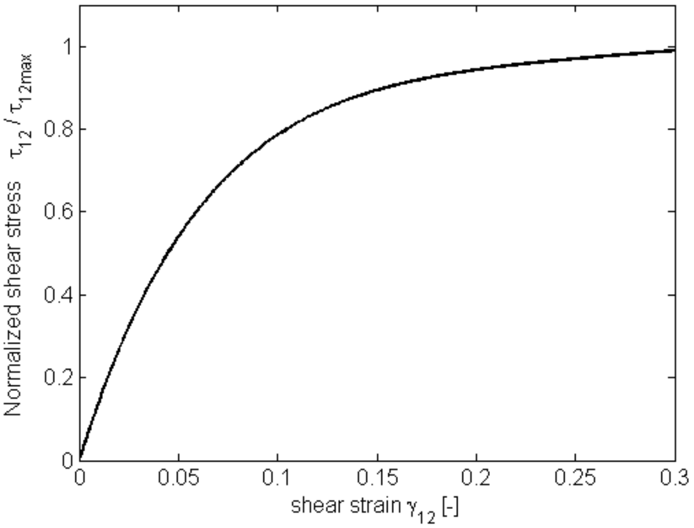

Figure 3.2: In-situ shear stress-strain obtained from ±45 coupon tests

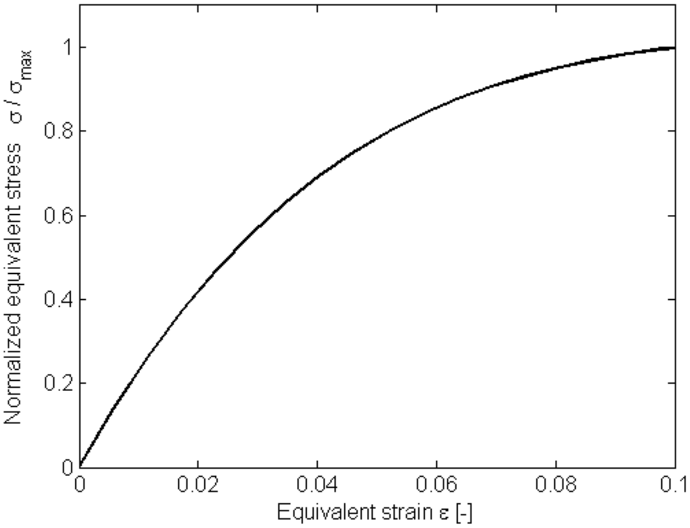

Figure 3.3: Equivalent stress-strain curve

3.3 Zeroth level prediction

In multi-directional laminates, compression strength is generally dominated by the 0° ply kink banding failure. Even though the problem of predicting compressive strength of laminated composite with a cut-out is complex, it can be simplified by focusing attention on the failure of 0° laminae within the laminate. More specifically, the failure of 0° laminae occurs at the location of maximum stress, which, in case of laminates with cut-outs like a hole, are at the hole edge. Hence, the simplest approach would involve; (a) knowing the compressive strength of 0° lamina and, (b) knowing the value of stress at the hole edge. Therefore, the compressive strength of laminates with a hole is taken to be the applied stress which causes the maximum stress at the hole edge to reach the compressive strength of the 0° lamina. This approach is implemented using a combination of the Considere construction [89], and Lekhnitskii's [62] formulation. Considere construction is a geometric construction which utilizes the lamina shear stress-strain response to obtain the compressive strength of a 0° lamina (X_c^0) for a given fiber misalignment ϕ, as shown in figure 3.4.

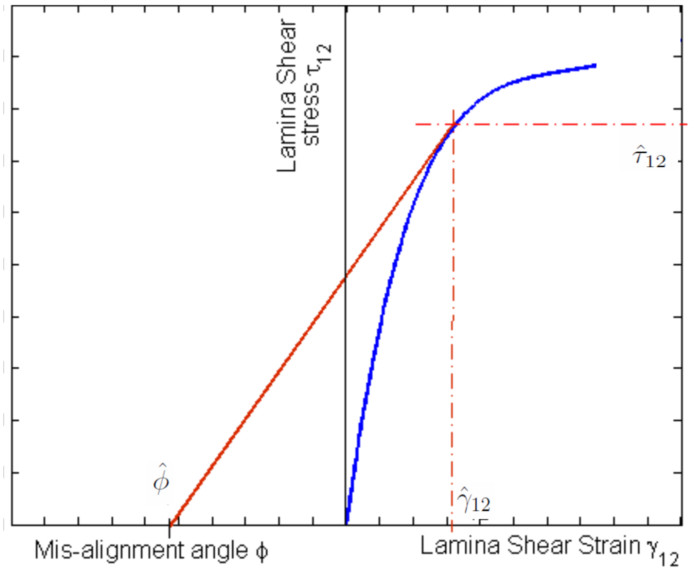

Figure 3.4: Considere construction

$$X_c^0 = \frac{\hat{\tau}_{12}}{\hat{\phi} + \hat{\gamma}_{12}} \tag{3.1}$$

where, $\hat{\phi}$ is the fiber misalignment, $\hat{\tau}_{12}$ is the shear stress and $\hat{\gamma}_{12}$ shear strain. The compressive strength of a laminate, $X^L{}_c$, is obtained by,

$$X_c^L = X_c^0 (\frac{E_{11}^L}{E_{11}^0}) \tag{3.2}$$

where, E_{11}^L and E_{11}^0 are the elastic moduli of the laminate and the 0° ply, respectively, in the direction of compressive load. Further, X_c^0 is the compressive strength of a 0° lamina for a given fiber misalignment ϕ.

The equation above provides the compressive strength of a laminate without any stress-raisers (such as at cutout edges). In the presence of a hole, the maximum stresses occur at the hole edge due to non-uniform stress distribution. Using the Lekhnitskii [62] solution, Filiou and Soutis, [22], have provided an approximation

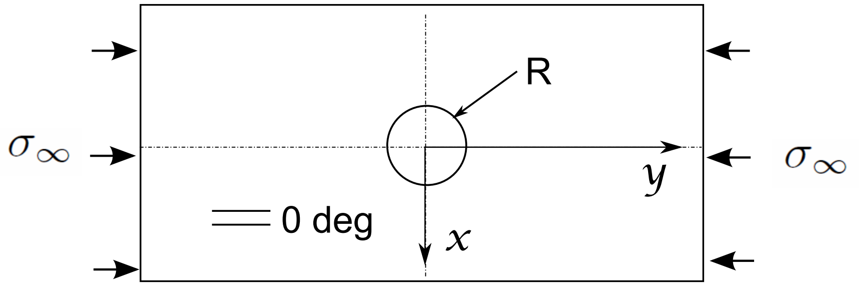

Figure 3.5: Infinite plate with a hole under compression

to the stress distribution in an orthotropic infinite plate with a hole (shown in figure (3.5)). The equation below provides an accurate description of the axial stress, ($\sigma_{yy}(x,0)$) distribution due to a far field stress, σ_∞,

$$\begin{aligned} &\tfrac{\sigma_{yy}(x,0)}{\sigma_\infty} \approx 1 + \tfrac{1}{2}(\tfrac{R}{x})^2 + \tfrac{3}{2}(\tfrac{R}{x})^4 - \tfrac{3}{2}(H_A - 1)[5(\tfrac{R}{x})^6 - 7(\tfrac{R}{x})^8] \\ &H_A = \tfrac{(1+n)}{3} \\ &n = \sqrt{2(\sqrt{\tfrac{E_{yy}}{E_{xx}}} - \nu_{yx}) + \tfrac{E_{yy}}{G_{yx}}} \end{aligned} \tag{3.3}$$

Using the above equation, we can approximate the stress at the edge of the hole (for $x = R$) as,

$$\frac{\sigma_{yy}(R,0)}{\sigma_\infty} \approx 3H_A \tag{3.4}$$

Assuming the material at the edge of the hole, where the stress is maximum, fails at the strength provided by equation 3.4, above, ie; $\sigma_{yy}(R,0) \approx X_c^L$ we can obtain the corresponding far field stress. This far field stress will be the critical strength of the laminate with a hole in compression.

$$X_c^L \approx \frac{\sigma_{yy}(0,R)}{3H_A} = \frac{X_c^0}{3H_A}(\frac{E_{11}^L}{E_{11}^0}) \tag{3.5}$$

Thus, this equation provides the OHCS of a laminate (X_c^L, in terms of the pristine lamina compressive strength, (X_c^0). The approach presented here can also be used to estimate the open hole compressive strength for other cutout shapes and for multiaxial planar loading, provided an expression that relates the maximum stress at the cutout edge in terms of the applied far-field loading is available.

3.4 Numerical predictions - first order analysis

First order analysis is based on the same mechanism as the zeroth order approach, that the failure in laminates under compressive loading is due to kink banding. However, instead of analysing the kink banding of a pristine 0° lamina, and the non-homogeneous stress field due to a cut-out separately, the kink band formation in a 0° lamina in a non-homogeneous stress field is analysed. This is achieved through a micro-mechanical, finite element model of the 0° lamina with a cut-out. In the micro-mechanics model, the fibers are explicitly modeled as homogeneous orthotropic continua and the matrix is modeled as an isotropic material with in-situ elastic-plastic properties. Micro-mechanics model, however, is a computationally expensive method, because of the difference in length scale of fiber and lamina. To model a complete lamina using micro-mechanics will require thousands of fiber-matrix layers, which is computationally prohibitive. To overcome the issue of computational cost the model is reduced by analysing a micro-region around the hole. Boundary conditions to be applied on the micro-region are obtained from a global homogeneous model. This method is called the *global-local* approach as defined in the work by Ahn & Waas [3] and Davidson & Waas [33]. In some reports, this method has also been referred to as the embedded cell method (see, for example, [43])

The local-global approach implemented here is a three step procedure (each subsequent step relies on the results of the prior step) using a macro-mechanical model and this is as depicted in figure(3.6). The macro-model, outside the micromechanics sub-region, is a 2D half symmetric model with homogenized transversely isotropic lamina properties of the 0° lamina. Step 1, is a linear elastic step where a known far-field displacement is applied in the axial(y) direction and the displacements ($\Delta_{x,y}$) at nodes corresponding to the micro-region boundary ($A-B-C-D$) are obtained. These displacements $\Delta_{x,y}$ are then applied on the isolated local micro-mechanics model boundary and another linear elastic analysis is performed in step 2, henceforth called "Local Linear Model". In step 3, the reaction forces, ($R_{x,y}$), obtained in step 2 are applied on boundaries $(A-D)\&(B-C)$ along with $\Delta_{x,y}$ on $(A-B)\&(C-D)$ and a non-linear Riks response analysis is conducted ("Local Non-linear Model") on the isolated local micro-mechanics model. Only step 3 is an incremental analysis while steps 1 and 2 are linear and hence done only once. Step 2 is needed to obtain the consistent reaction forces on parts of the boundary of the micro-region, since step 3 uses mixed boundary conditions on the micro-region boundary.

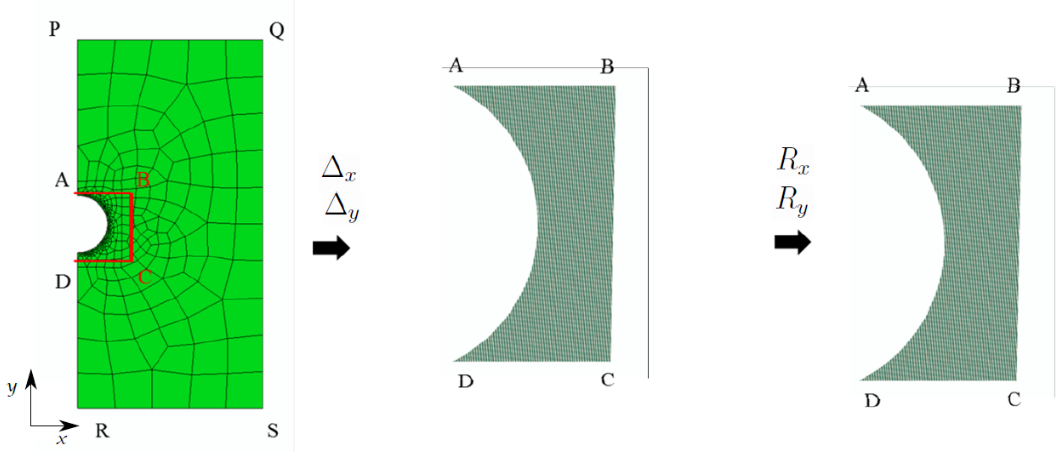

Step 1	Step 2	Step 3
Global linear analysis	Local liner analysis	Local response analysis
Lamina: Ortho	Fiber-ortho, Matrix-iso	Fiber-ortho, Matrix-iso
(P-Q) $u = 0$, $v = -\delta$	(A-B) $u = \Delta_x$, $v = \Delta_y$	(A-B) $u = \Delta_x$, $v = \Delta_y$
(Q-S) $u = free$, $v = free$	(B-C) $u = \Delta_x$, $v = \Delta_y$	(B-C) $F_x = R_x$, $F_y = R_y$
(S-R) $u = 0$, $v = 0$	(C-D) $u = \Delta_x$, $v = \Delta_y$	(C-D) $u = R_x$, $v = R_y$
(R-D,A-P) $u, v = X\ symm$	(D-A) $u = \Delta_x$, $v = \Delta_y$	(D-A) $F_x = R_x$, $F_y = R_y$

Figure 3.6: Steps in global-local analysis

Typically, as seen in past studies, there are no boundary conditions imposed on

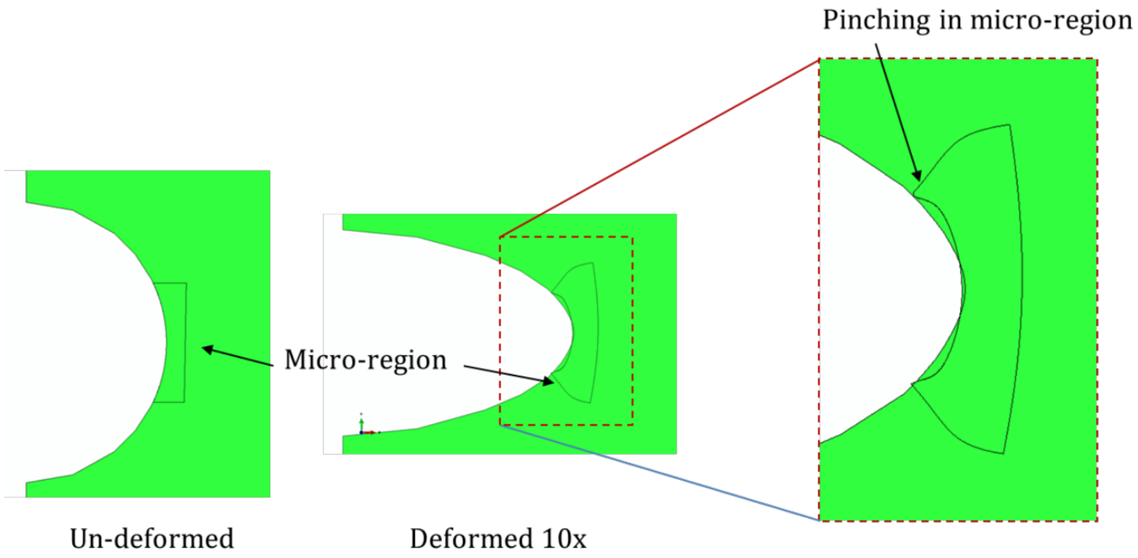

Figure 3.7: Pinching in local analysis when reaction forces are not applied on the free-edge.

the free edge of a local model. This however, can lead to incorrect results because the local model which is non-homogeneous will deform in a manner different from the global model. In figure 3.7, the un-deformed and deformed profiles of global and local model are shown. Pinching of the corners of the micro-region is observed as compared to the global model, during deformation, which will lead to artificial stress concentration developing at the corners. These stress concentrations will cause premature kink formation at the corners. Hence, application of reaction forces at the free boundaries is important to ensure that the local model follows the global deformation profile, in the elastic regime. By applying reaction forces instead of displacements, the left and right boundaries are kept free of constraints, thereby allowing for the kink band to form without displacements being constrained on the boundaries.

The axial reaction force R_y obtained from steps 1 & 2 provide the linear relation between the local and global model as a simple ratio $\hat{R} = (R_y^{global}/R_y^{local})$. Now, from step 3, we get the micro-kink band initiation load (R_k^{local}) which corresponds to the global compressive strength of the zero lamina due to kink banding, X_N^0 as ;

$$X_N^0 = (R_k^{global})/A = (\hat{R}\ R_k^{local})/A \tag{3.6}$$

In the above expression, A, is the load bearing cross-sectional area of the specimen in the far field. The size of the micro (local) region is an unknown of the global-local method. A converged solution is obtained when the peak compressive strength of the first order analysis shows no difference with respect to the size of the micro-region. The size of the region was scaled based on the ratio of width (length A-B) to the height (length B-C) of the micro-region.

Typical response of the micro-region is shown in figure (3.10) and corresponding snap-shots at different stages of loading leading to kink banding failure are provided. Figure (3.8) shows the scaling study to determine the converged micro-region size and the corresponding compressive strength of the 0° ply. The results are normalized by the compressive strength of the 0° ply with $\phi = 1°$ obtained from the Considere construction ie; the un-notched zero ply strength. Using the converged value of compressive strength from the 2D global local X_N^0 analysis, the laminate compressive strength can now be obtained by simple scaling,

$$X_c^L = X_N^0(\frac{E_{11}^L}{E_{11}^0}) \tag{3.7}$$

As with zeroth order, this first order approach provides compressive strength prediction for laminates that show kink band formation in the 0° lamina. Hence, this method of predicting compressive strength is predicated on zero ply kink banding being the dominant failure mechanism. However, this may not provide satisfactory predictions in cases where off-axis laminae dominate, ie; in cases where the percentage of 0° laminae is small and where there is significant non-linear behavior before failure, as in pure angle-ply laminates or laminates with a large percentage of angle plies. For

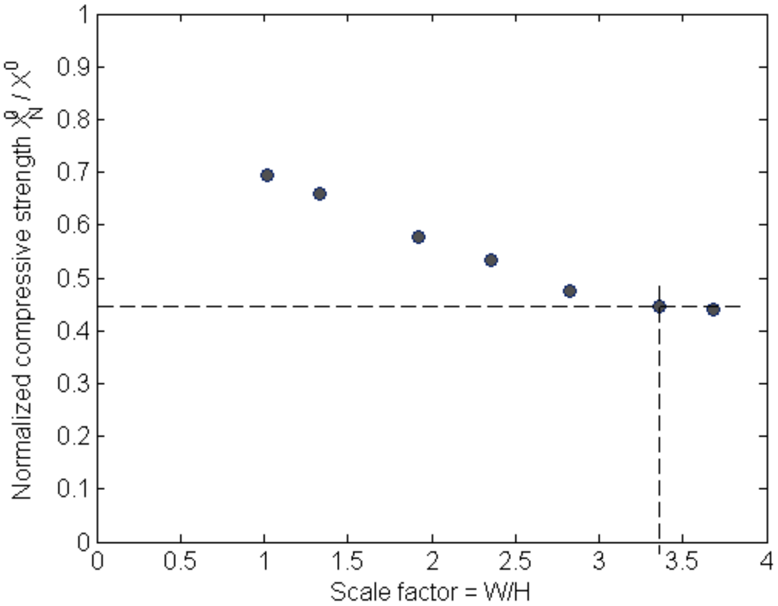

Figure 3.8: Scaling study result

these latter cases, a higher order analysis, based on extended Schapery theory, as developed by Pineda et al[74], in Appendix-B.

3.5 Results

The results corresponding to the zeroth order and first order models are compared with experiments for different laminates and shown in figure (3.9). The results are normalized by the compressive strength of the 0° ply with $\phi = 1°$ obtained from the Considere construction ie; the zero ply un-notched strength. The nomenclature used to label laminates describe the percentage of $0°, 45°\&90°$ plies in a laminate. For example laminate (10/70/20) is made of 10% 0° plies, 70% 45° plies and 20% 90° plies. It is evident from the results that the OHCS increases with increasing percentage of 0° plies. Though both the zeroth order and first order model predictions are close to experiment, the first order local-global model is seen to be a better match, especially in laminates with high percentage of 0° plies.

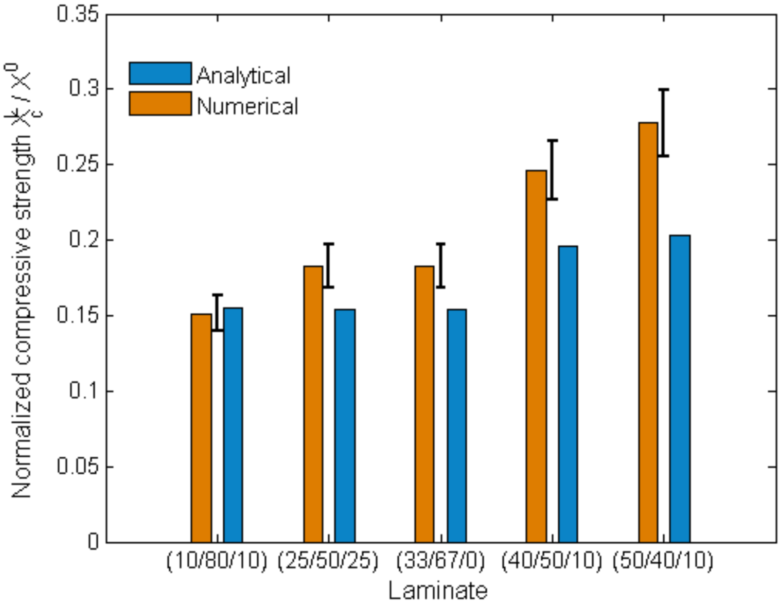

Figure 3.9: Comparison of experiment (error bar), analytical and numerical results

3.6 Summary

Analytical and numerical models are presented to predict the compressive strength of a composite laminate with an open hole (OHCS). In the analytical model strength estimate from Considere construction is used in Lekhnitskii's formulation to predict the compressive strength of the composite with hole. In numerical model, the zero ply is isolated and a micro-mechanics model using a global-local approach is employed to predict the kink banding and consequently the compressive strength of the plate with hole. Both methods promise good predictive capability and are within $2 - 10\%$ of the experimental values.

The methods outlined here are based on the idea that compressive strength in composites is dictated by the strength of the 0° ply. Therefore, these methods are not applicable where there are no 0° in the loading direction. Also, these models do not account for damage and failure of off-axis plies and de-lamination. The off-axis ply damage and failure becomes important for laminates with lower percentage of 0°

plies and where the matrix is brittle.

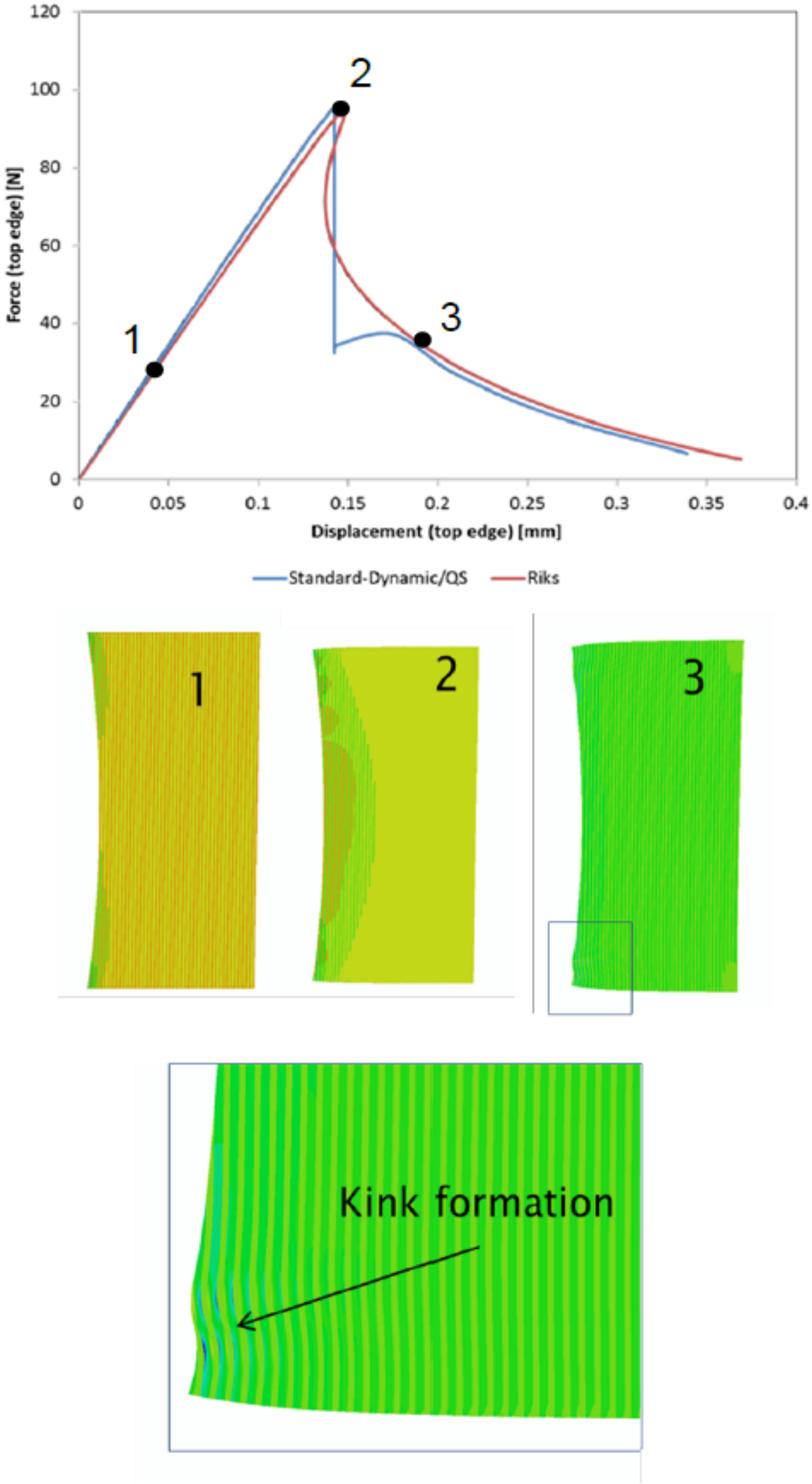

Figure 3.10: Typical result in global-local analysis. Top: Load displacement plot from response analysis of micro region. Two methods are shown, Standard-dynamic and Riks analysis. Middle: Shows the axial stress plots at load points indicated on the load-displacement curve. Bottom: shows the kink band formation in the micro region.

CHAPTER IV

Analytical model for kinking of fibers in composites under compressive loading

4.1 Introduction

As illustrated in previous sections, kink band formation is the dominant failure mode in composite with 0° ply, under compressive loading. To accurately capture the physics of kink failure mode a finite element micro-mechanics approach is required. However, micro-mechanics approach using finite element methods is computationally expensive and cannot be used when modeling larger structures. The alternative is to use an analytical solution which is capable of predicting the compressive strength of composite while preserving the physics of kink band formation.

From literature, models proposed for kink band formation can be classified into three categories; *micro-buckling model*, *kinking model*, and *bending theory*. Micro-buckling analysis was first proposed by Rosen [83], where the compressive strength was equated to the buckling strength of perfectly straight fiber-matrix layer. Micro-buckling models does not take fiber mis-alignment in consideration and thereby severely over-predict the compressive strength. Argon [6] was the first to consider kinking and not micro-buckling as the phenomenon for failure in compression. Budiansky and Fleck [19, 20, 18, 40], Hahn and Williams [46], among others significantly improved on Argon's model kinking model, by incorporating initial misalignment. These models however, were developed to predict compressive strength and not post-peak behaviour. To account for post peak behaviour the, *bending theory*, where the fiber bending resistance is taken in to account was proposed by Fleck et al [40]. Bending theory has since been taken up by other researchers like Chung and Weitsman [26], Morais and Marques [34]. The authors assume an initial sinusoidal fibre imperfection, forming an initial misaligned band inclined at an angle; fibres and matrix are smeared in a homogeneous anisotropic solid. The material is in equilibrium under compressive stresses, bending moments, and shear stresses; the corresponding differential equilibrium equation is solved numerically, giving as outputs the deformed shape of the material. These models are based on elastic-perfectly plastic matrix model. More recently Pimenta et al [72], have used bending theory approach to obtain close form solution to kink strength and kink band formation. The basic premise of their model is that the problem can be divided into two domains, elastic and plastic. To implement this assumption, matrix is assumed to be elastic-perfectly plastic and peak load is assumed to occur at the yield point. Therefore, behaviour till peak load is the same as models proposed by previous researchers [26, 34]. The post peak behaviour is found by equilibrium analysis of elastic and plastic domains. They have then compared the results with finite element analysis which clearly shows that peak load does not occur at the yield point of the matrix [71]. This discrepancy can be attributed to the assumption on peak load and the discretization of the domains.

There are two main issues with previous approaches, specifically, kinking model and bending theory based model. First, these models rely on the on the yield point of the matrix to define compressive strength and switch from continuous to discrete. This is not the case, and is a fact shown by finite element micro-mechanical analysis. Second, the models assume elastic-perfectly plastic matrix models which are non-physical.

Formulation presented here follows similar 2D micro-mechanical procedure as described by Chung & Weitsman [26] and Pimenta et al [72], where bending equilibrium of single fiber, embedded in a non-linear matrix, is analysed. However, no assumptions are made on the yield point, peak load or on the pre- and post-peak deformation shape. Also, the model is continuous, in that there is no discrete elastic and/or plastic domains. The main difference between past models and proposed model is that two generalized displacement that define the amplitude and shape of deformation is used, instead of just one. In following section details of micro-mechanical formulation, equilibrium and elastic stability analysis, and results are provided.

4.2 Micromechanical formulation

4.2.1 Geometry and assumptions

The problem configuration is shown in figure 4.1, in which a single crooked fiber of thickness t^f, and matrix layers of total thickness, 2 t^m, associated with the fiber, are isolated from a uniformly packed multiple fiber composite, figure 4.2. This unit cell is assumed to undergo plane strain deformation in the x-z plane. For fiber volume fractions in excess of 50%, it has been shown, through finite element analysis, [61], [76], that a 2D representation of the composite suffices for understanding the main mechanistic aspects of compression response. The following additional assumptions are also made for this model; (a) the fiber is assumed to deform according to Euler-Bernoulli beam theory, (b) the non-linear matrix takes only shear load, (c) fiber and matrix share the same z-displacement, $w(x)$. With the stated assumptions, the non-linear longitudinal strain in the fiber ϵ_x^f and the linear shear strain in the matrix γ_{xy}^m, are given by:

$$\begin{aligned}
\epsilon_x^f(x) &= \epsilon_0^f(x) - z\kappa(x) \\
&= (u_0^{'} + \frac{1}{2}w^{'2} - \frac{1}{2}{w_0}^{'2}) - zw^{''} \\
\gamma_{xy}^m(x) &= \frac{1}{(1 - V^f)}(w^{'} - {w_0}^{'})
\end{aligned} \tag{4.1}$$

where, a prime superscript refers to differentiation with respect to x, $w_0(x)$ denotes the shape of the initial crookedness (or initial geometrical imperfection), $w(x)$ is the transverse displacement in the z direction. Both, $w(x)$ and $w_0(x)$ are measured from the reference axis $z = 0$. Fiber axial displacement in the x direction is u_0, $\kappa(x)$ is the curvature and V^f denotes the fiber volume fraction. In writing the shear strain in the matrix and reducing it to depend only on x, it has been assumed that the axial displacement, $u_m(x, z)$, varies linearly in the z-direction, between two adjacent fiber layers, [100].

4.2.2 Matrix shear response model

In prior analytical studies of kink banding, authors have modelled the non-linear matrix shear response using elastic-perfectly plastic [72], hyperbolic tangent [97], bi-linear [26] and Ramberg-Osgood [26] models. In the current study, the non-linear shear response of the matrix is modelled using an odd polynomial series that includes upto seventh order terms given by the equation 4.2, where G_e^m is the linear elastic shear modulus and η_0, η_1 & η_2 are fitting parameters to match measured test data. By using a polynomial function, fitting an experimental shear response becomes easier and no assumption need to be made with respect to identifying the shear yield stress of the matrix.

$$\tau_{xy}^m = G_e^m[\gamma_{xy}^m - \eta_0(\gamma_{xy}^m)^3 + \eta_1(\gamma_{xy}^m)^5 - \eta_2(\gamma_{xy}^m)^7] \tag{4.2}$$

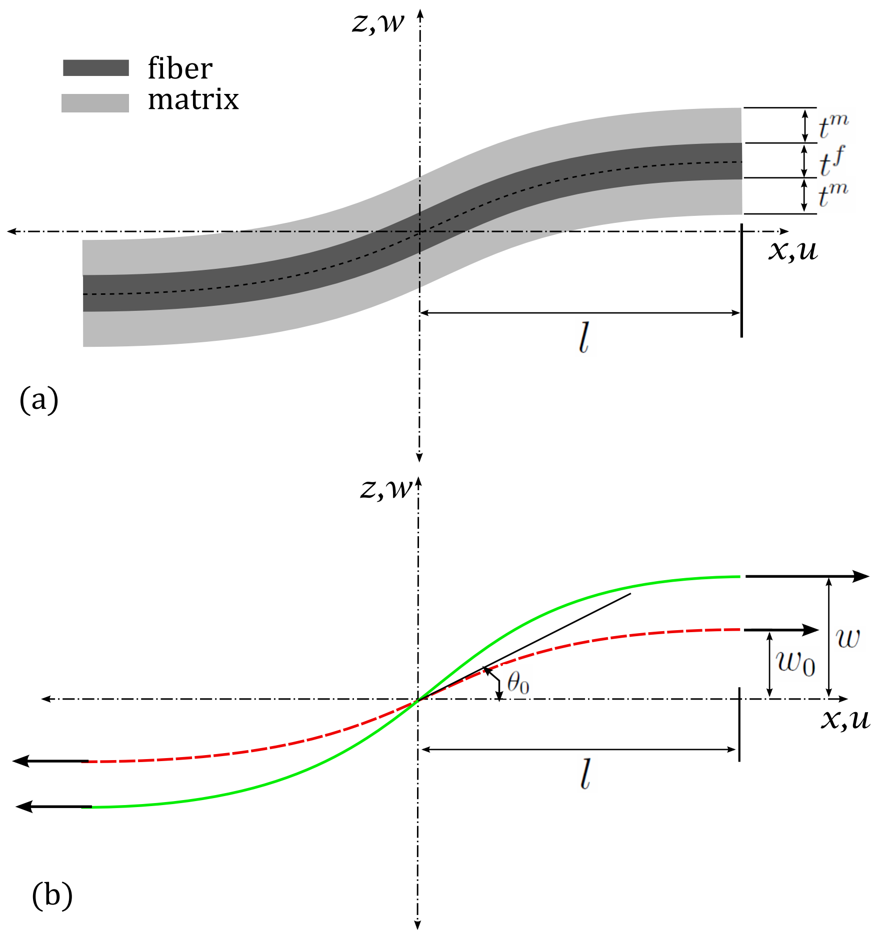

Figure 4.1: Composite unit cell representation.

Although a complete seventh order representation of the matrix shear strain has been used in this study, to keep equations concise, the formulation using upto and including cubic terms is illustrated here. It will be further shown, in section 4.4.1, that a cubic approximation is sufficient for the purposes of determining the pre-peak response and post peak behaviour of the model.

4.2.3 Potential energy

The total potential energy of the unit cell consists of contributions from the fiber (axial and bending energy) and the matrix (shear energy), and external work (W). The strain energy can be further simplified into linear (U_l), and non-linear (U_{nl}) parts.

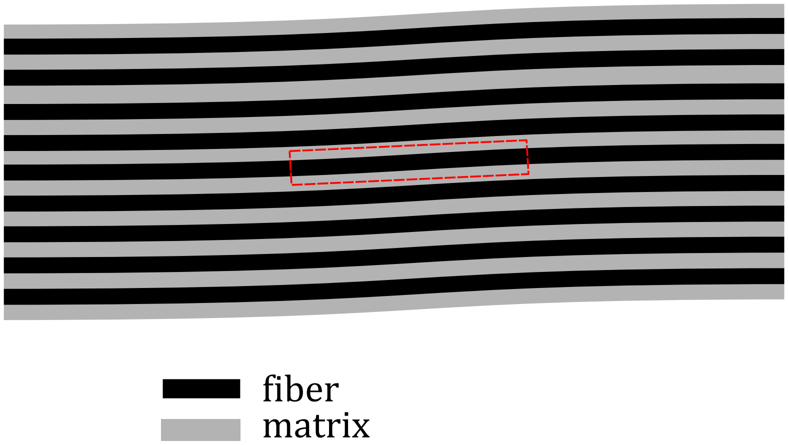

Figure 4.2: Composite representation.

Furthermore, due to the implied asymmetric deformation, only half of the unit cell need be considered. Thus,

$$
\begin{aligned}
U_l &= \frac{1}{2}\int_0^l \{(E_o^f A^f){\epsilon_0^f}^2 + G_1(w' - w_0')^2 + (E_o^f I^f)(w'' - w_0'')^2\}dx \\
U_{nl} &= -\int_0^l \frac{\eta_0}{4}\{G_2(w' - w_0')^4\}dx \qquad (4.3) \\
W &= \int_0^l (-P)u_0' dx
\end{aligned}
$$

where, E_0^f is the plane strain fiber elastic modulus[1] $I^f = b(t^f)^3/12$ is fiber area moment of inertia, $A^f = t^f b$ is the area of fiber, $G_1 = G_e^m/(1 - V^f)^2$ and $G_2 =$

---

[1] in plane strain, $E_0^f = E^f/(1 - \nu_f^2)$, where E^f and ν_f are the Young's modulus and poissons ratio of the fiber, respectively.

$G_e^m/(1-V^f)^4$. Hence, the potential energy Π is written as;

$$\begin{aligned}\Pi =& U_l + U_{nl} - W \\ =& \frac{1}{2}\int\limits_0^l \{(E_o^f A^f){\epsilon_0^f}^2 + G_1(w^{'} - w_0^{'})^2 + (E_o^f I^f)(w^{''} - w_0^{''})^2\}dx \\ &- \int\limits_0^l \frac{\eta_0^m}{4}\{G_2(w^{'} - w_0^{'})^4\}dx - \int\limits_0^l (-P)u_0^{'}dx\end{aligned} \tag{4.4}$$

In what follows, minimizing the potential energy with respect to assumed fiber deflection profiles, motivated by experimental observations, is discussed.

Deformation approximation

From the literature it is understood that most composites have regions of fiber misalignments, and it is known that these play a significant role in the observed deformation modes, [60, 107, 76, 100, 61]. In this study, the initial imperfection, $w_0(x)$ is approximated as a sinusoidal function, with amplitude ξ_0 and periodicity of $2l$.

$$w_0(x) = \xi_0 \mathrm{Sin}[\frac{\pi}{2}\frac{x}{l}] \tag{4.5}$$

When an initially imperfect fiber composite is compressed, the fibers undergo both an increase in amplitude of the initial imperfection and rotation, which precipitates the formation of a kink band. Therefore, when approximating the deflected shape, the choice of function describing the deflected shaped must account for changing amplitude and rotation, with increasing load. In addition to this, the function should also satisfy the kinematic boundary conditions, $w(0) = 0$, $w'(l) = 0$, where l is the length of the unit cell. In the present study, the deflection of the fiber is assumed to be a hyperbolic tangent function with two constants; one for the amplitude (ξ), and the other for the shape (ζ);

$$w(x) = \xi \text{ Tanh}[\zeta x] \tag{4.6}$$

The choice of a sine function to describe the initial misalignment and a hyperbolic tangent function for current displacement has a slight drawback. This is because the sine function reaches its peak at $x = l$, but the hyperbolic tangent will reach its peak at $x = \infty$. This difference will lead to small errors in estimating the matrix shear strain along the length from $x = 0$ to $x = l$. However, the error is only significant at $x = l$, which is the location of minimum shear.

The choice of l is based on ensuring that when a localized deformation band (such as in kind banding) does occur, its details are independent of l. Further, because it is simpler to integrate a sigmoid function upto infinity, the integration bounds are taken to be $[0, \infty]$, implying that l is much larger than any characteristic lengths in the model. Of course, this must be verified after the solution is obtained and details of the deformed shape are established.

4.2.4 Model summary

In summary, potential energy of current model is given by equation 4.4, which includes a linear and non-linear part. There are three unknowns depending on the loading conditions used. For load control, where P is applied, the unknowns are generalized displacements, u_0, ξ and ζ. For displacement control, where u_0 is applied, the unknowns are load P and two generalized displacements ξ, ζ. The solution for both the cases can be found by an equilibrium analysis, where the stationarity of potential energy is evaluated with respect to each displacement.

4.3 Equilibrium and stability

4.3.1 Equilibrium path

For equilibrium to be satisfied, the first variation of Π with respect to the generalized displacements, $w(x)$ and $u(x)$ must vanish. With $w_0(x)$ and $w(x)$ established as given earlier, we first substitute these transverse displacements in Π, so that Π is a semi-discrete function of ξ and ζ. Therefore, the equilibrium conditions are, $\Pi_{,\xi} = 0$, $\Pi_{,\zeta} = 0$ and $\Pi_{,u(x)} = 0$. From $\Pi_{,u(x)} = 0$, after using the boundary conditions, we get

$$P = -(E_o^f A^f)\epsilon_0^f \tag{4.7}$$

where, it shows that the axial load is a constant. This equation, then, establishes a relation between the applied axial load and the end shortening, $\Delta = u(l) - u(0)$, as,

$$\Delta = \int_0^l u_0' dx = \int_0^l \{\frac{-P}{(E_o^f A^f)} - (\frac{1}{2}w'^2 - \frac{1}{2}{w_0}'^2)\}dx \tag{4.8}$$

Using equations 4.7 in equation 4.4 we can write the potential energy as;

$$\begin{aligned} \Pi =& \frac{1}{2}\int_0^l \{(-P)\epsilon_0^f + G_1(w' - {w_0}')^2 + (E_o^f I^f)(w'' - {w_0}'')^2\}dx \\ & - \int_0^l \frac{\eta_0^m}{4}\{G_2(w' - {w_0}')^4\}dx - \int_0^l (-P)u_0' dx \end{aligned} \tag{4.9}$$

Expanding for ϵ_0^f from equation 4.1 we get;

$$\begin{aligned}\Pi =&\frac{1}{2}\int\limits_0^l \{(-P)(u_0^{'}+\frac{1}{2}w^{'2}-\frac{1}{2}{w_0}^{'2})+G_1(w^{'}-{w_0}^{'})^2+(E_o^f I^f)(w^{''}-{w_0}^{''})^2\}dx\\ &-\int\limits_0^l \frac{\eta_0^m}{4}\{G_2(w^{'}-{w_0}^{'})^4\}dx-\int\limits_0^l (-P)u_0^{'}dx\end{aligned} \tag{4.10}$$

Combining the two terms in u_0;

$$\begin{aligned}\Pi =&\frac{1}{2}\int\limits_0^l \{Pu_0^{'}+(-P)(\frac{1}{2}w^{'2}-\frac{1}{2}{w_0}^{'2})+G_1(w^{'}-{w_0}^{'})^2+(E_o^f I^f)(w^{''}-{w_0}^{''})^2\}dx\\ &-\int\limits_0^l \frac{\eta_0^m}{4}\{G_2(w^{'}-{w_0}^{'})^4\}dx\end{aligned} \tag{4.11}$$

Now, substituting for $\int_0^l u_0^{'}dx$ from equation 4.8, term in u_0 can be eliminated to get potential energy only in terms of w and w_0;

$$\begin{aligned}\Pi =&\frac{1}{2}\int\limits_0^l \{P(\frac{-P}{(E_o^f A^f)}-(\frac{1}{2}w^{'2}-\frac{1}{2}{w_0}^{'2}))+(-P)(\frac{1}{2}w^{'2}-\frac{1}{2}{w_0}^{'2})+G_1(w^{'}-{w_0}^{'})^2\\ &+(E_o^f I^f)(w^{''}-{w_0}^{''})^2\}dx-\int\limits_0^l \frac{\eta_0^m}{4}\{G_2(w^{'}-{w_0}^{'})^4\}dx\end{aligned} \tag{4.12}$$

Simplifying,

$$\begin{aligned}\Pi =&\frac{1}{2}\int_{0}^{l}\{\frac{-P^2}{(E_o^f A^f)}+(-2P)(\frac{1}{2}w'^2-\frac{1}{2}{w_0}'^2)+G_1(w'-{w_0}')^2\\&+(E_o^f I^f)(w''-{w_0}'')^2\}dx-\int_{0}^{l}\frac{\eta_0^m}{4}\{G_2(w'-{w_0}')^4\}dx\end{aligned}\tag{4.13}$$

By substituting for w and w_0 from equation 4.6-4.5, we convert potential energy as a function in x, which can now be integrated. Resulting potential energy form will be dependent only on load and two of the generalized displacements, $\Pi = \Pi(P, \xi, \zeta)$. Now, from the two equilibrium conditions, $\Pi_{,\xi} = 0$, $\Pi_{,\zeta} = 0$, an expression for the load P is obtained, and this can be expressed as,

$$\begin{aligned}P =&P_\xi(\xi, \zeta)\\P =&P_\zeta(\xi, \zeta)\end{aligned}\tag{4.14}$$

Closed form solutions for $P_\xi(\xi, \zeta)$ & $P_\zeta(\xi, \zeta)$ can be obtained by using a symbolic solver like Mathematica® and such solutions are listed in Appendix A. At the same time, for each triplet, $\{P, \xi, \zeta\}$ that corresponds to an equilibrium solution, the end shortening, Δ is obtained from 4.8.

Solutions for equations 4.14, will form surfaces in the $\{P, \xi, \zeta\}$ space where the potential energy is stationary with respect to individual displacement q_i, as shown in figures 4.3 & 4.4. An equilibrium path is then defined by the set of points (ξ^*, ζ^*), where both equations, $P_\xi(\xi^*, \zeta^*) = P_\zeta(\xi^*, \zeta^*)$. These (ξ^*, ζ^*) points are essentially the intersection of the two surfaces in equation (4.8), as is shown in figure 4.5. Pairs of (ξ^*, ζ^*) that lie on the intersections provide equilibrium configurations for a given value of P, and in turn, 4.8 provides the end shortening.

A closed form solution for (ξ^*, ζ^*) of the equilibrium path can be obtained by solving the simultaneous equations 4.14. However, this is a highly non-linear problem and requires cumbersome derivations. Instead, the solution for the equilibrium path can be obtained by solving the constrained minimization problem numerically;

$$min\{\ |P_\xi - P_\zeta| = 0\ \} \quad \forall \quad \xi > 0, \zeta > 0 \tag{4.15}$$

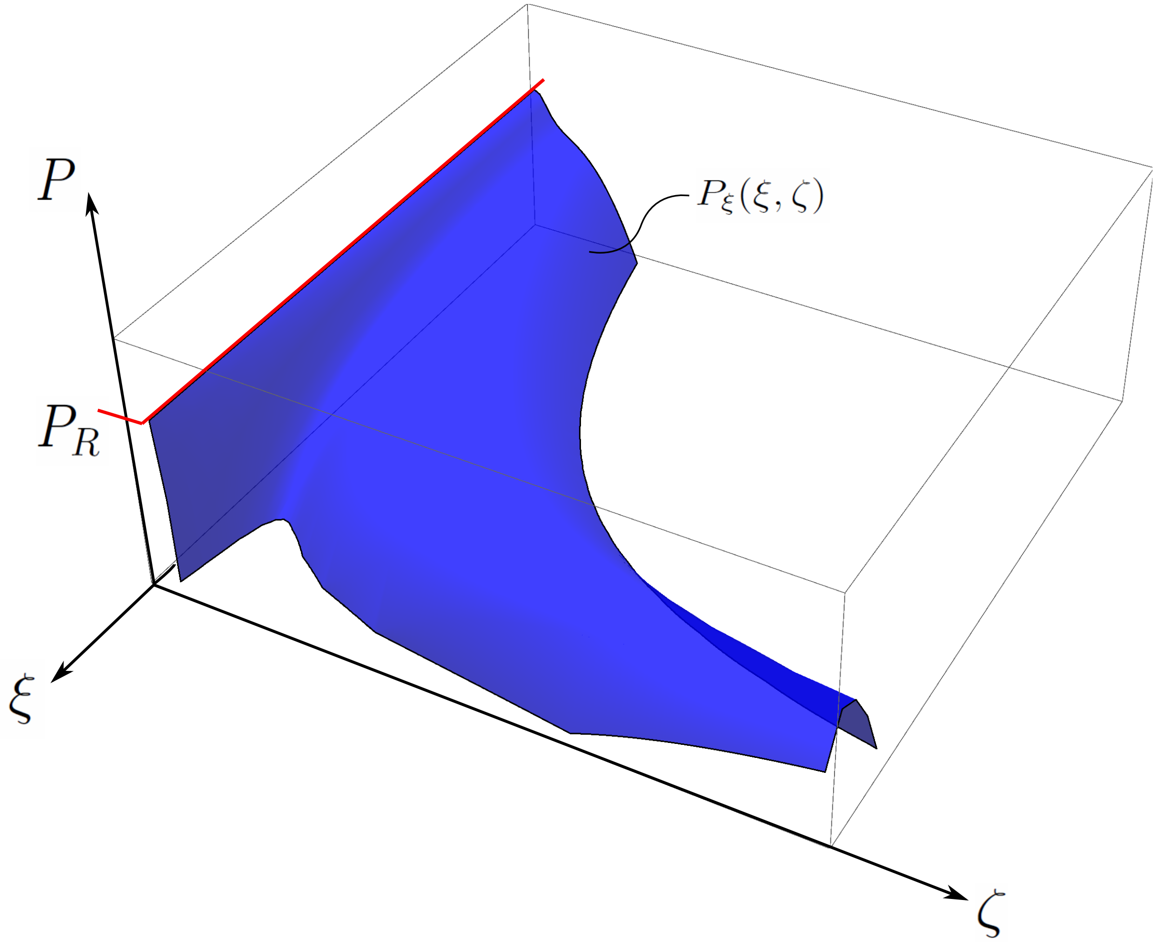

Figure 4.3: Surface defined by function $P_\xi(\xi, \zeta)$ with non-linear matrix assumption $\eta_n > 0$

4.3.2 Stability analysis

To analyse the stability of these equilibrium points, the second derivatives and cross-derivative of Π with respect ξ and ζ are calculated. Here, we will be interested

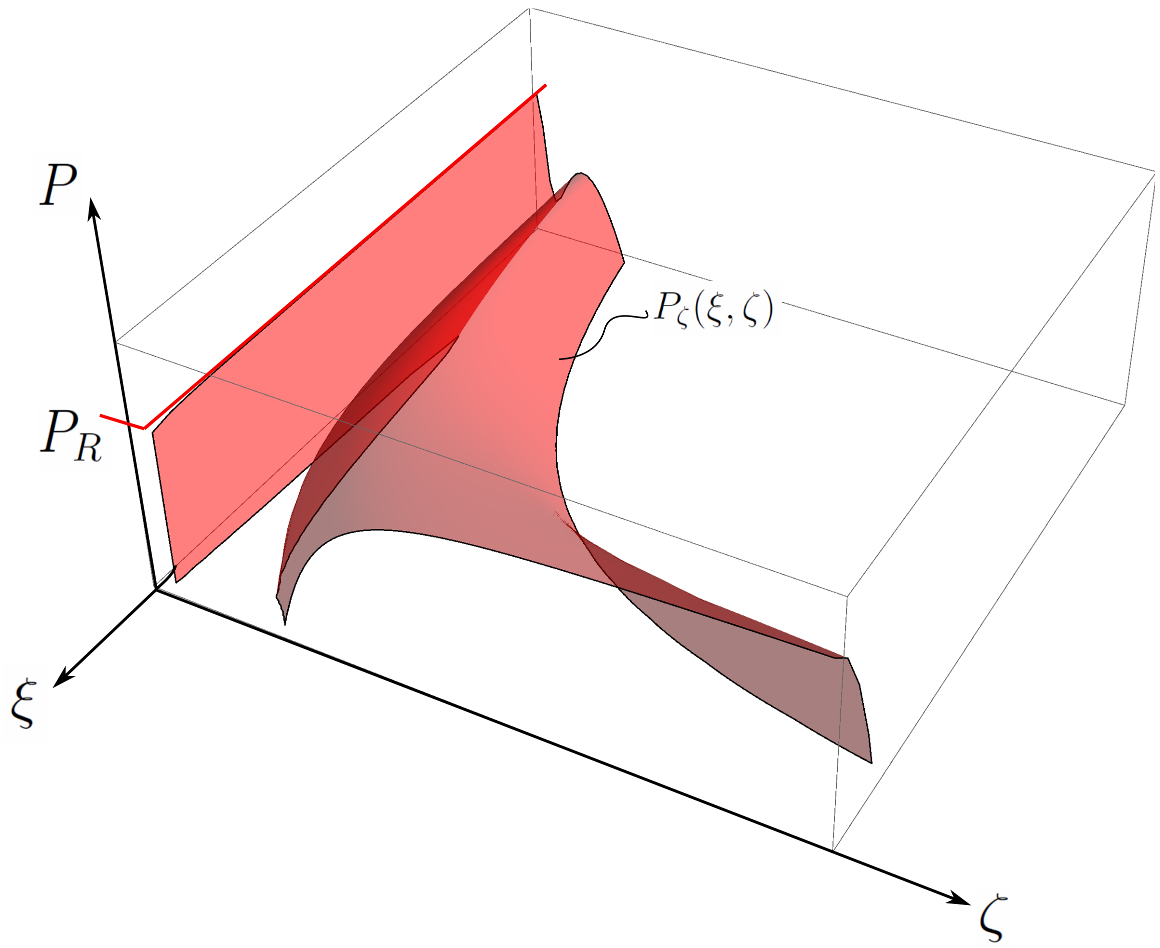

Figure 4.4: Surface defined by function $P_\zeta(\xi,\zeta)$ with non-linear matrix assumption $\eta_n > 0$

in displacement control loading and in this case, only the internal strain energy, U will contribute to Π in evaluating the stability derivatives. It follows that stability is furnished by the 2×2 matrix, K, where,

$$K_{ij} = \frac{\partial^2 \Pi}{\partial q_i \partial q_j} \tag{4.16}$$

An equilibrium configuration given by the triplet, P, ξ^*, ζ^* is stable if K_{ij} evaluated at P, ξ^*, ζ^* is positive definite and one of the diagonal terms is positive. Positive definiteness of the symmetric matrix K_{ij} requires that the determinant of K_{ij} be positive. This condition will cease to exist when, with increasing load, starting at

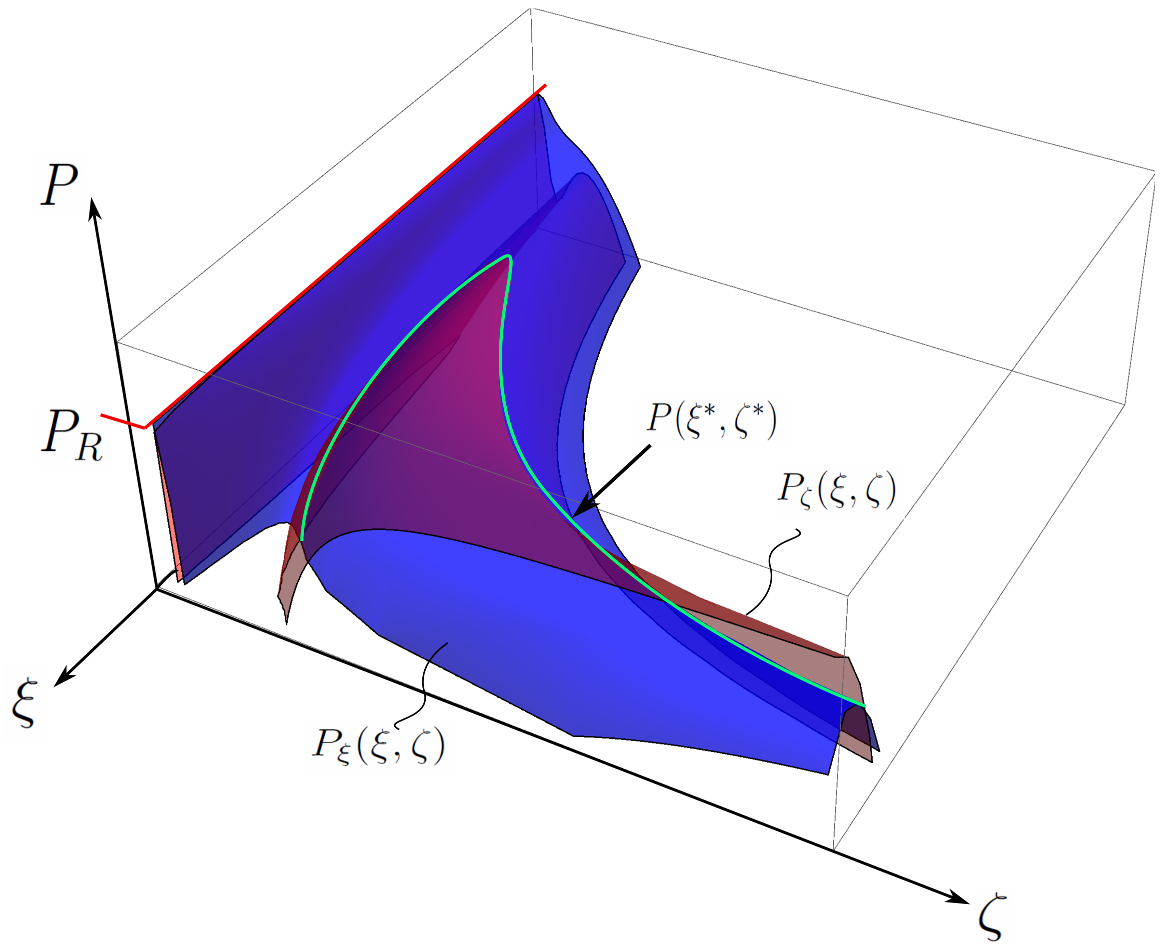

Figure 4.5: Intersection of surface defined by function $P_\xi(\xi, \zeta)$ & $P_\xi(\xi, \zeta)$ with nonlinear matrix assumption $\eta_n > 0$. Equilibrium path $P(\xi^*, \zeta^*)$ is defined by the intersection points.

$P = 0$, the determinant of K_{ij} becomes zero for the first time. The load at which this happens signals a change in the stability of the equilibrium path, and the load obtained is referred to as a critical load. If the tangent to the load vs. load point displacement ($P-\delta$, or $P-u(l)$) curve is unique and is equal to zero, the critical point corresponds to a limit-load. If not, the equilibrium path will bifurcate, and depending on whether the solution is sought as a load-control or displacement-control problem, the interpretation of the load vs. load point displacement response will differ. Since the unit cell problem started out with an initial fiber misalignment, the condition, determinant of $K_{ij} = 0$ is likely to signal a limit load and this will be discussed later.

4.4 Results

Results of the model are illustrated using constituent properties reported by Prabhakar et al [76] for carbon composite. Properties of carbon fiber and volume fraction are listed in table 4.1. *In-situ* non-linear matrix shear properties are taken from Ng et al [70].

Table 4.1: Composite constituent properties

E_o^f	t^f	ν^f	V^f
(GPa)	(μm)	$(-)$	$(-)$
280	6	0.3	0.5

4.4.1 Matrix non-linearity

Non-linear matrix curve is approximated by fitting, polynomial curves to experimental *in-situ* matrix shear data. Polynomial fit of third, fifth and seventh orders are shown in figure 4.6.a. In figure 4.6.b, assumed yield point at 5% tangent stiffness and the maximum stress point or matrix failure point, are indicated. Fifth order polynomial fit shows extreme hardening, which is non-physical and is not used for the analysis. Most epoxy materials fail close to shear strain of 10% [34], hence, a third order polynomial should suffice. This is further investigated by comparing results of third order and seventh order approximations.

A typical equilibrium paths in $\xi - \zeta$ space is shown in figure 4.7. Small variation in the equilibrium paths due to third order or seventh order approximations does not impact the peak behaviour, as is shown in the composite axial stress-strain results, figures 4.8. However, the post peak behaviour will have small impact, since, in the seventh order approximation the maximum shear will not be attained till much later in the post peak regime.

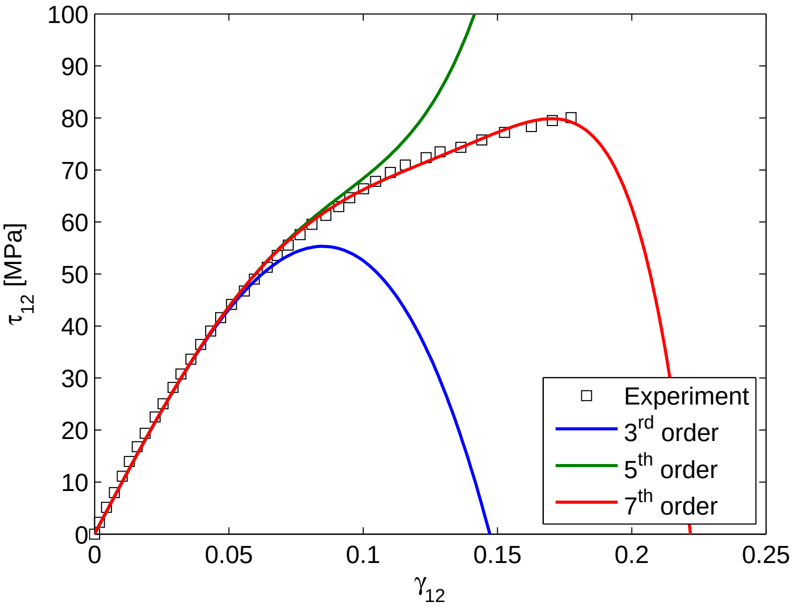

(a) Curve fits

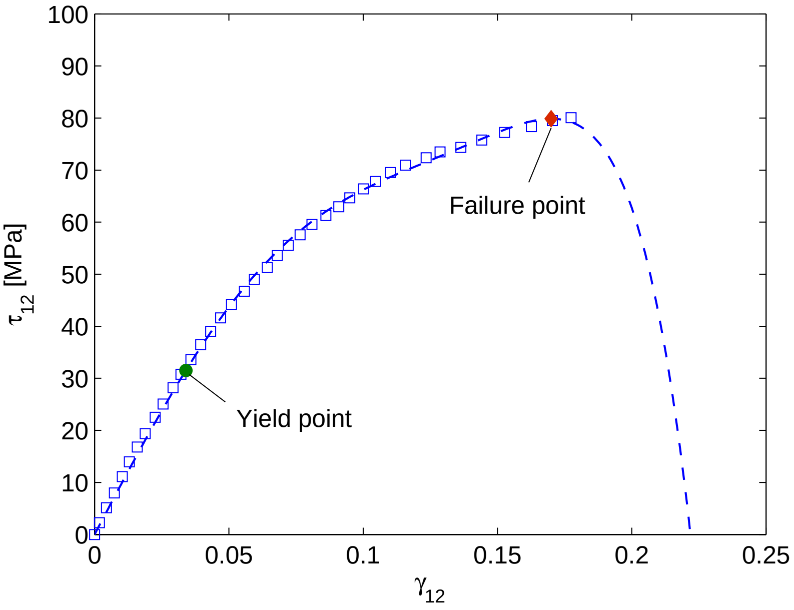

(b) Yield and failure points

Figure 4.6: Fitting experimental matrix in-situ data with $3^{rd}, 5^{th}$ and 7^{th} order polynomial.

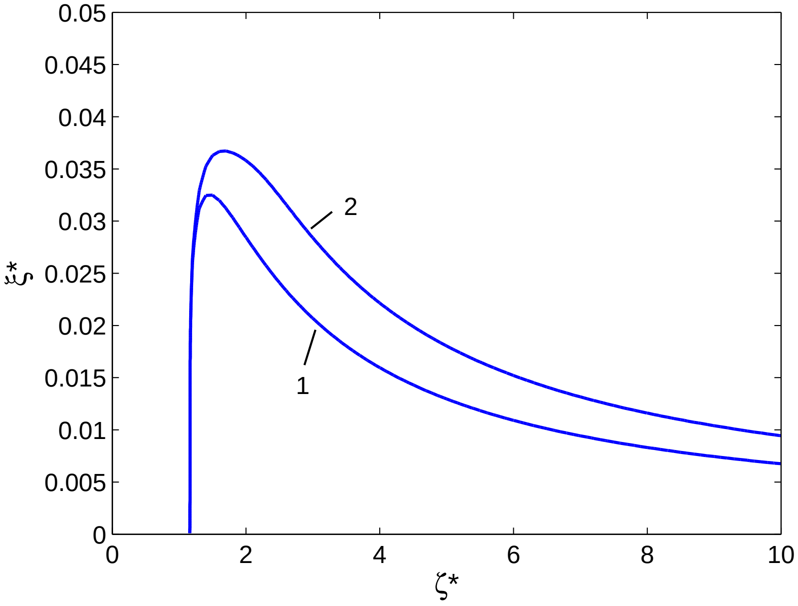

Figure 4.7: Equilibrium path for (1) Non-linear matrix with 3^{rd} order fit, (2) Non-linear matrix with 7^{th} order fit

4.4.2 Kink band formation

A typical stress stain curve obtained from analysis is shown for an initial misalignment amplitude of $\xi_0 = 2\ t^f$ [60] and half wave length of $l = 275\ t^f$ [60], is show in figure 4.9. Points corresponding to; (a) initial imperfection, (b) matrix yield, (c) maximum load, (d) matrix failure, and (e) end point are highlighted. Corresponding to these points, the transverse displacement and fiber axial strain are shown in figure 4.9-b,c. The sequence of events shown in this analysis is similar to one observed by Pimenta et al [72] in their experiments, and represented in figure 4.10, as points $(1) - (5)$ in figure 4.9. The matrix yield occurs prior to maximum load. The yield region first starts from the center of the cell, then spreads axially. There will come a point when the yield region is wide enough to facilitate local rotation of fiber, thus causing a kink to form. Now, the matrix inside the kink band will continue to shear, where as the matrix outside the kink band will unload. The continued shearing of matrix will lead to failure of the matrix, starting from the mid point. The failed

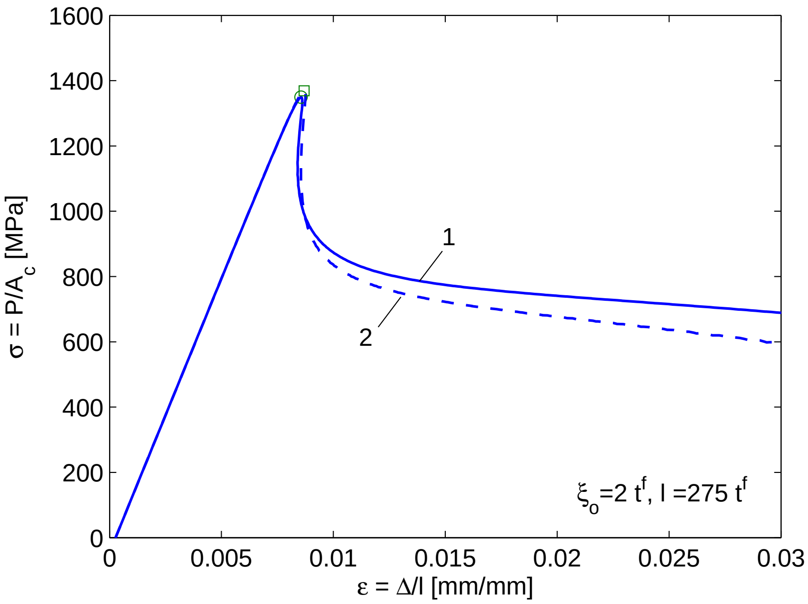

Figure 4.8: Stress strain plot for (1) Non-linear matrix with 3^{rd} order fit, (2) Non-linear matrix with 7^{th} order fit

matrix now does not contribute to the shear stiffness of the cell, and all the load is taken by the fiber, causing it to rotate rapidly.

Using this analysis methods the complete sequence of events till matrix failure can be captured, without any assumption made on the maximum load point or region of softening as done by Pimenta et al [72].

4.4.3 Stability and imperfection sensitivity

Using above constituent properties, equilibrium path is calculated and corresponding axial stress strain curves for varying imperfection amplitudes are shown in figure 4.11a. Limit load instability is determined by checking for positive definiteness at each point. To illustrate this we take the example with very low imperfection of $\xi = 0.2\ t^f$ & $l = 275\ t^f$, for which a distinct snap back behaviour is seen in figure 4.11b. The zoomed-in area in figure 4.11b, shows the stable and unstable equilibrium paths. In case of displacement control, from limit load point the composite will snap

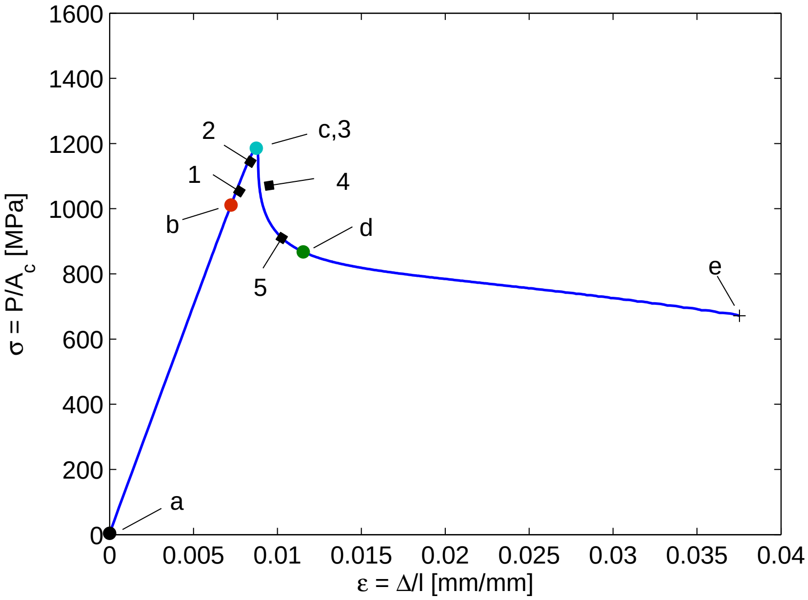

(a) Axial stress-strain

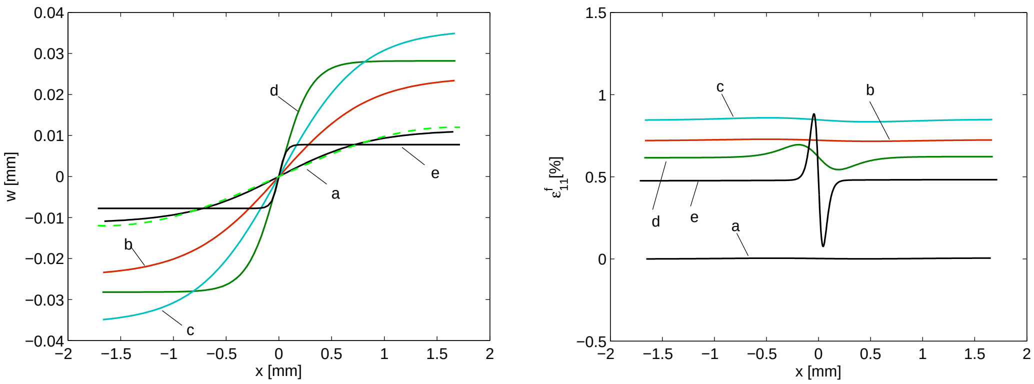

(b) Transverse displacement

(c) Fiber strain

Figure 4.9: Results for $V^f = 0.5$. Point on the graphs: (a) initial misalignment, (b) matrix yield in shear, (c) max load, (d) matrix failure, and (e) end

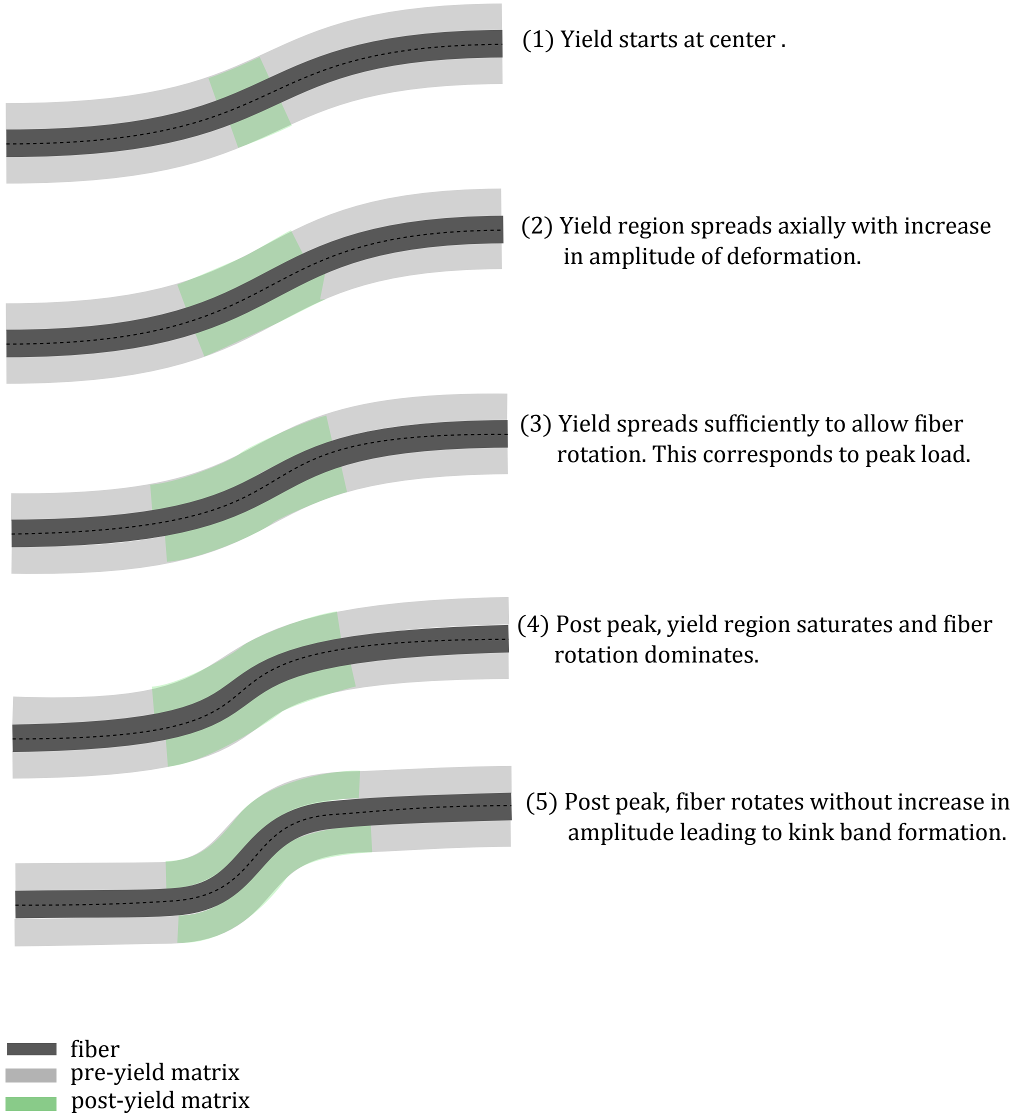

Figure 4.10: Sequence leading to kink formation in composite.

to the next equilibrium. In case of load control, no stable equilibrium path exists after limit load.

The snap back behaviour indicates imperfection sensitivity [11]of composite under compression. In current model, although there are two imperfection parameters ie; the imperfection amplitude ξ_0, and wavelength l, the only parameter that influences the composite response is the imperfection angle, θ_0, given by;

$$\theta_0 = \frac{\xi_0 \pi}{l} \tag{4.17}$$

Angle θ_0 can be changed by keeping the imperfection length constant and changing the imperfection amplitude. The results for which are shown in figure 4.11a. This sensitivity to imperfection angle is because shear strain increases with increasing imperfection angle. In figure 4.12, the imperfection angle is kept fixed and the imperfection height is changed, thereby changing the length of imperfection. The change in length has no effect on the peak compressive strength or the post peak behaviour of the composite.

4.4.4 Yield point and peak point

One of the ideas from previous analytical models of Pimenta et al[72] and Chung et al[26], is that the peak compressive stress would be close to the yield point of the system. To check if this is true, two cases are analysed, where the ratio between yield point (point *b* in figure 4.9a) and peak compressive stress (point *c* in figure 4.9a) is plotted against; (a)volume fraction, and (b)misalignment angle. Figure 4.14 and table 4.2 refers to the case where initial imperfection was kept fixed at $\theta_0 = 0.65°$ and the volume fraction was varied. The result shows an increase in the gap between yield point and peak compressive stress as volume fraction increases. Figure 4.13, refers to the case where volume fraction was kept fixed at $V^f = 0.5$ and the imperfection angle was varied. This result also shows an increase in the gap between yield point and peak compressive stress as imperfection angle increases. However, at low imperfection angles, $\theta_0 < 0.2°$, the yield and peak points are the same. Hence, we can conclude that assumption that yield point corresponds to the maximum compressive strength is only valid for low imperfection angles.

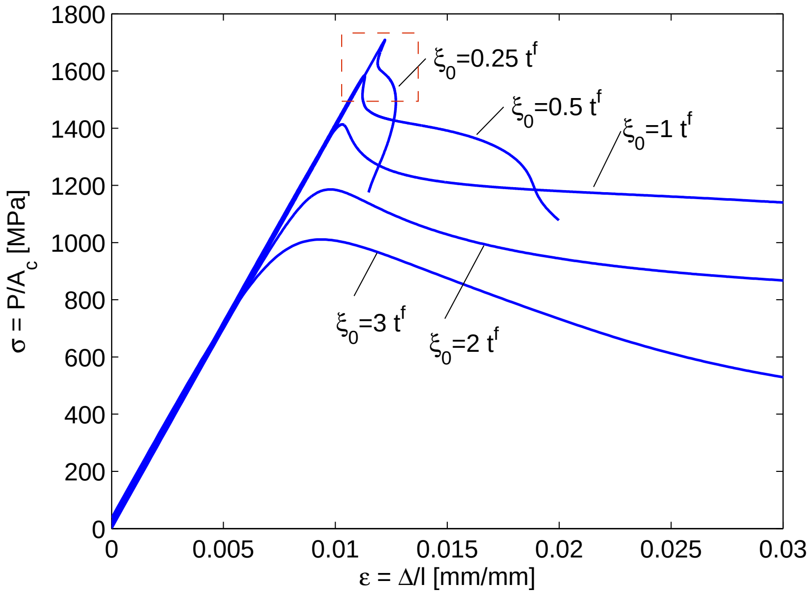

(a) Influence of ξ_0 on response

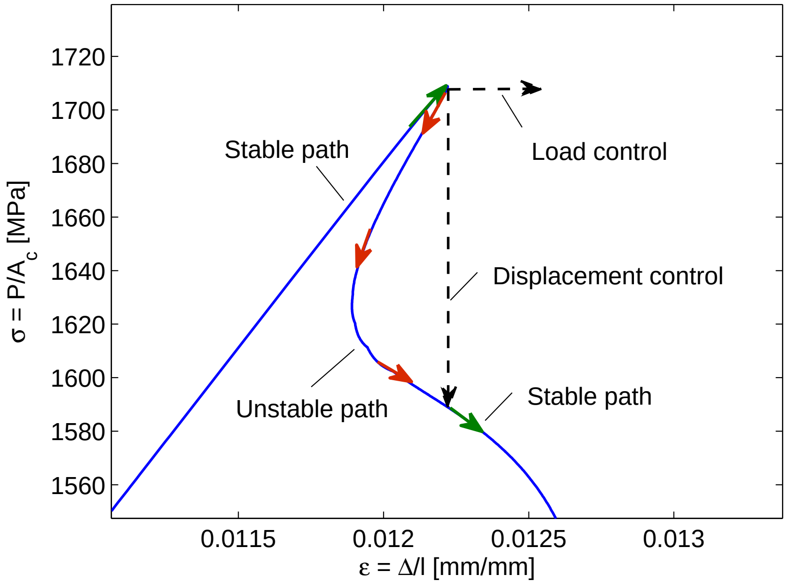

(b) Zoomed in region

Figure 4.11: Zoomed in region shows the stable and unstable paths.

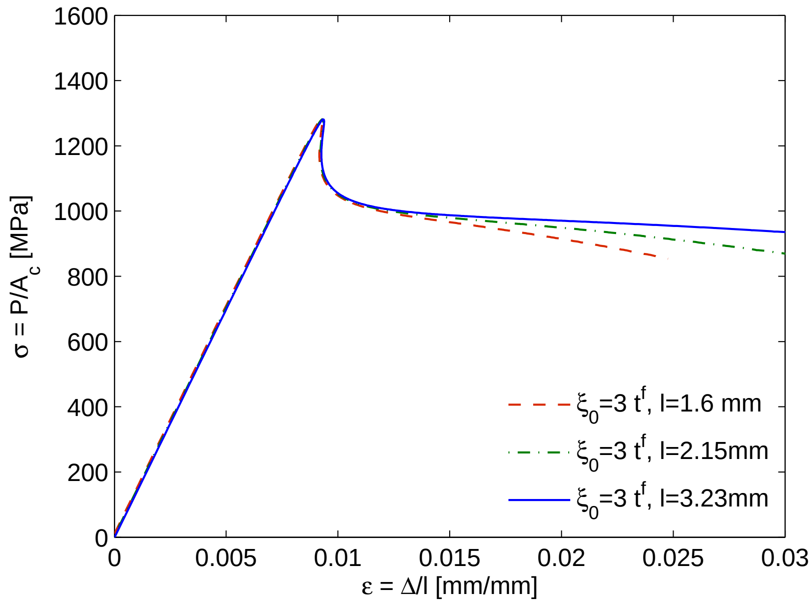

Figure 4.12: Influence of l on compressive strength and post peak response for a fixed imperfection amplitude $\xi = 3t^f$ and $V^f = 0.5$

4.4.5 Comparison with literature

Results from the model was compared against experimental data provided by Morais et al [34], for T300 fiber and 4 different epoxy systems. The results are shown for same imperfection $\xi = 1.5t^f$ and $\zeta = 275t^f$. Current model and experimental data compare well with most configuration, but not all. This discrepancy, as explained by Morais [34], is attributed to difficulty in measuring precise imperfection details in a

Table 4.2: Comparison of stress at matrix yield point and peak load

V^f $(-)$	σ_y^c (MPa)	σ_{max}^c (MPa)
0.40	921	1043
0.45	964	1110
0.50	1011	1186
0.55	1061	1272
0.60	1114	1370

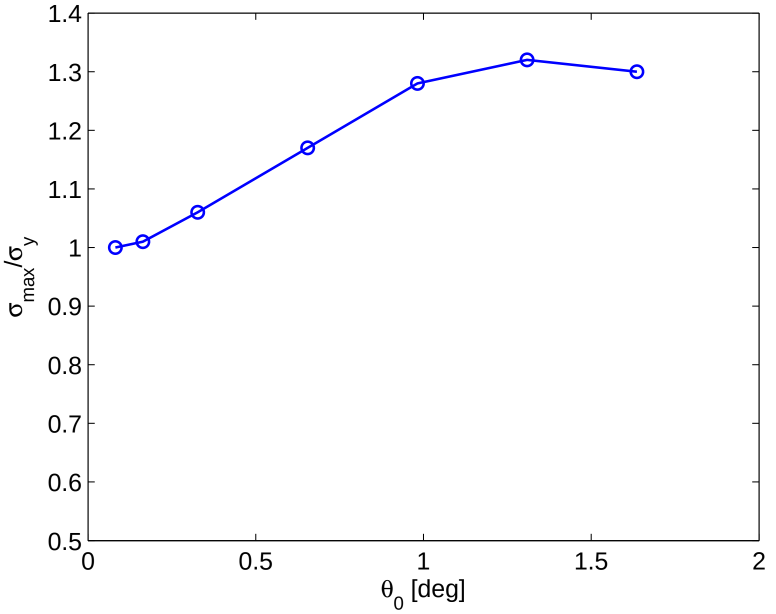

Figure 4.13: Ratio of σ_{max}/σ_y with changing imperfection angle θ_0

composite.

4.5 Conclusion

In conclusion, the following points are highlighted from this study:

- Kink formation is modelled using a continuous beam modeled as compared to discrete beam models proposed by Pimenta et al [72] and Chung [26].

- The choice of matrix non-linear polynomial fit order assumption does not have an effect on the compressive strength prediction. This indicates that kink formation does not require significant non-linearity in the matrix shear response, and occurs at small matrix yield strains.

- Current model is able to capture pre-peak and post-peak behaviour. Post peak behaviour is valid upto matrix failure, since model does not account for fracture. The model can be extended to include fracture by accounting for energy due to

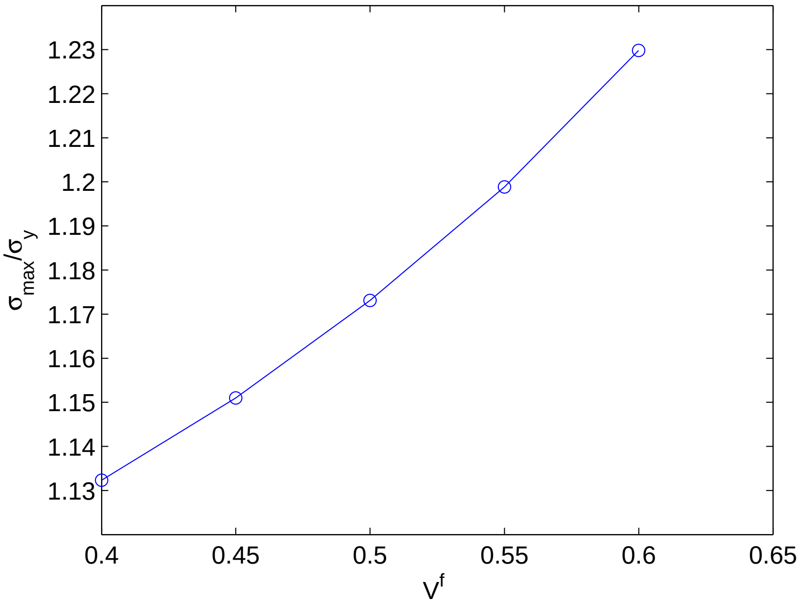

Figure 4.14: Ratio of σ_{max}/σ_y with volume fraction V^f

fracture in potential energy formulation. However, this is beyond the scope of this study.

- Stability analysis shows that the kink formation is due to interaction of two buckling modes; first, modes corresponding to amplitude change, and second, mode due to rotation. This important concept is not highlighted in previous analytical formulations.

- Deviation from linearity affects the compressive strength, however, there is no distinct relationship between the two. Peak compressive strength will be close to yield point for very small imperfections.

- The analysis indicates that matrix can fail close to peak load and before fiber failure. Hence, kink band width is not only decided by fiber failure but also by matrix failure. Matrix failure precipitates localization of kink, which in turn causes fibers to fail earlier than what would have been predicted using intact

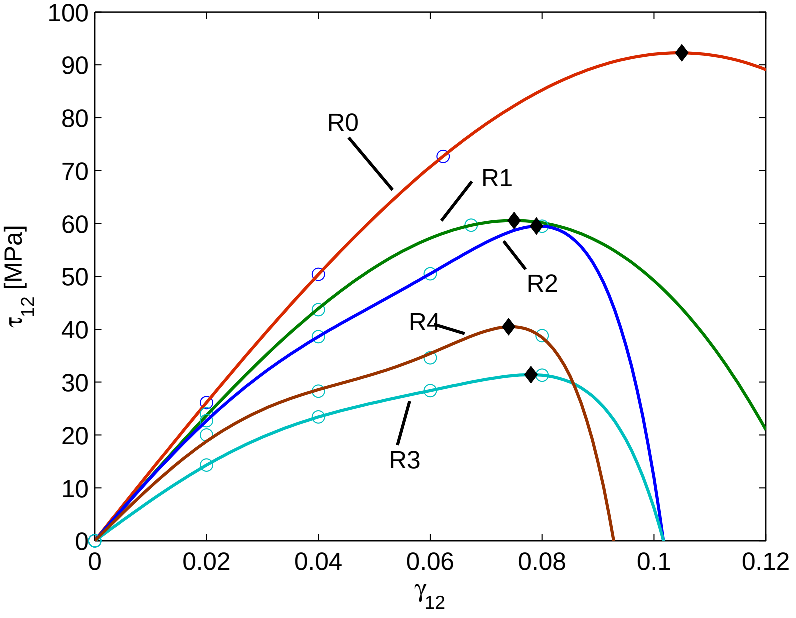

(a) Matrix shear stress.

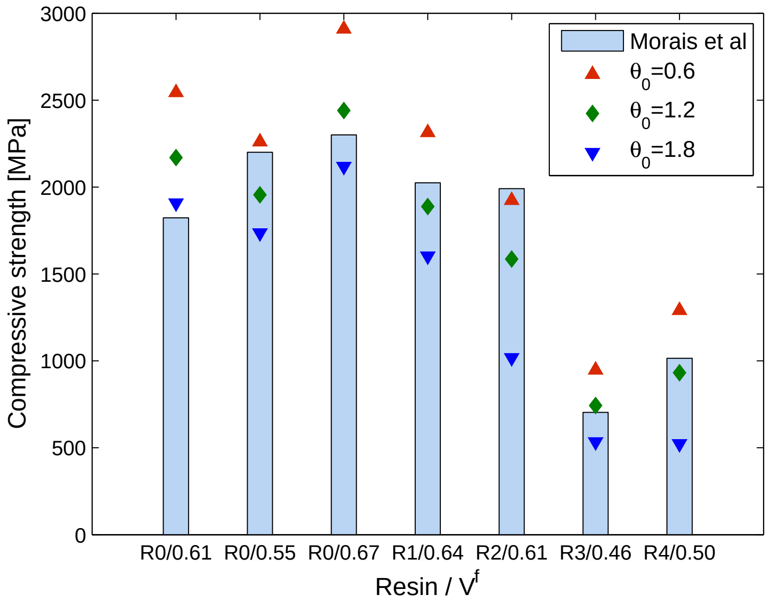

(b) Comparison with experiments.

Figure 4.15: Comparison of current model with experimental results [34].

matrix. Therefore, kink band width cannot be predicted using a model that does not include matrix failure.

CHAPTER V

Introduction: Fracture mechanics

Fracture is one of the many energy dissipation modes available for a solid to release energy due to external or internal forces causing it to move away from its natural equilibrium state. What distinguishes fracture from other modes of energy dissipation is the fact these cause discontinuities in the topology of the solid. It is these discontinuities that cause problems in formulation of a unified fracture theory since mathematically the continuum field around a crack tip has a $1/\sqrt{r}$ singularity, where r is the distance from the crack tip.

In fracture mechanics, much of the earlier work has been concentrated on developing approaches that circumvent the problem of mathematical singularities. Most methods can be roughly classified under energy equilibrium, continuum field approximation and cohesive zone methods. Energy equilibrium approach was first introduced by Griffith [44], which was further advanced by Mott and Irwin to include inertia and non-linear elasticity, respectively. The idea of a stress intensity factor introduced by Irwin provided an alternative to circumventing the traditional continuum stress singular stress field at the crack tip. Irwins stress intensity factor can and has been used to characterize the crack initiation and growth [88]. Another important approach was to define fracture by appealing to small scale yielding zone or process zone, which became the basis for the now popular cohesive zone model of Barenblatt [8] and J-Integral theory of Rice [82] and Cherepenov [25]. Hellan [48], Freund [41] and Anderson [5] have covered these early development in fracture mechanics in detail.

Common to all the above fracture mechanics ideas is the notion of thermodynamic equilibrium and thus, their usefulness is strictly valid for predicting the initiation of crack growth. However, these theories have been applied also to predict crack propagation by assuming that a propagating crack to be a series of equilibrium increments of crack growth [41, 67]. Although this approach provides satisfactory results for cracks propagating at extremely high velocities in brittle materials the same is not true for ductile materials, nor for crack growth situations that clearly warrant deviating from a “static equilibrium” state.

In the following section, the applicability of the basic assumption of thermodynamic equilibrium when applied to crack initiation and propagation is investigated. This is done by first looking at the conditions for applicability of thermodynamic equilibrium. Based on the outcomes obtained, the applicability of Griffith’s theory for crack propagation and at its apparent deficiencies are discussed. With this background, an alternative theory to study crack growth is described some examples in support of the proposed model are introduced.

5.1 Thermo-statics & Griffith’s theory

Mathematically, when crack propagation in a solid occurs, an energy dissipation function can be used to describe the process of crack growth. This function describes how much a crack should grow in a continuum for given external conditions. These dissipation functions are based on the combination of Theory of Irreversible Processes (TIP) and Griffith’s theory. In this section we re-examine the applicability of these theories to a crack propagation problem.

5.1.1 Theory of Irreversible Processes and closeness to equilibrium

TIP uses *Axiom of local state* to approximate a thermo-dynamic process, *close* to equilibrium, as a sequence of *thermo-static* equilibria [67]. Therefore, the progress of a crack through a solid, which is a non-equilibrium process, is assumed as a sequence of smaller (*close to equilibrium*) thermo-static equilibrium jumps. This is the basis of Griffth's theory. A critical point to note here is that the validity of *TIP* hinges on the definition of closeness to equilibrium in a spactio-temporal domain. This closeness to equilibrium also decides the validity of *Theory of Minimum Potential (TMP)* in fracture mechanics. Maugin [67] states two conditions for closeness. First is the spatial condition given by,

$$\lambda := \frac{\chi/L}{|\nabla\chi|} \gg 1 \tag{5.1}$$

where, χ is a typical variable of state, $|\nabla\chi|$ is its microscopic gradient and L is a macroscopic length scale. In fracture mechanics, the crack opening near the tip of crack can be considered as the variable of state describing fracture and the resulting strain field is the microscopic gradient. The strain gradient near the tip has a mathematical value of infinity hence, the above equation is a always satisfied for continuum fracture mechanics. Second is the temporal condition which requires that the *Deborah number* $\mathcal{D}_e^2$ (the ratio of characteristic response time, τ_R which allows the thermostatic system to recover to a new state of thermodynamic equilibrium, to the characteristic duration,τ_M, of the kinematic and dynamic evolution of the solid medium), to be negligible. In the study of fracture we can consider the time for unit extension of the crack to be the characteristic response time and the time required for unit deformation of the solid as the evolution time.

$$(\mathcal{D}_e)_{TIP} := \tau_R/\tau_M = \frac{1/\dot{a}}{1/\dot{u}} = \frac{\dot{u}}{\dot{a}} \ll 1 \tag{5.2}$$

where, $\dot{a}$ is the crack velocity and $\dot{u}$ deformation velocity or loading rate. Satisfaction of above condition decides the validity of TIP and TMP as applied to fracture mechanics. Eqn (5.2) gives an idea of when the TIP can be used for fracture analysis in solids. If the rate of deformation is relatively much smaller than the rate of crack growth then TIP is valid. However, if the rate of deformation is relatively much larger than rate of crack growth then TIP is not a viable choice for fracture analysis. The former mechanism is seen in brittle fractures (like glass and ceramics) and the latter is seen in ductile fracture (like metals and rubber). This effect of closeness criterion is further studied in the next section where Griffith's criterion is revisited.

5.1.2 Griffith's fracture theory revisited

Griffith's fracture theory [44] states that the total reduction in potential energy is the increase in strain energy U less the potential energy of the crack surface W_{dis}.

$$\Pi = \Delta U + W_{dis} = \Delta U + 2\gamma\ w\ da \tag{5.3}$$

where, γ is the surface energy, $w\ da$ is the area created due to an increment, da, of crack growth, through the width of the specimen w. Griffith claimed that crack growth will initiate once the strain energy release rate $\mathscr{G}$ equals a threshold value $\mathscr{G}_c$, which is found by applying the theory of minimum potential energy, ie; for $d\Pi/da = 0$ and $da \to 0$. The threshold value is given by;

$$\mathscr{G}_c = 2\gamma \tag{5.4}$$

Hence, according to Griffth,

$$\dot{a} \quad \begin{cases} = 0 \quad if \quad \mathscr{G} < \mathscr{G}_c \\ > 0 \quad if \quad \mathscr{G} = \mathscr{G}_c \end{cases} \tag{5.5}$$

The main reasoning behind the above formulation is that some amount of energy is consumed for creating additional surface due to the fracture process. Now, since the surface energy is a constant the manifold defining equilibrium states would be the one where the current energy release rate will be equal to the critical value; $\mathscr{G} = \mathscr{G}_c = 2\gamma$. Since, the surface energy is a constant value at a given temperature, eqn(5.5) seems valid. However, there is an implicit assumption that the condition given in eqn(5.2) is always met.

Let us now examine the general case where we observe the system *far* from equilibrium but still enforce TMP to obtain the manifold describing equilibrium states. Let us consider a body which undergoes a displacement $d\mathbf{u}$ due to a crack growth of da, without body forces and inertia effects. Then the change in potential energy with respect to crack increment can be written as

$$\frac{d\Pi}{da} = \frac{dU}{da} - \frac{dW}{da} + \frac{dW_{dis}}{da} = \frac{dU}{da} - (\int_A \mathbf{t}.\frac{\partial \mathbf{u}}{\partial a}\ dA) + 2\gamma\ w \tag{5.6}$$

Dividing above equation by the width w and defining energy release rate as $\mathscr{G} = -\frac{1}{w}\frac{dU}{da}$ we get

$$-\frac{1}{w}\frac{d\Pi}{da} = \mathscr{G} + \frac{1}{w}(\int_A \mathbf{t}.\frac{\partial \mathbf{u}}{\partial a}\ dA) - 2\gamma \tag{5.7}$$

Now if we apply the principle of minimum potential energy, as per Griffith's theory, the energy release rate should correspond to the critical threshold value. However, it is clear that this is possible only if $\frac{\partial \mathbf{u}}{\partial a} = 0$. In all other cases,

$$\mathscr{G} = -\frac{1}{w}(\int_A \mathbf{t}.\frac{\partial \mathbf{u}}{\partial a}\ dA) + 2\gamma = -\hat{\mathscr{G}_c} + \mathscr{G}_c \tag{5.8}$$

Hence, the manifold defining equilibrium states would be the one where $\mathscr{G} = (-\hat{\mathscr{G}_c} + \mathscr{G}_c)$. This equation states that the critical strain energy release rate is not a constant but a function of the rate of deformation of the body with respect to crack growth. Clearly, any dissipation function based on Griffth's theory will only find application in fracture processes that satisfy the condition stated by eqn(5.2), which is limited to fracture where crack growth rate is much higher than the deformation rate ($\partial a \gg \partial \mathbf{u}$). Alternatively, eqn(5.8) can be implemented if evolution of $\hat{\mathscr{G}_c}$ is known a-priori. This is not feasible as deformation of the system will depend on system dimensions and boundary conditions, hence $\hat{\mathscr{G}_c}$ will not be a unique function.

If we strictly adhere to the condition stated in eqn(5.2), then for any point *far* from equilibrium we cannot apply TIP or TMP. If TMP is not applied, strain energy release rate will have no meaning as potential energy will not be stationary $d\Pi/da \neq 0$. From the above relations it is clear that the energy release rate is an outcome of crack formation and is problem dependent, hence its criticality to describe crack growth warrants further consideration. However, the notion of a critical energy release rate, either as a total, G_{total} or broken into component modes, as, G_{Ic}, G_{IIc} and G_{IIIC} is quite popular as described in [5].

5.2 Implementation

Ideas outlined in previous sections are explored further and illustrated using examples in the next two chapters. In chapter VI, a novel approach to analyzing the fracture of fiber-reinforced composites is proposed. Experimental results on mode I fracture of glass fiber and carbon fiber unidirectional laminates form the basis for the analytical and numerical results. When details of the external loading rate are explicitly accounted for, a new picture of fracture emerges which encompasses the possibility for non-smooth crack growth and the necessity to relax the use of a critical strain energy release rate as a criterion for crack advancement. Results predicted by adopting the analytical model proposed are seen to capture a wide variety of fracture responses that have been observed previously.

In chapter VII, instabilities in fracture of certain types of polymers are studied using a fracture physics model based on the over-stress at the crack-tip and the micro-damage that forms ahead of the crack-tip. These polymers are those for which several experimental results are available in the open literature. The proposed model is seen to provide the physical basis for the interplay between different energy dissipation modes when a brittle polymer fails by rapid crack propagation. Results from the new fracture model, which are in agreement over a wide range of reported experimental results, suggests that deviations from steady state crack propagation in brittle fracture is an artifact of micro-damage ahead of the advancing crack and is unrelated to crack velocity. In fact, the relationship is reverse; i.e., it is the over-stress at the crack-tip that causes micro-damage which in turn influences the crack growth velocity in a rapidly fracturing brittle polymer.

5.3 Fracture property measurement of sandwich panels

In addition to above chapters, in appendix C, a validated experimental approach to obtaining critical mode I & mode II energy release rates for interfacial failure by fracture in a sandwich composite panel is outlined. By modifying the geometry of the sandwich structure to align the face sheet-core interface to coincide with the neutral axis, it is possible to obtain critical mode I & mode II energy release rates by conducting Double Cantilever Beam (DCB) and End Notch Flexure (ENF) tests, respectively. The values so obtained were used to predict the crack growth histories of modified DCB and ENF tests, and a Single Leg Bend (SLB) test, using a discrete cohesive zone method (DCZM). In addition, the influence of material and geometry were also analyzed.

CHAPTER VI

Non-smooth mode I fracture of fiber reinforced composites

6.1 Introduction

Layered materials are ubiquitous in nature spanning a wide range of length scales as observed in human muscle to sedimentary rocks. Delamination is a commonly observed mode of failure in synthetic layered materials. Characterizing the delamination resistance of continuous fiber polymer matrix composite laminates (PMCLs) is of importance in assessing the structural integrity of components made of PMCLs. A popular contemporary approach in achieving this is through a combination of standardized coupon level tests in conjunction with finite element based numerical analysis of the test specimen/s which use cohesive zone modeling strategies [103, 99, 45, 98]. With this approach, the modes I,II and III fracture toughness, G_{Ic}, G_{IIc} and G_{IIIc}, and associated cohesive strengths, $\sigma_{Ic}, \tau_{IIc}, \tau_{IIIc}$, respectively, are obtained and used in subsequent structural analyzes, as input data, in characterizing a composite structure and its ability to resist delamination growth. In those instances where the loading at the delamination tip involves the presence of more than one mode of crack growth, a suitable mixed-mode crack growth law is also needed.

While a substantial number of delamination crack-growth studies have focused on smooth quasi-static crack growth, regardless of the externally applied loading rate, there are many instances in which crack growth can occur in a non-smooth manner, where periods of stable smooth growth can occur bounded by regions of unstable fast crack growth even though the external loading rate is quasi-static. In these instances, there is a need to examine how rate dependence affects fracture toughness, cohesive strengths and the associated mixed-mode crack growth laws. Early investigations pertaining to examining the rate dependence of G_{Ic} were conducted by Aliyu and Daniel [4], while a conflicting result was later reported by Yaniv and Daniel [105]. Maikuma et al. [65] examined rate dependence of G_{IIc} and reported a decrease in value with an increase in loading rate. A comprehensive study, using double cantilever beam (DCB) specimens, on the effects of loading rate on mode I fracture of unidirectional carbon fiber composites was reported by Kusaka et al.[59]. They found that G_{Ic} decreased in a step-wise fashion with a transition region in which G_{Ic} showed a strong dependence on rate, however, above and below this region G_{Ic} was found to be fairly constant. Below the transition region, fracture was found to be unstable and non-smooth exhibiting stick-slip response, while above the transition region stable fracture was observed. The experimental findings were explained by incorporating rate dependence in G_{Ic} and kinetic energy contributions of the DCB loading arms. This finding was in contrast to that observed in Blackman et al. [15] who observed stable crack growth at low loading rates in a carbon fiber/PEEK composite that transitioned to unstable stick-slip behavior as the loading rate increased. Stick-slip behavior, but with a stochastic ductile to brittle transition is also reported in the studies by Sun et al. [93] who examined fracture of adhesively bonded metallic specimens.

In the present work, the mode I fracture of glass fiber unidirectional composite (GC) samples and carbon fiber unidirectional composite (CC) samples are studied under quasi-static loading rates using the ASTM standard [7] DCB test specimens.

It is found that crack growth, under the examined quasi-static loading rates, exhibits both, smooth and non-smooth responses, rendering the interpretation of an initiation toughness, G^i_{Ic} problematic. Moreover, while a R-curve like response is observed in the CC laminates, a plateau toughness, G^p_{Ic}, which is called for in the ASTM standard is not attained. In GC laminates, the observed test results are difficult to interpret with respect to identifying G^i_{Ic} and G^p_{Ic}. Non-smooth response has also been observed by Kusaka et al. [59], who explained the cause by appealing to rate dependence of G^i_{Ic}. Blackman et al. [15] also found non-smooth, stick-slip crack growth in a carbon fiber/PEEK composite as the loading rate was increased, suggesting that a definition of a critical load to back out a value of G^i_{Ic} would be problematic.

The present paper is organized as follows; details of the experimental investigation including experimental results and observations are presented first. This is followed by an analysis of the test data using a cohesive zone finite element (FE) model, while at the same time attempting to extract data according to the ASTM D 5528 standard. The numerical results, obtained using the cohesive zone FE model, are also used to illustrate the difficulty in defining critical fracture initiation, G^i_{Ic}, and propagation G^p_{Ic} parameters. Subsequently, the non-smooth crack growth response is explained by adopting a new analytical formulation of the DCB fracture problem that uses an alternative set of hypothesis associated with examining rate of crack growth energetics. A discussion of the results obtained through the different approaches is followed by concluding remarks to complete the paper.

6.2 Experiment

6.2.1 Quasi-static Double Cantilever Beam Test

Displacement controlled DCB experiments were conducted on GC and CC unidirectional laminate coupons. The geometry of the sample is shown in figure 6.1 and

Table 6.1: Nominal specimen dimensions for DCB test

Type	L (mm)	h (mm)	b (mm)	a_0 (mm)
GC	130	2.5	25.4	50
CC	155	2	25.4	45

table 6.1 lists the dimensions that follow the ASTM D 5528 standard. The initial crack was introduced using a Teflon® film, inserted during manufacturing of the laminates. Steel blocks with a transverse through hole at its center were bonded to the free end of the laminates for pin joint load transfer. The pin joint was lubricated using Teflon lubricant to reduce frictional loss. Clear markings on the specimen side surfaces were used to track crack growth. The modulus, E_{11} in the fiber direction is 11.5 GPa for the GC and 117 GPa for the CC respectively, while the major Poisson's ratio is 0.3 for the GC and 0.29 for the CC, respectively.

The tests were conducted on an Instron 4201 universal test machine with crosshead displacement rate of 5mm/min for GC and 1mm/min for CC. Load was measured continuously using a 1,000 N high accuracy tension/compression load cell linked up to a data acquisition system. A high resolution SLR camera, time synchronized with loading, was used to capture crack zone images with a framing rate of 1 frame per second. The images were then analyzed manually, using a linear pixel measuring software calibrated against a reference grid pattern marked on a typical specimen. This method gives crack length in the time domain which can be converted to plot crack length against load and load point displacement. After the test, each sample was checked for through the width variation and was found to conform to ASTM D 5528 standard, [7]. Each test was terminated when the crack extended for approximately 30mm from the initial position. Seven samples of each material were tested to ensure repeatability in test data.

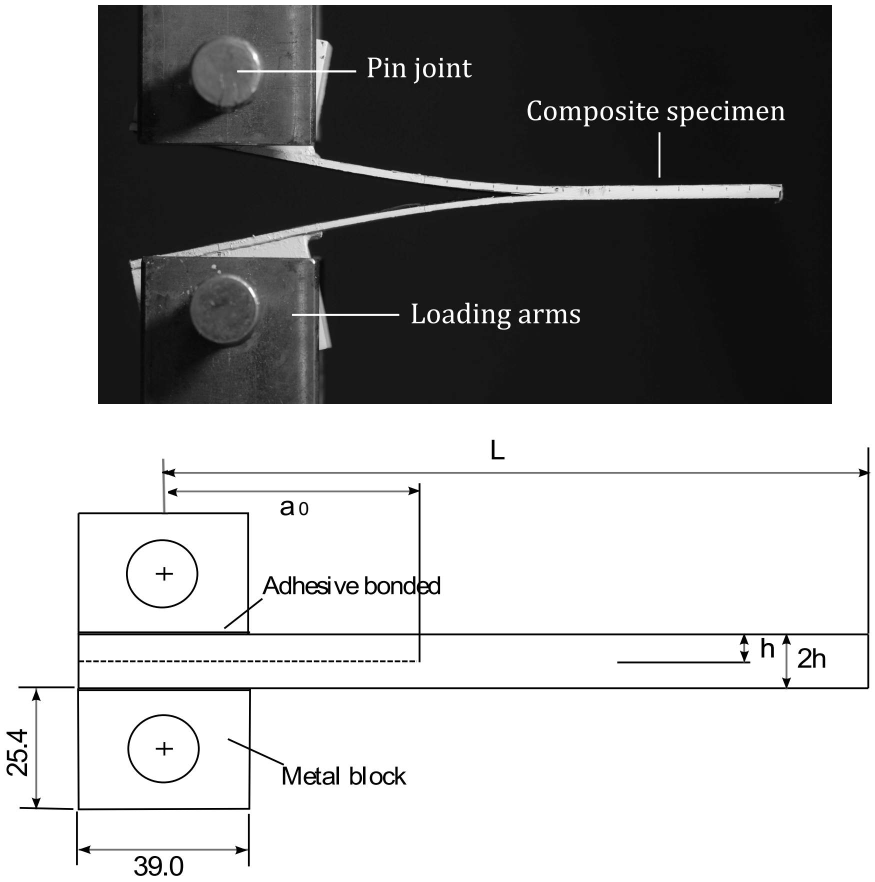

Figure 6.1: Double Cantilever Beam (DCB) test coupon geometry

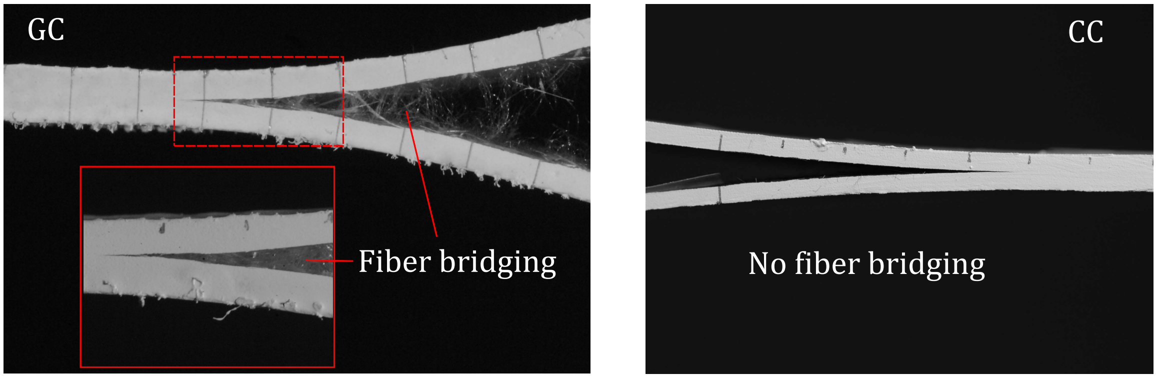

Figure 6.2: Fiber bridging seen in glass composite laminate (GC). Little or no fiber bridging seen in carbon composite laminate (CC).

6.2.2 Observations & Results

Both, GC and CC, showed repeatable, linear behavior up to the point of crack initiation with continued loading. GC specimens showed a higher compliance when compared with the CC specimens. Upon unloading, both types of specimens exhibited negligible permanent deformation. The mild permanent set, caused by some matrix micro-cracking and fiber bridging, the latter being the case for GC laminates. The majority of the energy dissipation can be attributed to the Mode I crack growth, and thus effects of micro-cracks in the DCB arms are not considered in this study. Significant fiber bridging was observed in the GC laminates, whereas negligible fiber bridging is seen in the CC laminates, as shown in (figure 6.2).

Figure 6.3 shows the normalized load-displacement response and figure 6.4 shows the crack growth versus the crosshead displacement for GC and CC laminates. Results are normalized to a value of $P_0 = 120N$ for ease of comparison. As seen in the crack extension plots (in figure 6.4) the failure history is quite different for the two different sets of coupons. In GC laminates, non-smooth type crack growth is observed. This non-smooth crack growth is also reflected in the force displacement plot, where each jump is associated with a sharp drop in force. This was an unexpected phenomenon since DCB tests, by design are expected to result in smooth crack (no crack jumps) growth under quasi-static loading ($0.5 mm.s^{-1}$ to $5 mm.s^{-1}$ as defined in ASTM standard [7]). Furthermore, others have reported smooth crack growth with R-curve response for GC laminates [28]. The fact that there is significant fiber bridging should facilitate smooth crack growth as reported by Morais and Pereira [68].

Kusaka et al [59] have reported non-smooth crack growth in brittle carbon epoxy uni-directional laminates at loading rates of $0.01 mm.s^{-1}$ which is below the rate used for defining quasi-static loading rate. However, they also demonstrated smooth crack growth with the same material system at higher loading rates of $5 mm.s^{-1}$. The reverse trend is reported in Blackman et al. [15], who show a transition from smooth to stick-slip behavior as the loading rate increases. In CC laminates, even though the crack growth is smooth, the force continued to increase *even after initial crack growth* up to a certain point after which a gradual decrease in force was observed in the present experimental results. This result is similar to the results reported by Morais and Pereira [68], where an increase in fracture energy is seen with smooth crack progression. The key differentiator is the significant fiber bridging observed by Morais and Pereira, which is not present in the CC laminates studied here.

6.2.3 Energy release rate

Fracture energy was calculated using Modified Beam Theory (MBT), Compliance Calibration (CC) and Modified Compliance Calibration (MCC) methods as specified by ASTM D 5528 [7]. The expression for the strain energy release rate in the DCB test (G_I), based on MBT, CC and MCC methods are

$$G_I^{MBT} = \frac{3Pw}{2b(a + |\Delta|)} \tag{6.1}$$

$$G_I^{CC} = \frac{\kappa Pw}{2ba} \tag{6.2}$$

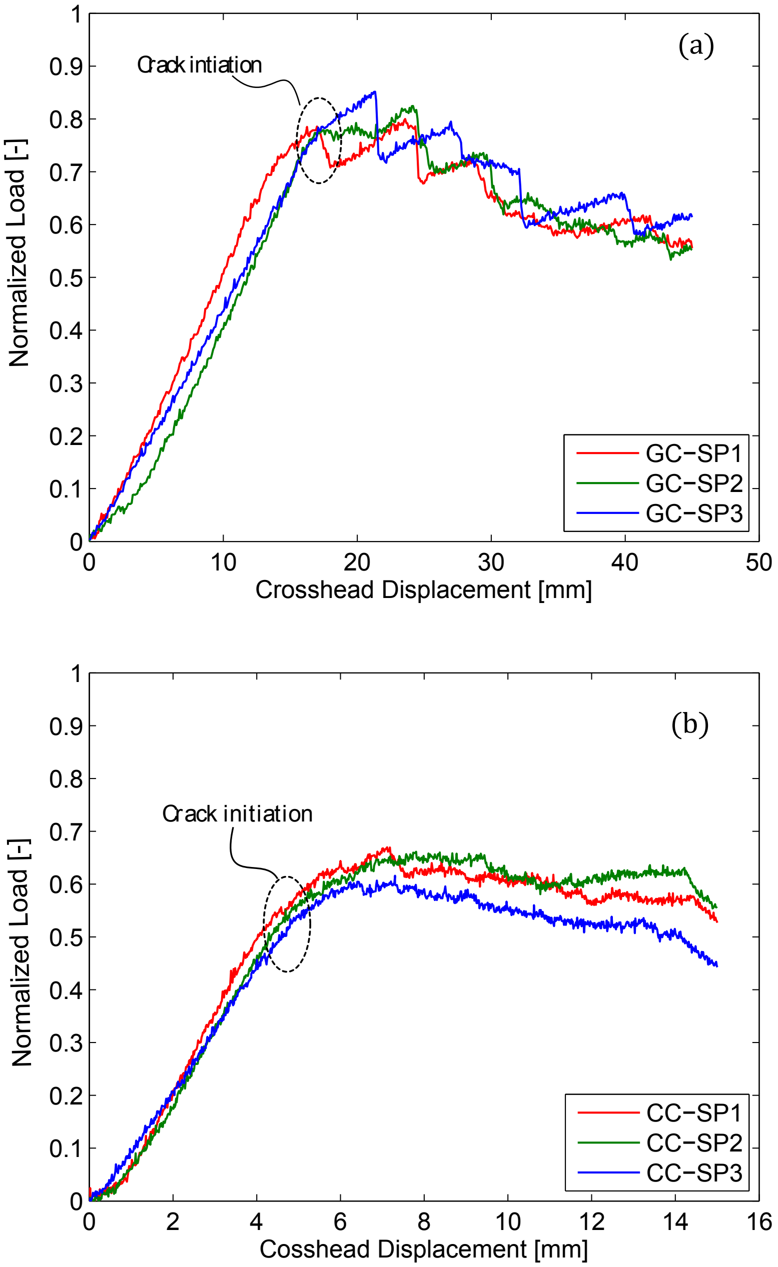

Figure 6.3: Normalized load (P/P_0) versus cross head displacement (w) for (a) GC & (b) CC. Glass composite results show fluctuation in load displacement behavior whereas in Carbon composite the results show an progressive increase in load after the crack initiated.

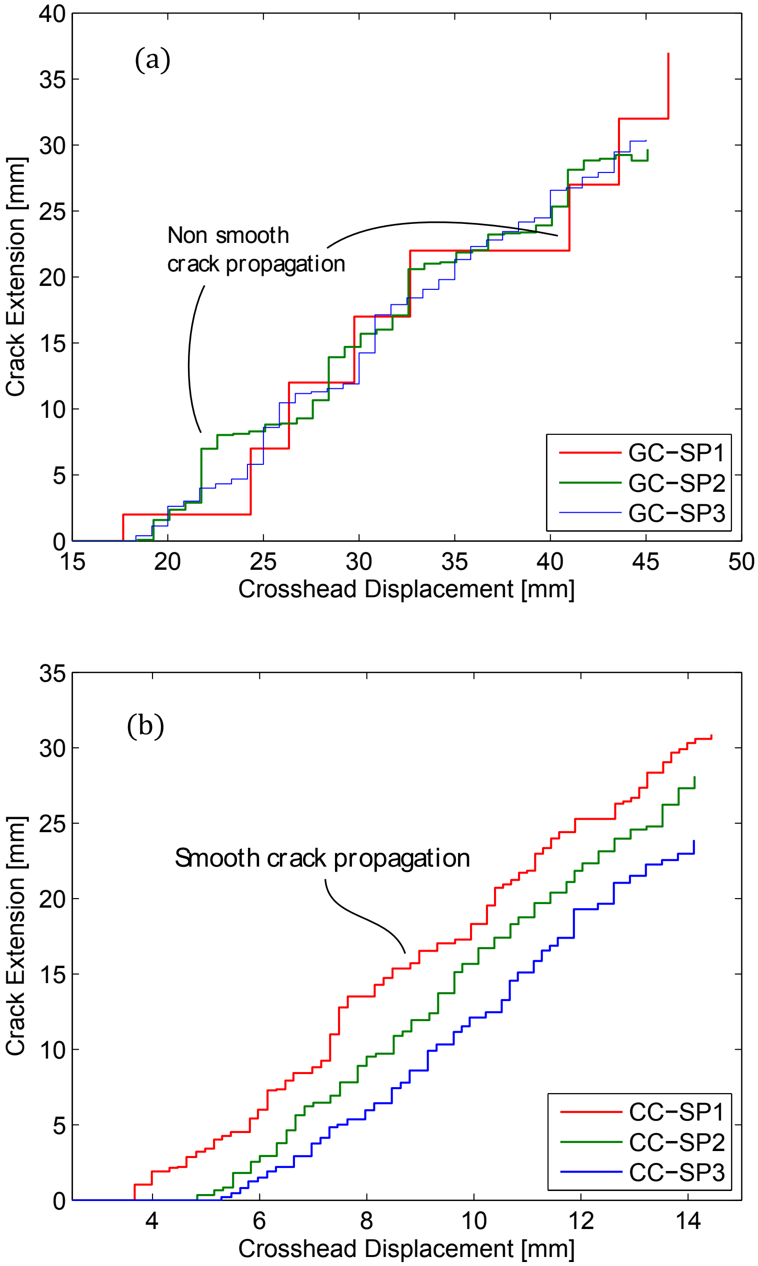

Figure 6.4: Crack extension (a) versus cross head displacement (w) for (a) GC & (b) CC. The non-smooth behavior in glass composite laminate is seen in crack growth whereas there is a steady growth in crack in carbon composite.

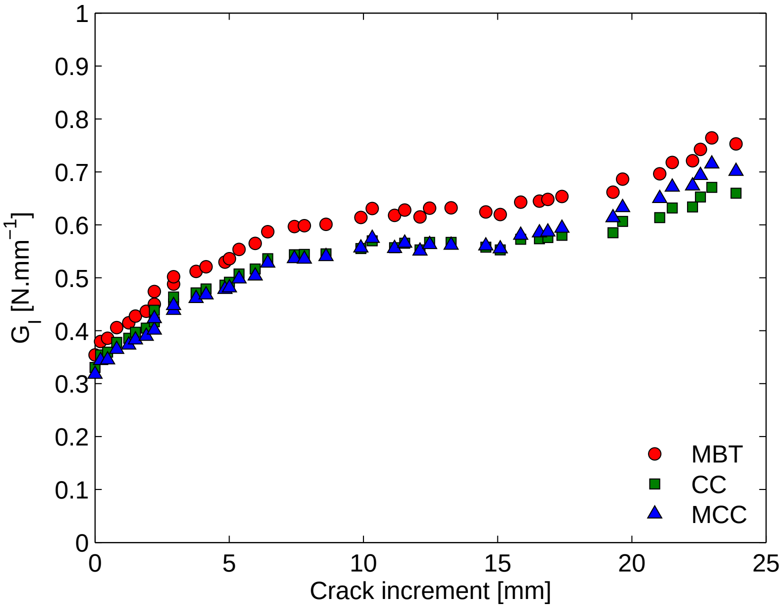

Figure 6.5: Typical result obtained for CC samples with MBT, CC and MCC method of strain energy release rate calculation

$$G_I^{MCC} = \frac{3P^2C^{2/3}}{2A_1bah} \tag{6.3}$$

where P is the measured load, w is the prescribed displacement, b is the width of the specimen and a is the measured crack length, C is the compliance, κ is the slope of compliance calibration curve [7], A_1 is the slope of modified compliance calibration curve [7] and h is the height of the specimen. Figure 6.5 shows a typical strain energy release rate with respect to crack increment. Strain energy release rate values obtained from MBT are used for simulation and comparison purposes because MBT gives the upper bounds for energy release rates.

Figure 6.6 shows the G_I distribution with crack growth for GC and CC based on MBT calculation method. A cubic curve fit is used to obtain the resistance (R) curve in each case. In the case of GC laminates, an oscillatory pattern is seen for G_I with crack extension, which reflects non-smooth crack growth. The fitted R curve of GC on the other hand conforms to a typical R curve described in ASTM D 5528 [7]. The pattern observed showed values ranging from a minimum of $1.47 N.mm^{-1}$ to a maximum of $2.2N.mm^{-1}$ and a mean value of $1.8N.mm^{-1}$. In CC laminates, smooth crack growth is observed, hence, it is expected that the R curve in case of CC should also follow the one described in the ASTM standard [7]. However, the R curve shows a monotonic increase with increase in crack extension. Similar results are also seen in experiments conducted by Morais and Pereira [68] for carbon-epoxy laminates with high fiber bridging. The increase in G_I, in the present study for CC laminates, is almost two times the initiation energy release rate. The G_I value ranged from $0.25N.mm^{-1}$ to $0.75N.mm^{-1}$ with a mean of $0.5N.mm^{-1}$.

6.2.4 Experimental Results: Summary & discussion

In the previous section, two different crack growth histories are described for DCB tests conducted on GC and CC laminates corresponding to external loading regimes classified as quasi-static. The results show a mixture of smooth and non-smooth crack growth responses. Related experimental findings reported by others in the literature, [68, 15, 59], also show a mixture of smooth and non-smooth crack growth histories. This poses a problem when critical energy release rates from coupon DCB tests are needed for predicting the response and failure of larger structures made of the same material or for comparisons between different material systems. For a typical DCB simulation, the critical value of G_I for initiation and propagation is identified from the experimental R curve. As specified in ASTM Standard D 5528, the point of non-linearity in the resistance curve is recommended for failure initiation, G_{Ic}^{i}, and the stabilized value is recommended for propagation G_{Ic}^{p}. The pre-condition to obtaining the critical parameters from a DCB test is that crack propagation should be smooth ie; the crack growth rate with loading is constant. This definition of critical parameters can pose a significant constraint on different material systems because there is no clear initiation or propagation value that can be inferred from the experimental results, even with smooth crack growth. In the case of GC, G_I values have a large scatter

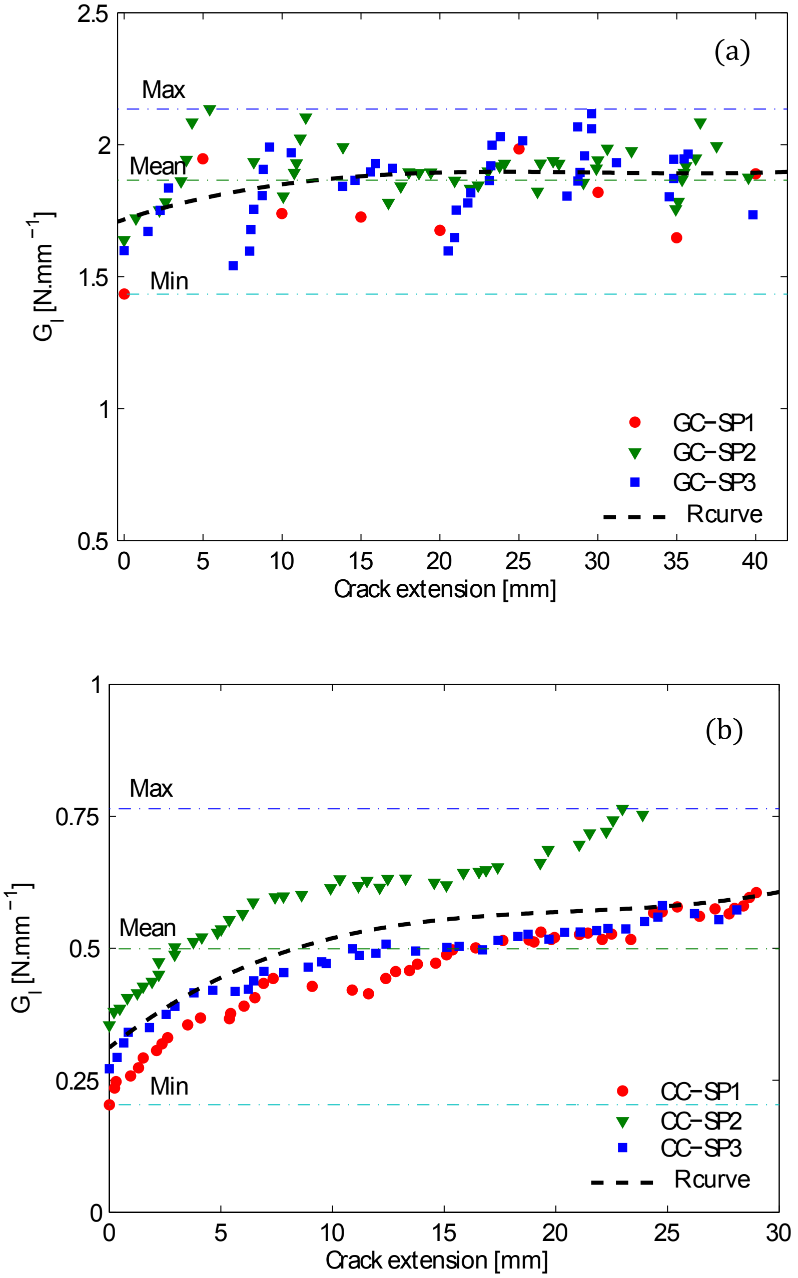

Figure 6.6: Delamination resistance curve (R curve) for GC & CC laminates, obtained by fitting G_I data obtained from experiments. Glass composite laminates show an oscillatory pattern in G_I whereas in carbon laminates there is a steady increase in G_I with crack length. Minimum, mean and maximum values for GC & CC are also shown.

and do not follow the typical R curve behavior given in ASTM standard [7]. In the case of CC laminates, there is a steady increase in G_I. Even though the initial point of non-linearity can be used for G_{Ic}^i, the crack propagation G_{Ic}^p cannot be determined, since there is no stabilization of the R curve. Similar difficulties were also faced by Morais and Pereira [68] and Blackman et al. [15]

6.3 Numerical Analysis

From the experimental results, the critical value of G_I that should be used for simulation and prediction of mode-I fracture in the given material system has now to be posed. To answer this question and investigate the variance of G_I and its effect on the predictive capability, two approaches were used for the numerical simulation of the DCB test results. The first was to assume a fixed value of G_{Ic} along the length of the crack path (figure 6.7-(a)), and the second was to vary the G_{Ic} value along the length of the crack path based on the observed experimental values (figure 6.7-(b)). The latter was done to illustrate the limitations of using critical toughness values.

The numerical simulation of the DCB fracture experiment was conducted using the finite element method in conjunction with the Discrete Cohesive Zone Method (DCZM). Several papers in literature have employed non-linear traction separation curves to explain the R-curve behavior. The main reasoning behind these methods has been to incorporate fiber bridging in to cohesive formulation. The ability of these methods to capture R-curve behavior is highly dependent on the fitting parameters used for both G_{Icr} and σ_{Ic} which may not be unique, hence limiting the application of these methods. To limit the design parameter used for numerical simulation, in this paper we employ only a triangular traction separation law.

The triangular traction-separation law (figure 6.8)is implemented through a user defined interface element (UEL) subroutine in Abaqus®[45]. UELs are placed at the

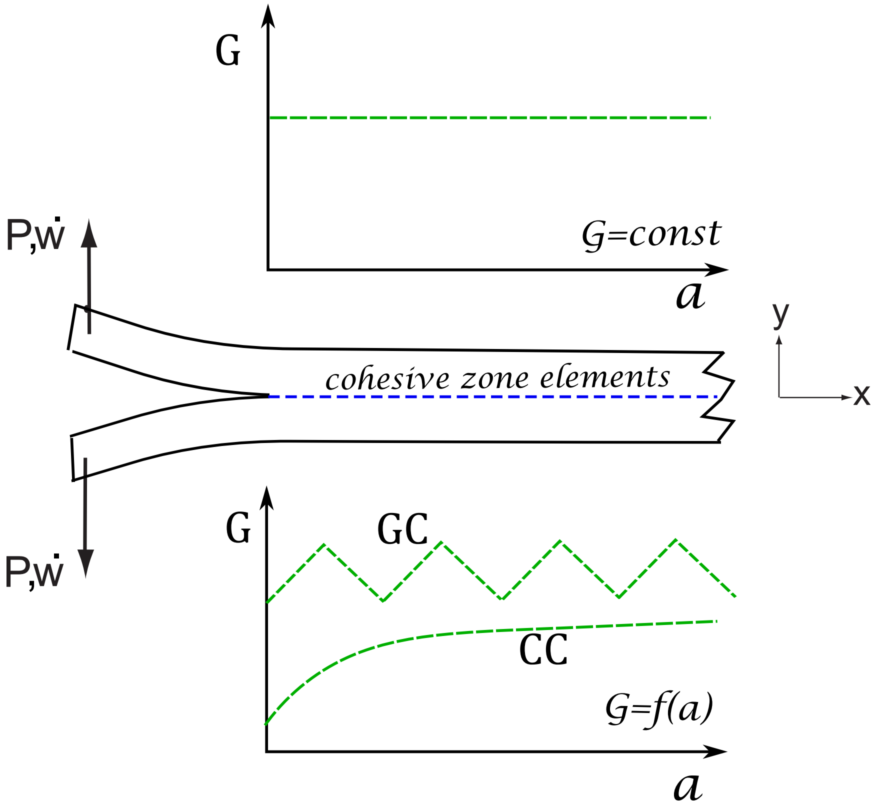

Figure 6.7: DCZM UEL implementation in FEM simulation model. (a) Approach 1: with fixed G_{Ic}=constant, along the crack length. (b) Approach 2: with variable $G_{Ic} = f(a)$. For GC a saw tooth pattern is employed, for CC experimental R-curve is used.

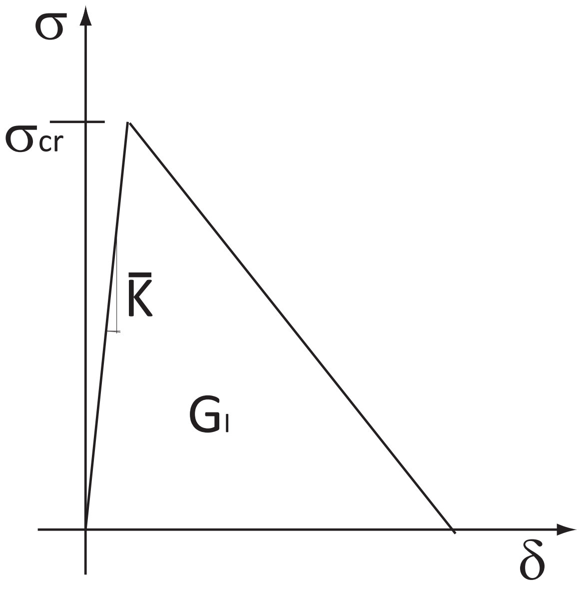

Figure 6.8: Traction separation law used for simulation showing critical strength σ_{cr}, mode I toughness G_I and initial stiffness $\bar{K}$

interface between the two arms of the DCB which is the intended crack path. The critical traction corresponding to the mean G_{Icr} was found in each case by matching the simulation's first crack initiation point with the experimental crack initiation point. This resulted in, for GC $\sigma_{Ic} = 13MPa$ and for CC $\sigma_{Ic} = 47MPa$.

6.3.1 DCB Numerical Simulation - Constant G_{Ic}

As mentioned earlier, the first approach to analyze the variations seen in the experimental G_{Ic} was to use a fixed value of critical strain energy release rate along the crack path figure 6.7. The upper bound, mean and lower bound of the experimental G_{Ic} was used. Figure 6.9 (a)&(b) show the numerical simulation results for GC and CC specimens, respectively. Simulations of both material systems showed similar behavior. When the minimum experimental G_{Ic} value is used for simulation, the crack initiation point is captured reasonably well, however, the post initiation curve is severely under-predicted. If the mean experimental G_{Ic} value is used, the results show a higher load for crack-initiation and the response follows the minimum load line in the propagation phase. In the case of the maximum experimental G_{Ic} value, the results over predict both the crack-initiation point and the propagation phase. For the GC simulation, the use of fixed G_{Ic} is not able to predict the *non-smooth* crack growth as seen in experiments. In the case of CC laminates, the simulation is not able to replicate the increase in load with crack progression. It is clear that the general assumption of a fixed critical strain energy release rate cannot capture the increase in load during crack propagation, and while this can be addressed by appealing to R-curve response, the question of *non-smooth* crack growth still begs to be resolved. Even though non-smooth crack growth has been observed here and also reported by others in the literature, a satisfactory model that can replicate non-smooth crack growth histories is presently unavailable.

6.3.2 DCB Numerical Simulation - Variable G_{Ic}

Here we demonstrate that oscillatory G_{Ic} values along the intended crack path are necessary to capture non-smooth crack growth using a DCZM modeling approach. Simulations were conducted by varying the G_{Ic} value along the length of the intended crack path according to the values obtained from the experiment. For simulation of GC laminates, a saw-tooth function was used for the G_{Ic} distribution over every $5mm$, with an amplitude of $0.73N.mm^{-1}$, and a baseline value of $1.47N.mm^{-1}$, as shown in figure 6.7. In case of CC laminates, the experimental R curve (fig 6.7) was used to vary the critical energy release rate along the crack path. Figure 6.10 (a)&(b) shows the simulation results for GC and CC laminates, respectively. By varying the G_{Ic} values, both crack initiation and propagation are matched well. What is not clear is whether such an approach, when used to *predict* the fracture response of another structure made of the same material system, can replicate the experimental findings. Furthermore, the usefulness of the classical strain energy release rate as a suitable metric to drive cracks, at least for the two material systems studied here, is now

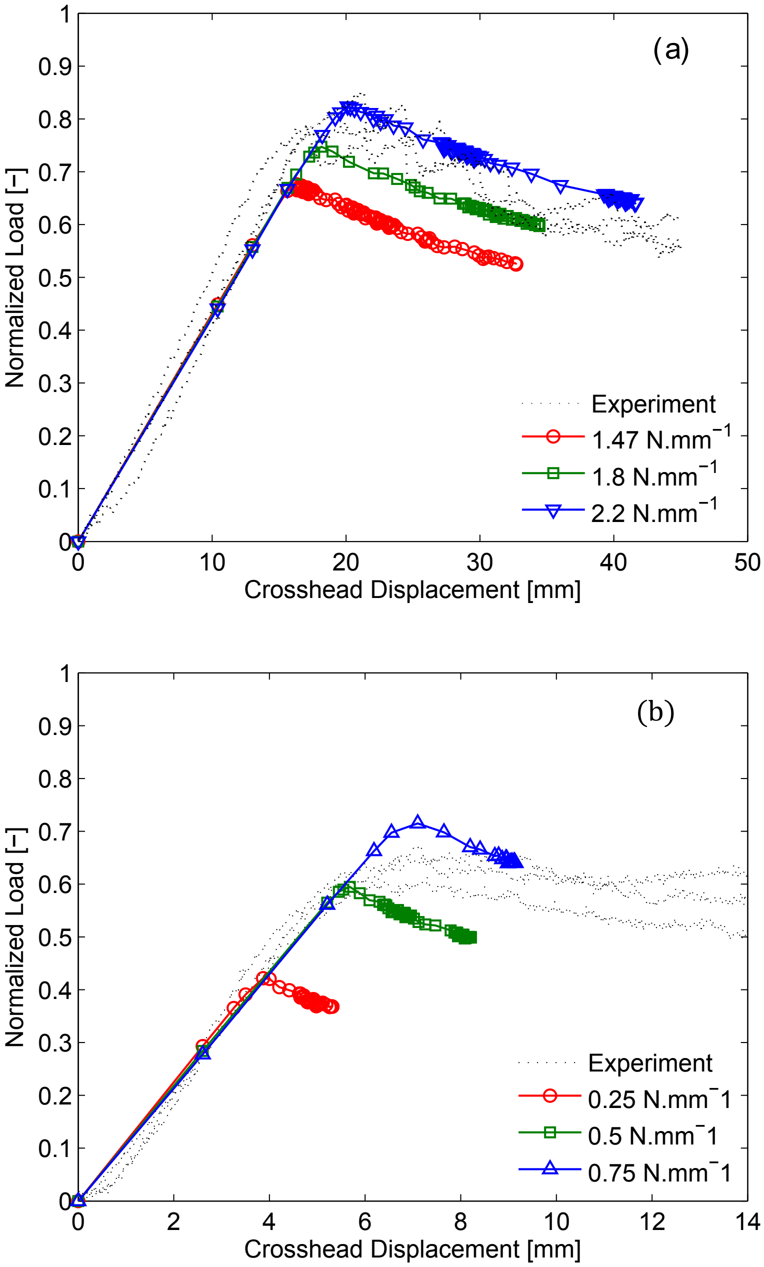

Figure 6.9: Comparison of simulation (solid lines) with experimet (dash lines) using DCZM with fixed G_{Ic} value. (a) GC simulation with min,max and mean G_{Ic} value from experiment. (b) CC simulation with min, max and mean G_{Ic} value from experiment.

brought into question.

6.3.3 DCZM Simulations: Summary & discussion

From the simulation results presented, it can be inferred that the notion of a critical strain energy release rate (constant value) may not exist for a given material system even when the loading rates are quasi-static. The classical assumption that the critical strain energy release rate is a constant value is not true for the material systems studied here. More troubling is the case corresponding to *non-smooth* crack growth. These issues show that ”critical” parameters obtained from coupon level tests (following as closely as possible the suggested ASTM Standard) may not be reliable for failure prediction in other structures. Many authors who were faced with similar issues have attributed discrepancies between experiment and analysis, to rate dependence of G_{Ic} [59, 68]. It is possible that rate dependence of G_{Ic} can explain the overall fracture response in the case of *smooth crack growth*. Non-smooth crack growth, spanning a large range of loading rates, including those that have been hitherto specified as ”quasi-static”, as stated in the ASTM Standard D5528, cannot be explained by appealing to rate dependence of G_{Ic}.

6.4 Revisiting classical fracture theory

From the experimental and numerical analysis presented, it is evident that the critical strain energy release rate approach might be sufficient to predict the onset of fracture but it is not sufficient for predicting the subsequent growth of a crack because G_{Ic} is not constant in all cases studied here. Furthermore, a model that can capture both, smooth and non-smooth crack growth, is required to distinguish between the variety of responses that have been observed in the results presented here and elsewhere, in the literature.

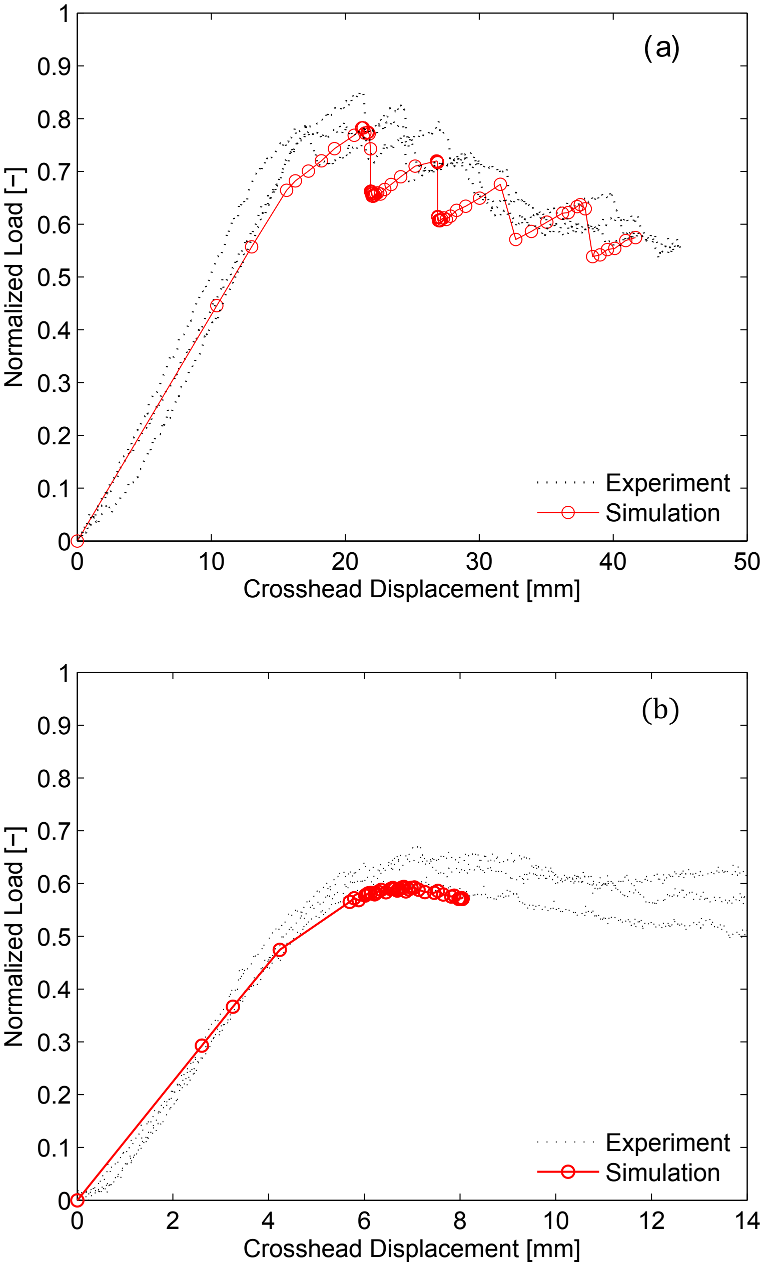

Figure 6.10: Comparison of simulation (solid lines) with experimet (dash lines) using DCZM with variable G_{Ic} value. (a) GC simulation with oscillatory variation in G_{Ic}. (b) CC simulation with varying G_{Ic} same as R curve from experimental data.

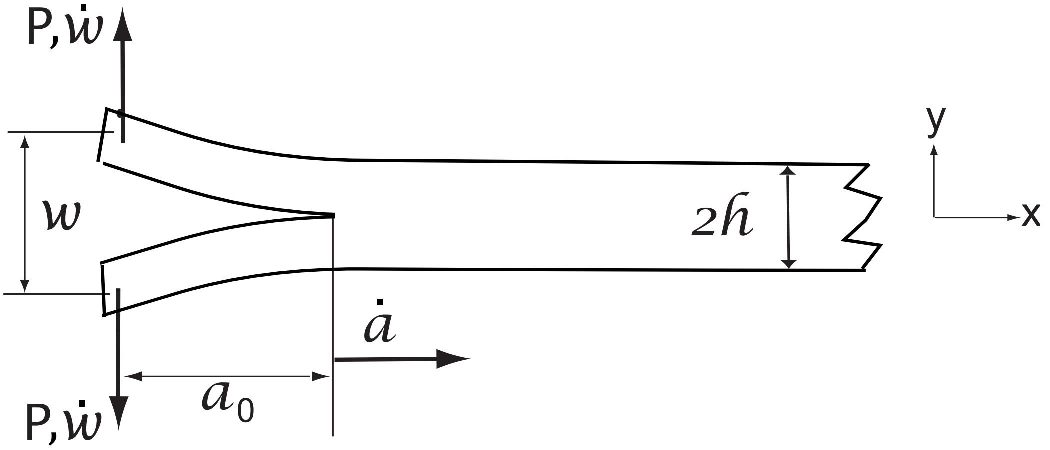

Figure 6.11: Coupon geometry for analytical model

6.4.1 DCB energy release rate

Consider a DCB of thickness $2h$, with a starter crack of length a_o at the center line and subjected to displacement control loading at the ends as shown in figure(6.11). The elastic energy of the system, based on simple beam theory, can be written as:

$$U = \frac{1}{2}Pw = \frac{3EIw^2}{4a^3} \tag{6.4}$$

Differentiating (6.4) with respect to time

$$\frac{dU}{dt} = \frac{3}{4}EI(\frac{2w\dot{w}}{a^3} - \frac{3w^2\dot{a}}{a^4}) \tag{6.5}$$

Now, by definition, the strain energy release rate , $G_I = -\frac{1}{b}\frac{dU}{da}$, hence, (6.5) can be rearranged and written as,

$$G_I = -\frac{1}{b}\frac{dU}{da} = \frac{1}{b}[(\frac{9w^2EI}{4a^4}) - (\frac{3EIw}{2a^3}\frac{\dot{w}}{\dot{a}})] = \hat{G}_I - \breve{G}_I(\dot{w}, \dot{a}) \tag{6.6}$$

A similar analysis, using higher order (including shear deformation of the DCB arms) beam theory leads to somewhat different expressions, however, here we wish to use Euler-Bernoulli beam theory to illustrate the main points of this work. The above equation shows that the energy release rate is dependent on both crack velocity and loading rate.For quasi-static loading, it is assumed that $\breve{G}_I(\dot{w}, \dot{a}) \to 0$ because, either for fixed grip conditions or for dead loading, the crack is assumed to advance in infinitesimal steps, with each step leading to an adjacent state of *equilibrium.* The crack propagation history is thus assumed to be a series of equilibrium configurations where Griffith's theory [44], is assumed valid . However, it is important to note that Griffith's theory is only valid for a crack initiating from an equilibrium position. Once the crack has initiated and starts to grow, the system is no longer in equilibrium. In fact, crack advancement is due to a lack of *equilibrium.* Hence, during propagation, the application of Griffith's theory is an assumption; when this assumption is relaxed, $\breve{G}_I(\dot{w}, \dot{a})$ must be taken into account in calculations. Note that these arguments remain unchanged also for cracks that propagate at large velocities. In those instances, dissipation due to kinetic energy must also be accounted for.

Let us look at the different scenarios that emerge from (6.6), for a displacement controlled loading test ($\dot{w} = const$). Figure 6.12 refers to each scenario explained below,

1. If the crack velocity is significantly larger than the loading rate ie; $\dot{w} << \dot{a}$, then $\frac{\dot{w}}{\dot{a}} \to 0$ and $G_I = \hat{G}_I$.

2. If the crack velocity is significantly smaller than the loading rate ie; $\dot{w} >> \dot{a}$, the second term can no longer be ignored and the overall energy release rate will be lowered.

3. If the crack velocity is of the same order as the loading rate ie; $\frac{\dot{w}}{\dot{a}} = const$, then the energy release rate will be lower than in case (1),ie; $G_I = \hat{G}_I - \breve{G}_I(\dot{w}, \dot{a})$.

4. If $\dot{w} > \dot{a}$ but is of the same order of magnitude and $\dot{a}$ is increasing with time, then the energy release rate starts at a lower value and increases at the same rate as that of the crack velocity.

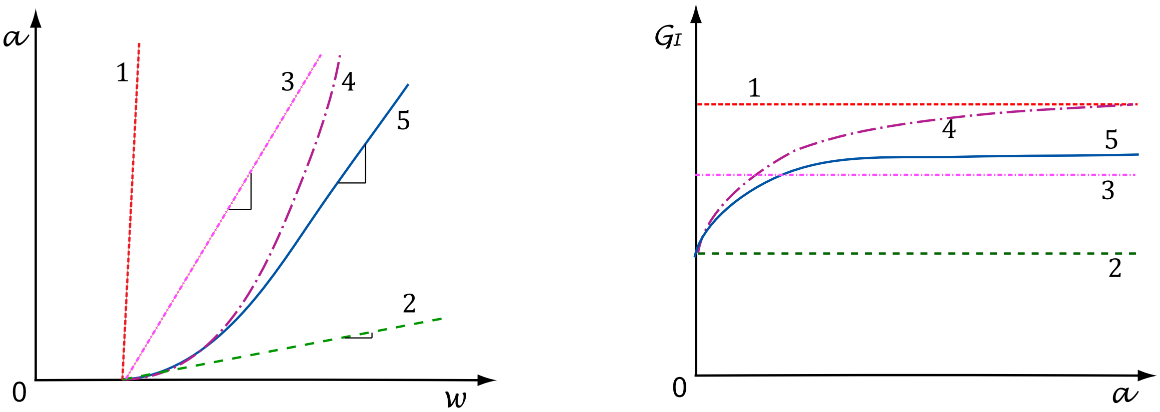

Figure 6.12: Different scenarios that emerge from (6.6).Slope of each curve on the left hand side graph shows the variation of $\dot{w}/\dot{a}$. Graph on right shows the R-curve obtained corresponding to the crack propagation scenarios shown on the left.

5. If $\dot{w} > \dot{a}$ but is of the same order of magnitude and $\dot{a}$ increases to reach an asymptotic value, then the energy release rate will also increase and reach an asymptote.

From the various scenarios given above, the first refers to the case when the rate of work done by the external load is negligible compared to the rate of change of elastic strain energy due to crack growth, which is the case in unstable crack growth. Case (4) provides the situation that corresponds to the results seen in the experimental R-curve of CC, where an asymptotic value is not reached. Case(5) corresponds to the case where the classical description of an R-curve is observed (with smooth crack growth), where G_I is seen to increase and reach an asymptote.

6.4.2 Fracture theory: Summary & discussion

Equation (6.6) not only shows that G_I is dependent on loading rate and crack velocity but also provides the phenomenological reasoning behind the existence of an R-curve behavior seen in Mode-I DCB tests. The dependence on crack velocity is shown to be inherent even at loading rates which are considered to be quasi-static. The traditional characterization of loading rate as being quasi-static or dynamic, based solely on the nature of crack growth (stable or unstable and driven by inertial effects) is not sufficient. Instead, the rate of loading with respect to crack velocity should be used as a discriminator even in cases that have hitherto been characterized as quasi-static.

6.5 Alternative hypothesis and a novel approach to fracture analysis

Griffith's [44] original motivation to formulate the problem of determining the maximum load required to advance an existing crack in a solid, stemmed from an inability to use an available local solution to the stress field [51], around an elliptical cutout in a planar body of infinite extent, due to it's singular nature. This led to a formulation that invoked a macroscopic energy balance, with the result being a criterion for crack growth *initiation*. Noting the development related to the DCB in the previous section, we now pose four basic questions that one faces in a combined continuum mechanics/fracture analysis:

(a) When (in terms of external loads) will an existing crack start to grow ?

(b) How much will the growing crack propagate by ?

(c) Which direction will the crack propagate ?

(d) Is the crack growth stable, in the sense of continued growth or arrest ?

Since, we are examining a symmetrical DCB specimen in this study, for which crack propagation is along the mid-plane, we will examine answers to questions (a), (b) and (d) posed above.

6.5.1 Crack initiation criteria

Fracture is a process involving separation and severing of atomic bonds. The rate of fracture is proportional to the number of bond ruptures per unit time. Thus, atomistically informed calculations (for instance, those that consider interactions among atoms at atomistic length scales) are necessary to properly capture precise physical processes that take place at such length scales. An approach to connect the two scales (atomistic and continuum) is to apply the concept of an equivalent continuum (EC) [112, 92] . The equivalence between the continuum and the discrete atomic level, in a dynamically deforming particle system, includes conservation of internal, external and inertial work. This equivalence can be provided by introducing the concept of a virial stress, which, for atomic systems is a tensor quantity that measures the time rate of change of momentum for spatial regions. For the discussion in this paper, we assume that there exist a critical internal stress beyond which the atomic separation is large enough to break the attractive bond. Furthermore, we assume that this internal stress is proportional to the continuum based notion of Irwin's stress intensity factor [52]. This gives us the first hypothesis, that we introduce;

Hypothesis 1 : Crack initiation takes place when the internal stress at the crack tip σ_t *reaches or exceeds a critical value* σ_{cr}*. Alternatively, the crack initiates when the internal strain at the crack tip,* ϵ_t *reaches a critical value,* ϵ_{cr}*. The two criteria are related through an appropriate constitutive relation of the solid*

Parallels can be drawn to yield criteria used in plasticity (Von Mises or Tresca) or Irwin's stress intensity factors (critical $K_{I/II/III}$) in LEFM [106]. For simplicity and ease of analysis we assume the system to be linear elastic and energy loss in the system is only due to crack growth. For the condition of irreversibility to be satisfied, crack healing is not allowed.

Since the proposed hypothesis requires a measure of internal stress at the crack tip which can be obtained using atomistic or molecular dynamic simulations, and is beyond the scope of this study, we employ a more workable form of hypothesis 1, where we assume that there is a linear relationship between the internal atomistically informed stress at the crack tip and the stress state around the crack tip at a finite distance away, thereby allowing the use of Irwin's stress intensity factor as an equivalent measure of stress state around the crack tip.

We now cast a necessary condition for crack initiation:

$$da \begin{cases} = 0 \quad \forall \quad \sigma_t < \sigma_{cr} \approx K_t < K_{cr} \\ \\ > 0 \quad \forall \quad \sigma_t \geq \sigma_{cr} \approx K_t \geq K_{cr} \end{cases} \tag{6.7}$$

6.5.2 Crack progression criterion

Many researchers have developed crack-velocity formulations especially when pertaining to dynamic fracture studies. Since crack growth releases stored energy, stress waves are emitted that transmit this energy as kinetic energy. These waves influence the further motion of the crack within the body. Hellan [48] provides a relation for particle velocities in a body based on stress waves in a 1D and 2D setting. Taking the simplest case of 1D, the particle velocity due to stress wave loading is given by,

$$\dot{u} = \mp \frac{C_0}{E} \sigma \tag{6.8}$$

where, C_0 is a material constant and E is the elastic modulus. Hellan [48] also provides the relation between crack velocity and particle velocity given in (6.9). From hypothesis 1, we may assume the stress corresponding to crack formation as the critical stress σ_{cr}:

$$\dot{u} = -\frac{\dot{a}}{E}\sigma = -\frac{\dot{a}}{E}\sigma_{cr} \tag{6.9}$$

Combining the two equations we get a relation for crack velocity in terms of the ratio of instantaneous stress at the crack tip, and the critical fracture stress at the crack tip. Since crack propagation cannot be reversed, the negative sign is removed. The resulting equation forms the second hypothesis:

Hypothesis 2 : Crack progresses with a velocity proportional to the ratio of instantaneous crack tip stress to the critical crack tip stress.

$$\dot{a} = C_0(\frac{\sigma_t}{\sigma_{cr}})^n \approx C_0(\frac{K_t}{K_{cr}})^n \tag{6.10}$$

This equation is similar to an empirical power law relationship given by Evans [36] for slow crack growth in brittle materials. According to Evans, it is found that the velocity of the crack V, is proportional to the stress intensity factor, raised to some power, n, i.e. K^n. This equation is also similar to the dislocation velocity relation proposed by Stein & Low [91], and, Gilman & Johnston [49], where dislocation velocity, $V_d = (\frac{\tau}{D})^m$, where, τ is the applied resolved shear stress, and D and m are material constants. Using activation energy theory, as shown in [56] and as discussed in [13], it is theoretically more sound to express the crack velocity with a hyperbolic sine (*sinh*) dependence instead of a power-law relationship. However, the power-law form is favored for reducing test data and extending the analysis to treat fatigue crack growth.

We can see from (6.10) that the material constant C_0 should have units of velocity. Hence, there exists a characteristic crack velocity for a given material configuration around the crack tip. This implies that when the stress at the crack tip just reaches the critical stress value, ie; $\sigma_t/\sigma_{cr} = 1$, the crack will progress with a velocity C_0. A similar conclusion is also provided by Kotousov [55].

Combining the two hypothesis (eqn 6.7&6.10) we get the necessary condition for continued crack growth,

$$\dot{a} = \begin{cases} 0 & \forall \quad \sigma_n < \sigma_{cr} \approx K_t < K_{cr} \\ \\ C_0(\frac{\sigma_t}{\sigma_{cr}})^n \approx C_0(\frac{K_t}{K_{cr}})^n & \forall \quad \sigma_t \geq \sigma_{cr} \approx K_t \geq K_{cr} \end{cases} \tag{6.11}$$

6.5.3 Rate equation of energy

From the previous section, we observe that the crack velocity is an important factor in strain energy release rate calculations. A more general explanation of smooth and non-smooth crack growth can be made if we examine the rate form of the energy balance equation. Consider, the DCB described in figure (6.11). The total potential energy (Π) in the system, prior to crack initiation due to a load F, can be written as:

$$\Pi = -W_{ext} + U = -Pw + \frac{1}{2}Pw = -\frac{1}{2}Pw = -\frac{3EIw^2}{4a_o^3} \tag{6.12}$$

where, U is the elastic strain energy in the body, W_{ext} is work done by external load. Now, if the body develops a crack, the energy released can be attributed to dissipation associated with the crack formation. We can re-write the equation for potential energy of the system by deducting the energy dissipated W_{dis} to create additional area attributed to the crack, as;

$$\Pi = -W_{ext} + U - W_{dis} = -(\frac{3EIw^2}{4a^3}) - 2\gamma\ b\ da \tag{6.13}$$

where, γ is the fracture energy[1] per unit area. Griffith [44], using the notion of surface energy, stated that the above equation is only valid for a system where fracture has occurred. Also, according to the theory of minimum potential energy, during the fracture process, the system will reduce its potential energy by crack growth. However, there is a subtle but key observations that needs to be made. Griffith [44] stated that the total reduction in potential energy due to fracture is equal to the increase in strain energy less the increase in surface energy. The point to note here is that the increase in strain energy has two components. First the increase in strain energy due to a change in system stiffness and second, the increase in energy due to continued loading of the system. Let us look at the rate form of (6.13). Differentiating both sides with respect to time

---

[1] Fracture energy is more general in that in includes all mechanisms of dissipation associated with the creation of a crack, whereas Griffith's surface energy accounts only that portion associated with the creation of free surfaces

$$\dot{\Pi} = -\dot{W}_{ext} + \dot{U} - \dot{W}_{dis} = -(\frac{3EIw}{2a^3}\ \dot{w}) + (\frac{9EIw^2}{4a^4}\dot{a}) - (2\gamma\ b\ \dot{a}) \tag{6.14}$$

The first term on the right hand side is the strain energy stored due to continued loading and is dependent on the loading rate. The second term corresponds to the strain energy stored due to change in stiffness which is dependent on instantaneous crack velocity. The third term accounts for energy dissipation due to creation of fracture surfaces, which is also a function of instantaneous crack velocity. From the above equation three scenarios emerge :

1. if $-(\frac{3EIw}{2a^3}\ \dot{w}) + (\frac{9EIw^2}{4a^4}\dot{a}) < (2\gamma\ b\ \dot{a})$

   This scenario reflects the condition where instantaneous dissipative work is larger than the cumulative energy due to external load and strain energy stored. The overall potential energy in the body will decrease, which will reflect as a drop in the force displacement plot. Indicated as curve section I in figure 6.13.

2. if $-(\frac{3EIw}{2a^3}\ \dot{w}) + (\frac{9EIw^2}{4a^4}\dot{a}) = (2\gamma\ b\ \dot{a})$

   Here, the instantaneous dissipated energy equalizes the sum of energies due to external load and strain energy stored causing the overall potential energy in the body to remain constant, which will reflect as a horizontal line in the force displacement plot. Indicated as curve section II in figure 6.13.

3. if $-(\frac{3EIw}{2a^3}\ \dot{w}) + (\frac{9EIw^2}{4a^4}\dot{a}) > (2\gamma\ b\ \dot{a})$

   In this scenario, the instantaneous dissipated energy is smaller than the sum of energies due to external load and strain energy stored. Thus, the overall potential energy in the body will increase, which will reflect as a increase in the force displacement plot. Indicated as curve section III in figure 6.13.

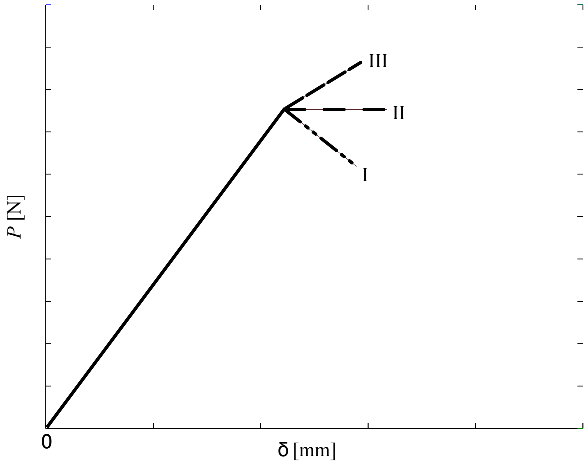

Figure 6.13: Energy change scenario based on (6.14)

Now, the continued growth of the crack in time can be visualized as a sequence of these scenarios in an order decided by the crack velocity. By combining the two hypothesis and the rate equation, (6.14), we get the discrete form of instantaneous potential energy.

$$\dot{\Pi} = \begin{cases} -(\frac{3EIw}{2a^3}\ \dot{w}) & \forall \quad \dot{a} = 0 \quad \forall \quad \sigma_t < \sigma_{cr} \approx K_t < K_{cr} \\ \\ -(\frac{3EIw}{2a^3}\ \dot{w}) + (\frac{9EIw^2}{4a^4}\dot{a}) - (2\gamma\ b\ \dot{a}) & \forall \quad \dot{a} > 0 \quad \forall \quad \sigma_t \geq \sigma_{cr} \approx K_t \geq K_{cr} \end{cases} \tag{6.15}$$

6.5.4 Crack stability & crack arrest

From the above equation it is evident that non-smooth crack growth is afforded by the first scenario with very high instantaneous dissipated energy. For a given increment in time, if the stress at the crack tip equals or exceeds the critical value, then based on the instantaneous crack velocity one of the above three scenarios will occur. If in the next time increment, the stress condition (hypothesis 1) is still met, then again one of the three scenarios will be met. However, if the condition is not met, then the crack will arrest and the system will follow Hooke's law.

6.5.5 Algorithm for Computing Crack Growth

To summarize the two sections above, it is seen that the crack will only initiate when the stress at the crack tip (σ_t) reaches a critical value (σ_{cr}), as given in 6.7. After attaining the critical stress, the increment in crack growth is determined by the resistance provided by the material to crack growth, which is in turn determined by the crack propagation velocity due to the stresses at the crack tip (6.10). We can now develop a general algorithm for fracture analysis of the DCB as shown in the flow chart in figure 6.14. From this flowchart, we see that there is no energy calculation required to determine crack initiation and crack progression. Since the algorithm uses incremental time steps (N) to calculate both the change in loading and the increment of crack growth, a sample DCB geometry was used to check for convergence and is shown in figure 6.15.

6.6 Implementation

6.6.1 DCB Formulation

Consider the case of the DCB (figure 6.11) with dimensions symmetrical about the neutral axis, which is also the fracture path. The relation between force and displacement is given by:

$$F = 3wEI/2a^3 \tag{6.16}$$

The stress intensity at the crack tip is given by

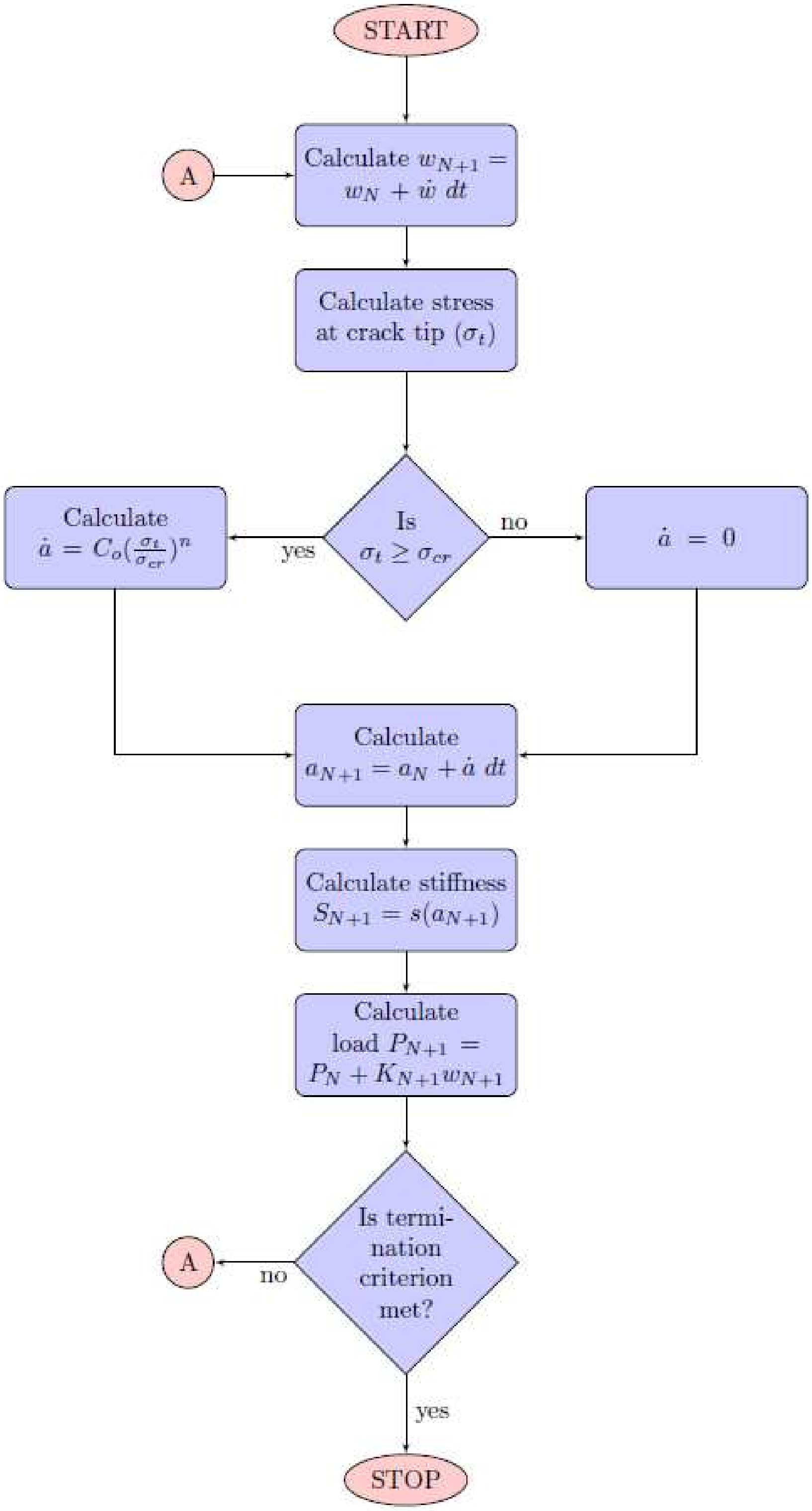

Figure 6.14: General algorithm for crack initiation and progression based on crack tip over-stress and crack velocity as per equation 6.10

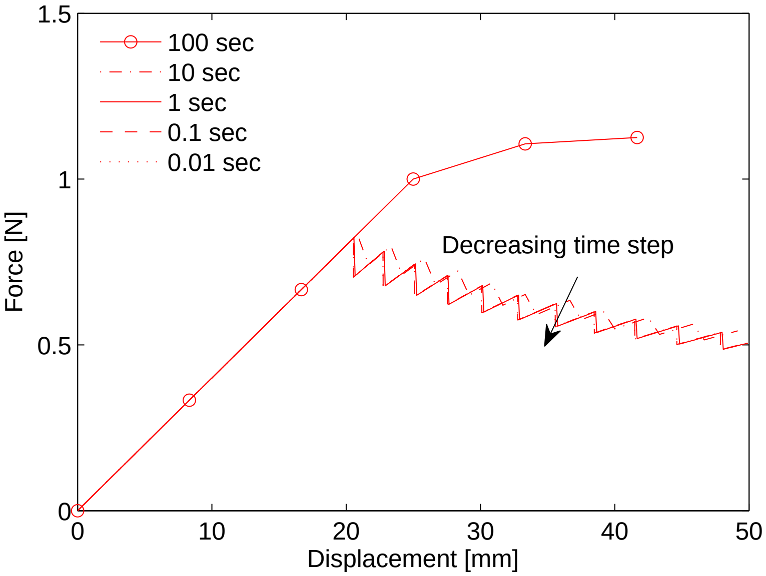

Figure 6.15: Computed load-displacement curve at varying time step sizes demonstrating convergence

$$K_t = \frac{F\ a}{\sqrt{b\ I}} \tag{6.17}$$

where, b=width of specimen and I=moment of inertia of arms. The critical value of the stress intensity (K_{cr}) can be calculated from the average critical strain energy release rate, at initiation, obtained from the experiment.

$$K_{cr} = \sqrt{G^i_{Ic}\ E} \tag{6.18}$$

Therefore, for implementation of the algorithm, the crack initiation criterion will now be $K_t \geq K_{cr}$. The second parameter, the characteristic velocity C_0, was found by trial and error by matching the load-displacement curves of the experiment corresponding to each material system.

Table 6.2: Parameters used in analysis

Type	K_{cr} $(MPa\sqrt{mm})$	$C_0(mm.s^-1)$
GC	152.56	3.88
CC	178.28	0.0286

6.6.2 DCB Analysis

Figure 6.16 shows the analysis results for the two laminates, when computed using the algorithm specified in the prior section. Table 6.2 gives the parameters used for the analytical model.

In the case of the GC laminates, non-smooth crack growth behavior is captured quite well. As the crack velocity is high in GC, there is a rapid loss of energy from the system after initiation. The sudden release of energy also relaxes the system (reduction in stiffness) and the stress at the crack tip reduces below the critical threshold, causing the crack to arrest (figure 6.17-a). Since, the body is under constant displacement loading and the crack has been arrested, the energy of the system will increase, thereby gradually increasing the stress at the crack tip. This cycle repeats to provide the non-smooth crack growth that is observed in the GC laminate.

In the CC laminate, the phenomenon is quite unique. After the crack initiates, the system does not have a net loss of energy. This is because the rate of energy input to the system due to loading is more than the rate of energy loss from the system due to crack propagation, thus giving a smooth crack growth (figure 6.17-b). Since, the stiffness of the system is also reducing with crack propagation, there is a point after which the input to the system due to loading drops below that lost due to crack propagation.

Since the new crack growth algorithm provides the load-deflection relation as an output, it is a simple task to *calculate* G_I as the crack progresses. Figure 6.18 shows the calculated G_I values for GC and CC laminates using the present analytical formulation. We now see that the release of strain energy is a *consequence* of crack growth and not the *cause* of crack growth. Thus, it's use as a critical parameter to advance cracks is brought into question.

6.7 Discussion

In the cohesive zone modeling framework, implemented using the finite element method, two parameters are needed, the cohesive strength and the energy release rate. It has been shown that the energy release rate may not be a constant value during crack propagation, hence, an R-curve is also required. Using the stress intensity factor alone, only crack initiation can be predicted. The new approach proposed here, on the other hand, required only two material constants, the critical stress at the crack tip and the characteristic velocity.

As mentioned earlier, most of current theory, with the exception of molecular dynamics or atomistic simulations, uses a macro scale approach to fracture. Current macroscopic approaches use either energy based or strength based techniques, both of which are very accurate at predicting the onset of cracking (crack initiation). This is because the continuum continuity definition holds until the final equilibrium point (crack initiation) is reached, hence, the energies are quantifiable and easily calculated. However, these techniques fail to provide accurate predictions for crack progression in general. The reasons stems from the fact that during crack propagation the system is not in equilibrium. By assuming a constant strain energy release rate or stress intensity factor during crack propagation, equilibrium is enforced, which is only possible if every crack in every material propagates from one equilibrium point to another in negligible time, ie; at extremely high crack velocities, which is not the case in actual materials.

The theory proposed in this paper overcomes this apparent disconnect by acknowledging that the process of crack growth is not an equilibrium process and introduces the crack velocity as an internal variable in the calculation of crack growth. The valid-

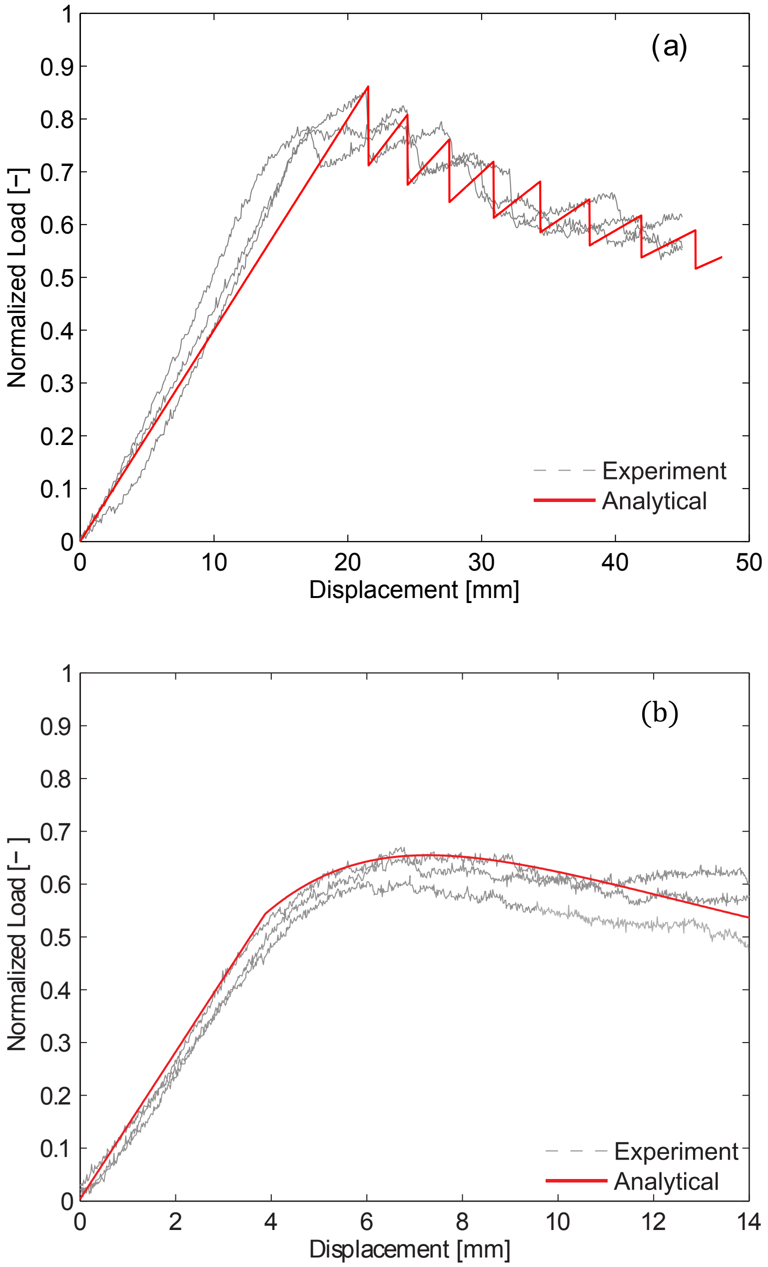

Figure 6.16: Comparison of analytical (solid line) and experimental (dotted line) force displacement data (a) GC, (b) CC.

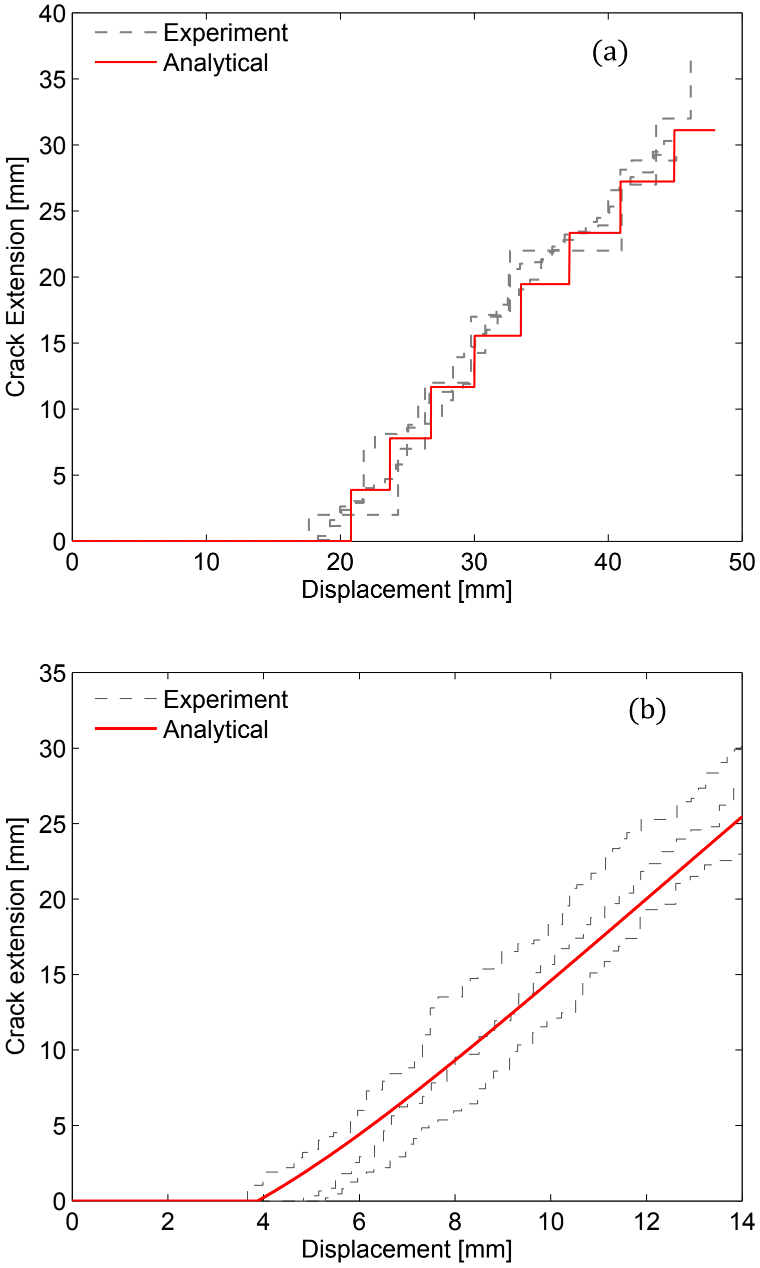

Figure 6.17: Comparison of analytical (solid line) and experimental (dotted line) crack extension v/s crosshead displacement, (a) GC, (b) CC.

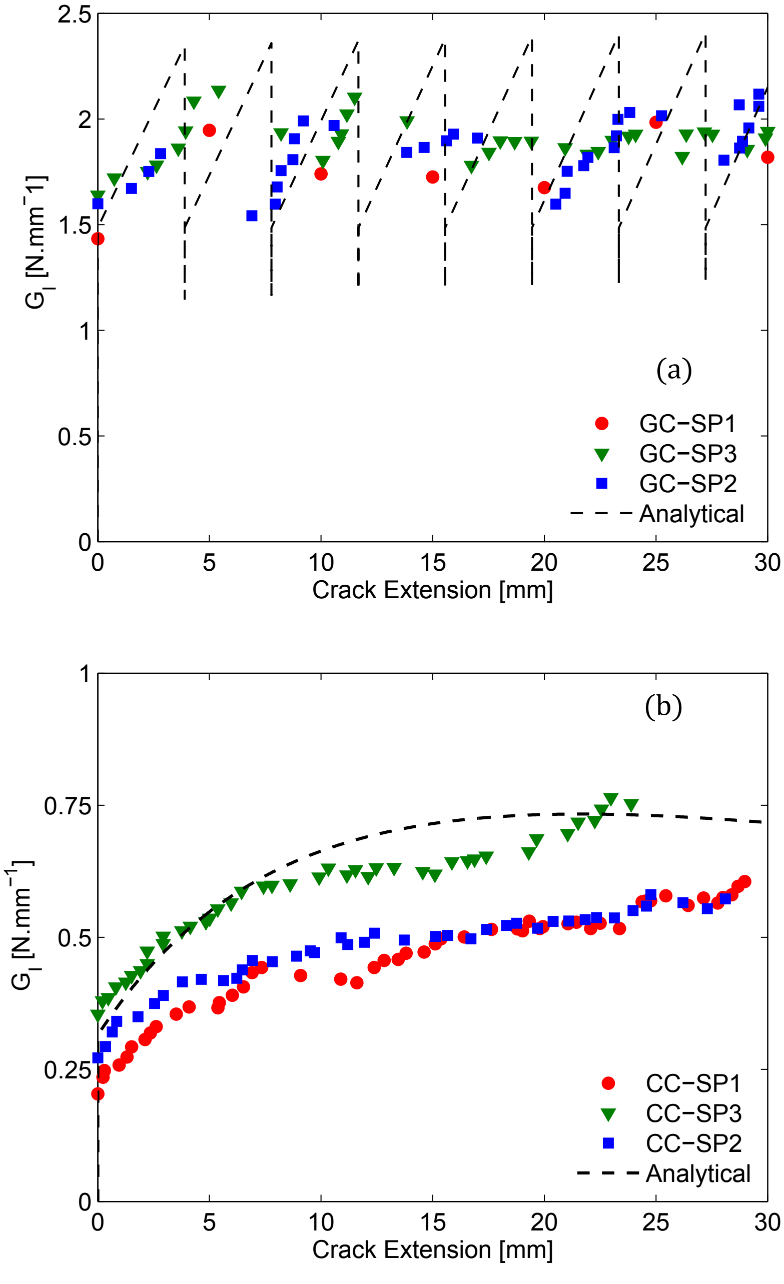

Figure 6.18: Comparison of analytical (dotted line) and experimental (points) strain energy release rate (a) GC, (b) CC.

ity of the crack velocity as an internal variable is shown to be sound in the analytical solutions, however, the question of existence of a unique characteristic velocity C_o can be argued. The characteristic crack velocity term, C_0, is in essence a parameter that captures the effects of the process zone (dislocations, plasticity, micro-damage due to micro-cracking etc) and its ability to dissipate energy, which is specific to a given material system. Phenomenologically, one can argue that C_o should be a fraction of the Rayleigh wave speed and hence be a constant for a given material system, but a rigorous way to establish this, for example, using atomistic or micro-mechanical simulations is needed.

6.8 Conclusions

We have introduced a novel approach to predict non-smooth crack growth observed in mode I fracture of a composite material DCB specimen. By postulating the existence of a critical fracture internal stress or strain, and a critical crack velocity, non-smooth crack growth (and smooth crack growth, as a special case) observed in DCB experiments was predicted. The method is able to predict, both, smooth and non-smooth crack growth. Using the critical fracture internal stress or strain, and a critical, material specific crack velocity, a simple algorithm was formulated to explain and replicate the experimental results well. In our approach, the strain energy released is an *outcome* of the crack growth process instead of a value that is postulated to drive and control crack advancement. Numerical simulation results, using cohesive zone models that use constant G_{Ic} values, were not able to capture the non-smooth crack growth seen in GC laminates nor was it able to capture the steady increase in load *after* crack initiation, observed in CC laminates. By including the rate terms in the G_I formulation it was shown that strain energy release rate is a function of both loading rate and crack velocity. This formulation explains the reason attributed to R-curve behaviour and the linear decrease in G_{Ic} with increasing loading rate. Both phenomena are explained by the use of the crack velocity as a parameter in the energy calculation.

CHAPTER VII

Instability in dynamic brittle fracture

7.1 Introduction

Fracture in brittle polymers is complex owing to its catastrophic nature and is compounded by the difficulty in observing fast moving cracks experimentally. Over the past three decades experiments conducted by several groups [77, 37, 54, 29] have led to a better understanding of the dynamics of fracture processes in brittle solids. The experimental results have shown that the process of fracture tends to follow a specific pattern. Unstable crack growth is found to occur in progressive stages, identified using the characteristic roughness of the fracture surface. Crack surfaces near the initial crack tip tend to have a smooth surface finish which is followed by increasing roughness [80, 17] or patterned ramified surfaces [38]. At higher crack velocities, the main crack is seen to micro-branch into multiple cracks. Detailed section analysis of the fracture specimens [29, 80] show that these rough features are also seen below the crack surface in the form of micro-cracks. The cumulative effects of these secondary energy dissipation modes (micro-cracking or micro-damage) are noticed in the crack propagation velocity ($\dot{a}$) profile. Theoretically, in brittle materials, the crack velocity has a unique upper bound set by the critical Rayleigh wave speed (C_R). In mode I crack propagation experiments for monolithic brittle materials, it is found that $\dot{a}$ achieves a maximum value well below C_R. On the other

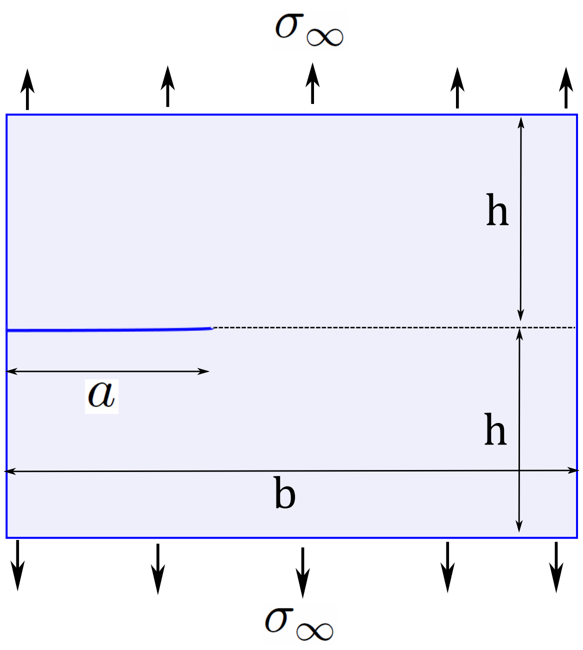

Figure 7.1: Single Edge Tension Plate (SETP) test coupon geometry

hand, Coker et al., [27], have demonstrated crack speeds close to C_R for mode I fracture in uni-directional composites. The ratio of observed peak velocity to critical Rayleigh wave speed is found to vary for each material, but for most monolithic brittle materials, micro-branching is observed at $\dot{a} \sim 0.4C_R$ [17]. The linear elastic fracture mechanics (LEFM) formulation for crack velocity [41] is found to provide quantitative agreement with experiments (glass and PMMA) for $\dot{a} \sim< 0.4C_R$ [85, 38]. The LEFM approach however, does not provide satisfactory results for $\dot{a} > 0.4C_R$, where, the crack tends to become unstable in the sense of developing micro-cracks & micro-branches along the crack path which cause rapid oscillations in crack velocity [17]. Multiple approaches haves been used to explain and predict the observed phenomenon of "mirror-mist-hackle-branch" failure, but with little success. Analytical models proposed by Yoffe [110] predict the start of instability at $73\%C_R$, whereas, models proposed by Freund [41] predict the stability velocity limit to be around $50\%C_R$. Two different analytical approaches were proposed by Gao, a wavy-crack model [42] and a crack tip hyper-elasticity [21] model. Recently, a time-delay non-linear crack tip zone

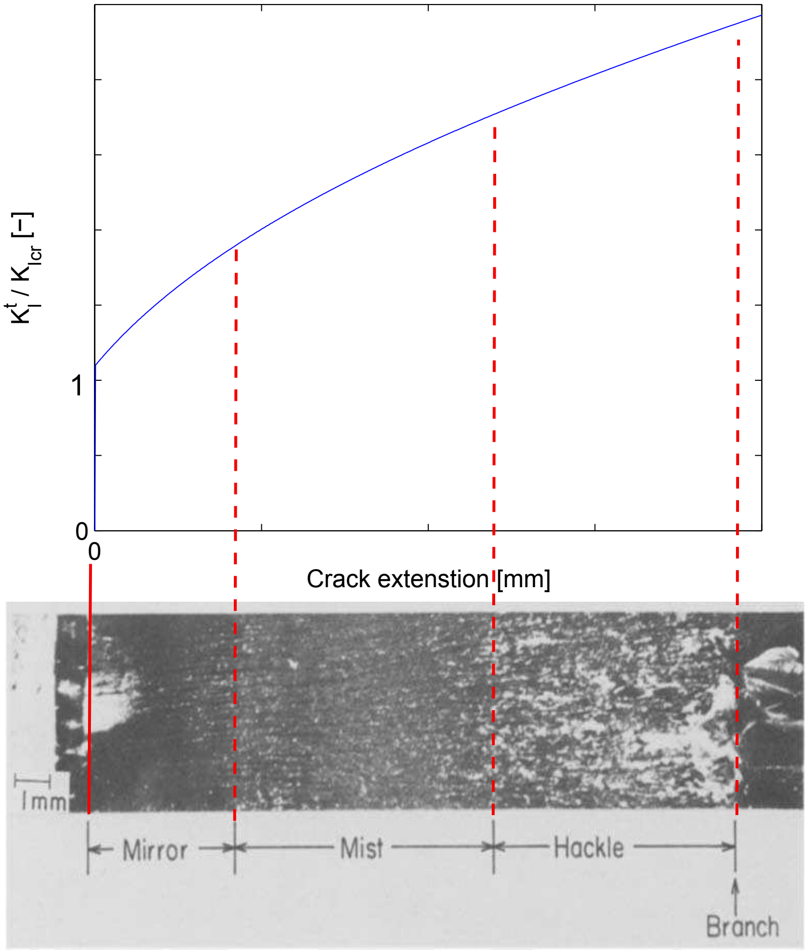

Figure 7.2: Over-stress at crack tip causing roughening of fracture surface. Image source: [79]

approach was proposed by Bouchbinder [16].

From a review of past experimental and theoretical studies, the following outstanding questions emerge; (a) What dictates crack growth velocity in rapid crack propagation in monolithic brittle materials ? (b) What is the cause of secondary modes of energy dissipation, and (c) Why do crack velocities tend to stabilize with increasing growth ? In this paper, we examine the physics of crack growth and arrest, based on crack tip over-stress, to address the above questions. We are able to calculate crack growth velocity, and in conjunction with a evolution parameter that accounts for micro-damage, are also able to predict the limiting crack speed. Our analytical predictions are found to be in agreement with measurements reported in the open literature.

7.2 Conditions for crack growth

In classical linear elastic fracture mechanics (LEFM), the external loading can be related to the crack tip stresses using Irwin's stress intensity factor. For the purposes of this paper, it is assumed that there exists a critical internal stress (virial stress [92] or Hardy's approximation [114]), σ_{cr} at the sub continuum scale, and a corresponding critical stress intensity factor [52], K_{cr} at the continuum scale, beyond which the atomic separation is large enough to break the attractive bond, causing new crack growth. Thus, we now formulate the first hypothesis of our analytical model;

Hypothesis 1 : Crack growth initiates from a pre-existing flaw or an initial crack when a measure of the internal stress at the crack tip σ_n reaches or exceeds a critical value σ_{cr}.

Parallels can be drawn with yield criteria in classical plasticity (such as the Von Mises or Tresca criteria). Here, it is assumed that the system (body and loading device) is linear elastic and it is further assumed that the energy loss (dissipation) in the system is only due to crack growth. For the condition of irreversibility to be satisfied, crack healing is not allowed. Hence, we propose a necessary condition for crack growth:

$$\dot{a} \quad \begin{cases} = 0 \quad \forall \quad \sigma_t < \sigma_{cr} \approx K^t < K_{cr} \\ > 0 \quad \forall \quad \sigma_t \geq \sigma_{cr} \approx K^t \geq K_{cr} \end{cases} \tag{7.1}$$

Many researchers have developed crack growth - velocity formulations, especially when pertaining to rapid crack growth events. The dissipation of energy due to crack growth leads to the emission of stress waves that influences the subsequent motion of the crack within the body. Hellan [48] has provided a relation for particle velocities in a fracturing body based on stress waves, in a 1-dimensional and 2-dimensional setting. Considering the 1-dimensional case, the particle velocity due to a stress wave caused by an applied stress σ is of the form

$$\dot{u} = \mp \frac{C_o}{E} \sigma \tag{7.2}$$

where, C_o is the speed of sound in the solid, and E is the elastic Young's modulus. Hellan [48] also provides another relation between crack velocity and particle velocity, as shown in eqn(7.3). Freund, [41], also provides a relation for crack velocity in terms of a bluntness parameter, the material specific Kostrov surface energy and the static critical stress intensity factor. From hypothesis 1 in the previous section, and assuming that the stress associated with crack formation is the critical stress σ_{cr}, it follows that,

$$\dot{u} = -\frac{\dot{a}}{E} \sigma = -\frac{\dot{a}}{E} \sigma_{cr} \tag{7.3}$$

These two equations suggest a relation for crack velocity in terms of the ratio of instantaneous stress to critical fracture stress at the crack tip. Since crack propagation cannot be reversed, the negative sign is removed. This forms the second hypothesis that is proposed:

Hypothesis 2 : The crack growth velocity is proportional to the ratio of instantaneous crack tip stress to critical crack tip stress.

$$\dot{a} = V_0 (\frac{\sigma_t}{\sigma_{cr}})^n \approx V_0 (\frac{K^t}{K_{cr}})^n \tag{7.4}$$

This relationship is similar to the empirical logarithmic relationship suggested by Evans [36] for slow crack growth in brittle materials. According to Evans, it is found that the velocity of the crack $\dot{a}$ is proportional to the stress intensity factor raised to some power, K^n. The proposed equation is also similar to the dislocation velocity relation proposed by Stein & Low, and Gilman & Johnston, as given in [49], where the dislocation velocity $v_d = (\frac{\tau}{D})^m$, where, τ is the applied resolved shear stress and D, m are material properties. We can see from eqn(7.4) that the material constant V_o should have units of velocity. This means that when the stress at the crack tip just reaches the critical stress value, ie; $\sigma_n/\sigma_{cr} = 1$, the crack will progress with a velocity V_o.

From these two hypotheses, crack growth is understood to be a sequential process with two requirements. First the body deforms under loading without crack growth initiation until the critical stress at the crack tip is reached. Second, at the point of initiation, the strain energy stored by the body will be released with a rate proportional to the characteristic crack velocity, given by V_o in eqn(7.4). Crack growth will continue until the stress at the crack tip falls below the critical threshold. However, the stress at the crack tip will continuously depend on the system stiffness, which in turn depends on the rate of crack growth.

Combining the two hypothesis (eqns 7.1&7.4) we get a necessary condition for crack growth.

$$\dot{a} = \begin{cases} 0 & \forall \ \ \sigma_n < \sigma_{cr} \approx K^t < K_{cr} \\ V_0(\frac{\sigma_t}{\sigma_{cr}})^n \approx V_0(\frac{K^t}{K_{cr}})^n & \forall \ \ \sigma_t \geq \sigma_{cr} \approx K^t \geq K_{cr} \end{cases} \tag{7.5}$$

7.3 Framework for rapid crack growth analysis

We look at the most common geometry used for studying Mode-I rapid fracture, the Single Edge Tension Plate (SETP) test as shown in figure 7.1. Considerable data on crack velocities (theoretical, experimental and computational), are available in the literature, [36, 37, 38, 85, 78, 79, 80, 81]. The data presented in these papers will be used to illustrate the proposed framework for rapid crack growth.

7.3.1 Definition of crack

With secondary energy dissipation modes, the definition of a crack becomes difficult, especially when crack branches or crack bifurcations are observed. Hence, it is important to define crack length, which for a symmetric SETP test is defined as the measure of crack extension from the initial crack along the center transverse plane. Therefore, crack extension due to micro-branching is not accounted for in the crack length calculations. This is reasonable, since we will be looking at glassy polymer single edge test plate (SETP) specimens which exhibit a central crack with smaller cracks branching out [38, 85].

7.3.2 Crack initiation and propagation

For ease of analysis eqn (7.5) can be written in terms of the stress intensity factor, since for mode I, $\sigma = K_I \frac{f(\theta)}{\sqrt{2\pi r}}$. Therefore, we get,

$$\dot{a} = \begin{cases} 0 & \forall \quad K_I^t < K_{Icr} \\ \\ C_o(\frac{K_I^t}{K_{Icr}})^n & \forall \quad K_I^t \geq K_{Icr} \end{cases} \tag{7.6}$$

The static stress intensity factor at the crack tip for a SETP with a crack of length, a and width of $2b$, loaded by a far-field stress of σ_∞, is given by the equation [5, 90]:

$$K_I^s = \sigma_\infty \sqrt{\pi a}(1.12 - 0.23\frac{a}{b} + 10.6(\frac{a}{b})^2 - 21.7(\frac{a}{b})^3 + O(\frac{a}{b})^4) \tag{7.7}$$

Now, following Freund's [41] formulation for dynamic stress intensity factor at the crack tip is given by;

$$K_I^t = k(\dot{a})K_I^s \tag{7.8}$$

where, $k(\dot{a}) \approx (1 - \dot{a}/C_R)/(\sqrt{1 - \dot{a}/C_d})$, C_R is the Rayleigh wave speed, C_d is the Dilitational wave speed. Therefore, according to hypothesis 1, the crack growth in the SETP will initiate when the stress intensity factor at the crack tip reaches or exceeds the critical stress intensity factor K_{Icr}, and from hypothesis 2, the crack will progress with an initial velocity of V_o. If the far field stress is kept constant after initiation, the crack growth criterion will always be met and the crack velocity will be dictated by the over-stress factor (K_I^t/K_{Icr}). Hence, the crack will propagate with a velocity proportional to the over-stress at the crack tip and the values will be dictated by the two material parameters V_o and n.

7.3.3 Secondary modes of energy dissipation

In a typical fracture event of monolithic brittle materials like PMMA, glass, and ceramics like Alumina, a characteristic fracture surface pattern is observed [39]. This phenomenon can be explained by the over-stress condition at the crack tip. Physically, the over-stress condition in front of the crack tip indicates that the main crack is not able to liberate energy fast enough for the system to reach an equilibrium state. When the stresses in front of the crack tip become unsustainable, secondary modes of energy dissipation become significant. Micro-cracking and micro-branching are the most common secondary energy dissipation modes and these have the effect of reducing the crack tip stress intensity, [79]. Since energy is dissipated away from the crack tip, the stress intensity at the crack tip will be lowered. This physical correction has to be included in the analytical frame work.

Experimental studies by Kuksenko et al [57, 58] and Zurkov et al [113] have shown an exponential relation between the rate of accumulation of micro-cracks $\dot{N}$ with respect to tensile stress in glassy polymers ie; $\dot{N} \propto exp(\alpha\sigma)$. They have also shown that submicroscopic crack-growth, in number as well as size, will increase with tensile stress, finally leading to coalescence, to form a larger crack. From the proposed relationship pertaining to over-stress, we see that an increase in over-stress will cause an increase in micro-crack accumulation, which in turn will lead to a reduction in stress at the crack tip. Therefore, a damage parameter (λ) can be defined, that displays an inverse relationship to the relative over-stress parameter at the crack tip.

$$\lambda = (exp(K_I^t/K_I^d))^{-1} \tag{7.9}$$

where, K_I^d is the stress intensity at which secondary modes of dissipation become significant. K_I^d is an indirect measure of the tensile stress at which submicroscopic cracks form in the specimen. The stress intensity at the crack tip due to damage $\hat{K}_I^t$ can be written as

$$\hat{K}_I^t = \beta \ K_I^d \ (1 - \lambda) \tag{7.10}$$

where, β is a constant of proportionality.

7.4 Comparison with experiments & discussion

7.4.1 Algorithm

From the equations in the above sections, we can now formulate a generic algorithm, shown through a flow-chart in figure(7.3), for computing crack growth trajectories and velocities in a monolithic brittle solid with constant loading. This algorithm describes crack growth as a discrete set of events depending only on the instantaneous crack tip stress state. First the question is asked if this instantaneous crack tip stress state meets or exceeds the crack initiation criterion? If the stress state is higher than the critical (over-stress) but not sufficient to induce secondary modes of dissipation like micro cracks then the crack will propagate as per the velocity relation given by equation 7.5. If secondary modes of dissipation become significant, which will be at certain stress state in front of the crack tip, the instantaneous crack tip stress will reduce based on the damage parameter in equation 7.10 and the crack will propagate based on the reduced instantaneous stress state. It can be seen that this sequential approach is a time marching algorithm, with a time increment, dt. To ensure that results are not dependent on this increment size, figure(7.4) shows the dependence of crack velocity with decreasing dt, which shows convergence as dt decreases, but at a finite value of dt. To implement the algorithm, five parameters K_{Icr}, C_0, K_{Icr}^d, n and β are required. The first three parameters are directly taken from experimental data published by Fineberg et al., [39, 85] and Ravi-Chandar et al., [79, 80] for PMMA and Homalite respectively, and is shown in figure(7.5). The last two parameters are material specific constants and should be found experimentally. To demonstrate the feasibility of the approach here we obtain the material specific constant by matching one of experimental data curves. Table 7.1, provides the values used in the computations presented with units; stress intensity factor in $MPa.\sqrt{m}$,and V_0 in $m.s^{-1}$.

Table 7.1: Fracture parameters for analytical model taken from experimental data *fig(7.5)

Material	$K_{Icr}*$	V_0*	K_I^d*	n	β
PMMA	5.69	150	12.65	1.3	1.6
Homalite	0.39	180	0.39	1.3	1.65

Values for fracture parameters were obtained from one set of experiments on SETP

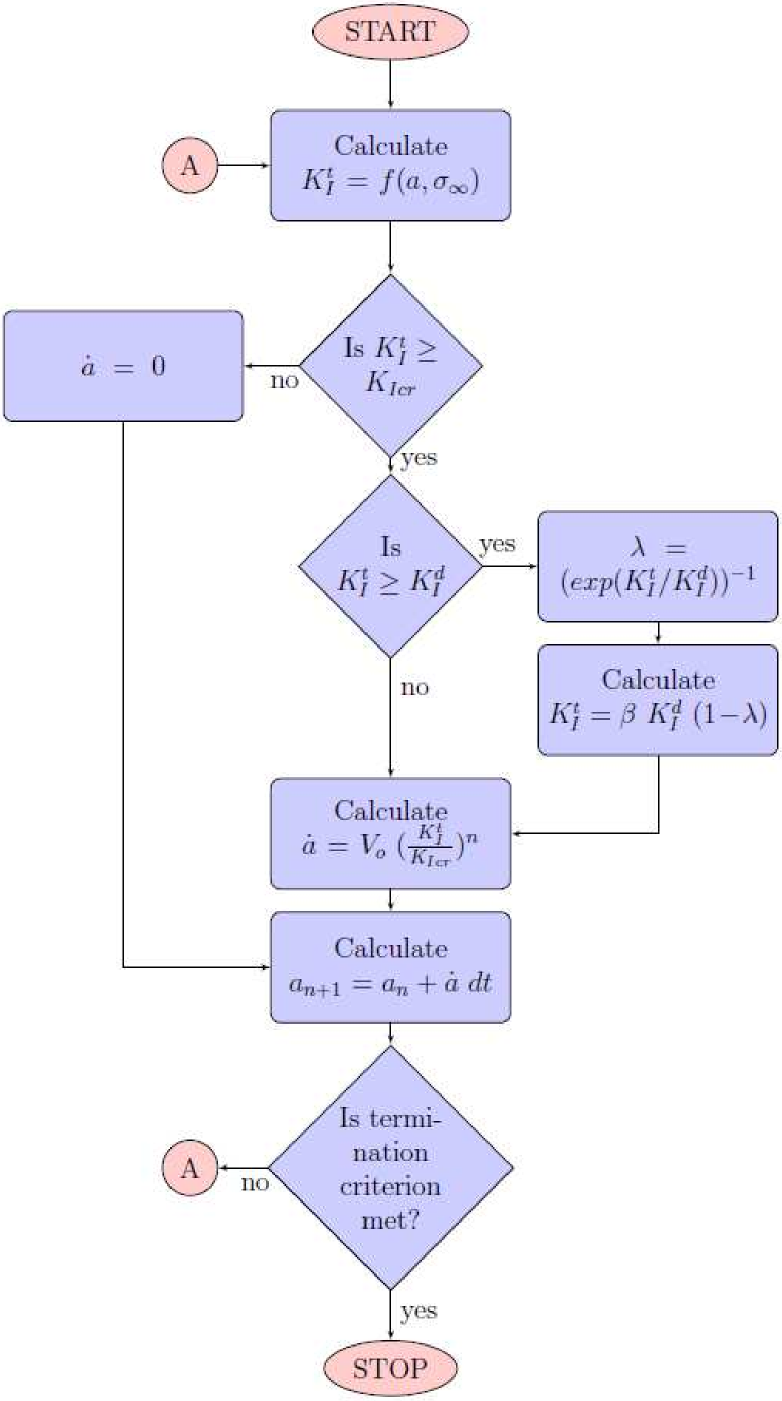

Figure 7.3: Generic algorithm for crack initiation and progression based on crack tip over-stress and crack velocity

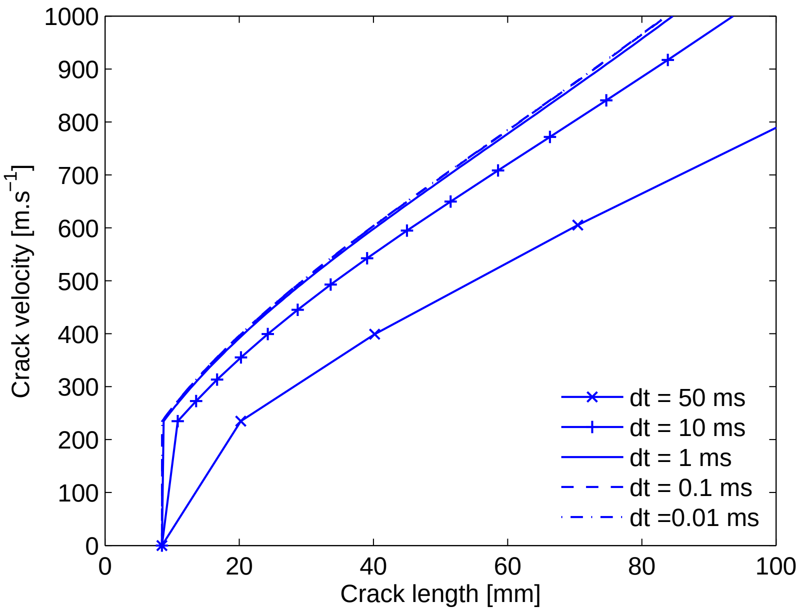

Figure 7.4: Crack length vs. crack velocity curves as a function of time-step

specimens. After this, all other experimental data points were *predicted* using the values in table 7.1. Comparison of crack velocity profile for PMMA with and without a micro-branching correction factor is shown in figure(7.6). By including the correction factor, the results show good agreement with experiment. The same is seen for other configurations of PMMA samples, figure(7.7)and Homalite samples, figure(7.8). The difference between using a static and dynamic stress intensity is shown in figure(7.9). The results indicate that the evolution of micro-damage is independent of specimen configuration ie; damage evolution is a material specific process and is based on the over-stress at the crack tip. It also shows that for a given material K_{Icr} and V_o are constants.

7.5 Conclusion & discussion

In summary, we have demonstrated the validity of a new crack growth model based on crack tip over stress and a material characteristic velocity, deviating from

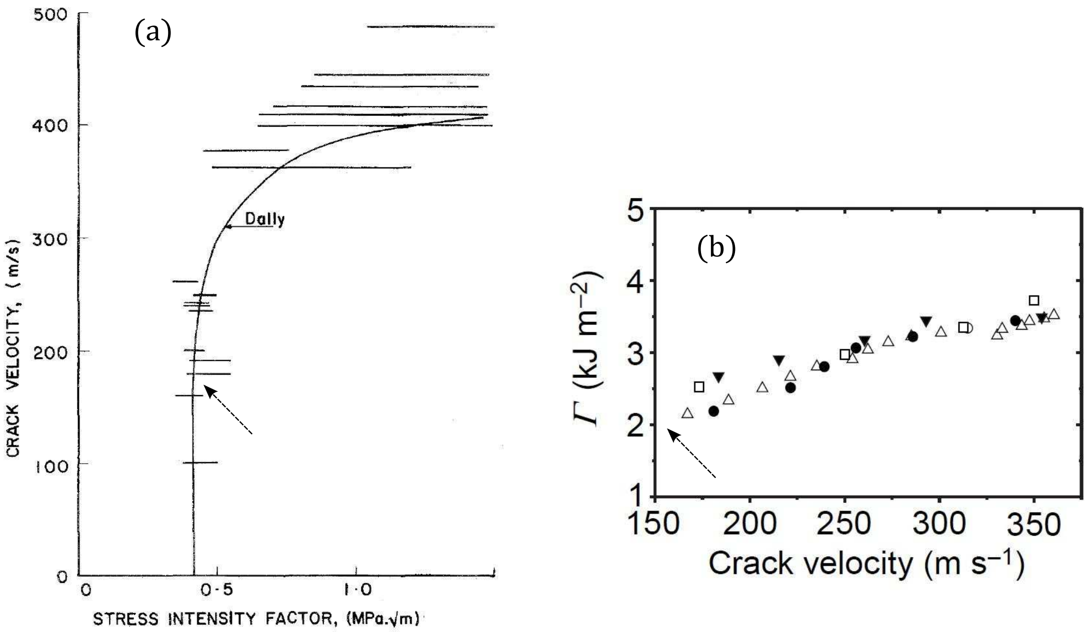

Figure 7.5: Parameters taken from experimental results (indicated by arrow), (a) RaviChandar et al [80], (b) Sharon et al [85]

the standard LEFM model of crack growth. A generic framework and algorithm for the analysis of fast (rapid crack growth) brittle fracture, largely dictated by the physics of fracture reported in the open literature, has been presented. The proposed model is seen to re-produce a variety of experimental results reported in the literature (see Fineberg et al [39]). Some key points of the proposed model needs to be highlighted. First, fracture initiation and propagation are treated as two distinct events. The crack tip over-stress is seen as the driver of crack growth and the over-stress is directly proportional to the crack-growth velocity. In theory, if the over-stress is large enough, the crack velocity can go beyond the Rayleigh wave speed limit. However, the existence of a limit is due to the inability of the material at and ahead of the crack tip to sustain the increasing over-stress state. As the stress ahead of the crack tip increases, other stress relieving dissipation mechanisms like micro-cracking, and micro-branching are formed. The reduction in primary crack velocity is due to reduction in over-stress caused by these alternate dissipation mechanisms. We also note

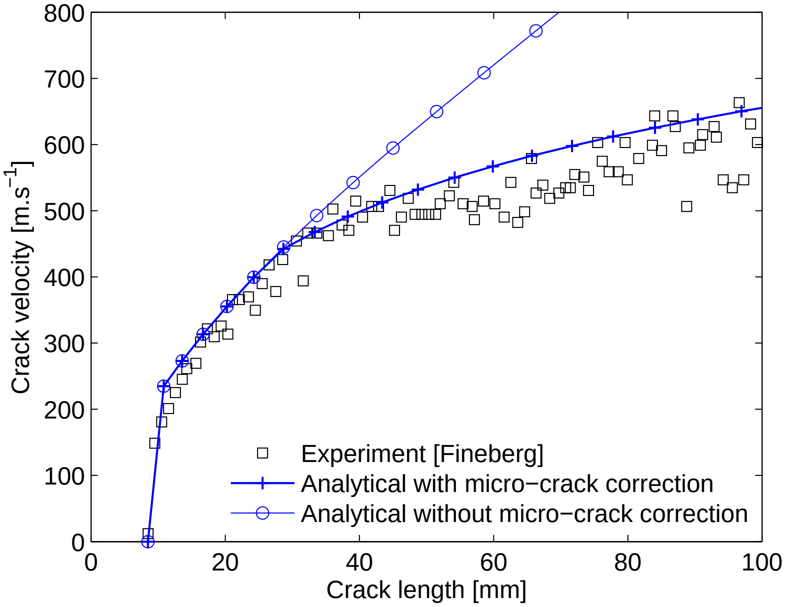

Figure 7.6: Example of analysis result with and without micro-crack correction

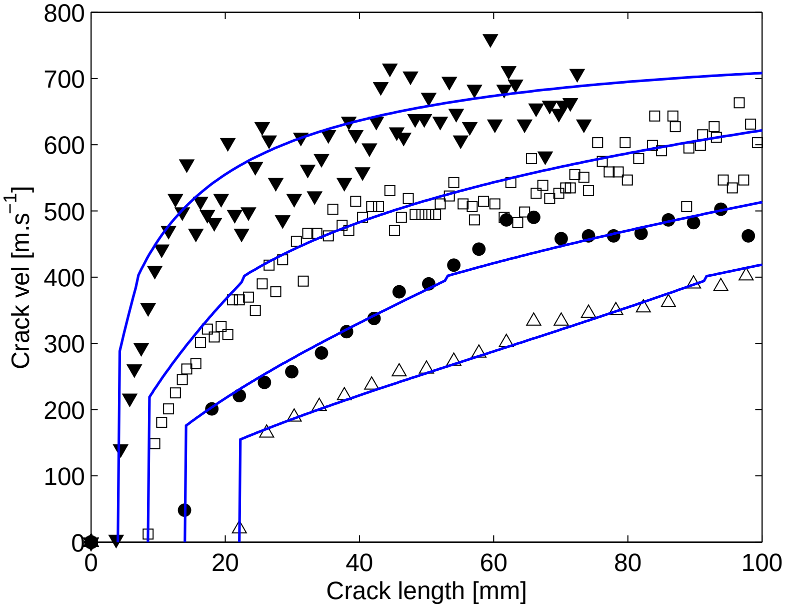

Figure 7.7: Comparison of experimental[85] and analytical result for specimen configuration.

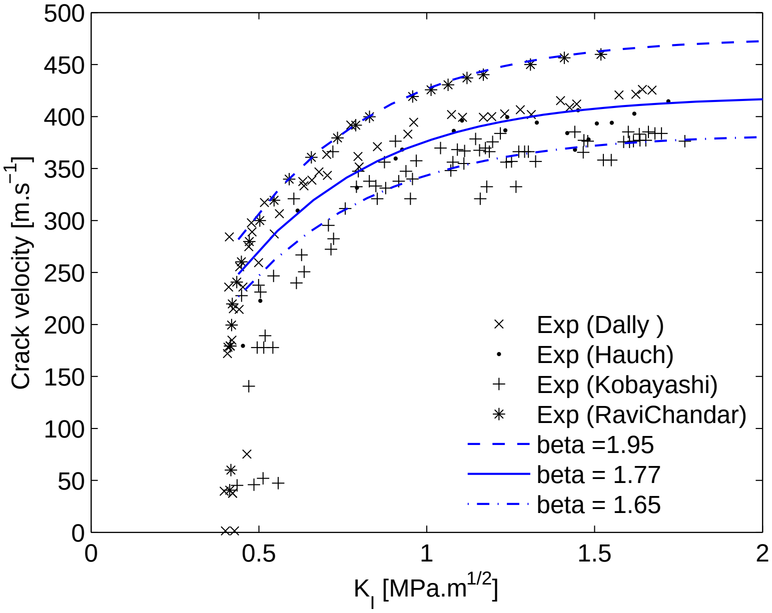

Figure 7.8: Comparison of experimental and analytical results. Bounds of experimental data found by changing the proportionality parameter β are also shown.

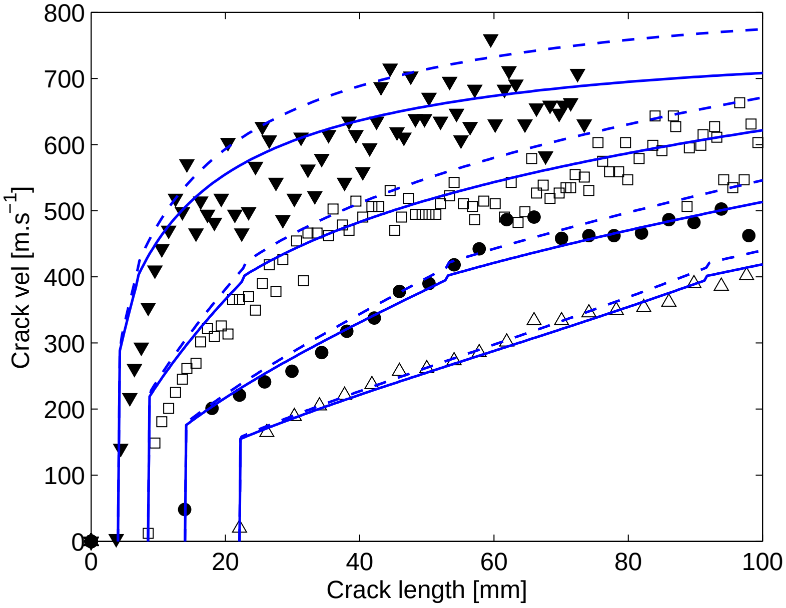

Figure 7.9: Results with static (solid line) and dynamic (dash line) stress intensity factor.

that the strain energy released during crack growth is an *outcome* of the cracking event, thus the use of its criticality as a condition for crack growth (suggesting that the critical energy release rate is a material parameter), is not needed in the proposed fracture framework.

CHAPTER VIII

Summary of key contributions

The study presented in this dissertation explores two fundamental failure mechanisms in composites, *kinking failure* and *fracture*. These mechanisms are activated in composites when subjected to predominantly compressive loading. However, fracture can also occur under other external loading states, whereas, kinking is the main mode of failure under compressive loading. In the first part of the thesis, the kinking failure mechanism was investigated for different loading and geometries. In each case, presented in chapters I-III, conclusions that were significant for each chapter were highlighted at the end of each chapter. In the second part of the thesis the fracture failure mode was analyzed in the context of application to composites and also in the context of application to fracture in polymers (motivated by the fact that polymer matrix composites are currently a favored structural material). Highlights of the major findings and key contributions are summarized below.

In chapters I-III, kinking failure and the influence of defects were studied. Multiple approaches to analyse defect induced kinking failure are provided. These approaches are validated against experimental results and shown to provide good correlation. A physically accurate kinking analysis requires a micro-mechanical formulation which can tend to be computationally expensive. Instead a new analytical formulation for kink band formation is provided in chapter IV. The analytical model shows a greater insight to the mechanics of kink band formation and also illustrates some of the drawbacks of previous analytical models. The current analytical model is able to capture both pre-peak and post peak behavior of kink band formation. Through the analytical model it is shown that kink formation is an instability problem, but, one that *evolves* with continued loading. Previous analytical approaches were not able to capture this instability in a unified manner. In the current model, by using two generalized displacements, to account for both amplitude and shape change of a load bearing fiber within a representative unit cell, the evolution of amplitude and fiber rotation before (pre-kinking) and during (kinking) the attainment of a maximum load is captured. It is also shown that the matrix yield stress (or onset of nonlinear matrix response) has no bearing on the peak load or kink band formation as assumed in some of the previous models. The current model also shows that matrix failure can occur before fiber failure during kink band formation. The current model is valid only upto matrix failure hence, the analysis does not provide a fully formed kink band width value. By incorporating a fracture model in the post-kinked regime, the current model can be modified to remove this deficiency. This is left as a future study.

The topic of fracture mechanics is explored at a fundamental level and a critical review of classical energy based fracture mechanics is conducted in chapter V. Two examples are provided, in chapters VI & VII, that point to drawbacks and limitations of current understanding of fracture mechanics. It is shown that the LEFM (linear elastic fracture mechanics) based energy release rate is applicable only for cases where the crack velocity is significantly greater than the deformation of the body. In all other cases energy release rate based methods, which assume that crack growth is driven by a critical value of strain energy released, do no apply and should not be used. An alternative theory, based on an over-stress criterion is proposed. This theory is shown to cover a wider class of crack growth problems. The theory also provides phenomenological explanation for observed non-smooth crack growth and provides an upper bound for crack velocity. The examples that have been provided in this thesis (chapters VI & VII), use empirical data to support the new theory, which in itself is insufficient to show that critical crack velocity is a material parameter. This can only be achieved thorough a sub-scale, molecular dynamics and/or atomistic model, which is beyond the scope of this dissertation and is left for future study.

APPENDICES

APPENDIX A

Close form solution for P_ξ and P_ζ

$$
\begin{aligned}
P_\xi = &-(\frac{1}{2})\frac{E_0^f I^f}{35840\xi\zeta^4 l^6}(-57344\xi\zeta^6 l^6 + 3360\xi_0\zeta^2 l^2\pi^5 Csch\left[\frac{\pi^2}{4\zeta l}\right]) \\
&-(\frac{1}{2})\frac{G_1}{35840\xi\zeta^4 l^6}(-71680\xi\zeta^4 l^6 + 13440\xi_0\zeta^2 l^4\pi^3 Csch\left[\frac{\pi^2}{4\zeta l}\right]) \\
&-(\frac{1}{2})\frac{\eta_1 G_2}{35840\xi\zeta^4 l^6}(49152\xi^3\zeta^6 l^6 + 26880\xi{\xi_0}^2\zeta^4 l^4\pi^2 - 1260{\xi_0}^3\zeta^2 l^2\pi^5 Coth\left[\frac{\pi^2}{8\zeta l}\right] \\
&-1260{\xi_0}^3\zeta^2 l^2\pi^5 Coth\left[\frac{3\pi^2}{8\zeta l}\right] - 21504\xi^2\xi_0\zeta^4 l^4\pi^3 Csch\left[\frac{\pi^2}{4\zeta l}\right] \\
&-1680\xi^2\xi_0\zeta^2 l^2\pi^5 Csch\left[\frac{\pi^2}{4\zeta l}\right] - 21\xi^2\xi_0\pi^7 Csch\left[\frac{\pi^2}{4\zeta l}\right] \\
&+13440\xi{\xi_0}^2\zeta^3 l^3\pi^4 Csch\left[\frac{\pi^2}{2\zeta l}\right] + 3360\xi{\xi_0}^2\zeta l\pi^6 Csch\left[\frac{\pi^2}{2\zeta l}\right] + 1260{\xi_0}^3\zeta^2 l^2\pi^5 Tanh\left[\frac{\pi^2}{8\zeta l}\right] \\
&+1260{\xi_0}^3\zeta^2 l^2\pi^5 Tanh\left[\frac{3\pi^2}{8\zeta l}\right])
\end{aligned}
\tag{A.1}
$$

$$\begin{aligned}
P_\zeta =& -(\frac{1}{2})\frac{E_0^f I^f}{71680\xi}(-344064\xi\zeta^2 + \frac{26880\xi_0\pi^5}{\zeta^2 l^4}Csch\left[\frac{\pi^2}{4\zeta l}\right] + \frac{1120\xi_0\pi^3}{\zeta^3 l^5}Csch\left[\frac{\pi^2}{4\zeta l}\right] \\
& \left(-4\zeta l\left(16\zeta^2 l^2 + 3\pi^2\right) + \pi^2\left(16\zeta^2 l^2 + \pi^2\right)Coth\left[\frac{\pi^2}{4\zeta l}\right]\right) + \frac{2240\xi_0}{\zeta^3 l^5}\pi^3 Csch\left[\frac{\pi^2}{4\zeta l}\right]^2 \\
& \left(\pi^2\left(-8\zeta^2 l^2 + \pi^2\right)Cosh\left[\frac{\pi^2}{4\zeta l}\right] + 4\zeta l\left(8\zeta^2 l^2 - 3\pi^2\right)Sinh\left[\frac{\pi^2}{4\zeta l}\right]\right)) \\
& -(\frac{1}{2})\frac{G_1}{71680\xi}(-143360\xi + \frac{53760\xi_0\pi^3 Csch\left[\frac{\pi^2}{4\zeta l}\right]}{\zeta^2 l^2} \\
& + \frac{13440\xi_0\pi^3\left(-8\zeta l + \pi^2 Coth\left[\frac{\pi^2}{4\zeta l}\right]\right)Csch\left[\frac{\pi^2}{4\zeta l}\right]}{\zeta^3 l^3}) \\
& -(\frac{1}{2})\frac{\eta_1 G_2}{71680\xi}(147456\xi^3\zeta^2 - \frac{84\xi^2\xi_0\pi^3}{\zeta^4 l^6}\left(16\zeta^2 l^2 + \pi^2\right)\left(64\zeta^2 l^2 + \pi^2\right)Csch\left[\frac{\pi^2}{4\zeta l}\right] \\
& - \frac{7\xi^2\xi_0\pi^3}{\zeta^5 l^7}\left(-8\left(1024\zeta^5 l^5 + 160\zeta^3 l^3\pi^2 + 3\zeta l\pi^4\right) + \pi^2\left(1024\zeta^4 l^4 + 80\zeta^2 l^2\pi^2 + \pi^4\right)Coth\left[\frac{\pi^2}{4\zeta l}\right]\right) \\
& Csch\left[\frac{\pi^2}{4\zeta l}\right] + \frac{13440\xi{\xi_0}^2\pi^2 Csch\left[\frac{\pi^2}{2\zeta l}\right]\left(4\zeta^2 l^2\pi^2 + \pi^4 + 8\zeta^3 l^3 Sinh\left[\frac{\pi^2}{2\zeta l}\right]\right)}{\zeta^3 l^5} \\
& + \frac{3360\xi{\xi_0}^2\pi^2}{\zeta^4 l^6}Csch\left[\frac{\pi^2}{2\zeta l}\right]^2\left(\pi^4\left(4\zeta^2 l^2 + \pi^2\right)Cosh\left[\frac{\pi^2}{2\zeta l}\right] - 8\zeta l Sinh\left[\frac{\pi^2}{2\zeta l}\right]\left(2\zeta^2 l^2\pi^2 + \pi^4 + 2\zeta^3 l^3 Sinh\left[\frac{\pi^2}{2\zeta l}\right]\right)\right) \\
& - \frac{5040{\xi_0}^3\pi^5 Coth\left[\frac{\pi^2}{4\zeta l}\right]Csch\left[\frac{\pi^2}{4\zeta l}\right]\left(5\pi^2 Cosh\left[\frac{\pi^2}{2\zeta l}\right] + \pi^2 Cosh\left[\frac{\pi^2}{\zeta l}\right] - 8\zeta l\left(Sinh\left[\frac{\pi^2}{2\zeta l}\right] + Sinh\left[\frac{\pi^2}{\zeta l}\right]\right)\right)}{\zeta^3 l^5\left(1 + 2Cosh\left[\frac{\pi^2}{2\zeta l}\right]\right)^2} \\
& - \frac{5040{\xi_0}^3\pi^5\left(Coth\left[\frac{\pi^2}{8\zeta l}\right] + Coth\left[\frac{3\pi^2}{8\zeta l}\right] - Tanh\left[\frac{\pi^2}{8\zeta l}\right] - Tanh\left[\frac{3\pi^2}{8\zeta l}\right]\right)}{\zeta^2 l^4}
\end{aligned} \tag{A.2}$$

APPENDIX B

Test and modelling procedures for damage and failure prediction in laminates with hole

Introduction

Predicting the open hole compression strength (OHCS) and the open hole tensile strength (OHTS) of a laminated fiber reinforced composite is an important consideration in material qualification for aerospace structural design. Experimental results of fiber reinforced composite panels with holes and cut-outs show a significant drop in compressive strength as a function of hole size due to stress gradients generated by the hole and because of the large stresses that concentrate at the hole edge. The situation is similar for tensile loading.

In traditional multi-layered laminates the failure in compression is generally dominated by the 0° ply kink banding mechanism B.1, while in tension, transverse cracks in the 90 degree layers, and matrix microcracks between fibers in off-axis layers are observed prior to the onset of catastrophic failure, the latter resulting due to failure of the significant load-bearing zero plies, and sometimes also accompanied by delamination. Even though the problem of predicting compressive strength of laminated composite panels with a cut-out is complex, it can be simplified by focussing attention on the failure of the 0° lamina within the laminate. There are two main points that needs to be taken into consideration; first the compressive strength of the 0° lamina and second, the influence of the hole on the stress distribution around the hole. Prior studies [2, 3, 23, 100], have examined the problem in detail and have developed both analytical and numerical methods based on careful experimental results to predict OHCS with varying degrees of sophistication in the modeling. In tension loading, in addition to transverse cracking in the 90 degree layers, matrix microcracking and fiber-matrix splitting in off-axis layers, and delaminations can all influence tensile strength. Hence, both damage and failure has to be taken into consideration in modeling for OHTS prediction.

At the zeroth order, we present a simple engineering approach using a combination of the Considere construction [89], and Lekhnitskii's [62] formulation to approximate OHCS. For OHTS, we use a modified Lekhnitskii's analysis which uses a strain based failure index for predicting strength. At the first order, these models are refined by a combination of micromechanics and classical lamination theory, implemented using the finite element method to capture kink-band formation using a global-local approach[3], for accurate prediction of OHCS for a class of popular laminates. For OHTS, a similar modeling strategy with the smeared crack approach (SCA), described in Heinrich and Waas [47], can be used for a single fiber reinforced lamina to predict OHTS. For both cases, the modeling uses constitutive properties of the fiber and *in-situ* lamina shear-stress strain response. In the second order analysis, which has higher fidelity, we employ the thermodynamically-based Schapery work potential damage theory for capturing the in-plane damage in each lamina, and we also use the enhanced Schapery theory (EST), as described in Pineda et al[73], to model in-plane failure including post-peak softening using the crack band model[12]. In this paper, results for OHCS are predicted using the zeroth, first and second order analysis methods, while results for OHTS are predicted using the zeroth order and second order analysis methods.

Zeroth order analysis

In multi-directional laminates, compression strength is generally dominated by the 0° ply kink banding failure. Even though the problem of predicting compressive strength of laminated composite with a cut-out is complex, it can be simplified by focusing attention on the failure of 0° laminae within the laminate. More specifically, the failure of 0° laminae occurs at the location of maximum stress, which, in case of laminates with cut-outs like a hole, are at the hole edge. Hence, the simplest approach would involve; (a) knowing the compressive strength of 0° lamina and, (b) knowing the value of stress at the hole edge. Therefore, the compressive strength of laminates with a hole is taken to be the applied stress which causes the maximum stress at the hole edge to reach the compressive strength of the 0° lamina. This approach is implemented using a combination of the Considere construction [89], and Lekhnitskii's [62] formulation. Considere construction is a geometric construction which utilizes the lamina shear stress-strain response to obtain the compressive strength of a 0° lamina (X_c^0) for a given fiber misalignment ϕ, as shown in figure B.2.

$$X_c^0 = \frac{\hat{\tau}_{12}}{\hat{\phi} + \hat{\gamma}_{12}} \tag{B.1}$$

where, $\hat{\phi}$ is the fiber misalignment, $\hat{\tau}_{12}$ is the shear stress and $\hat{\gamma}_{12}$ shear strain. The compressive strength of a laminate, ${X^L}_c$, is obtained by,

$$X_c^L = X_c^0 (\frac{E_{11}^L}{E_{11}^0}) \tag{B.2}$$

where, E_{11}^L and E_{11}^0 are the elastic moduli of the laminate and the 0° ply, respectively, in the direction of compressive load. Further, X_c^0 is the compressive strength of a 0°

lamina for a given fiber misalignment ϕ.

The equation above provides the compressive strength of a laminate without any stress-raisers (such as at cutout edges). In the presence of a hole, the maximum stresses occur at the hole edge due to non-uniform stress distribution. Using the Lekhnitskii [62] solution, Filiou and Soutis, [22], have provided an approximation to the stress distribution in an orthotropic infinite plate with a hole (shown in figure (B.8)). The equation below provides an accurate description of the axial stress, $(\sigma_{yy}(x,0))$ distribution due to a far field stress, σ_∞,

$$\begin{aligned}&\tfrac{\sigma_{yy}(x,0)}{\sigma_\infty} \approx 1+\tfrac{1}{2}(\tfrac{R}{x})^2+\tfrac{3}{2}(\tfrac{R}{x})^4-\tfrac{3}{2}(H_A-1)[5(\tfrac{R}{x})^6-7(\tfrac{R}{x})^8]\\ &H_A=\tfrac{(1+n)}{3}\\ &n=\sqrt{2(\sqrt{\tfrac{E_{yy}}{E_{xx}}}-\nu_{yx})+\tfrac{E_{yy}}{G_{yx}}}\end{aligned} \tag{B.3}$$

Using the above equation, we can approximate the stress at the edge of the hole (for $x = R$) as,

$$\frac{\sigma_{yy}(R,0)}{\sigma_\infty} \approx 3H_A \tag{B.4}$$

Assuming the material at the edge of the hole, where the stress is maximum, fails at the strength provided by equation B.4, above, ie; $\sigma_{yy}(R,0) \approx X_c^L$ we can obtain the corresponding far field stress. This far field stress will be the critical strength of the laminate with a hole in compression, which corresponds to the zeroth order approximation.

$$X_c^L \approx \frac{\sigma_{yy}(0,R)}{3H_A} = \frac{X_c^0}{3H_A}(\frac{E_{11}^L}{E_{11}^0}) \tag{B.5}$$

Thus, this equation provides the OHCS of a laminate (X_c^L, in terms of the pristine lamina compressive strength, (X_c^0). The approach presented here can also be used to estimate the open hole compressive strength for other cutout shapes and for multiaxial planar loading, provided an expression that relates the maximum stress at the cutout edge in terms of the applied far-field loading is available.

To estimate OHTS, we utilize a similar approach except we assume that the laminate will fail when the strain in the 0° ply reaches its ultimate tensile strain ($X^0_{\epsilon t}$) obtained from a coupon $[0_4]$ tensile test. A uniform through-the-thickness strain is also assumed in this model. Equation B.5 will now be modified to,

$$X^L_t \approx \frac{\sigma_{yy}(0,R)}{3H_A} = \frac{E^L_{11} X^0_{\epsilon t}}{3H_A} \tag{B.6}$$

Equations B.5-B.6 provide the zeroth order estimates for OHCS and OHTS. With the assumptions used for this simplified analysis, there is a significant drawback. The model does not account for material degradation due to in-plane damage and inter-laminar failure. In-plane damage and delamination is seen to be negligible in laminates with high percentage of 0° plies, but that is not always the case with laminates with higher percentage of off-axis plies, such as quasi-isotropic laminates. This method should only be used as a starting point for the more refined methods that will be next described.

First order analysis

First order analysis is based on the same mechanism as the zeroth order approach, that the failure in laminates under compressive loading is due to kink banding. However, instead of analysing the kink banding of a pristine 0° lamina, and the non-homogeneous stress field due to a cut-out separately, the kink band formation in a 0° lamina in a non-homogeneous stress field is analysed. This is achieved through a micro-mechanical, finite element model of the 0° lamina with a cut-out. In the micro-mechanics model, the fibers are explicitly modeled as homogeneous orthotropic continua and the matrix is modeled as an isotropic material with in-situ elastic-plastic properties. Fibers are misaligned by 1° to account for average fiber misalignment angles commonly observed in carbon composite materials [111]. This misalignment is the same as the one used in the zeroth level analysis. Micro-mechanics model, however, is a computationally expensive method, because of the difference in length scale of fiber and lamina. To model a complete lamina using micro-mechanics will require thousands of fiber-matrix layers, which is computationally prohibitive. To overcome the issue of computational cost the model is reduced by analysing a micro-region around the hole. Boundary conditions to be applied on the micro-region are obtained from a global homogeneous model. This method is called the *global-local* approach as defined in the work by Ahn & Waas [3] and Davidson & Waas [33]. In some reports, this method has also been referred to as the embedded cell method (see, for example, [63]).

The local-global approach implemented here is a three step procedure (each subsequent step relies on the results of the prior step) using a macro-mechanical model and this is as depicted in figure(B.9). Each step is an individual simulation and only the boundary information is passed from one step to the other. The macro-model, outside the micromechanics sub-region, is a 2D half symmetric model with homogenized transversely isotropic lamina properties of the 0° lamina. Step 1, is a linear elastic step where a known far-field displacement is applied in the axial(y) direction and the displacements ($\Delta_{x,y}$) at nodes corresponding to the micro-region boundary ($A - B - C - D$) are obtained. These displacements $\Delta_{x,y}$ are then applied on the isolated local micro-mechanics model boundary and another linear elastic analysis is performed in step 2, henceforth called "Local Linear Model". In step 3, the reaction forces, ($R_{x,y}$), obtained in step 2 are applied on boundaries $(A - D)\&(B - C)$ along with $\Delta_{x,y}$ on $(A - B)\&(C - D)$ and a non-linear Riks response analysis is conducted ("Local Non-linear Model") on the isolated local micro-mechanics model. Only step 3 is an incremental analysis while steps 1 and 2 are linear and hence done only once.

Step 2 is needed to obtain the consistent reaction forces on parts of the boundary of the micro-region, since step 3 uses mixed boundary conditions on the micro-region boundary.

Typically, as seen in past studies, there are no boundary conditions imposed on the free edge of a local model. This however, can lead to incorrect results because the local model which is non-homogeneous will deform in a manner different from the global model. In figure B.10, the un-deformed and deformed profiles of global and local model are shown. Pinching of the corners of the micro-region is observed as compared to the global model, during deformation, which will lead to artificial stress concentration developing at the corners. These stress concentrations will cause premature kink formation at the corners. Hence, application of reaction forces at the free boundaries is important to ensure that the local model follows the global deformation profile, in the elastic regime. By applying reaction forces instead of displacements, the left and right boundaries are kept free of constraints, thereby allowing for the kink band to form without displacements being constrained on the boundaries.

The axial reaction force R_y obtained from steps 1 & 2 provide the linear relation between the local and global model as a simple ratio $\hat{R} = (R_y^{global}/R_y^{local})$. Now, from step 3, we get the micro-kink band initiation load (R_k^{local}) which corresponds to the global compressive strength of the zero lamina due to kink banding, X_N^0 as ;

$$X_N^0 = (R_k^{global})/A = (\hat{R}\ R_k^{local})/A \tag{B.7}$$

In the above expression, A, is the load bearing cross-sectional area of the specimen in the far field. The size of the micro (local) region is an unknown of the global-local method. A converged solution is obtained when the peak compressive strength of the first order analysis shows no difference with respect to the size of the micro-region. The size of the region was scaled based on the ratio of width (length A-B) to the height (length B-C) of the micro-region.

Typical response of the micro-region is shown in figure (B.11) and corresponding snap-shots at different stages of loading leading to kink banding failure are provided. Figure (B.13) shows the scaling study to determine the converged micro-region size and the corresponding compressive strength of the 0° ply. The results are normalized by the compressive strength of the 0° ply with $\phi = 1^\circ$ obtained from the Considere construction ie; the un-notched zero ply strength. Using the converged value of compressive strength from the 2D global local X_N^0 analysis, the laminate compressive strength can now be obtained by simple scaling,

$$X_c^L = X_N^0 (\frac{E_{11}^L}{E_{11}^0}) \tag{B.8}$$

As with zeroth order, this first order approach provides compressive strength prediction for laminates that show kink band formation in the 0° lamina. Hence, this method of predicting compressive strength is predicated on zero ply kink banding being the dominant failure mechanism. However, this may not provide satisfactory predictions in cases where off-axis laminae dominate, ie; in cases where the percentage of 0° laminae is small and where there is significant non-linear behaviour before failure, as in pure angle-ply laminates or laminates with a large percentage of angle plies.

Second order analysis

Zeroth and first order analysis methods do not account for stiffness degradation of off-axis laminae. The difficulty in analytically modeling off-axis plies is because significant damage accumulates in these plies during loading. A second order modeling method should capture both damage and failure. This is achieved by modeling damage using Schapery theory and failure using the crack-band model, [12], which is referred to as Enhanced Schapery Theory (EST).

The EST formulation developed by Pineda et al [73] is used, which assumes that three major intralaminar mechanisms are responsible for all observed non-linearities in the stress-strain curve of a composite lamina: matrix microdamage, matrix macroscopic cracking (modes I and II), and axial fiber failure (mode I). Each of these mechanisms can be accommodated by partitioning the total dissipated energy density, W_S, into portions associated with each mechanism. It is assumed that the evolution of these failure mechanisms (i.e., macroscopic cracking and fiber breakage) yields an immediate reduction in the load-carrying capability of a local subvolume where the mechanism is active.

EST in combination with Cohesive Zone methods, such as the discrete cohesive zone method (DCZM), [53], can be used to account for both in-plane and inter-ply damage. However, failure due to delamination is not considered in the second order analysis, since the material system studied here did not exhibit significant delamination.

EST Evolution Equations for a Fiber-Reinforced Lamina

EST is a multiple-internal state variable (ISV) formulation, which utilizes separate ISVs for modeling the effects of damage and failure. Four ISVs are used; S, for damage, S_I^f, for fiber failure, S_I^m, for transverse matrix failure, and S_{II}^m for matrix shear failure. To arrive at the evolution equations for the ISVs, the elastic strain energy density must be defined for a material which may contain cohesive cracks. Therefore, the elastic strain energy W_E is comprised of a contribution from the continuum W and any possible cohesive cracks W_M^j. The plane stress, elastic strain energy density in the continuum is defined as,

$$W = \frac{1}{2}(E_{11}\epsilon_{11}^2 + E_{22}(S)\epsilon_{22}^2 + G_{12}(S)\gamma_{12}^2) + Q_{12}\epsilon_{11}\epsilon_{22} \tag{B.9}$$

where stress in the laminae are related to strain assuming plane stress conditions.

$$\begin{aligned} \sigma_{11} &= Q_{11}\epsilon_{11} + Q_{12}\epsilon_{22} \\ \sigma_{22} &= Q_{12}\epsilon_{11} + Q_{22}\epsilon_{22} \\ \tau_{12} &= Q_{66}\gamma_{12} \end{aligned} \tag{B.10}$$

where γ_{12} is the engineering shear strain and

$$\begin{aligned} Q_{11} &= \frac{E_{11}}{1 - \nu_{12}\nu_{21}} \\ Q_{22} &= \frac{E_{22}}{1 - \nu_{12}\nu_{21}} \\ Q_{12} &= \nu_{12}Q_{22} \\ Q_{66} &= G_{12} \\ \nu_{21} &= \frac{\nu_{12}E_{22}}{E_{11}} \end{aligned} \tag{B.11}$$

where E_{11} is the axial elastic modulus, E_{22} is the transverse elastic modulus, ν_{12} is the Poisson's ratio, ν_{21} is the transverse Poisson's ratio, and G_{12} is the elastic shear modulus. After assuming that the quantity $\nu_{12}\nu_{21} << 1$, Equations (B.11) simplify,

$$\begin{aligned} Q_{11} &= E_{11} \\ Q_{22} &= E_{22} \\ Q_{12} &= \nu_{12}Q_{22} \\ Q_{66} &= G_{12} \end{aligned} \tag{B.12}$$

Note that only the transverse and shear moduli (E_{22} and G_{12}) are functions of S since matrix microdamage only accrues in the matrix of the laminae. The Poisson's ratio is assumed to evolve such that the quantity $Q_{12} = E_{22}\nu_{12}$ remains constant; however, this restriction can be relaxed if deemed necessary. The degraded moduli are related to the virgin moduli (E_{220} and G_{120}) and the ISV through a set of microdamage functions ($e_s(S)$ and $g_s(S)$).

$$E_{22} = E_{220} e_s(S) \tag{B.13}$$

$$G_{12} = G_{120} g_s(S) \tag{B.14}$$

Degrading E_{22} and G_{12} exclusively is consistent with the intralaminar damage typically observed in PMC laminates.

The elastic strain energy density of the cohesive cracks are defined as the recoverable energy per unit crack surface area smeared over the entire element.

$$W_I^f = \frac{t_I^f \delta_I^f}{2 l_e^{(\theta+90^\circ)}} \tag{B.15}$$

$$W_I^m = \frac{t_I^m \delta_I^m}{2 l_e^{(\theta)}} \tag{B.16}$$

$$W_{II}^m = \frac{t_{II}^m \delta_{II}^m}{2 l_e^{(\theta)}} \tag{B.17}$$

The cohesive cracks are not active until some initiation criterion is met. Prior to that, the crack tip opening displacements δ_M^j are zero, and the do not contribute to the elastic strain energy density. The tractions in Equations (B.15)-(B.17) can be related to the secant stiffness' using triangular traction-separation laws, k_M^j shown in figure B.12.

$$t_I^f = k_I^f \delta_I^f \tag{B.18}$$

$$t_I^m = k_I^m \delta_I^m \tag{B.19}$$

$$t_{II}^m = k_{II}^m \delta_{II}^m \tag{B.20}$$

Hence, the total elastic strain energy density in the continuum is given by

$$\begin{aligned} W_E = & \frac{1}{2}\left(E_{11}\epsilon_{11}^2 + E_{22}(S)\epsilon_{22}^2 + G_{12}(S)\gamma_{12}^2\right) + Q_{12}\epsilon_{11}\epsilon_{22} \\ & + \frac{k_I^f(S_I^f)}{2 l_e^{(\theta+90^\circ)}}\delta_I^{f\,2} + \frac{k_I^m(S_I^m)}{2 l_e^{(\theta)}}\delta_I^{m\,2} + \frac{k_{II}^m(S_{II}^m)}{2 l_e^{(\theta)}}\delta_{II}^{m\,2} \end{aligned} \tag{B.21}$$

Invoking the stationarity of potential with respect to each ISV, gives the ISV evolution equations.

$$\frac{1}{2}\left(\epsilon_{22}^2 E_{220}\frac{de_s}{dS_r}+\gamma_{12}^2 G_{120}\frac{dg_s}{dS_r}\right)=-3S_r^2 \tag{B.22}$$

$$\frac{1}{2l_e^{(\theta+90^\circ)}}\frac{dk_I^f}{dS_I^f}{\delta_I^f}^2=-1 \tag{B.23}$$

$$\frac{1}{2l_e^{(\theta)}}\frac{dk_I^m}{dS_I^m}{\delta_I^m}^2=-1 \tag{B.24}$$

$$\frac{1}{2l_e^{(\theta)}}\frac{dk_{II}^m}{dS_{II}^m}{\delta_{II}^m}^2=-1 \tag{B.25}$$

The use of a reduced ISV $S_r = S^{\frac{1}{3}}$ has been employed in Equation (B.22). Sicking [87] has shown that the use of this reduced ISV yields polynomial forms of the micro-damage functions in Equations (B.13) and (B.14). Thus, Equation (B.22) becomes a polynomial equation that can be readily solved for S_r for a given strain state $(\epsilon_{22}, \gamma_{12})$. No mixed-mode law is incorporated in this work; thus, mode I and mode II failure are uncoupled. Future iterations of EST will implement a mixed-mode fracture law to introduce this coupling. However, since the mode I and mode II displacements are uncoupled here, $S_I^f, S_I^m,\ and\ S_{II}^m$ can be determined from Equations (B.23) - (B.25), *a priori*, in terms of the applied strain using the traction separation laws and kinematics.

Using the chain rule and the fact that

$$\frac{dS_I^f}{d\delta_I^f}=\frac{t_{IC}^f}{2l_e^{(\theta+90^\circ)}} \tag{B.26}$$

$$\frac{dS_I^m}{d\delta_I^m}=\frac{t_{IC}^m}{2l_e^{(\theta)}} \tag{B.27}$$

$$\frac{dS_{II}^m}{d\delta_{II}^m}=\frac{t_{IIC}^m}{2l_e^{(\theta)}} \tag{B.28}$$

by traction separation laws [73], the cohesive secant stiffnesses are determined. Where, the cohesive strengths of the material are t_{IC}^{f} (mode I fiber strength), t_{IC}^{m} (mode I matrix strength), and t_{IIC}^{m} (mode II matrix strength)

$$k_I^f = -\int \frac{t_{IC}^f}{{\delta_I^f}^2} d\delta_I^f \tag{B.29}$$

$$k_I^m = -\int \frac{t_{IC}^m}{{\delta_I^m}^2} d\delta_I^m \tag{B.30}$$

$$k_{II}^m = -\int \frac{t_{IIC}^m}{{\delta_{II}^m}^2} d\delta_{II}^m \tag{B.31}$$

Evaluating the integrals in Equations (B.29)-(B.31), while enforcing $k_M^j = 0$ when $\delta_M^j = \frac{2G_{MC}^j}{t_{MC}^j}$ results in expressions for k_M^j in terms of δ_M^j.

$$k_I^f = t_{IC}^f \left(\frac{1}{\delta_I^f} - \frac{t_{IC}^f}{2G_{IC}^f} \right) \tag{B.32}$$

$$k_I^m = t_{IC}^m \left(\frac{1}{\delta_I^m} - \frac{t_{IC}^m}{2G_{IC}^m} \right) \tag{B.33}$$

$$k_{II}^m = t_{IIC}^m \left(\frac{1}{\delta_{II}^m} - \frac{t_{IIC}^m}{2G_{IIC}^m} \right) \tag{B.34}$$

where G_{IC}^f is the mode I fracture toughness of the fiber, G_{IC}^m is the mode I fracture toughness of the matrix, and G_{IIC}^m is the mode II fracture toughness of the matrix. The thermodynamically consistent stiffnesses derived in Equations (B.32)-(B.34) can also be derived directly from the traction-separation laws using geometry.

Finally, it is assumed that following failure initiation the strains are related to the crack tip opening displacements by

$$l_e^{(\theta+90^\circ)} \epsilon_{11} = l_e^{(\theta+90^\circ)} \epsilon_{11}^C + \delta_I^f \tag{B.35}$$

$$l_e^{(\theta)} \epsilon_{22} = l_e^{(\theta)} \epsilon_{22}^C + \delta_I^m \tag{B.36}$$

$$l_e^{(\theta)}\gamma_{12} = l_e^{(\theta)}\gamma_{12}^C + 2\delta_{II}^m \tag{B.37}$$

where ϵ_{11}^C, ϵ_{22}^C, and γ_{12}^C are the strains when, the Hashin-Rotem matrix failure criterion involving contributions from both the transverse (ϵ_{22}) and shear (γ_{12}) strains, are satisfied.

$$\begin{gathered}\left(\frac{\epsilon_{22}}{Y_T}\right)^2 + \left(\frac{\gamma_{12}}{Z}\right)^2 = 1 \quad \epsilon_{22} \geq 0 \\ \left(\frac{\epsilon_{22}}{Y_C}\right)^2 + \left(\frac{\gamma_{12}}{Z}\right)^2 = 1 \quad \epsilon_{22} < 0\end{gathered} \tag{B.38}$$

where Y_T is the transverse lamina failure strain in tension, Y_C is the transverse failure lamina strain in compression, and Z is the shear failure strain. The fiber failure criterion only involves the axial strain ϵ_{11}.

$$\left(\frac{\epsilon_{11}}{X_T}\right)^2 = 1 \quad \epsilon_{11} \geq 0 \tag{B.39}$$

where X_T is the maximum allowable axial strain of the lamina. The Hashin-Rotem initiation criterion is utilized here for its tractability and computational efficiency, but virtually any initiation criterion could be used to govern the onset of matrix failure due to macroscopic cracking or axial failure due to fiber breakage.

Equations (B.35)-(B.37) imply that the strain in the continuum remains at the values obtained when failure initiates, and that any incremental change in the global strain after failure initiation is used wholly to advance the crack tip opening displacement. To account for changes in the continuum strain after failure initiates, it can be assumed that the stress state in the cracked body is homogenous and the tractions on the crack tip faces are equal to the stresses in the continuum. Then, the strains in Equation (B.21) can be formulated in terms of the cohesive secant stiffnesses and the crack tip opening displacement. However, it is assumed that the evolution of strain in the continuum is negligible once cohesive cracks form. Equations (B.35)-(B.37) can be utilized in Equations (B.32)-(B.34) to obtain k_M^j as functions of the global strain at an integration point.

$$k_I^f = t_{IC}^f \left[\frac{1}{l_e^{(\theta+90^\circ)} \left(\epsilon_{11} - \epsilon_{11}^C\right)} - \frac{t_{IC}^f}{2G_{IC}^f} \right] \tag{B.40}$$

$$k_I^m = t_{IC}^m \left[\frac{1}{l_e^{(\theta)} \left(\epsilon_{22} - \epsilon_{22}^C\right)} - \frac{t_{IC}^m}{2G_{IC}^m} \right] \tag{B.41}$$

$$k_{II}^m = t_{IIC}^m \left[\frac{2}{l_e^{(\theta)} \left(\gamma_{12} - \gamma_{12}^C\right)} - \frac{t_{IIC}^m}{2G_{IIC}^m} \right] \tag{B.42}$$

Once failure initiates, the effects of failure supersede the effects of microdamage and evolution of S ceases. The cohesive stiffness in a cracked element is calculated using Equations (B.40)-(B.42) for a given strain state; then, Equations (B.18)-(B.20) and (B.35)-(B.37) are used to calculate the tractions on the crack tip faces and the crack tip opening displacement. It is assumed that the stress state in the integration point subvolume of the element is homogenous, and the tractions on the crack tip faces are equal to the stresses in the element. Lastly, the axial, transverse, and shear moduli of the element can be calculated [12]:

$$E_{11} = \left\{ \frac{1}{E_{110}} - \frac{\epsilon_{11} - \epsilon_{11}^C}{t_{IC}^f \left[1 + \frac{l_e^{(\theta+90^\circ)} t_{IC}^f}{2G_{IC}^f} \left(\epsilon_{11} - \epsilon_{11}^C\right) \right]} \right\}^{-1} \tag{B.43}$$

$$E_{22} = \left\{ \frac{1}{E_{22}^*} - \frac{\epsilon_{22} - \epsilon_{22}^C}{t_{IC}^m \left[1 + \frac{l_e^{(\theta)} t_{IC}^m}{2G_{IC}^m} \left(\epsilon_{22} - \epsilon_{22}^C\right) \right]} \right\}^{-1} \tag{B.44}$$

$$G_{12} = \left\{ \frac{1}{G_{12}^*} - \frac{\gamma_{12} - \gamma_{12}^C}{2t_{IIC}^m \left[1 + \frac{l_e^{(\theta)} t_{IIC}^m}{4G_{IIC}^m} \left(\gamma_{12} - \gamma_{12}^C\right) \right]} \right\}^{-1} \tag{B.45}$$

where E_{22}^* and G_{12}^* are the degraded transverse and shear moduli, due to microdamage, when Equation (B.38) is satisfied.

It should be noted that EST also account for kink band formation under axial compression [84, 9, 10]. As the lamina is loaded, the fibers in the composite rotate by some angle ϕ, and attain the new direction e_f, given by the deformation gradient $\mathbf{F}$ in the model.

$$\mathbf{e_f} = \frac{1}{\lambda}\mathbf{F} \cdot \mathbf{e_{f0}} \tag{B.46}$$

where $\mathbf{e_{f0}}$ is the fiber orientation in the undeformed configuration and λ is the stretch ratio.

$$\lambda = \sqrt{\mathbf{e_{f0}} \mathbf{F} \mathbf{F^T} \mathbf{e_{f0}}} \tag{B.47}$$

To model the kink band mechanism, all calculations are then executed in the instantaneous fiber frame; therefore, fiber rotation can induce large shear strains, γ_{12}. As shear strain increases, more damage, is induced leading to a reduction in the local tangent shear modulus. The increase in local shear compliance allows for further increase in the shear strain. Under increasing axial compression, this mechanism leads to a runaway (negative feedback) instability, and a kink band eventually precipitate.

In summary, Equations (B.38) and (B.39) mark the transition from evolving microdamage to failure to macroscopic cracking. Prior to failure initiation, Equation (B.22) is used to calculate the microdamage reduced ISV S_r, and the failure ISVs S_I^f, S_I^m, and S_{II}^m remain zero. Equations (B.13) and (B.14) are used to calculate the degraded transverse and shear moduli. Subsequent to matrix failure initiation, microdamage growth is precluded, and S_r remains at S_r^*, the value of S_r when Equation (B.38) was satisfied. The degeneration of the transverse and shear moduli, resulting from matrix transverse and shear cracking, is calculated using Equations (B.44) and (B.45). Finally if Equation (B.39) is satisfied, the axial modulus is calculated using Equations (B.43) as fiber breakage evolves in the element. Once the material moduli have been calculated using the appropriate evolution equations, the stresses can be updated accordingly using Equations (B.12).

Material damage and failure characterization

General requirements for laminate with cut-outs, like a hole, are shown in figure(B.14). There are two stages to the analysis, first is the measurement and modeling to obtain input parameters from coupon level tests and micromechanics predictions. These are then used in the second stage, which is the prediction of OHCS, OHTS and any other progressive failure scenario. There are four categories of inputs(figure B.14), geometry, elastic material properties, damage properties, and failure properties. Some of the parameters are measured while others are derived based on the measured values. Different input details are required in each category ranging from constitutive fiber and matrix properties in the micro level to the laminate properties at the coupon level as shown in figure B.15.

Due to propriety nature of the composite material used, no information about the material will be provided. However, a complete set of EST input and respective test requirements are listed in table B.1, and are described in subsequent sections.

Measuring lamina in-situ shear response

In all the methods described , the common and critical data required is the *in-situ* elastic-damage response of the matrix. Characterization of the *in-situ* lamina shear response is done using the procedure described by Ng et al [70]. Tensile tests of dogbone shaped specimens of $\pm 45^{\circ}{}_s$ were conducted to obtain the in-plane lamina shear response, and the tests followed the guidelines of ASTM D3518 and D3039 for strain gage requirements and gage section dimensions. Dogbone-shaped specimens were used rather than standard coupon-shaped specimens because previous work showed a tendency of specimen failure within the grips for straight-sided coupons and within the gage section for dog-bone coupons.

A speckle pattern was also implemented on one side of the specimens to capture full field strain data using an optical camera. Subsequently, the speckle images were analysed using the ARAMIS digital image correlation (DIC) software. Strain gage data was compared to, and agreed with, the strains obtained through DIC. However, strain gages did not cover the full range of strains seen in the experiments and failed prior to sample ultimate failure. Hence, DIC measurements were used for calculating full field strain data and used for the analysis.

Using the shear response of the lamina, the in-situ shear response of the damaging matrix, which is shown in figure (B.4) was extracted as described in [70]. From this, the in-situ matrix equivalent stress vs equivalent strain response can be calculated (Ng et al [70]) and is shown in figure (B.5).

Damage parameters

Items 1-3 in table B.1 refer to the Schapery damage evolution curves described by the polynomial forms of e_s and g_s as

$$e_s(S_r) = e_{s0} + e_{s1}S_r + e_{s2}S_r^2 + e_{s3}S_r^3 + e_{s4}S_r^4 + e_{s5}S_r^5 \tag{B.48}$$

$$g_s(S_r) = g_{s0} + g_{s1}S_r + g_{s2}S_r^2 + g_{s3}S_r^3 + g_{s4}S_r^4 + g_{s5}S_r^5 \tag{B.49}$$

The shear microdamage function g_s was obtained from the shear stress-shear strain (τ_{12}-γ_{12}) response of [45°/-45°] angle-ply coupon tests as recommended by Sicking [87]. The transverse tensile micro-damage function e_s requires testing of [30°/-30°] angle-ply coupon tests, also recommended by Sicking [87]. However, e_s can also be obtained from the *in-situ* matrix equivalent stress-equivalent strain response. Using the non-linear in-situ matrix properties in a cubic close-packed repeating unit cell, and applying transverse loading, the lamina transverse response curve can be obtained.

Transverse non-linear response curve is then used to calculate e_s following Sicking's procedure [87]. The two curves are shown in figure B.6 & B.7.

Intralaminar failure strain

Intralaminar failure strains are measured using DIC analysis of tests listed in items 4,6 & 8 of table B.1. Compressive failure strain in the fiber direction can be obtained from [0] compression tests, which require thicker coupons such that kink band formation can be captured using DIC. Alternatively, compressive failure strain can instead be found using a micro-mechanics finite element model (FEM) [61] or analytical model [32] of the composite micro-section. The transverse compression response (item 7) is generally taken to be the same as in tension, but the failure strengths are different and the tensile failure strength (or strain) is measured from a coupon test.

Intralaminar failure toughness

Fiber direction tension failure toughness can be measured from Compact Tension Specimen (CTS) [75] or Single Edge Notch Tension (SENT) tests of $[90/0]_s$ laminates. The transverse direction tension toughness can be obtained from Single Edge Notch Tension (SENT) test. However, in this study it is assumed that this value is the same as the interlaminar mode I toughness because in both cases, toughness is due to matrix failure only. The transverse direction compressive toughness is assumed to be the same as the transverse tension toughness. Shear direction toughness is difficult to measure, because it is difficult to obtain a pure shear stable crack propagation. Hence, shear toughness is back calculated from a simulation of the SENT test of a [0] ply laminate. Before the shear test and the corresponding simulation are conducted, items 1-12 should be completed, so that shear toughness is the last unknown variable that needs characterization.

Interlaminar failure toughness

Interlaminar failure toughness and strength are measured using standard test procedures. For mode I toughness and strength, a Double Cantilever Beam (DCB) test is conducted. For mode II toughness, an End Notch Flexure (ENF) test is used. Further, for mode II strength, a Single Lap Joint (SLJ) test is conducted, with a short intact region so that the join failure is strength dominated.

Finite Element Model and results

EST was integrated into the Abaqus FEM software using the user material Fortran subroutine `UMAT` for implicit solver and `VUMAT` for explicit solver [1]. The EST Fortran subroutines are compiled into a static library and linked to Abaqus through the `abaqus_v6.env` environment file. At each integration point, during each FEM iteration, the `UMAT/VUMAT` calls the main EST subroutine.

Open hole laminate is modeled using layered shell elements (S4R) with three integration point through thickness for each lamina. For OHTS simulation, a total displacement of $2mm$ was applied over $1000sec$ using the `*DYNAMIC, IMPLICIT` keyword in Abaqus with the parameter `APPLICATION = QUASI-STATIC`. For OHCS, a ramped total displacement of $2mm$ was applied using the `*EXPLICIT, EXPLICIT` keyword in Abaqus. For compression loading, the explicit solver was used to avoid convergence issues cause by a sudden post-peak instability.

Results from the simulations were compared with experiments for four different laminates. The nomenclature used to label laminates describe the percentage of $0°, 45°\&90°$ plies in a laminate. For example laminate (10/70/20) is made of 10% 0° plies, 70% 45° plies and 20% 90° plies.

Results corresponding to the zeroth order, first order, and second order models are shown in figure (B.16). The results are normalized by the compressive strength of the 0° ply with $\phi = 1°$ obtained from the Considere construction ie; the zero ply un-notched strength. Though all the predictions are close to experiment, the first and second order models are seen to be a better match with experiments (within 5%), especially in laminates with high percentage of 0° plies.

The difference between the zeroth order and second order analysis is more pronounced in tension. Results corresponding to the zeroth order and second order models are shown in figure (B.17). The results are normalized by the tensile strength of the 0° ply obtained from an experiment ie; the zero ply un-notched tensile strength. Second order analysis results were found to be within 5% of the experimental results.

Conclusion

In this paper, different modeling approaches and coupon level test requirements for predicting compressive (OHCS) and tensile (OHTS) strength of laminates with a hole are outlined. A zeroth order approach which utilized Considere construction and Lekhnitski approximations is described. This approach is useful for a quick and fast approximation of the OHCS and OHTS, as it provides conservative values for OHCS and OHTS.

A first order approach based on global-local micro-mechanical modeling is also outlined. This approach can be used for OHCS prediction and is found to be within 5% of experimental values. First order approach can capture kink band formation which is the dominant failure mechanism in compression. However, this approach does not capture the damage in off-axis plies within a laminate.

A unified tension compression formulation which captures both damage and failure was finally described. EST formulation addressed both pre-peak and post-peak non-linearities appropriately. Matrix micro-damage, predominantly responsible for the observed pre-peak non-linearity in a composite lamina, was accounted for with a single ISV representing the dissipated potential associated with micro-damage, along the lines of the original Schapery theory formulation. The relationship between the transverse and shear moduli of the lamina were related to the ISV through a pair of experimentally-obtainable micro-damage functions. Three major in-plane failure mechanisms applicable to continuous fiber-reinforced, laminated, polymer matrix composites were identified: mode I matrix cracks, mode II matrix cracks, and fiber breakage. A failure initiation criterion was used to mark the transition from a damaging continuum to a damaged continuum with an embedded discontinuity. Currently, a quadratic failure criterion is employed, but future work will focus on utilizing a more physics-based initiation criterion. After failure initiation, micro-damage evolution ceases and separate ISVs are introduced to incorporate the effects of the three major failure mechanisms. Evolution of the failure ISVs is based upon traction-separation laws that are material specific and that which can be measured. Good agreement is seen with first and second order predictions of both OHCS and OHTS. The material used for this study did not show significant delamination. This however is not true for all material systems. Future studies are aimed at incorporating delamination capability using cohesive zone elements, as reported in [53]. This "third order" model will be able to capture all possible failure modes associated with PMC laminates, including delamination.

Item	Parameter	Test
Damage: Schapery evolution polynomial		
1	Shear	$[+45_2/-45_2]_s$ tension
2	Trans. tension	$[+30_2/-30_2]_s$ tension
$3^\dagger$	Trans. compression	$[+30_2/-30_2]_s$ compression
Intralaminar failure strain		
4	Fiber tension $X_{\epsilon t}$	[0] tension
5	Fiber compression $X_{\epsilon c}$	[0] compression or FEM
6	Trans. tension $Y_{\epsilon t}$	[90] tension
$7^\dagger$	Trans. compression $Y_{\epsilon c}$	N/A
8	Shear Z_ϵ	$[+45_2/-45_2]$ tension
Intralaminar failure toughness		
9	Fiber tension G_{If-t}	CTS $[90/0]_s$ tension
$10^\dagger$	Fiber compression G_{If-c}	CCS $[90/0]_s$ compression
$11^\ddagger$	Trans. tension G_{It-t}	SENT [90] tension
$12^\dagger$	Trans. compression G_{It-c}	N/A
$13^\ddagger$	Shear G_{IIs}	SENT [0] tension & FEM
Interlaminar failure		
14	Mode I G_I, σ_I	DCB
15	Mode II G_{II}	ENF
16	Mode II strength τ_c	SLJ
† assumed the same as in tension ‡ assumed same as interlaminar failure		

Table B.1: Parameters required for modeling

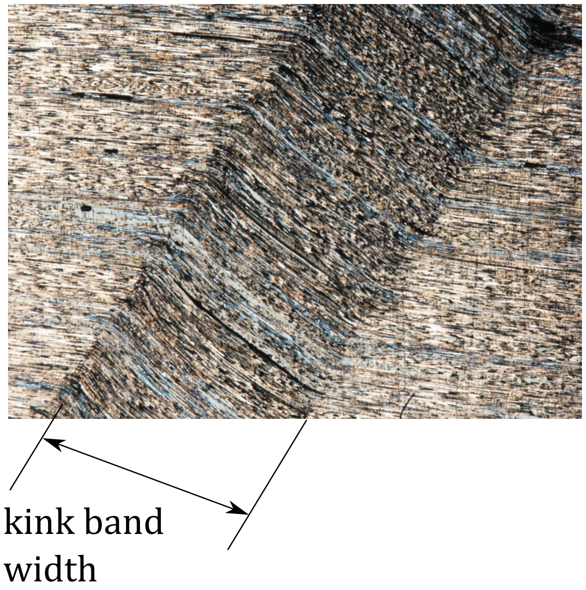

Figure B.1: Typical kink band in a carbon fiber composite.

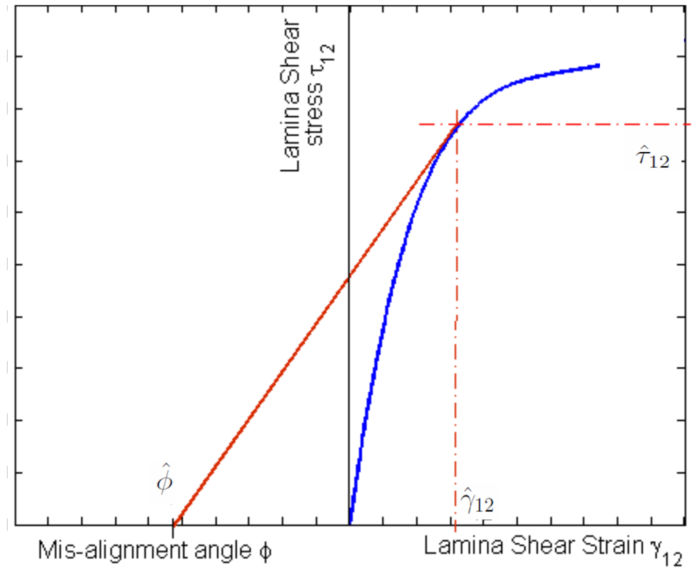

Figure B.2: Considere construction

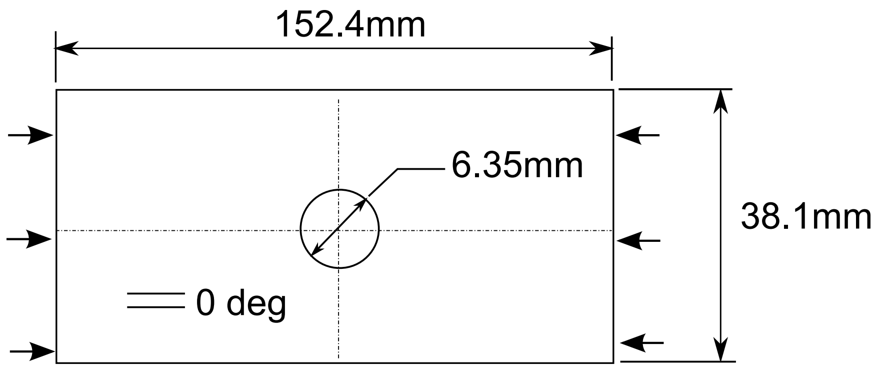

Figure B.3: Dimensions of compression test coupons with hole.

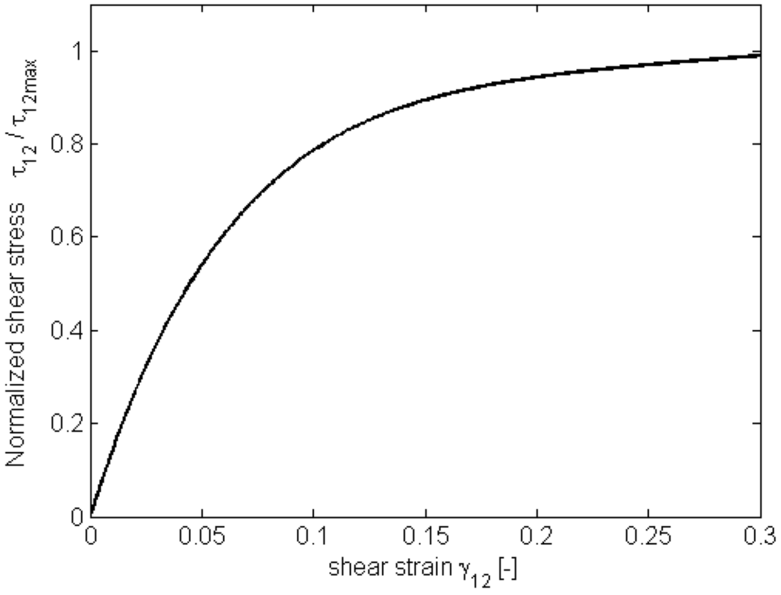

Figure B.4: In-situ shear stress-strain

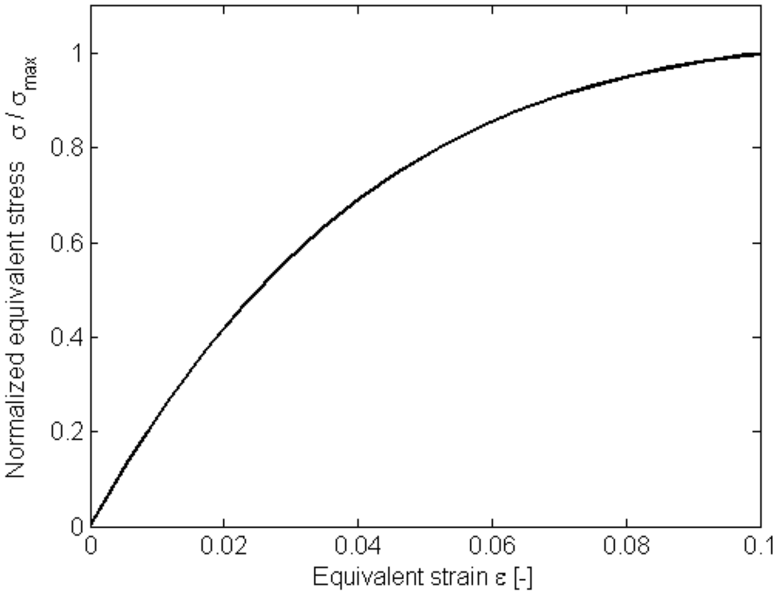

Figure B.5: Equivalent stress-strain curve

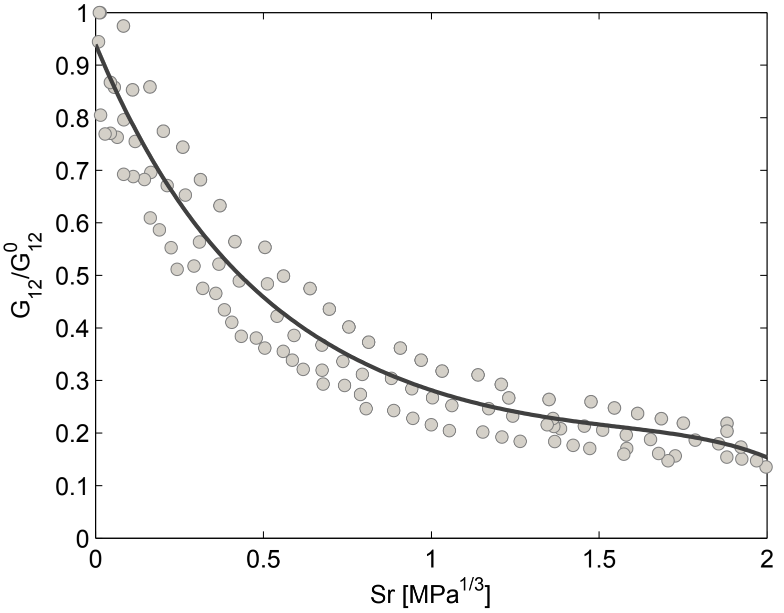

Figure B.6: Shear damage curve

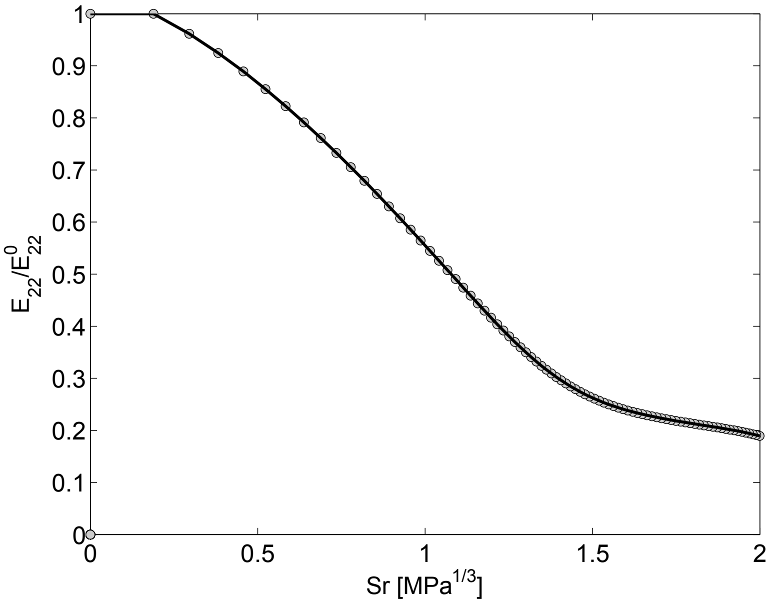

Figure B.7: Transverse damage curve

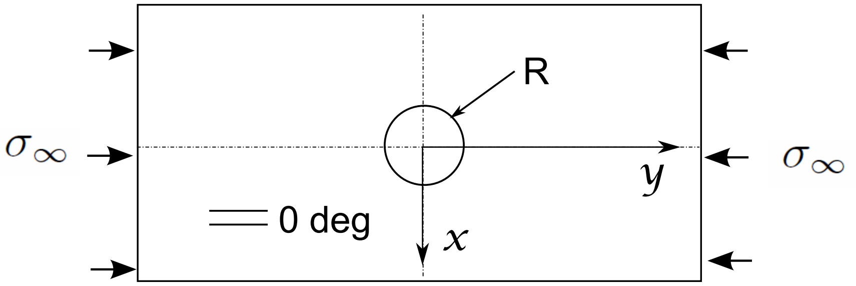

Figure B.8: Infinite plate with a hole under compression

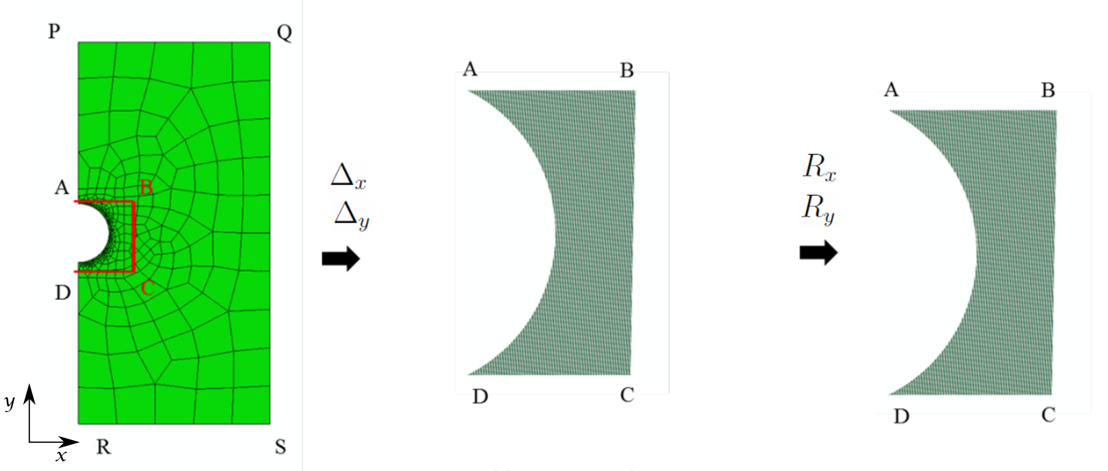

Step 1	Step 2	Step 3
Global linear analysis	Local liner analysis	Local response analysis
Lamina: Ortho	Fiber-ortho, Matrix-iso	Fiber-ortho, Matrix-iso
(P-Q) $u = 0, v = -\delta$	(A-B) $u = \Delta_x, v = \Delta_y$	(A-B) $u = \Delta_x, v = \Delta_y$
(Q-S) $u = free, v = free$	(B-C) $u = \Delta_x, v = \Delta_y$	(B-C) $F_x = R_x, F_y = R_y$
(S-R) $u = 0, v = 0$	(C-D) $u = \Delta_x, v = \Delta_y$	(C-D) $u = R_x, v = R_y$
(R-D,A-P) $u, v = X\ symm$	(D-A) $u = \Delta_x, v = \Delta_y$	(D-A) $F_x = R_x, F_y = R_y$

Figure B.9: Steps in global-local analysis

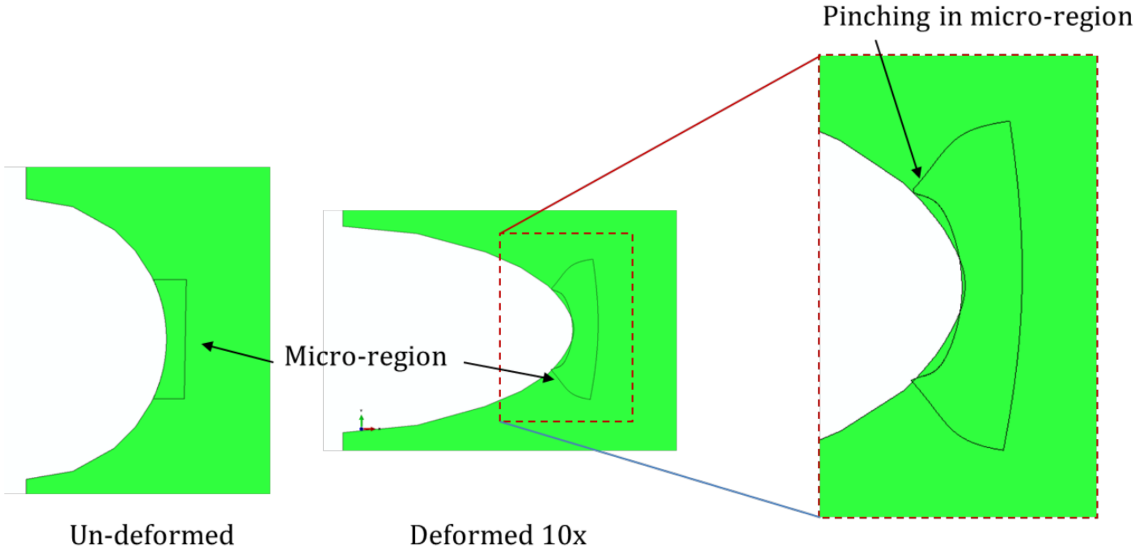

Figure B.10: Pinching in local analysis when reaction forces are not applied on the free-edge.

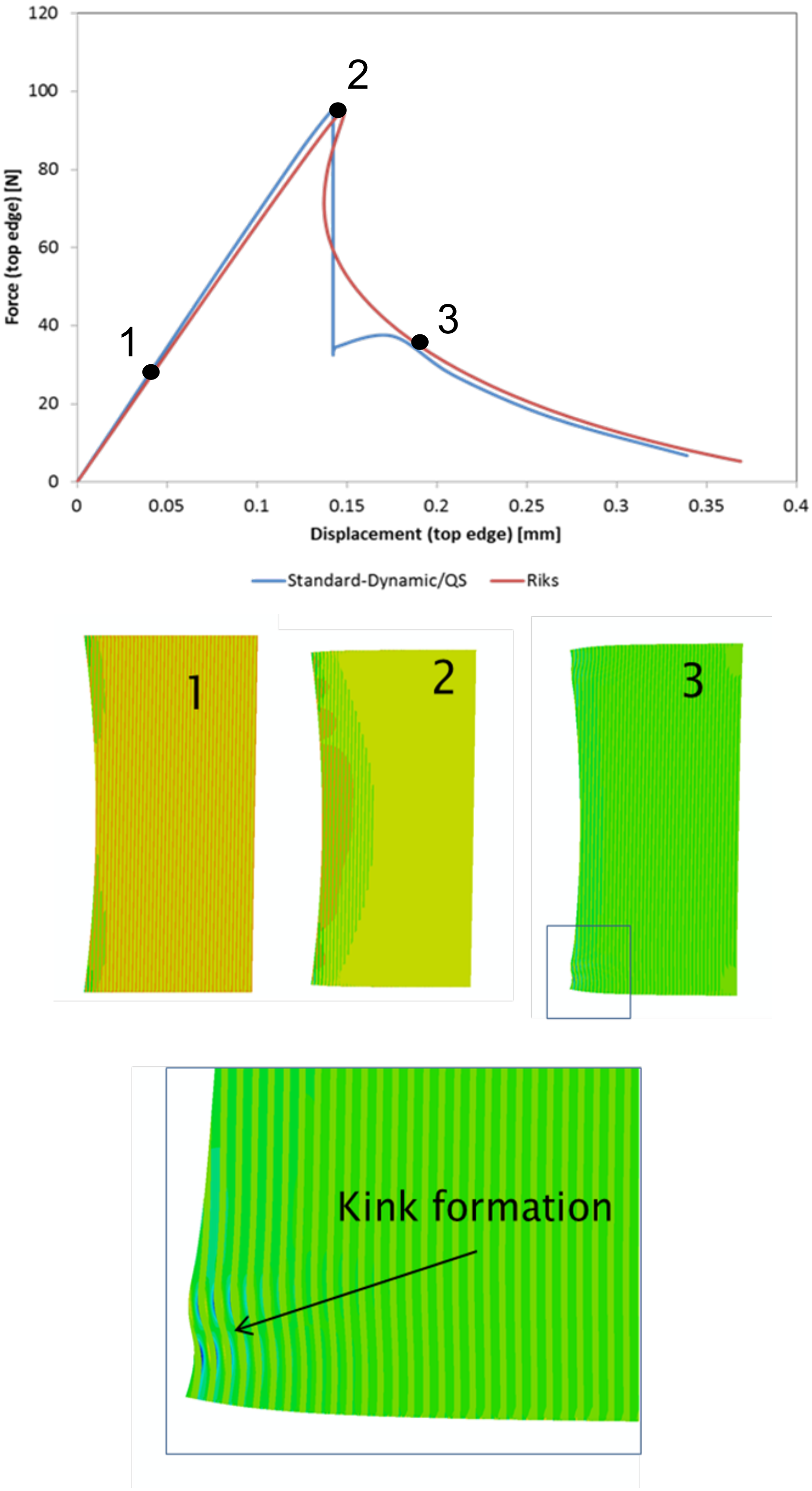

Figure B.11: Typical result in global-local analysis. Top: Load displacement plot from response analysis of micro region. Two methods are shown, Standard-dynamic and Riks analysis. Middle: Shows the axial stress plots at load points indicated on the load-displacement curve. Bottom: shows the kink band formation in the micro region.

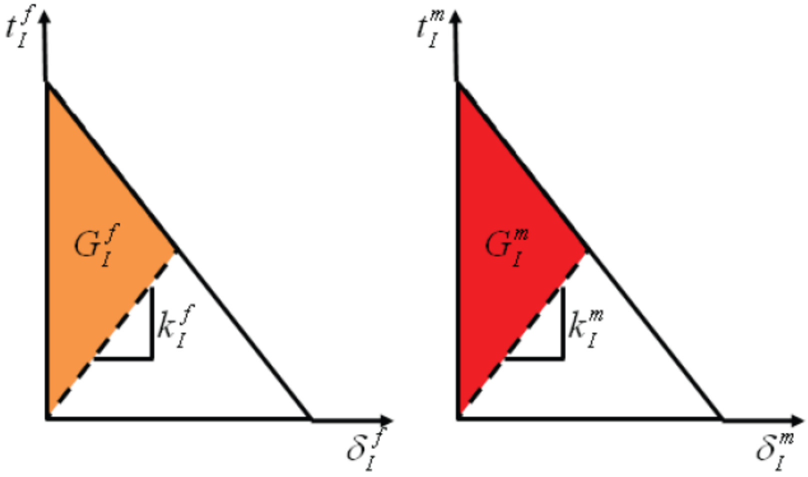

(a) Mode I fiber fracture. (b) Mode I matrix fracture.

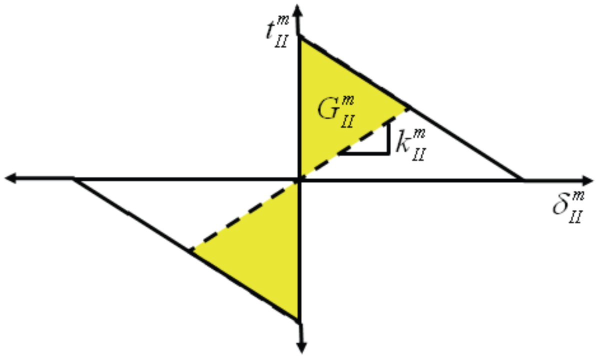

(c) Mode II matrix fracture.

Figure B.12: Traction-separation laws used in second order analysis

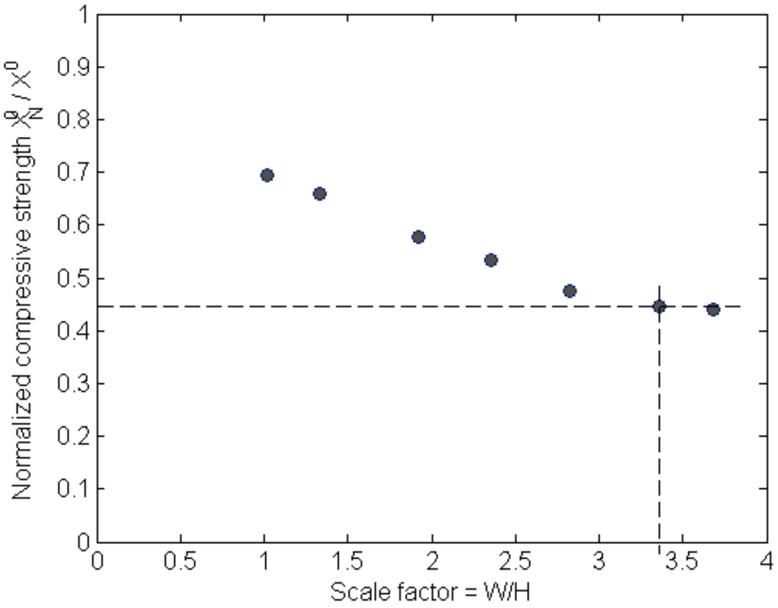

Figure B.13: Scaling study result

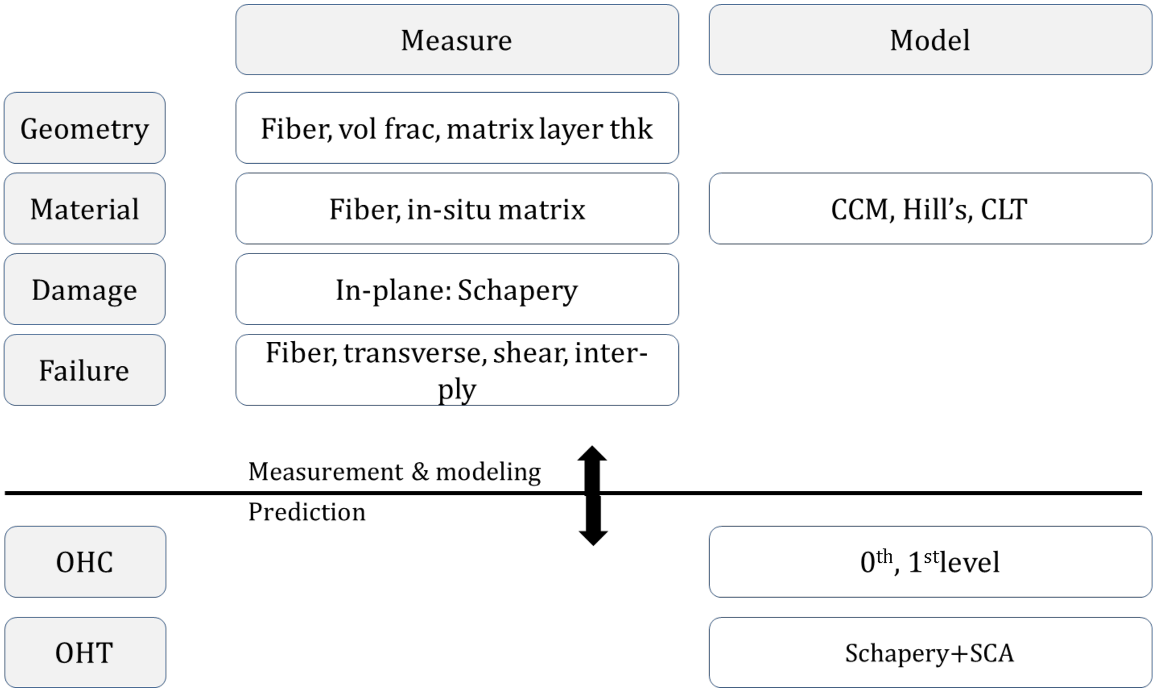

Figure B.14: General procedure for OHC & OHT analysis

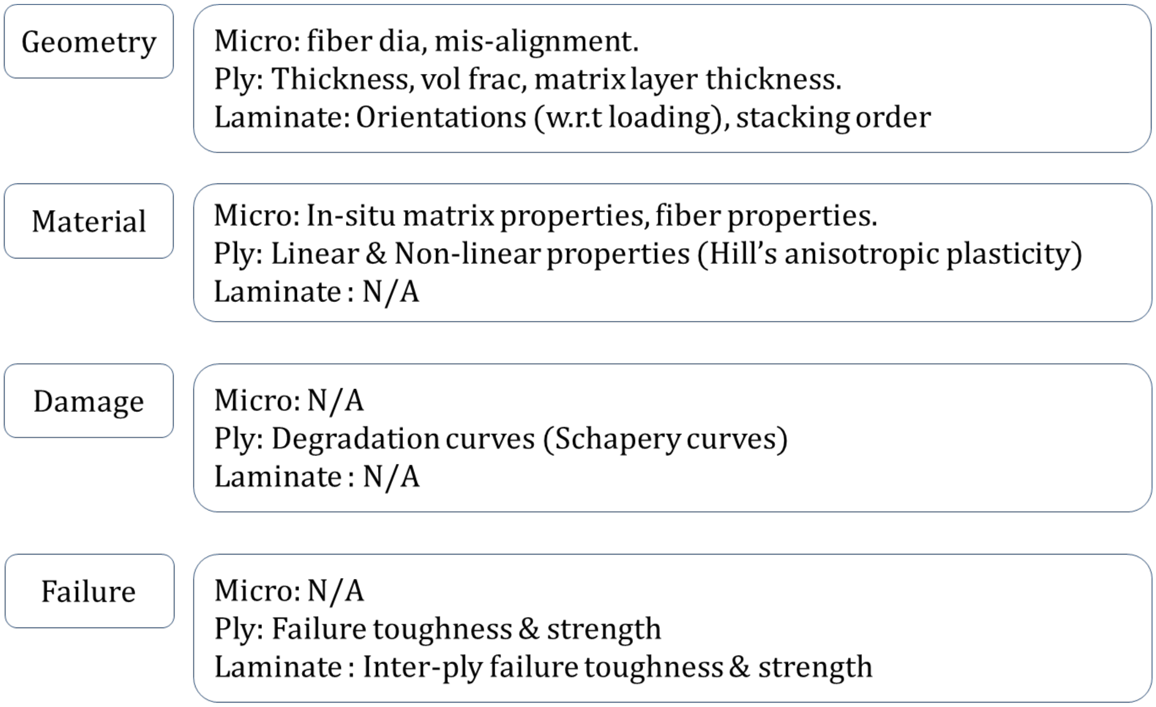

Geometry	Micro: fiber dia, mis-alignment. Ply: Thickness, vol frac, matrix layer thickness. Laminate: Orientations (w.r.t loading), stacking order
Material	Micro: In-situ matrix properties, fiber properties. Ply: Linear & Non-linear properties (Hill's anisotropic plasticity) Laminate : N/A
Damage	Micro: N/A Ply: Degradation curves (Schapery curves) Laminate : N/A
Failure	Micro: N/A Ply: Failure toughness & strength Laminate : Inter-ply failure toughness & strength

Figure B.15: Measurements required for a typical laminate analysis

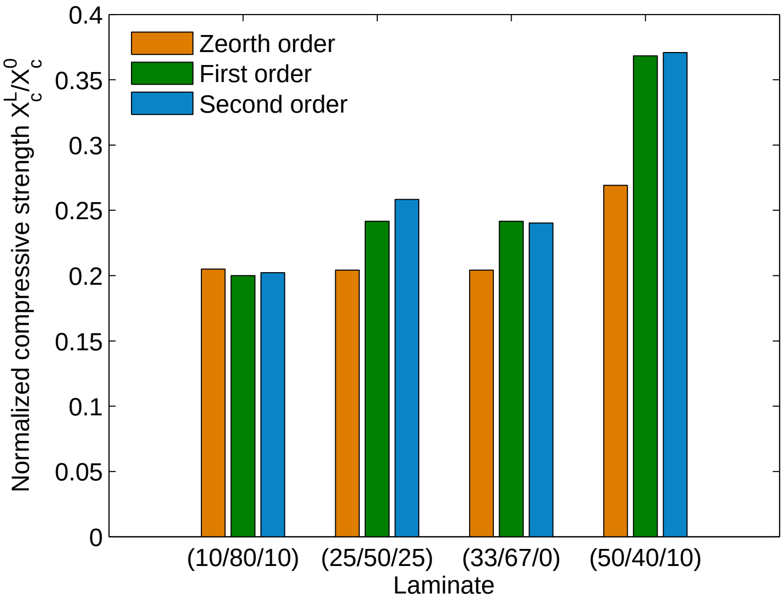

Figure B.16: OHCS results

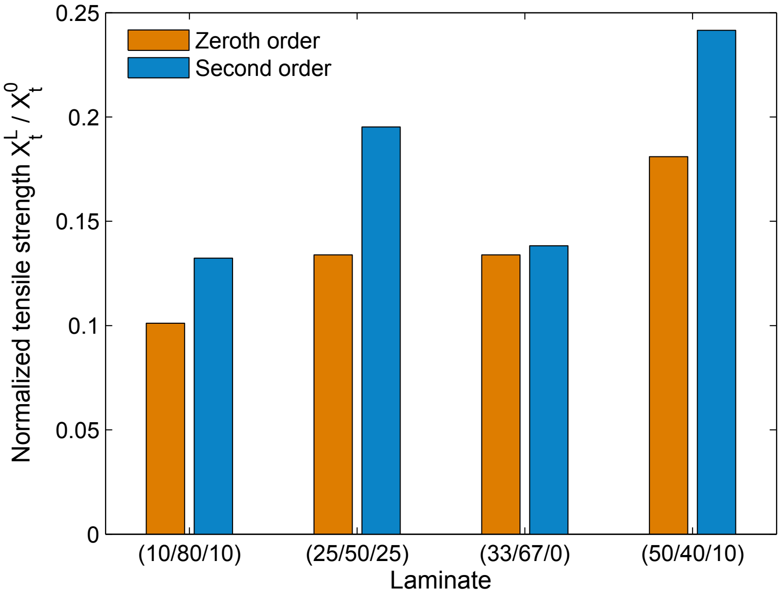

Figure B.17: OHTS results

APPENDIX C

Experimental determination of validated, critical interfacial mode I & II energy release rates in a composite sandwich panel

Introduction

Sandwich composite materials are finding increasing applications in the aerospace and wind turbine industry due to high specific (per unit mass) shear strength properties. A typical sandwich structure is a two material system with a low stiffness core and high stiffness face sheets. The face sheets are bonded to the core material, which makes the interface the weakest section of the structure. Most failure in sandwich composites is initiated at the interface which is a transition region in a bi-material system. Considerable research has been devoted to understanding and characterizing bi-material interface fracture using analytical, numerical and experimental methods. Analytical approaches can be classified into global (based on beam theory [102, 101]) and local (based on crack tip region singular field [96]) formulations. These methods are developed to extract energy release rate and/or stress intensity factor and mode mixity ratios. Pioneering work by Suo & Hutchinson [96], based on linear elastic fracture mechanics (LEFM), has been extended to many different test configurations to extract mode I and mode II energy release rates [30, 95, 94]. Improvements by accounting for shear deformation [101] and root rotations [64] have also been made to classical formulations.

Available numerical methods used for analysis, generally follow two approaches; they are either based on Irwin's stress intensity factor [52], or on energy release rates [13] attaining critical values, either as single mode problems or as mixed mode ones. For failure prediction, particularly under mixed-mode conditions, cohesive zone based methods implemented using the finite element method, for example, [104], are more suitable because of its ease of implementation and versatility in analysing complicated geometries. Cohesive zone based methods require critical energy release rates and cohesive strengths in pure mode I (G_{Ic},σ_c) and mode II (G_{IIc},τ_c). Traditionally, DCB, ENF and lap-shear (and sometimes, button-peel) tests are employed to determine these critical quantities, [45]. However, this is not as straight forward in the case of sandwich structures, because the crack plane at the face-sheet/core interface, needed to determine critical interfacial parameters, is not situated at a location that allows single mode (pure) tests to be carried out.

There have been experimental methods reported to extract mode I and mode II energy release rates,[14, 24]. These methods are in general a modification of two fundamental test configurations, Double Cantilever Beam (DCB) and End Notch Flexure (ENF) test. However, due to the location of the crack plane, all configurations have some element of mode mixity. Mixed mode tests, such as the un-symmetrical Double Cantilever Beam (UDCB) [94], Unsymmetrical End Notch Flexure (UENF) [95] and Single Leg Bend (SLB) [30, 24] test have found popularity among experimentalists due to their simplicity and available closed form solutions. Other more complicated test methods like Uneven Bending Moment DCB (DCB-UBM) [64] have also been used. All the methods mentioned above provide energy release rate contributions to the total G obtained, however, when total G is critical, the component values, G_I and G_{II} may not have attained criticality. Hence, extensive numerical iterations are required to match the load displacement curves of such coupon tests to subsequently extract the component critical parameters.

In this study, a simpler approach is employed to obtain G_{Ic} and G_{IIc} experimentally. These values are validated using the results from an independent mixed mode test in conjunction with a prediction using the DCZM and a finite element model.

Sandwich Specimen Designs

Obtaining critical mode I & mode II strain energy release rates and corresponding cohesive strengths, for an interface between the face-sheet and core of sandwich panel is difficult because this interface is shifted away from the neutral axis of the sandwich panel, causing both shear and peel to exist even for traditionally pure mode I & mode II tests that use DCB and ENF configurations. Formulations for unsymmetrical DCB and ENF have been developed; however, these methods only provide the contribution of individual failure modes and not the critical energy release rates from each mode. To obtain pure mode I & mode II energy release rates, the approach used here was to simply modify the geometry of the sandwich structure such that the intended plane of fracture coincides with the neutral axis. This is achieved by using a sandwich specimen that has approximately similar bending stiffnesses above and below the cracking plane. The resulting coupon geometry is an unsymmetrical sandwich with respect to the geometrical mid plane but is symmetrical with respect to the interface between the top face sheet and core, which is the plane of interest.

The approach, though simple, can be difficult to achieve with actual composite material, because thickness of the face sheets are multiples of individual lamina (ply) thickness, which provides discrete fixed values of thickness. Hence, an optimization formulation should be used to obtain geometries with fracture plane symmetry by minimizing the difference between the bending stiffness of laminates above and below the interface.

$$min\ e = |D_T - D_B| \tag{C.1}$$

with constraints on the thickness

$$h_1 + h_2 + h_3 - H = 0;\ h_2 > 0 \tag{C.2}$$

here, subscripts 'T' & 'B' refer to the top and bottom laminate of the bi-material sandwich interface, H is the total sandwich thickness, which is a fixed value and h_1,h_2 & h_3 are the top face sheet, core and bottom face sheet thicknesses respectively. D_i denotes the bending stiffness which is a function of material properties and thickness.

$$D_T = f(E^1_{jk}, \nu^1_{jk}, G^1_{jk}, h_1);\ D_B = f(E^{2,3}_{jk}, \nu^{2,3}_{jk}, G^{2,3}_{jk}, h_2, h_3) \tag{C.3}$$

where, superscripts '1','2','3' refer to the top face sheet, core and bottom face sheet respectively. E_{jk},G_{jk},ν_{jk} are the elastic modulus, shear modulus and Poison's ratio, respectively, for orthotropic material. The sub-laminate bending stiffnesses are calculated based on classical lamination theory, [50].

Influence of material and geometric parameters

The optimization procedure described above will provide the ideal geometry required for pure mode I and pure mode II testing. However, in practice this might not be the case due to variations in material and geometry. Hence, it is important to ensure that there is no significant change in test results due to material and geometric variation. To study the influence of material and geometry variation on pure DCB and ENF result, an analytical method was employed.

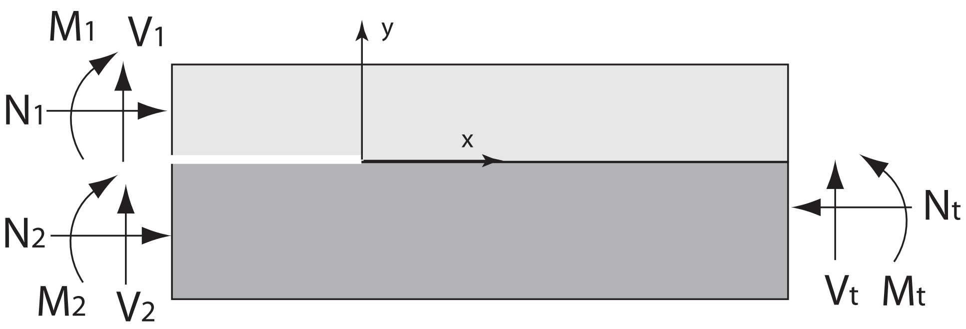

Figure C.1: Bi-material system under general loads

The basic analytical formulations used here follows the shear deformable bi-layer beam theory proposed by Wang & Qiao [101], as shown in figure(C.1). The formulation is based on split beam theory and the energy release rate in mode I and mode II are obtained using a global approach. The expressions for mode I and mode II energy release rates are given as:

$$G_I = \frac{1}{2}(\frac{1}{B_T} + \frac{1}{B_B})[V + k(M + \frac{h_T N}{2})]^2 \tag{C.4}$$

$$G_{II} = \frac{1}{h_T\xi + 2\eta}(\xi M - \eta N)^2 \tag{C.5}$$

here, M, N, V are the effective moment, normal and shear forces on the bi-material interface crack tip and corresponding parameters are, [101],

$$M = M_1 - (\frac{\eta}{\xi}A_M - \frac{1}{\xi}\frac{h_B}{2D_B})M_t + (\frac{\eta}{\xi}A_N - \frac{1}{\xi}\frac{1}{C_B})N_t \tag{C.6}$$

$$N = N_1 - A_M M_t + A_N N_t \tag{C.7}$$

$$V = V_1 - [(\frac{\eta}{\xi} + \frac{h_T}{2})A_M - \frac{1}{\xi}\frac{h_B}{2D_B}]V_t \tag{C.8}$$

$$\xi = \frac{h_T}{2D_T} - \frac{h_B}{2D_B},\ \eta = \frac{1}{C_T} + \frac{1}{C_B} + \frac{(h_T + h_B)h_B}{4D_B} \tag{C.9}$$

$$A_M = \frac{(D_T + D_B)h_B + \xi D_T D_B}{2D_B(D_T + D_B)\eta + \xi D_T D_B(h_T + h_B)} \tag{C.10}$$

$$A_N = \frac{2(D_T + D_B)}{2C_B[2(D_T + D_B)\eta + \xi D_T(h_T + h_B)]} \tag{C.11}$$

$$k = \sqrt{\frac{B_T B_B[2(D_T + D_B)\eta + D_T(h_T + h_B)\xi]}{D_T D_B(B_T + B_B)(2\eta + h_T\xi)}} \tag{C.12}$$

For DCB [31, 101],

$$M_1 = Pa,\ N_1 = V_1 = 0;\ M_t = N_t = V_t = 0 \tag{C.13}$$

For ENF [95],

$$M_1 = P_T a,\ N_1 = 0,\ V_1 = P_T;\ M_t = Pa/2,\ N_t = 0,\ V_t = P/2 \tag{C.14}$$

where, P is the applied load, a is the crack length. P_T is the load carried by the material above the interface in the ENF test and, the expression for P_T is provided by Sundararaman & Davidson [95].

Using the formulation above, a perturbation analysis was conducted, where independent material parameters were varied within ±10% of nominal, and thicknesses of the top and bottom face sheet were varied ±3 plies of nominal. Figure(C.2) shows the effect of material variation on G_I and G_{II} with respect to nominal values G_I^0 and G_{II}^0. Overall, with 10% variation in material properties only about ±6% variation in DCB G_I values and -4% to 8% variation in ENF G_{II} is seen, indicating material variations have small impact on values of $G_{I/II}$. As expected, the thickness variation

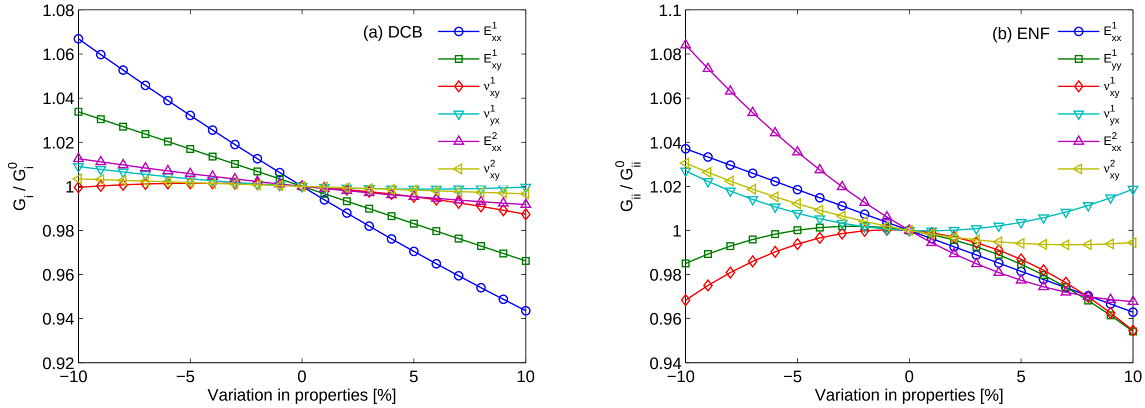

Figure C.2: Change in energy release rate due to variation in material properties in, (a) DCB test (b) ENF test.

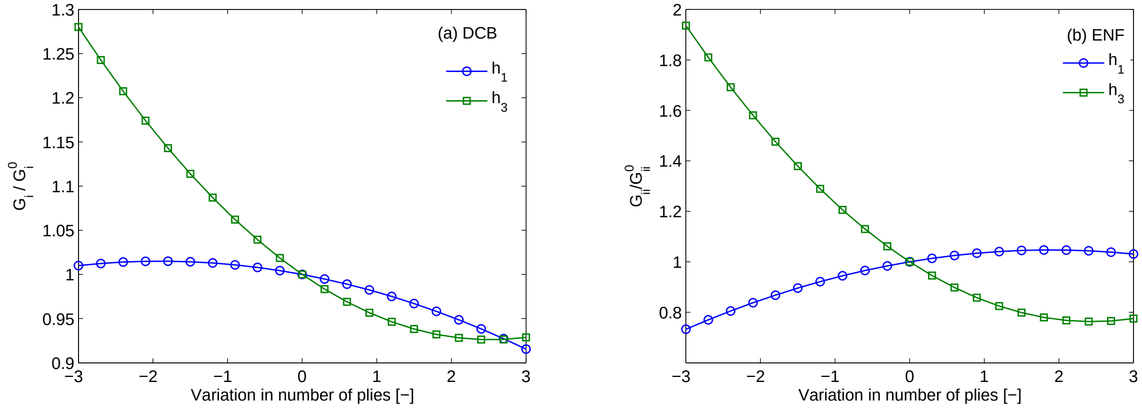

Figure C.3: Change in energy release rate due to variation in face sheet thickness in, (a) DCB test (b) ENF test.

due to changing the number of plies in the bottom face sheet laminate has a higher impact on the values obtained for both DCB and ENF energy release rates. Reduction in thickness has greater influence on $G_{I/II}$ with maximum change of about 25% in case of DCB and about double that in the case of ENF as shown in figure(C.3). The variation is particularly severe in case ofthe ENF test. Clearly, the analysis indicates criticality of the bottom face sheet thickness when modifying geometries for pure mode I and pure mode II experiments. Overall, if the material thickness is maintained at a given value, then the variation in $G_{I/II}$ are within ±10%, which is reasonable.

Experiment

Using the optimization formulation described above, coupon dimensions corresponding to DCB & ENF testing was determined. The manufactured specimen thickness are listed in table C.1.

Modified coupon DCB & ENF Test

Displacement controlled DCB and ENF experiments were conducted with the modified sandwich panels. The geometry of the sample is shown in figure(C.4) and table C.1 lists the dimensions. The initial crack was introduced between the top face sheet and the adhesive core using a Teflon® film, inserted during manufacturing of the sandwich coupons. For DCB tests, steel blocks with a transverse through hole at its center were bonded to the free end of the laminates for pin joint load transfer. The pin joint was lubricated using Teflon lubricant to reduce frictional loss. A three point bend fixture was employed for the ENF test. Clear markings on the specimen side surfaces were used to track crack growth. Material properties of the bi-axial face sheet and adhesive core are given in table C.2

Table C.1: Nominal specimen dimensions for DCB & ENF tests

Type	L (mm)	b (mm)	h_1 (mm)	h_2 (mm)	h_3 (mm)	a_0 (mm)
DCB	120	25.4	4.83	3.5	2.76	53
ENF	70	25.4	4.83	3.5	2.76	15

Table C.2: Nominal specimen material properties

Type	$E11$ (GPa)	$E22$ (GPa)	μ_{12} (-)	μ_{21} (-)	G_{12} (GPa)
Composite	11.5	8.0	0.3	0.25	3.0
Core	3.0	3.0	0.3	0.3	1.2

The tests were conducted on an MTS universal test machine with a crosshead displacement rate of 1mm/min. Load was measured continuously using a high accuracy

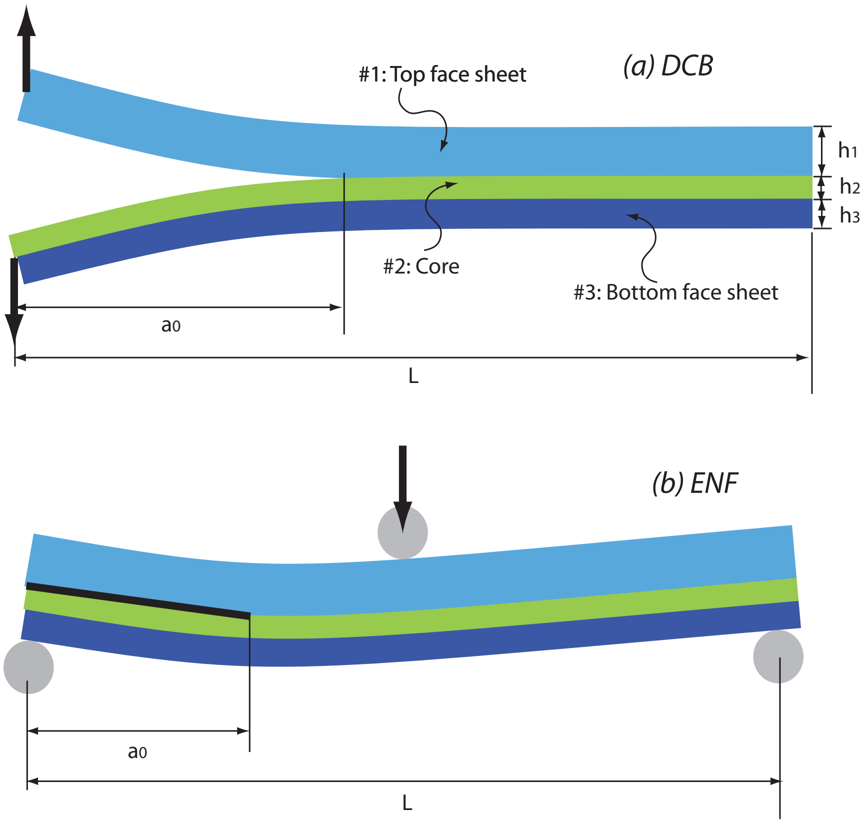

Figure C.4: Double Cantilever Beam (DCB) and End Notch Flexure (ENF) test coupon geometry tension/compression load cell linked up to a data acquisition system. A high resolution SLR camera, time synchronized with loading, was used to capture crack zone images with a framing rate of 1 frame per second. The images were then analyzed manually, using a linear pixel measuring software calibrated against a reference grid pattern marked on a typical specimen. This method gives crack length in the time domain which can be then converted to plot crack length against load and load point displacement.

In the DCB specimen, though the failure was mainly through the interface (figure (C.5 -a)), beyond crack growth of about 15 mm, an oscillatory pattern is observed indicating the crack turning in and out of the adhesive. This is confirmed by examining the completely broken samples of the tested coupons (figure C.5 -b). A small amount of rigid body rotation is also observed. These inconsistencies can be attributed to manufacturing constraints arising from difficulty in maintaining required dimensions, especially dealing with layered materials. However, the fact that the crack tends to turn back to the interface indicates that this test configuration can be used for pure mode I testing. Load displacement curves for the DCB tests are shown in figure(C.6). A through thickness fracture was observed in one of the sample after the crack had propagated by 12 mm. Overall, the load displacement response showed reasonable consistency in peak load and post-peak response. Energy release rates from the DCB test results were calculated using Modified Beam Theory [7]. Figure(C.7) provides the G versus crack length curve, which shows slightly larger values at the beginning but the spread diminishes as the crack length increases, suggesting a fairly constant value. The average and standard deviation of G_I is provided in table C.3, these are the values used as critical energy release rates, later in conjunction with the SLB test.

Figure(C.8) shows a side view of a ENF test specimen with the crack propagating entirely through the interface. There were two samples that showed de-lamination occurring in the face sheets and parallel to the interfacial crack propagation, but

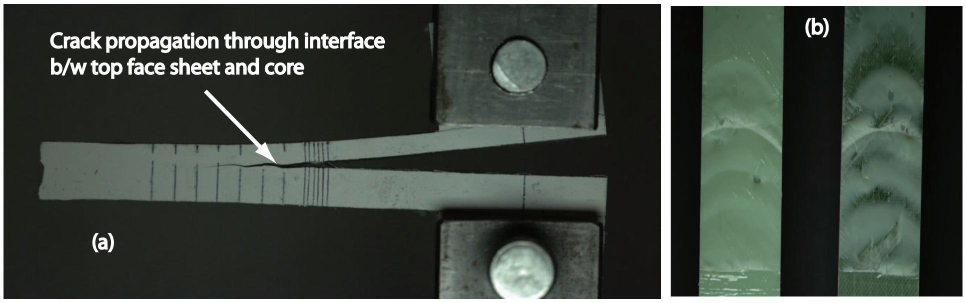

Figure C.5: Double Cantilever Beam (DCB)- modified sandwich coupon

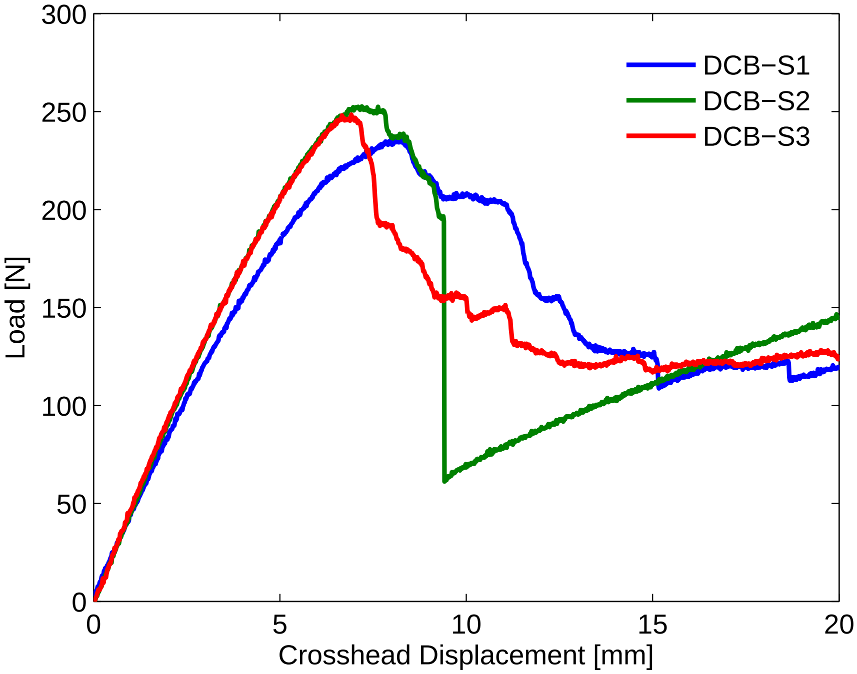

Figure C.6: Force-displacement plots for the DCB tests.

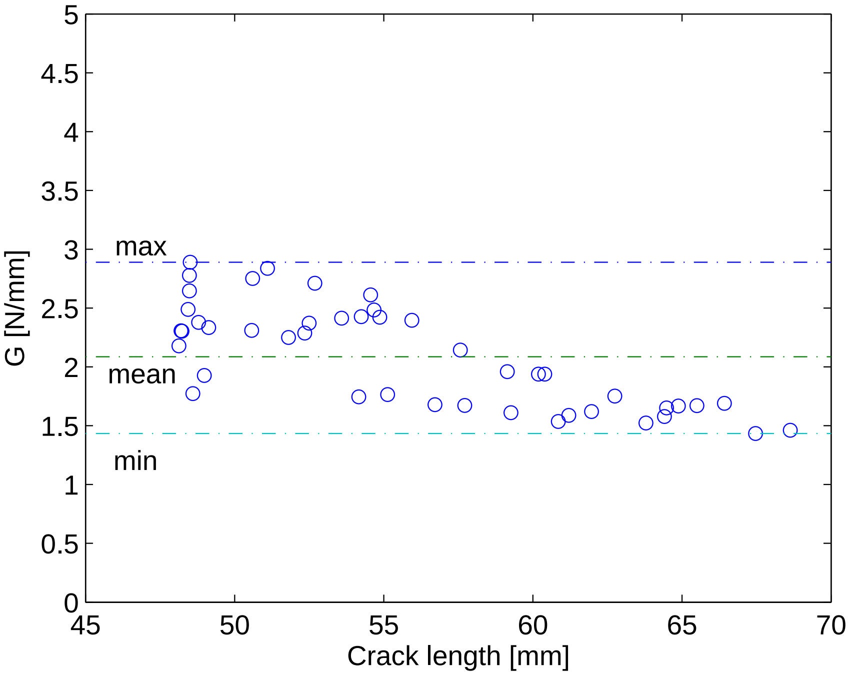

Figure C.7: G v/s crack length variation for DCB tests.

near the loading head. The majority of ENF tests showed consistency in peak load, figure(C.9), however, the difference in stiffness indicates variability due to manufacturing. The energy release rate for the ENF specimen was calculated based on the compliance method. The average and standard deviation of G_{II} are also given in table C.3.

Table C.3: Energy release rates obtained from DCB and ENF tests

Type	*Avg* G_I (N/mm)	*Std* (N/mm)	*Avg* G_{II} (N/mm)	*Std* (N/mm)
DCB	2.08	0.419	-	-
ENF	-	-	20.9	1.55

SLB Validation Test

To validate the critical G_I and G_{II} obtained using the modified DCB and ENF tests, an independent test is required. Hence, a displacement controlled Single Leg

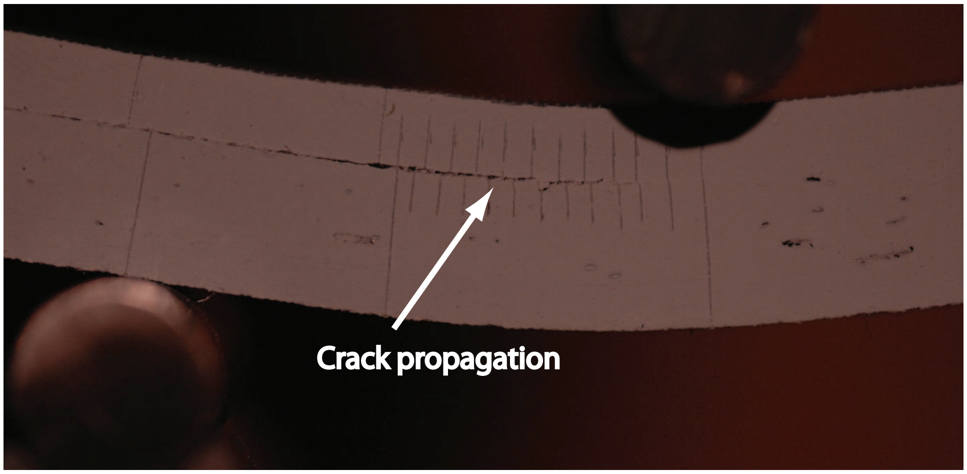

Figure C.8: End Notch Flexure (ENF) - modified coupon.

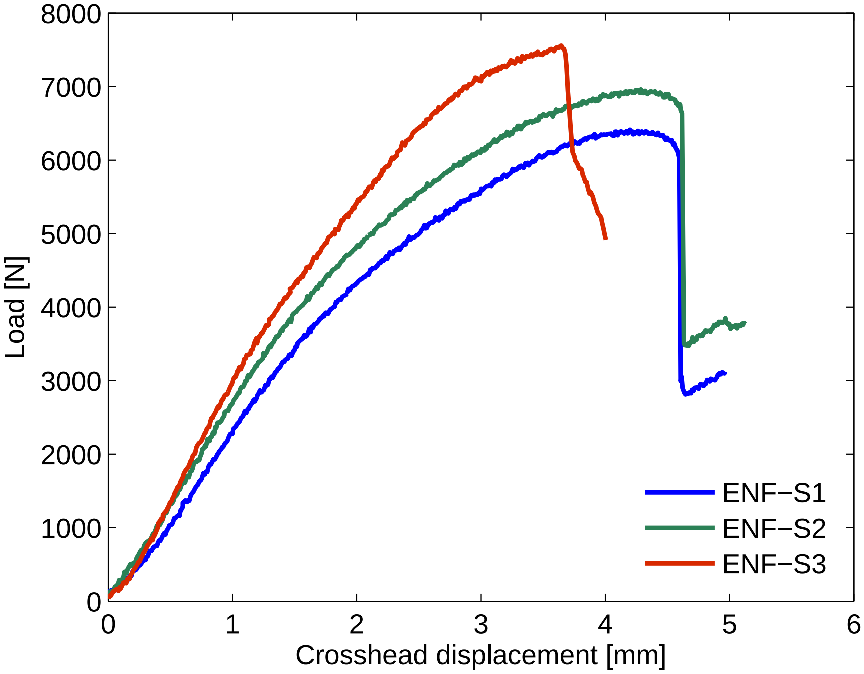

Figure C.9: Force-displacement plots for ENF tests.

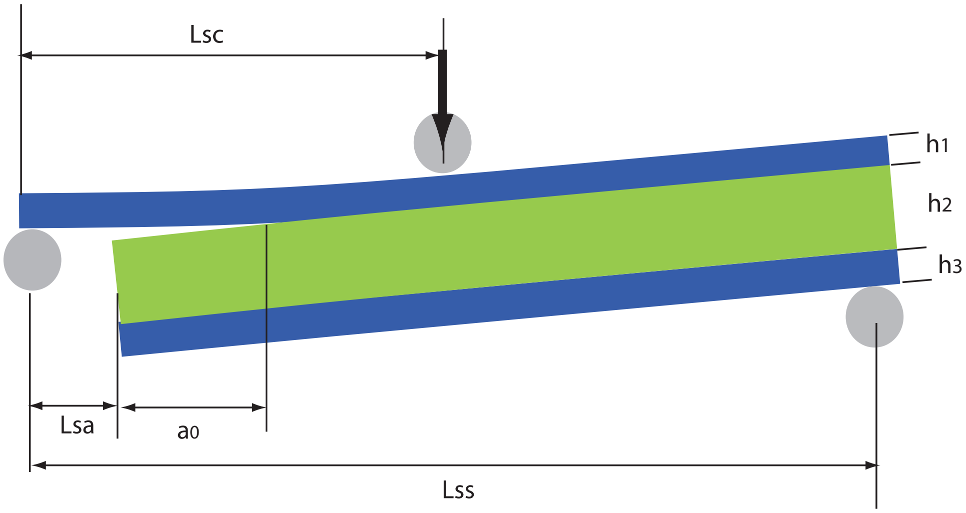

Figure C.10: Validation using the Single Leg Bend (SLB) test.

Bend (SLB) test was conducted that drives an interfacial crack under mixed-mode conditions. The SLB geometry and configuration used are shown in figure(C.10) and listed in table C.4. The single leg bend test is essentially a three point bend test with the lower half of the bi-material interface free of loading. Even though the SLB is a mixed mode test, it is mode I dominated, in the sense that majority of energy is released due to crack opening than crack sliding.

Table C.4: Nominal specimen dimensions for SLB tests

Type	L_{ss} (mm)	L_{sc} (mm)	L_{sa} (mm)	h_1 (mm)	h_2 (mm)	h_3 (mm)	a_0 (mm)
SLB	120	60	20	4.83	10	4.83	10

The SLB test specimens showed de-lamination in the top face sheet after about 10mm of interface de-bonding as shown in figure(C.11). This phenomenon confirms the basic notion that the SLB test starts from a mode I dominated contribution and gradually increases the mode II contribution. De-lamination in the face sheet may be caused because the mode II critical energy release rate of the composite face sheet is lower than the corresponding value at the interface.

The force displacement curve for the SLB test is shown in figure(C.12). Good

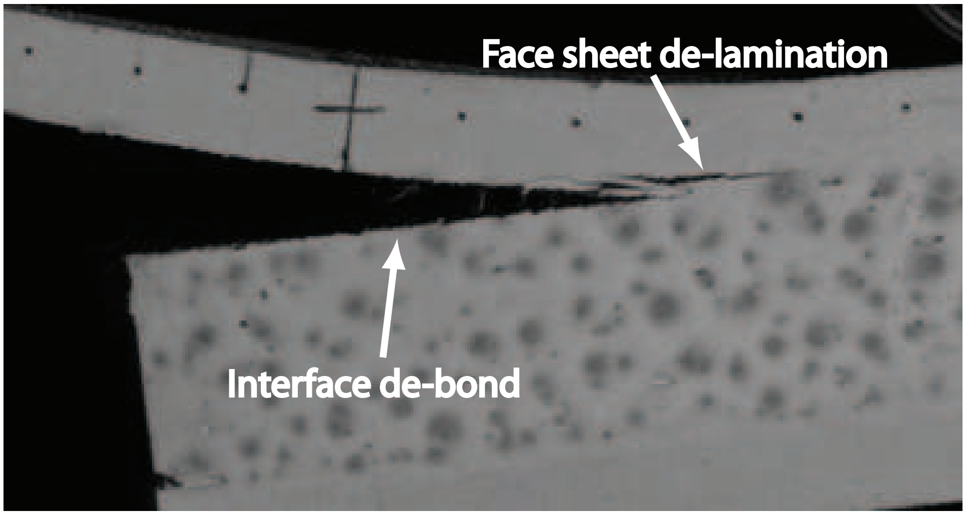

Figure C.11: Interface debond and face sheet delamination observed during the SLB test.

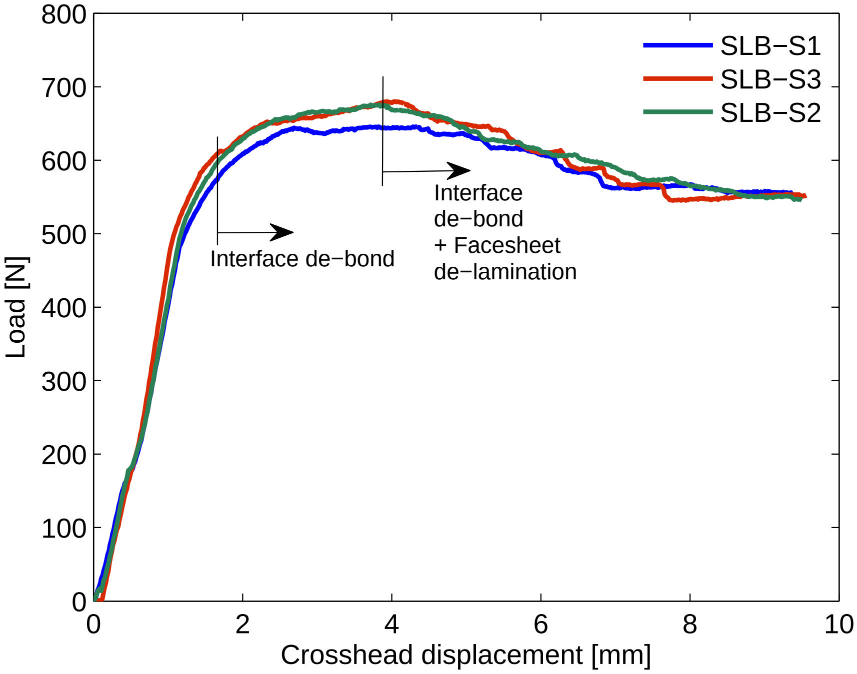

Figure C.12: Interface debond and face sheet delamination observed during SLB test.

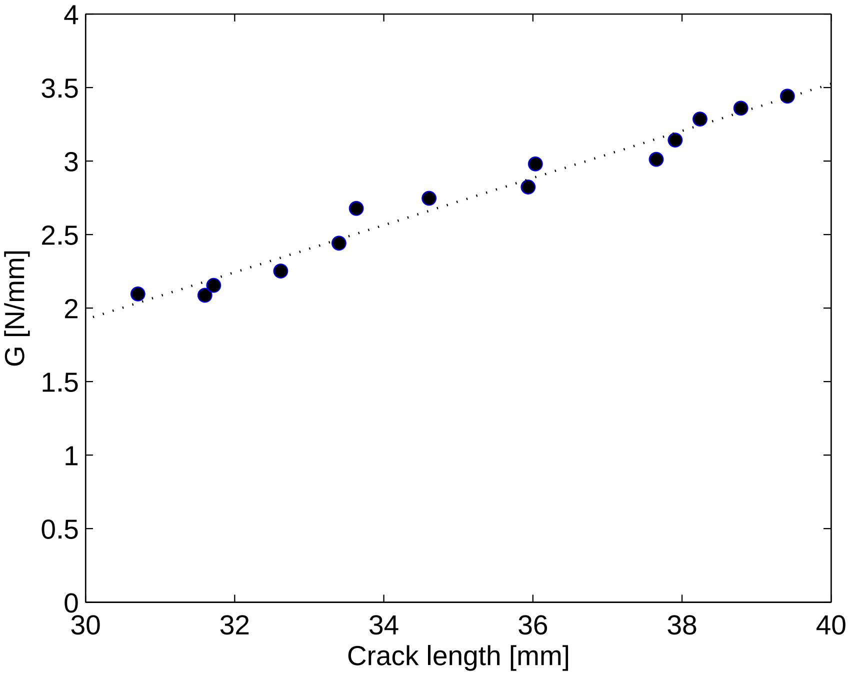

Figure C.13: Typical G v/s crack length curve for a SLB test.

test repeatability is seen between samples. A steady increase in the load is seen until start of composite de-lamination. The strain energy release rate for the SLB test, for the length of interface de-bonding, was calculated using the compliance method and is shown in figure(C.13). An increase in G also indicated the increasing mode II contribution.

Numerical simulation

The numerical simulations of the DCB, & ENF tests, and the prediction of the SLB test, were conducted using the finite element method in conjunction with the DCZM. An explicit DCZM code is implemented through a user defined interface element (UEL) subroutine in Abaqus®[45]. A triangular traction law was used in the simulation, where for mode I $G_{Ic} = 2.08N/mm$, $\sigma_c = 10MPa$ and for mode II $G_{Ic} = 20.9N/mm$, $\tau_c = 30MPa$ values were used. UELs are placed at the interface between the two arms of the DCB & ENF which is the crack path. The cohesive strengths, (σ_c and τ_c for mode I and II respectively) corresponding to the mean G_{Icr} ,G_{IIcr} (given in table C.3) was found in case of DCB and ENF geometries by matching the simulation's first crack initiation point with the experimental crack initiation point.

The DCZM parameters were validated by simulating the SLB experiment and comparing the load-displacement response against the experimental results. In the SLB experiments, composite face sheet de-lamination was observed, however, since the aim here is to validate interfacial DCZM parameters, we restricted the predictions to crack growth values of about BB mms, such that in this range there is no face sheet delamination. Figure(C.14) shows the comparison between the FE prediction and the experimental results. Good agreement is observed with both initiation and subsequent propagation. It is also interesting to note that the predicted force-displacement response over-shoots the experimental result approximately at the same displacement point as where de-lamination of the face-sheet composite is observed. Further work, which can capture the interaction between the face sheet delamination and interfacial cracking is the subject of a future paper. It is observed that the critical fracture parameters obtained using the modified sandwich specimens made with the same material systems, are able to successfully replicate the SLB test results, the latter being an independent validation.

Discussion & conclusion

Experiments, simulations and predictions reported here demonstrate that the critical traction separation parameters to be used in a combined FE-DCZM model of a composite sandwich panel can be obtained by conducting DCB and ENF tests on suitably designed, geometrically modified sandwich test coupons. By equalizing the bending stiffnesses of the two arms on either sides of the intended crack plane (such

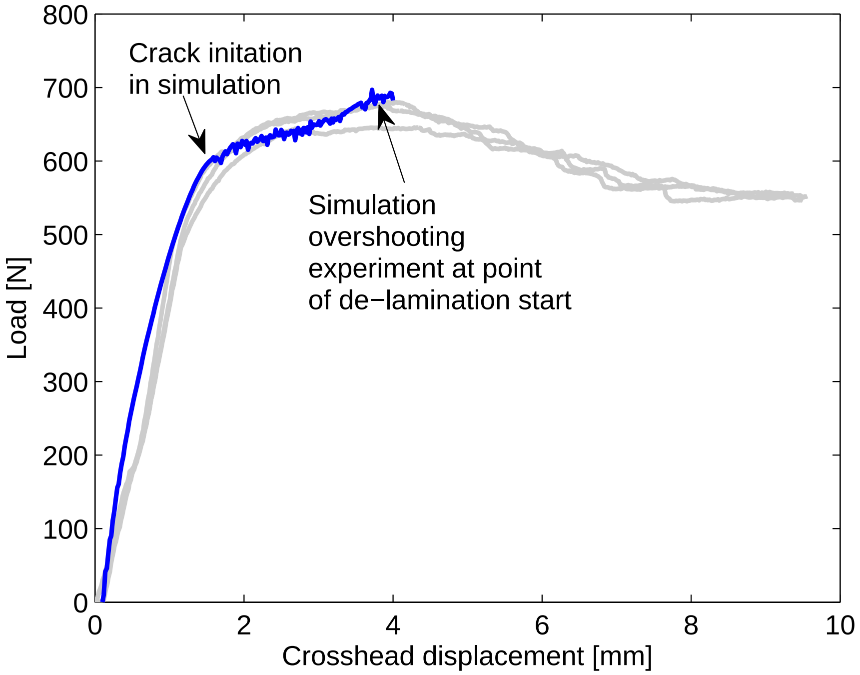

Figure C.14: The predicted force-displacement response compared against experiment for the SLB tests.

that crack plane and neutral axis coincide), it is possible to obtain pure mode I and pure mode II energy release rates experimentally. Though this is shown to be true for a thick composite and a stiff adhesive core sandwich system, this might not be the case for a soft core sandwich systems (soft foam cores for example) where extensive crack tip rotation, and through-the-thickness shear and damage, needs to be accounted for. Perhaps the major constraint for geometrical modifications of the test coupons for pure mode I & pure mode II, is in manufacturing of the composite sandwich panels to specified (and optimized) dimensions. As the perturbation study shows, DCB & ENF tests are relatively insensitive to the variation in material properties, however, they are highly sensitive to the bottom face sheet thickness variation. A tight control on the bottom face sheet thickness will be needed to ensure success of DCB and ENF test. Overall, the simple approach employed in this study can be an effective replacement to more complex experimental and numerical methods, as long as there is freedom to modify the coupon geometry. Other means of stiffening can also be employed if the basic sandwich structure cannot be modified. Bonding stiffeners on the outer surface of sandwich will also achieve the same effect.

BIBLIOGRAPHY

BIBLIOGRAPHY

[1] Abaqus. *Abaqus User's Manual, Vol. 1-3, Version 6.10-1.* Dassault Systèmes Simulia Corp., Providence, RI, 2008.

[2] J.H. Ahn and A.M. Waas. A micromechanics-based finite element model for compressive failure of notched uniply composite laminates under remote biaxial loads. *Trans. ASME J.Eng. Materials and Technology*, 121:360–366, 1999.

[3] J.H. Ahn and A.M Waas. Prediction of compressive failure in laminated composites at room and elevated temperature. *AIAA Journal*, 40 (2):346–358, 2002.

[4] A.A. Aliyu and I.M. Daniel. Effects of strain rate on delamination fracture toughness of graphite/epoxy. *ASTM Special Technical Publication*, pages 336–348, 1985.

[5] T.L Anderson. *Fracture Mechanics, Fundamentals and Applications.* CRC Press, 2 edition, 1995.

[6] A. S. Argon. Fracture of composites. treatise on materials science and technology. *Academy Press*, 1972.

[7] ASTMD. *Standard Test Method for Mode I Interlaminar Fracture Toughness of Unidirectional Fiber-Reinforced Polymer Matrix Composites.* Number ASTMD5528. ASTM International, 2007. DOI: 10.1520/D5528-01R07E03.

[8] G.I. Barenblatt. The formation of equilibrium cracks during brittle fracture. general ideas and hypotheses. axially-symmetric cracks. *Journal of Applied Mathematics and Mechanics*, 23(3):622–636, 1959.

[9] S. Basu. *Computational Modeling of Progrssive Failure and Damage in Composite Laminates.* PhD thesis, University of Michigan, Ann Arbor, MI, 2005.

[10] S. Basu, A. M. Waas, and D. R. Ambur. Compressive failure of fiber composites under multiaxial loading. *J. Mech. Phys. Solids*, 54(3):611–634, 2006.

[11] Z P. Bažant and L. Cedolin. *Stability of structures.* World Scientific, Ltd, 2010.

[12] Z. P. Bažant and B. H. Oh. Crack band theory for fracture of concrete. *Mater. and Struct.*, 16:155–77, 1983.

[13] Z.P Bažant and J. Planas. *Fracture and Size Effect in Concrete and Other Quasibrittle Materials.* CRC Press, 1998.

[14] C. Berggreen, B. C. Simonsen, and K. K. Borum. Experimental and numerical study of interface crack propagation in foam-cored sandwich beams. *Journal of Composite Materials*, 41(4):493–520, 2007.

[15] B. R. K. Blackman, J. P. Dear, A. J. Kinloch, H. Macgillivray, Y. Wang, J. G. Williams, and P. Yayla. The failure of fibre composites and adhesively bonded fibre composites under high rates of test. *Journal of Materials Science*, 30:5885–5900, 1995. 10.1007/BF01151502.

[16] E Bouchbinder. Dynamic crack tip equation of motion: High-speed oscillatory instability. *Phys. Rev. Lett.*, 103(16):164301, Oct 2009.

[17] E Bouchbinder, J Fineberg, and M. Marder. Dynamics of simple cracks. *Annual Review of Condensed Matter Physics*, 1(1):371–395, 2010.

[18] B. Budiansky and N. A. Fleck. Compressive failure of fiber composites. *J. Mech. Phys. Solids*, 41(1):183–211, 1993.

[19] B. Budiansky and N.A. Fleck. Compressive failure of fibre composites. *Journal of the Mechanics and Physics of Solids*, 41(1):183 – 211, 1993.

[20] B. Budiansky, N.A. Fleck, and J.C. Amazigo. On kink-band propagation in fiber composites. *Journal of the Mechanics and Physics of Solids*, 46(9):1637 – 1653, 1998.

[21] M. J. Buehler and H. Gao. Dynamical fracture instabilities due to local hyperelasticity at crack tips. *Nature*, 439, 307-310, 2006.

[22] Soutis C. and Filiou C. Stress distributions around holes in composite laminates subjected to biaxial loading. *Applied Composite Materials*, 5(6):365–378, 1998.

[23] N.A. Fleck C. Soutis and P.A. Smith. Failure prediction technique for compression loaded carbon fibre-epoxy laminates with open holes. *Journal of Composite Materials*, 25(11):1476–1498, 1991.

[24] W. J. Cantwell, R. Scudamore, J. Ratcliffe, and P. Davies. Interfacial fracture in sandwich laminates. *Composites Science and Technology*, 59(14):2079 – 2085, 1999.

[25] G Cherepanov. Crack propagation in continuous media pmm vol. 31, no. 3, 1967, pp. 476-488. *Journal of Applied Mathematics and Mechanics*, 31:503–512, 1967.

[26] I. Chung and Y. Weitsman. A mechanics model for the compressive response of fiber reinforced composites. *International Journal of Solids and Structures*, 31(18):2519 – 2536, 1994.

[27] D Coker, A J Rosakis, and Y Y Huang. Subsonic and intersonic dynamic crack growth in unidirectional composites. In *1999 ASME Mechanics & Materials Conference; Blacksburg, VA; USA*, pages pp. 273–274, 27-30 June 1999.

[28] P. Compston and P.-Y. B. Jar. The influence of fibre volume fraction on the mode i interlaminar fracture toughness of a glass-fibre/vinyl ester composite. *Applied Composite Materials*, 6:353–368, 1999. 10.1023/A:1008973211347.

[29] James W. Dally and Arun Shukla. Energy loss in homalite 100 during crack propagation and arrest. *Engineering Fracture Mechanics*, 13(4):807 – 817, 1980.

[30] B. D. Davidson and V. Sundararaman. A single leg bending test for interfacial fracture toughness determination. *International Journal of Fracture*, 78:193–210, 1996. 10.1007/BF00034525.

[31] B.D. Davidson. An analytical investigation of delamination front curvature in double cantilever beam specimens. *Journal of Composite Materials*, 24(11):1124–1137, 1990.

[32] P. Davidson and A.M Waas. Open hole compressive strength prediction of laminated composite plate. In *American Society for Composites 27th Technical Conference, Arlington, TX, 2012*, 2012.

[33] P. Davidson and Anthony M. Waas. Effect of fiber waviness on the compressive strength of unidirectional carbon fiber composites. In *53rd AIAA/ASME/ASCE/AHS/ASC Structures, Structural Dynamics and Materials Conference, AIAA 2012-1612, Honolulu, Hawaii, 2012*, 2012.

[34] Alfredo Balaco De Morais and Antoni Torres Marques. A micromechanical model for the prediction of the lamina longitudinal compression strength of composite laminates. *Journal of Composite Materials*, 31(14):1397–1412, 1997.

[35] Jared Nelson Douglas S. Cairns, Trey Riddle. Wind turbine composite blade manufacturing: The need for understanding defect origins, prevalence, implications and reliability. Technical report, Sandia National Laboratories, 2011.

[36] A. G. Evans. Slow crack growth in brittle materials under dynamic loading conditions. *International Journal of Fracture*, 10:251–259, 1974. 10.1007/BF00113930.

[37] Jay Fineberg, Steven P. Gross, M. Marder, and Harry L. Swinney. Instability in dynamic fracture. *Phys. Rev. Lett.*, 67(4):457–460, Jul 1991.

[38] Jay Fineberg, Steven P. Gross, M. Marder, and Harry L. Swinney. Instability in the propagation of fast cracks. *Phys. Rev. B*, 45(10):5146–5154, Mar 1992.

[39] Jay Fineberg and M. Marder. Instability in dynamic fracture. *Physics Report*, 67:141–144, 1999.

[40] N. A. Fleck, L. Deng, and B. Budiansky. Prediction of kink width in compressed fiber composites. *J. App. Mech.*, 62:329–337, 1995.

[41] L. B. Freund. *Dynamic Fracture Mechanics.* Cambridge University Press, 1990.

[42] Huajian Gao. Surface roughening and branching instabilities in dynamic fracture. *Journal of the Mechanics and Physics of Solids*, 41(3):457 – 486, 1993.

[43] C. Gonzaléz and J. Llorca. Mechanical behavior of unidirectional fiber-reinforced polymers under transverse compression: Microscopic mechanisms and modeling. *Compos. Sci. Technol.*, 67:2795–2806, 2007.

[44] A. A. Griffith. The phenomena of rupture and flow in solids. *Philosophical Transactions of the Royal Society of London. Series A, Containing Papers of a Mathematical or Physical Character*, 221:163–198, 1921.

[45] Peter A. Gustafson and Anthony M. Waas. The influence of adhesive constitutive parameters in cohesive zone finite element models of adhesively bonded joints. *International Journal of Solids and Structures*, 46(10):2201 – 2215, 2009. Special Issue in Honor of Professor Liviu Librescu.

[46] H Thomas Hahn and Jerry G Williams. Compression failure mechanisms in unidirectional composites. In *Composite Materials: Testing and Design (Seventh Conference), ASTM STP*, volume 893, pages 115–139, 1986.

[47] C. Heinrich and Anthony M. Waas. Investigation of progressive damage and fracture in laminated composites using the smeared crack approach. In *53rd AIAA/ASME/ASCE/AHS/ASC Structures, Structural Dynamics and Materials Conference, AIAA 2012-1537, Honolulu, Hawaii, 2012*, 2012.

[48] K Hellan. *Introduction to fracture mechanics.* McGraw-Hill., 1984.

[49] Richard W Hertzberg. *Deformation and fracture mechanics of engineering materials.* Wiley, 5 edition, 1983.

[50] Michael Hyer. *Stress Analysis of Fiber-Reinforced Composite Materials.* WCB McGraw-Hill, 1997.

[51] C.E. Inglis. Stresses in a plate due to the presence of cracks and sharp corners. *Transactions of the Institution of Naval Architects*, 55:219–230, 1913.

[52] G. Irwin. Analysis of stresses and strains near the end of a crack traversing a plate. *Journal of Applied Mechanics*, 24:361364, 1957.

[53] W. Ji and A.M. Waas. Progressive failure anaalysis for the interaction of interlaminar and intralaminar failure modes in composite structures with an initial delamination. *Aeronautical Journal*, 117:1–14, 2013.

[54] A. Kobayashi and S. Mall. Dynamic fracture toughness of homalite-100. *Experimental Mechanics*, 18:11–18, 1978. 10.1007/BF02326552.

[55] A. G. Kotousov. Dynamic criterion of fracture of brittle materials. *Materials Science*, 31:112–118, 1996. 10.1007/BF00565983.

[56] A. S. Krausz and K. Krausz. Fracture kinetics of crack growth. *Kluwer Academic Publishers, Dordrecht.*, 1988.

[57] V. S. Kuksenko, L. G. Orlov, and D. I. Frolov. Concentration criterion of crack growth in heterogeneous materials. *Mechanics of Composite Materials*, 15:147–152, 1979. 10.1007/BF00606091.

[58] V. S. Kuksenko, V. S. Ryskin, V. I. Betekhtin, and A. I. Slutsker. Nucleation of submicroscopic cracks in stressed solids. *International Journal of Fracture*, 11:829–840, 1975. 10.1007/BF00012900.

[59] Takayuki Kusaka, Masaki Hojo, Yiu-Wing Mai, Tomoaki Kurokawa, Taketoshi Nojima, and Shojiro Ochiai. Rate dependence of mode i fracture behaviour in carbon-fibre/epoxy composite laminates. *Composites Science and Technology*, 58(3-4):591 – 602, 1998.

[60] S Kyriakides, R Arseculeratne, EJ Perry, and KM Liechti. On the compressive failure of fiber reinforced composites. *International Journal of Solids and Structures*, 32(6):689–738, 1995.

[61] S.H. Lee and AnthonyM. Waas. Compressive response and failure of fiber reinforced unidirectional composites. *International Journal of Fracture*, 100:275–306, 1999.

[62] S. Lekhnitskii. *Anisotropic Elastic.* Mir Publishers, 1980.

[63] J. Llorca, C. Gonzalez, and J. Segurado. *Finite element and homogenization of materials.* CRC Press, 2007.

[64] Christian Lundsgaard-Larsen, Bent F. Srensen, Christian Berggreen, and Rasmus C. stergaard. A modified dcb sandwich specimen for measuring mixed-mode cohesive laws. *Engineering Fracture Mechanics*, 75(8):2514 – 2530, 2008.

[65] Hironori Maikuma, John W. Gillespie, and Dick J. Wilkins. Mode ii interlaminar fracture of the center notch flexural specimen under impact loading. *Journal of Composite Materials*, 24(2):124–149, 1990.

[66] JF Mandell, DD Samborsky, and L Wang. Effects of fiber waviness on composites for wind turbine blades. In *International SAMPE symposium and exhibition*, pages 2653–2666. SAMPE; 1999, 2003.

[67] G. Maugin. *The Thermodynamics of Nonlinear Irreversible Behaviors.* World Scientific, 1999.

[68] A.B. Morais and A.B. Pereira. Application of the effective crack method to mode i and mode ii interlaminar fracture of carbon/epoxy unidirectional laminates. *Composites Part A: Applied Science and Manufacturing*, 38(3):785 – 794, 2007.

[69] Marshall Space Flight Center (MSFC). Design and manufacturing guideline for aerospace composites. Technical Report GUIDELINE NO. GD-ED-2205, NASA.

[70] Wei H. Ng, Amit G. Salvi, and Anthony M. Waas. Characterization of the insitu non-linear shear response of laminated fiber-reinforced composites. *Composites Science and Technology*, 70(7):1126 – 1134, 2010. ¡ce:title¿Special issue on Chiral Smart Honeycombs¡/ce:title¿.

[71] S. Pimenta, R. Gutkin, S.T. Pinho, and P. Robinson. A micromechanical model for kink-band formation: Part i experimental study and numerical modelling. *Composites Science and Technology*, 69(78):948 – 955, 2009.

[72] S. Pimenta, R. Gutkin, S.T. Pinho, and P. Robinson. A micromechanical model for kink-band formation: Part ii analytical modelling. *Composites Science and Technology*, 69(78):956 – 964, 2009.

[73] E. Pineda and A.M Waas. Modelling progressive failure of fibre reinforced laminated composites: mesh objective calculations. *Aeronautical Journal,*, 116:1221–1246, 2012.

[74] Evan Pineda, Anthony Waas, Brett Bednarcyk, Craig Collier, and Phillip Yarrington. Progressive damage and failure modeling in notched laminated fiber reinforced composites. *International Journal of Fracture*, 158:125–143, 2009. 10.1007/s10704-009-9370-3.

[75] S.T. Pinho, P. Robinson, and L. Iannucci. Fracture toughness of the tensile and compressive fibre failure modes in laminated composites. *Composites Science and Technology*, 66:2069–2079, 2006.

[76] Pavana Prabhakar and Anthony M. Waas. Interaction between kinking and splitting in the compressive failure of unidirectional fiber reinforced laminated composites. *Composite Structures*, 98(0):85 – 92, 2013.

[77] K. Ravi-Chandar and W. G. Knauss. Dynamic crack-tip stresses under stress wave loading a comparison of theory and experiment. *International Journal of Fracture*, 20:209–222, 1982. 10.1007/BF01140336.

[78] K. Ravi-Chandar and W. G. Knauss. An experimental investigation into dynamic fracture: I. crack initiation and arrest. *International Journal of Fracture*, 25:247–262, 1984. 10.1007/BF00963460.

[79] K. Ravi-Chandar and W. G. Knauss. An experimental investigation into dynamic fracture: Ii. microstructural aspects. *International Journal of Fracture*, 26:65–80, 1984. 10.1007/BF01152313.

[80] K. Ravi-Chandar and W. G. Knauss. An experimental investigation into dynamic fracture: Iii. on steady-state crack propagation and crack branching. *International Journal of Fracture*, 26:141–154, 1984. 10.1007/BF01157550.

[81] K. Ravi-Chandar and W. G. Knauss. An experimental investigation into dynamic fracture: Iv. on the interaction of stress waves with propagating cracks. *International Journal of Fracture*, 26:189–200, 1984. 10.1007/BF01140627.

[82] J. R. Rice. Inelastic constitutive relations for solids: an internal-variable theory and its application to metal plasticity. *J. Mech. Phys. Solids*, 19:433–455, 1971.

[83] V. W. Rosen. Mechanics of composite strengthening. fibre composite materials. In *Metals Park, Ohio: American Society of Materials*, 1965.

[84] R. A. Schapery. Prediction of compressive strength and kink bands in composites using a work potential. *Int. J. Solids Structures*, 32(6):739–765, 1995.

[85] Eran Sharon and Jay Fineberg. Confirming the continuum theory of dynamic brittle fracture for fast cracks. *Nature*, 397:333–335, Jan 1999.

[86] Kunigal Shivakumar and Legunchim Emmanwori. Mechanics of failure of composite laminates with an embedded fiber optic sensor. *Journal of Composite Materials*, 38(8):669–680, 2004.

[87] D. L. Sicking. *Mechanical Characterization of Nonlinear Laminated Composites with Transverse Crack Growth*. PhD thesis, Texas A&M University, 1992.

[88] George C Sih. *Handbook of Stress-intensity Factors for Researchers and Engineers: Stress-intensity Factor Solutions and Formulas for Reference*. Institute of Fracture and Solid Mechanics, Lehigh University, 1973.

[89] W.S. Slaughter and N.A. Fleck. Compressive fatigue of fibre composites. *Journal of the Mechanics and Physics of Solids*, 41(8):1265 – 1284, 1993.

[90] R Solecki and R.J Conant. *Advanced Mechanics of Materials*. Oxford University Press, 2 edition, 2004.

[91] Dale F. Stein and J. R. Low. Mobility of edge dislocations in silicon-iron crystals. *Journal of Applied Physics*, 31:362–369, 1960.

[92] Arun K. Subramaniyan and C.T. Sun. Continuum interpretation of virial stress in molecular simulations. *International Journal of Solids and Structures*, 45(14-15):4340 – 4346, 2008.

[93] C. Sun, M.D. Thouless, A.M. Waas, J.A. Schroeder, and P.D. Zavattieri. Ductile-brittle transitions in the fracture of plastically-deforming, adhesively-bonded structures. part i: Experimental studies. *International Journal of Solids and Structures*, 45(10):3059 – 3073, 2008.

[94] V. Sundararaman and B.D. Davidson. An unsymmetric double cantilever beam test for interfacial fracture toughness determination. *International Journal of Solids and Structures*, 34(7):799–817, 1997. cited By (since 1996) 19.

[95] V. Sundararaman and B.D. Davidson. An unsymmetric end-notched flexure test for interfacial fracture toughness determination. *Engineering Fracture Mechanics*, 60(3):361 – 377, 1998.

[96] Zhigang Suo and John W. Hutchinson. Interface crack between two elastic layers. *International Journal of Fracture*, 43:1–18, 1990. 10.1007/BF00018123.

[97] John S. Tomblin, Ever J. Barbero, and Luis A. Godoy. Imperfection sensitivity of fiber microbuckling in elastic-nonlinear polymer-matrix composites. *International Journal of Solids and Structures*, 34(13):1667 – 1679, 1997.

[98] A. Turon, P.P. Camanho, J. Costa, and J. Renart. Accurate simulation of delamination growth under mixed-mode loading using cohesive elements: Definition of interlaminar strengths and elastic stiffness. *Composite Structures*, 92(8):1857 – 1864, 2010.

[99] Nunziante Valoroso and Roberto Fedele. Characterization of a cohesive-zone model describing damage and de-cohesion at bonded interfaces. sensitivity analysis and mode-i parameter identification. *International Journal of Solids and Structures*, 47(13):1666 – 1677, 2010.

[100] A.M. Waas, C.D. Babcock., and W.G. Knauss. An experimental study of compression failure of fibrous laminates in the presence of stress gradients. *International Journal of Solids and Structures*, 26:1071–1098, 1990.

[101] Jialai Wang and Pizhong Qiao. Fracture analysis of shear deformable bi-material interface. *Journal of Engineering Mechanics*, 132(3):306–316, 2006.

[102] J. G. Williams. On the calculation of energy release rates for cracked laminates. *International Journal of Fracture*, 36:101–119, 1988. 10.1007/BF00017790.

[103] M.R. Wisnom. Modelling discrete failures in composites with interface elements. *Composites Part A: Applied Science and Manufacturing*, 41(7):795 – 805, 2010.

[104] De Xie, Sherrill B. Biggers, and Jr. Strain energy release rate calculation for a moving delamination front of arbitrary shape based on the virtual crack closure technique. part i: Formulation and validation. *Engineering Fracture Mechanics*, 73(6):771 – 785, 2006.

[105] G Yaniv and I. M. Daniel. Height-tapered double cantilever beam specimen for study of rate effects on fracture toughness of composites. *ASTM Special Technical Publication*, STP(972):241–258, 1988. cited By (since 1996) 8.

[106] S. Ya. Yarema. On the contribution of g. r. irwin to fracture mechanics. *Materials Science*, 31:617–623, 1996. 10.1007/BF00558797.

[107] Chandra S. Yerramalli and Anthony M. Waas. In situ matrix shear response using torsional test data of fiber reinforced unidirectional polymer composites. *Journal of Engineering Materials and Technology*, 124(2):152–159, 2002.

[108] Chandra S Yerramalli and Anthony M Waas. The effect of fiber diameter on the compressive strength of composites-a 3d finite element based study. *Computer Modeling in Engineering and Sciences*, 6:1–16, 2004.

[109] C.S. Yerramalli, T. Miebach, K. Chandraseker, and S.C Quek. Fiber waviness induced strength knockdowns in composite materials used in wind turbine blades. In *EWEC 2010 Proceedings*, 2010.

[110] E Yoffe. The moving griffith crack. *Philosophical magazine*, 42:739–750, 1951.

[111] S.W. Yurgartis. Measurement of small angle fiber misalignments in continuous fiber composites. *Composites Science and Technology*, 30:279–293, 1987.

[112] Min Zhou. A new look at the atomic level virial stress: on continuum-molecular system equivalence. *Proceedings of the Royal Society of London. Series A: Mathematical, Physical and Engineering Sciences*, 459(2037):2347–2392, 2003.

[113] S. N. Zhurkov and V. S. Kuksenko. The micromechanics of polymer fracture. *International Journal of Fracture*, 11:629–639, 1975. 10.1007/BF00116370.

[114] J. A. Zimmerman, E. B. Webbiii, J. J. Hoyt, R. E. Jones, P. A. Klein, and D. J. Bammann. Calculation of stress in atomistic simulation. *Modelling and Simulation in Materials Science and Engineering*, 12(4):S319–S332, 2004.